### HIGH-RESOLUTION SOIL MOISTURE RETRIEVAL ALGORITHM WITH UNCERTAINTY ESTIMATES FOR THE NASA-ISRO SAR MISSION

By

Preet Lal

#### A DISSERTATION

Submitted to
Michigan State University
in partial fulfillment of the requirements
for the degree of

Civil Engineering – Doctor of Philosophy

2024

#### **ABSTRACT**

Soil moisture is a critical component of the Earth's water cycle, essential for various environmental and agricultural processes, and its significance is further underscored by the impacts of climate change. The change in soil moisture patterns can have profound implications for hydrological dynamics, agricultural productivity, and ecosystem sustainability. To understand these changes, an initial study was conducted to examine the long-term spatiotemporal evolution of soil moisture and its interactions with key hydrometeorological parameters using coarse-resolution data. Over a 40-year period, it was found that approximately 50% of the global vegetated surface layer (0-7 [cm] depth) experienced significant drying. Conversely, only 9% of the global vegetated area showed an upward trend in soil moisture, largely attributed to increasing precipitation levels. While these results provide valuable insights into broad-scale soil moisture trends and their primary drivers, and highlight the limitations of coarse-resolution data, which fail to capture the finer-scale processes and anthropogenic influences that are critical for understanding micro-scale feedback mechanisms. Therefore, high-resolution soil moisture data is required, but currently, none of the operational missions provide data at such a high resolution.

However, the retrieval of high-resolution soil moisture products at a global scale can be achieved in this "Golden Age of SAR". Among the upcoming L-band SAR missions, NISAR is in the final stages of preparation for launch. Therefore, taking advantage of the upcoming NISAR mission, an algorithm for high-resolution soil moisture retrieval is proposed i.e., "multi-scale" soil moisture retrieval algorithm. This algorithm is based on the disaggregation approach which combines the coarse-resolution (9 [km]) soil moisture data with fine-scale co-polarization and cross-polarization backscatter measurements to retrieve high-resolution soil moisture. The algorithm can take input of coarse resolution soil moisture either from satellite radiometer-based or climate model data. In this study, European Center for Medium Weather Range Forecast (ECMWF) ERA5-Land reanalysis data were used as an input coarse resolution soil moisture data. The ECMWF assimilates a large number of satellite and *in-situ* information to produce overall very reliable datasets. The major advantage of choosing the input dataset from climate model reduces dependency on satellite mission lifetimes. The end goal of the algorithm is to remove dependencies on any complex modeling, tedious retrieval steps, or multiple ancillary data needs, and subsequently decrease the degrees of freedom to achieve optimal accuracy in soil moisture retrievals. The proposed algorithm targets a spatial resolution of 200 [m], a specific spatial

resolution determined based on the user requirements. However, currently due to the unavailability of NISAR data, similar L-band data from UAVSAR acquired during the SMAPVEX-12 campaign and ALOS-2 SAR were utilized for algorithm calibration and validation. The algorithm has been initially tested on selected agricultural sites. The retrieved high-resolution soil moisture was validated with *in-situ* measurements, and the ubRMSE was below 0.06 [m³/m³], meeting the NISAR mission accuracy goals. Additionally, given the SAR's ability to provide fine-resolution backscatter measurements at 10 [m] spatial resolution. The analysis was conducted at spatial resolutions of 100 [m] and 200 [m] across various hydrometeorological settings globally. This includes sites from polar to arid regions and diverse land use. This retrieval and validation were performed using the ALOS-2 L-band SAR time-series data. The retrieved soil moisture at both spatial resolutions showed consistent patterns, with the finer 100 [m] resolution have more detailed information. The validation statistics show that the algorithm consistently maintained an ubRMSE below 0.06 [m³/m³] at both 100 [m] and 200 [m] spatial resolutions. The performance of the algorithm, even in forested regions with dense canopies, presents the robustness of the algorithm. This is attributed to the L-band SAR frequency's higher penetration capability.

However, since these validation statistics are based on limited sites, there is a need to calculate the error in the soil moisture retrieval for each grid to ensure comprehensive accuracy. Recognizing the limitations of *in-situ* measurements, which are sparse and geographically constrained, an analytical approach to estimate uncertainty in high-resolution soil moisture retrievals for the NISAR mission is also proposed. This approach accounts for errors in the input datasets and algorithm parameters. The approach was applied on the UAVSAR datasets from the SMAPVEX-12 campaign and compared with the ubRMSE for different crop types. The uncertainty estimates closely matches the ubRMSE, demonstrating the robustness of the analytical approach. Overall, this study demonstrates the effectiveness of the proposed algorithm for high-resolution soil moisture retrieval for the NISAR mission and future SAR missions, with the potential to achieve spatial resolutions finer than 100 [m].

This thesis is dedicated to my parents, whose support and love have been the cornerstone of my success.

I also dedicate this work to the NISAR mission and give a special shout-out to all the scientists and engineers who are making the upcoming launch of NISAR possible.

#### **ACKNOWLEDGEMENTS**

First and foremost, I would like to express my deepest gratitude to my advisor and mentor, Dr. Narendra Das, for his excellent mentorship. He taught me nearly every skill that I know now. At every opportunity, he has supported my personal, professional, and academic growth. I can say with absolute certainty that I consider myself exceptionally fortunate for the gift of his mentorship, and I would not be where I am today without his guidance. Dr. Das possesses not only vast knowledge but also a remarkable personality. His encouragement and appreciation for hard work, with his gentle approach to correcting mistakes, have guided me through many challenging situations.

I also extend my sincere thanks to Dr. David Roy, Dr. Phanikumar Mantha, and Dr. Andreas Colliander for serving on my graduate committee and providing their expertise, insight, time, and effort. I would like to especially thank Dr. Colliander for sharing all the relevant datasets required for my research. I am also thankful to Dr. Dara Entekhabi and Dr. Rowena Lohman for their critical input and suggestions for my manuscripts, which have all been successfully published. Your feedback was incredibly valuable in shaping the manuscripts and improving their quality.

I would also like to acknowledge the Department of Civil and Environmental Engineering and the Department of Biosystems and Agricultural Engineering of Michigan State University for providing all the facilities necessary for my academic and research.

I would like to sincerely thank Dr. Gurjeet Singh, who not only taught me the basic knowledge and skills required for soil moisture retrieval but also, together with his family, treated me as an extended family member. Your support, both academic and personal, has been a pillar of strength for me, and I am truly grateful. I am also thankful to all my lab members (Dr. Abhijeet Abhishek, Mr. Siddhesh Mane, Mr. Arunav Nanda and Mr. Vikas Rai), for their camaraderie and collaboration.

A special note of thanks to Dr. Soni Kumari, who provided support during times of unusual stress, particularly in the final stages of my PhD. Your presence and calming influence were invaluable, helping me find balance and clarity when things felt overwhelming. I truly appreciate your support and guidance. Your kindness and care have meant more to me than words can express.

I want to specially mention my younger brother, Mr. Prince Lal, who took care of Mom and Dad during tough times in India so that I could continue my PhD research work without stress. Thank you for your sacrifices and for always being there. I also extend my heartfelt thanks to my

entire family and friends for their unconditional love and support, which has made my life easier and happier.

I would like to extend my gratitude and give a special shout-out to all the scientists and engineers from ISRO and NASA working on the NISAR mission. Your tireless efforts in making the launch possible are truly inspiring. The successful launch of NISAR stands as a testament to your dedication, and it serves as a powerful motivation for researchers like me. The data and insights that will emerge from this mission will undoubtedly advance our understanding of Earth's systems and contribute to solving some of the most pressing challenges in environmental science. Thank you for your remarkable work and commitment to this groundbreaking mission.

This research was supported by the NISAR Science Team fundings (80NSSC21K1181 and 80NSSC22K1874). I am grateful for this support, which has been crucial in enabling the completion of my research.

Preet Lal

#### **PREFACE**

This thesis represents a personal and professional journey that began with a simple question: How can we better understand small-scale changes in soil moisture that are important in rapidly changing climate? The major challenge of accessing high-resolution soil moisture data on a global scale has been a significant barrier in this field. As I further advanced in my research, I realized that without this crucial data, many scientific efforts would continue to be hampered. This motivated me to focus on developing global high-resolution soil moisture data, which could be essential for both the scientific community and future SAR missions.

The timing of my research aligned perfectly with the upcoming NISAR mission. Knowing that my work could directly contribute to this mission provided both inspiration and direction. However, the path was far from easy. A major obstacle was the limited availability of low-frequency SAR data, particularly L-band data, which is important for accurate soil moisture retrieval. The existing ALOS-2 L-band SAR data is not only costly but also infrequently available, complicating efforts to obtain consistent data. Moreover, when such data was accessible, sometime the lack of coinciding *in-situ* measurements made it difficult to validate the retrieved soil moisture.

Despite these obstacles, I remained committed to my research, driven by the belief that high-resolution soil moisture data is crucial in this era of climate change. Completing this thesis was not just about development of soil moisture data; it was about contributing to a broader effort for improving our understanding of soil moisture dynamics and, by extension, the impact of climate change on our environment.

I am confident that this research will make a substantial contribution to the NISAR mission and provide essential data for advancing scientific understanding of soil moisture dynamics. Ultimately, I aspire for this work to help policymakers mitigating the impact of climate change and ensuring a sustainable future.

### TABLE OF CONTENTS

CHAPTER 1: PROSPECTS OF HIGH-RESOLUTION SOIL MOISTURE RETRIEV	AL
USING SYNTHETIC APERTURE RADAR	1
1.1 Introduction	
1.2 Current and Upcoming SAR Missions	
1.3 Current and upcoming Microwave Passive mission for soil moisture retrieval	11
1.4 Current and upcoming development in climate models for soil moisture	12
1.5 Soil moisture retrieval algorithm using SAR data.	14
1.6 Discussion	
1.7 Dissertation Outline	22
CHAPTER 2: SPATIOTEMPORAL EVOLUTION OF GLOBAL LONG-TERM PAT	
OF SOIL MOISTURE	
2.1 Introduction	
2.2 Data and Methods	
2.3 Results and Discussions	
2.4 Conclusions	40
CHAPTER 3: ASSESSMENT OF ERA5-LAND SOIL MOISTURE PRODUCT USIN	
SITU AND SMAP SOIL MOISTURE OBSERVATIONS	
3.1 Introduction	
3.2 Overview of Soil Moisture Datasets	
3.3 Methodology	
3.4 Soil Moisture Intercomparison	
3.5 Conclusion	52
CHAPTER 4: DEVELOPMENT OF MULTI-SCALE ALGORITHM FOR NISAR M	
HIGH RESOLUTION SOIL MOISTURE PRODUCT	
4.1 Introduction	
4.2 Algorithm for high-resolution soil moisture retrievals	
4.3 Test sites and Datasets	
4.4 Algorithm implementation	
4.5 High-resolution soil moisture retrievals and validation	
4.6 Discussion	
4.7 Conclusion	85
CHAPTER 5: COMPREHENSIVE VALIDATION OF THE NISAR MULTI-SCALE	
MOISTURE RETRIEVAL ALGORITHM ACROSS VARIOUS SPATIAL RESOLU	
AND LANDCOVERS USING THE ALOS-2 DATA	
5.1 Introduction	
5.2 Test Sites	
5.3 Data Used	
5.4. Methodology	
5.5 Result and Discussion	97 112
) O COUCHISION	11/

CHAPTER 6: UNCERTAINTY ESTIMATES IN THE NISAR HIGH-RESOLUTION SO	OIL
MOISTURE RETRIEVALS FROM MULTI-SCALE ALGORITHM	114
6.1 Introduction	114
6.2 Summary of NISAR multi-scale soil moisture algorithm and its uncertainties	117
6.3 Analytical approach for uncertainty estimation in high-resolution soil moisture	119
6.4 Data Used	
6.5 Methodology	122
6.6 Implementation of the analytical approach	123
6.7 Results	124
6.8 Discussion and Conclusion	137
CHAPTER 7: CONCLUSION	142
CHAPTER 8: LIMITATIONS AND FUTURE DIRECTIONS	147
	4.50
BIBLIOGRAPHY	150
A DDENING	175
APPENDIX	1/5

# CHAPTER 1: PROSPECTS OF HIGH-RESOLUTION SOIL MOISTURE RETRIEVAL USING SYNTHETIC APERTURE RADAR

#### 1.1 Introduction

Soil moisture, a critical variable in the Earth's hydrological cycle, plays an integral role in the exchange of water and energy between the land surface and the atmosphere (Chawla et al., 2018; Lal et al., 2023a). The importance of monitoring soil moisture extends across a wide range of scientific fields, including hydrology, meteorology, agriculture, and climate science (Jaeger and Seneviratne, 2011; Walker and Houser, 2001). High-resolution soil moisture data, obtained through advanced satellite remote sensing technologies, have increasingly become a focal point in environmental monitoring and modeling (Lal et al., 2023b; Peng et al., 2021). These data offer invaluable insights into various natural processes and human activities, leading to improved decision-making in fields such as water resource management, agricultural planning, and disaster mitigation (Crow et al., 2018). The transition from coarse to high-resolution soil moisture retrieval marks a significant advancement, addressing the growing demand for more precise and localized environmental data (Sishodia et al., 2020). The significance of soil moisture lies in its role as a key driver of several land surface processes (Betts et al., 1996). It directly influences the partitioning of precipitation into runoff, infiltration, and evapotranspiration, thereby regulating the availability of water in ecosystems. Soil moisture also affects the thermal properties of the soil, influencing the energy balance at the surface, which in turn affects atmospheric conditions and weather patterns (Lal et al., 2022a). In agriculture, soil moisture is crucial for plant growth, affecting root water uptake and nutrient availability (Sishodia et al., 2020). Given its importance, accurate and timely soil moisture data are essential for understanding and managing various environmental and societal challenges, including droughts, floods, and food security (Brocca et al., 2017; Singh and Das, 2022; Su et al., 2014).

Traditional methods of soil moisture measurement, such as *in-situ* sensors and hydrological models, have provided valuable data over the years. However, these methods are often limited by their spatial coverage and temporal resolution (Mane et al., 2024). *In-situ* measurements, while accurate at specific locations, are labor-intensive and cannot provide the extensive spatial coverage needed for large-scale applications (Dorigo et al., 2021; Walker et al., 2004). Hydrological models, on the other hand, rely on assumptions and simplifications that may not capture the full complexity of the natural environment (Devia et al., 2015; Peel and Blöschl, 2011). These limitations highlight

the need for alternative approaches that can provide comprehensive soil moisture data across different spatial and temporal scales (Peng et al., 2021).

Satellite remote sensing offers a solution to the challenges posed by traditional soil moisture measurement techniques. By utilizing the capabilities of Earth-observing satellites, soil moisture data can be obtained over larger areas, with high temporal resolution (Ahmad et al., 2010; Balenzano et al., 2021; Das et al., 2011). Among the various remote sensing techniques, microwave sensing has proven particularly effective for soil moisture retrieval. This is because microwaves can penetrate clouds and vegetation, making it possible to measure soil moisture under different environmental conditions. Microwave sensors can be classified into active and passive sensors. Passive microwave sensors, such as those on the Soil Moisture and Ocean Salinity (SMOS) satellite, measure the natural microwave emissions from the Earth's surface, which are influenced by the moisture content of the soil (Du et al., 2000; Njoku and Entekhabi, 1996). Active microwave sensors transmit microwave signals towards the Earth's surface and measure the backscatter, which is affected by soil moisture, surface roughness, and vegetation (El Hajj et al., 2016; Kornelsen and Coulibaly, 2013). While early satellite missions provided soil moisture data at coarse spatial resolutions, typically ranging from 25 to 50 [km], the demand for higherresolution data has grown in recent years (Brown et al., 2013; Kerr et al., 2010; Merlin et al., 2008). High-resolution soil moisture data, with resolutions of sub-kilometer or below 100 [m], are essential for applications that require detailed spatial information (Peng et al., 2021). For instance, in precision agriculture, high-resolution soil moisture data can help optimize irrigation practices by providing detailed information on the variability of soil moisture within a field. This can lead to more efficient water use, reduced agricultural inputs, and improved crop yields (González Perea et al., 2016). Similarly, in hydrology, high-resolution soil moisture data can enhance the accuracy of flood forecasting by providing detailed information on soil water content at the watershed level. This is particularly important for managing water resources in regions prone to flooding, where small differences in soil moisture can significantly impact the timing and magnitude of flood events (Chao et al., 2022; Wanders et al., 2014).

High-resolution soil moisture data play a transformative role in modern agriculture, offering precise insights that can significantly enhance crop management practices and overall agricultural productivity. Traditional agricultural methods often relied on generalized weather data and broad assumptions about soil conditions, which could lead to inefficient water usage, uneven

crop growth, and suboptimal yields (De Lannoy et al., 2014; Kashyap and Kumar, 2021). In contrast, high-resolution soil moisture data provide granular, field-level information, enabling farmers to make informed decisions to specific conditions within different parts of a field. This precision is particularly important in precision agriculture, a farming management concept that uses technology to optimize field-level management regarding crop farming. By accurately mapping the variability of soil moisture across a field, high-resolution data allow farmers to implement site-specific irrigation strategies (Hassan-Esfahani et al., 2015; Zappa et al., 2019). Moreover, high-resolution soil moisture data are also useful in optimizing the application of fertilizers and other inputs. Soil moisture influences the availability of nutrients to plants, as well as the effectiveness of fertilizers. By aligning fertilizer application with precise soil moisture levels, farmers can enhance nutrient uptake by crops, leading to better growth and higher yields (Kuang et al., 2019; Torbert et al., 1999). In addition, understanding soil moisture dynamics can help in predicting the best times for planting and harvesting, ensuring that crops are grown under optimal conditions (Black et al., 2023; Raes et al., 2004). In regions prone to drought, highresolution soil moisture data can be a critical tool for managing water scarcity and ensuring crop survival. This is particularly important in arid and semi-arid regions, where water resources are limited, and agricultural productivity is heavily dependent on efficient water management. The ability to monitor soil moisture at a high resolution also helps in assessing the impact of drought on different parts of a field, allowing for targeted interventions that can mitigate crop losses. Furthermore, high-resolution soil moisture data can improve the accuracy of yield predictions (Boas et al., 2023; White et al., 2020).

The applications of high-resolution soil moisture data extend beyond traditional fields such as agriculture and hydrology. In climate research, these data are critical for understanding land-atmosphere interactions and feedback mechanisms that influence weather patterns and climate change. For example, soil moisture plays a key role in the initiation of convection, which can lead to the formation of thunderstorms and other severe weather events (Barton et al., 2021; Zhao et al., 2021). By providing detailed information on the spatial distribution of soil moisture, high-resolution data can help improve the accuracy of weather and climate models, leading to better predictions of extreme weather events and their impacts (Peng et al., 2021). In addition, high-resolution soil moisture data are increasingly being used in ecosystem management and biodiversity conservation (Fischer et al., 2007). For example, soil moisture maps can help identify

areas that are vulnerable to changes in water availability, such as wetlands and drylands (Kannenberg et al., 2024). By monitoring soil moisture in these areas, conservationists can develop strategies to protect and preserve biodiversity in the face of climate change.

Urban planning and infrastructure development are other areas where high-resolution soil moisture data can play a significant role. In urban areas, soil moisture is a key factor in managing green spaces, stormwater, and urban heat islands (Tabassum et al., 2024). In addition, soil moisture data can be used to manage stormwater in urban areas, where impermeable surfaces can lead to increased runoff and flooding. By understanding the spatial distribution of soil moisture, urban planners can design more effective stormwater management systems, such as permeable pavements and green roofs, that reduce runoff and enhance water infiltration. Moreover, high-resolution soil moisture data can contribute to the development of sustainable land use practices. In areas where land degradation and desertification are concerned, soil moisture data can help identify regions at risk of becoming unproductive due to the loss of soil moisture (Rivera-Marin et al., 2022).

The retrieval of high-resolution soil moisture data from satellites is a complex task that involves several challenges. One of the main challenges is the influence of vegetation on the microwave signal (Jackson and Schmugge, 1991; Schmidt et al., 2023). Dense vegetation can obscure the underlying soil moisture signal, may lead to inaccuracies in the retrieved data. To address this issue, various researchers have developed algorithms that account for the effects of vegetation and surface roughness on the microwave signal (Njoku and Chan, 2006). These algorithms often combine data from multiple sensors, such as optical and thermal sensors, to improve the accuracy of soil moisture retrieval (Mattar et al., 2012; Tong et al., 2020). Another challenge is the integration of data from different satellite missions, each with its spatial resolution, temporal coverage, and sensor characteristics. This requires disaggregation/active-passive soil moisture retrieval method that can harmonize data from different sources, providing a consistent and reliable soil moisture product at a high-resolution (Das et al., 2019, 2014). Recent advancements in satellite technology have enabled the retrieval of high-resolution soil moisture with improved accuracy. For example, the SMAP mission provides soil moisture data at a 1 km resolution, such as the SMAP/Sentinel-1 product, with global coverage and a revisit time of 12 days (Das et al., 2019). The SMAP/Sentinel-1 soil moisture is derived using a disaggregated brightness temperature from SMAP radiometer data, employing an active-passive approach that

combines radiometer and SAR observations (Das et al., 2019). These high-resolution soil moisture products are increasingly used in applications requiring precise data. The upcoming NISAR mission is expected to provide operational soil moisture data at a 200 [m] spatial resolution, which is nearly five times finer than existing operational products (Lal et al., 2023b). However, there remains gap for further improvement in the spatial resolution of soil moisture data with upcoming satellite missions. Therefore, the aim of this chapter is to discuss the potential of upcoming microwave-based satellite missions to retrieve high-resolution soil moisture at kilometer and meter scales. Additionally, which algorithms could be most effective for achieving this high-resolution soil moisture retrieval.

#### 1.2 Current and Upcoming SAR Missions

There are several satellite missions specifically dedicated to soil moisture retrieval, such as SMAP (Soil Moisture Active Passive), AMSR2 (Advanced Microwave Scanning Radiometer 2), SMOS (Soil Moisture and Ocean Salinity), and METOP (Chan et al., 2018; Kawanishi et al., 2003; Wagner et al., 2013). These missions have been useful in advancing our understanding of global soil moisture patterns. However, none of these missions are dedicated to operational highresolution soil moisture retrieval. The launch of Sentinel-1A SAR by the ESA marked a significant advancement in this area, providing the capability for high-resolution soil moisture retrieval as an operational product (Das et al., 2019). Despite this progress, there remains a need for further research to achieve soil moisture retrieval at sub-kilometer or meter scales. Currently, the operational high-resolution soil moisture product from the SMAP mission is available at a resolution of 1 [km], which may be insufficient for certain applications, particularly in regions where finer spatial resolution is crucial for effective decision support systems (Peng et al., 2021). However, high-resolution soil moisture retrieval may become feasible with upcoming satellite missions that utilize various methods, such as combining radiometer and radar data, integrating climate model-derived soil moisture with radar data, or employing advanced retrieval methods that uses SAR data alongside ancillary information (Lal et al., 2023b). These approaches offer the potential to achieve finer-scale soil moisture mapping, which could significantly improve the accuracy and usefulness of soil moisture data for various decision-making processes.

Several C-band and L-band satellites are currently in operation and can potentially be used for soil moisture retrieval. Additionally, in the next 5-8 years, the continuation of existing missions and the launch of new satellite missions are expected, which could be used to retrieve high-

resolution surface soil moisture and root zone soil moisture. This can help to fill the current gap in the availability of high-resolution soil moisture data for various geophysical applications.

#### **1.2.1 C-band SAR**

There are several C-band SAR satellites operating globally but have limitations in the context of operational soil moisture retrieval. For example, EOS-4 is primarily focused on the Indian subcontinent, resulting in limited global coverage (Sharma et al., 2024). Similarly, the RADARSAT Constellation, despite global coverage, has challenges in terms of temporal resolution, which limits consistent soil moisture monitoring on a global scale (Thompson, 2015). In contrast, the Sentinel-1 mission, with its extensive global coverage, high temporal resolution, and high spatial information, is particularly used for soil moisture retrieval, making it a more reliable source for this application among C-band SAR satellites (Torres et al., 2012). The Sentinel-1 mission, a crucial mission of the European Union's Copernicus program, for Earth observation since the launch of Sentinel-1A on April 3, 2014. The Sentinel 1 mission consists of numbers of satellite and among which Sentinel-1A is only operation and others will be launched soon. Sentinel-1A operates in the C-band at a frequency of 5.4 GHz and provides high-resolution SAR imagery (https://www.esa.int/Applications/Observing\_the\_Earth/Copernicus/Sentinel-1). This capability has been essential for monitoring environmental changes, land use, and supporting disaster response efforts (Rucci et al., 2012). The satellite has spatial resolutions ranging from 5 m in Stripmap mode to 20 [m] in Interferometric Wide Swath mode, with a swath width of up to 400 km, enabling consistent and reliable radar imagery regardless of weather conditions. Following Sentinel-1A, Sentinel-1B was launched on April 25, 2016, to enhance the mission's capacity by reducing revisit times to just 6 days. However, Sentinel-1B encountered a critical failure in December 2021, which ended its operation, leaving Sentinel-1A to continue the mission alone. To maintain data continuity, ESA planned the launch of Sentinel-1C and Sentinel-1D, with Sentinel-1C expected in 2024 and Sentinel-1D in 2025. Once launched, Sentinel-1C and 1D will operate alongside Sentinel-1A, significantly enhancing the mission's observational capacity. With the combined operation of these satellites, the temporal resolution is expected to improve, reducing the revisit time to as little as 3-4 days for global coverage, depending on the location and specific mode of operation (Torres et al., 2017).

Looking ahead, the Sentinel-1 Next Generation (NG) mission will have significant advancement in Earth observation technology. Scheduled for launch in the late 2030, the Sentinel-

1 NG satellites are designed to ensure C-band data continuity beyond 2030, while introducing new imaging capabilities. These next-generation satellites will feature advanced SAR systems capable of providing better spatial resolution, shorter revisit times, and improved radar sensitivity, with a Noise Equivalent Sigma Zero (NESZ) of -26 dB. The dual-polarimetric SAR mode, with a 400 [km] swath width, will be particularly effective for monitoring land and coastal areas, including applications such as glacier monitoring, soil moisture retrieval, oil spill detection and maritime surveillance (Geudtner et al., 2021; Geudtner and Tossaint, 2021). Additionally, Sentinel-1 NG will incorporate innovative imaging techniques, such as Along-Track Interferometry (ATI) and multi-channel High-Resolution Wide Swath (HRWS) systems (Geudtner and Tossaint, 2021), which will enhance the mission's capabilities in ocean current monitoring, and land deformation analysis.

#### 1.2.2 L-band SAR

L-band SAR operates at a frequency of approximately 1.2 GHz, with a wavelength of ~ 24 [cm], making it particularly effective for penetrating vegetation and surface layers to provide detailed information on soil moisture content (Calvet et al., 2011; Zwieback et al., 2015). This is crucial for applications in agriculture, hydrology, and environmental monitoring, where understanding soil moisture dynamics is essential. Unlike shorter wavelength SARs, such as C-band, L-band SAR can penetrate more and this helps in retrieving soil moisture at high accuracy, which is critical for assessing plant water availability and predicting drought conditions. Currently, the availability of L-band SAR satellites is limited, with only a few missions like ALOS-2 (Zwieback et al., 2015). However, the importance of L-band SAR is well recognized, and there are several upcoming satellite missions scheduled for launch within the next five years. These future missions are expected to significantly expand the availability of high-resolution L-band SAR data, enhancing our ability to monitor soil moisture on a global scale with greater accuracy. This expansion will fill current gaps and support a broader range of geophysical applications, from precision agriculture to climate change adaptation.

#### 1.2.2.1 ALOS-2 and ALOS-4

ALOS-2 (Advanced Land Observing Satellite-2), launched by the Japan Aerospace Exploration Agency (JAXA) in May 2014, is an among few missions for Earth observation, particularly in monitoring environmental changes, disaster management, and resource exploration. ALOS-2 operates in the L-band with a frequency of 1.2 GHz, which enables it to penetrate

vegetation and provide high-resolution images even in densely forested areas (Rosenqvist et al., 2014). The satellite's SAR system offers various imaging modes, including the Fine Beam mode, which achieves spatial resolutions as high as 3 [m], and the ScanSAR mode, which covers wider areas at a lower resolution of 100 [m]. This allows ALOS-2 to provide critical data for applications ranging from land deformation monitoring to precise mapping of land cover changes. ALOS-2 also has lower NESZ, achieving values as low as approximately -50 dB, which helps to capture high-quality, low-noise data essential for detailed surface analysis (Rosenqvist et al., 2014).

Building on the success of ALOS-2, ALOS-4 was launched on July 1, 2024, further enhancing capabilities in Earth observation. ALOS-4 continues to operate in the L-band, offering improved SAR performance with advanced imaging modes. The satellite features a higher spatial resolution, with modes capable of achieving up to 1 m in high-resolution observation. ALOS-4 also includes enhanced radiometric accuracy and better NESZ (< -50 dB), ensuring more detailed information (Motohka et al., 2021). The mission's increased swath width and improved revisit time allow for more frequent and expansive coverage, making it an essential tool for continuous environmental monitoring and disaster response. With these advancements, ALOS-4 is set to provide critical data for a wide range of applications, including soil moisture retrieval, land use planning, and monitoring of natural disasters, contributing to both scientific research and practical decision-making processes. Together, ALOS-2 and ALOS-4 provide coverage with enhanced temporal resolution of ~7 days (Motohka et al., 2021).

#### 1.2.2.2 NISAR

The NASA-ISRO Synthetic Aperture Radar (NISAR) mission is a collaborative project between NASA and ISRO, with a scheduled launch in February 2025. NISAR will be the first satellite to carry SAR sensors at both L-band (1.25 GHz) and S-band (3.2 GHz) frequencies, enabling it to measure a wide range of Earth surface changes, from ecosystem dynamics to solid earth and cryosphere processes (Jones et al., 2021; Kellogg et al., 2020). The mission is designed for high-resolution imaging, with an azimuth resolution of around 7 [m] and a range resolution varying from 3 to 48 [m], depending on the mode of operation. The dual-frequency capability of NISAR allows it to achieve a swath width greater than 240 [km], providing extensive coverage with a temporal resolution of 12 days, which can be further refined to 6 days when combining ascending and descending passes. This frequent data collection is essential for applications like high-resolution soil moisture retrieval, monitoring tectonic activity, and glacier velocity

calculation. NISAR's innovative SweepSAR technique will enable full-resolution, multi-polarimetric observations across extended swaths.

#### 1.2.2.3 ROSE-L SAR

The ROSE-L mission, part of the European Space Agency's Copernicus Sentinel Expansion program, is designed to address key observational gaps by providing L-band SAR data, which is critical for various Earth monitoring applications (Petrolati et al., 2023). Scheduled for launch in 2028, ROSE-L will complement the existing C-band SAR capabilities provided by Sentinel-1 mission, enhancing coverage into areas such as land monitoring, emergency management (designed to address the Copernicus emergency management), and marine environment monitoring (Dierking, 2021). The L-band SAR instrument on ROSE-L is particularly useful due to its ability to penetrate vegetation, dry snow, and ice, making it ideal for monitoring soil moisture, geohazards, and agricultural areas (Davidson et al., 2023; Davidson and Furnell, 2021). The mission will operate primarily in a scanning synthetic aperture radar (ScanSAR) mode over land and coastal areas, with the capability to provide a 260 [km] wide swath at resolutions of 50 [m] and 100 [m] for dual-polarization and quad-polarization modes, respectively. Additionally, ROSE-L will have a NESZ lower than -28 dB. The mission's integration with Sentinel-1 will allow for improved temporal sampling, achieving a minimum revisit time of 6 days globally, 3 days over Europe, and daily revisits in the Arctic (Dierking, 2021).

#### 1.2.2.4 Tandem L-band

Tandem-L is a proposed L-band Synthetic Aperture Radar (SAR) mission by the German Aerospace Center (DLR), with an expected launch date in 2028. The mission is designed to observe dynamic processes on Earth's surface with high temporal and spatial resolution (Moreira et al., 2011). It will consist of two radar satellites operating in close formation, utilizing large deployable mesh reflectors and advanced digital beamforming techniques (Tridon et al., 2018). Tandem-L is particularly well-suited for soil moisture retrieval, offering a unique capability to penetrate vegetation and soil layers, making it possible to monitor soil moisture at high spatiotemporal resolution. The mission will provide global coverage with a swath width of up to 350 kilometers, while achieving a spatial resolution of approximately 7 [m] in azimuth and between 1.8 to 7.5 [m] in range, depending on the operational mode (Bachmann et al., 2021). Tandem-L is designed to with a NESZ of less than -30 dB, ensuring precise and accurate measurements. With a 16-day repeat cycle, the mission will offer frequent observations, allowing for consistent

monitoring of soil moisture dynamics, surface deformation, and changes in biomass. Tandem-L's ability to perform polarimetric SAR interferometry and multi-pass coherence tomography will further enhance the retrieval of soil moisture, as well as provide detailed assessments of vertical structures in vegetation and ice (https://www.eoportal.org/satellite-missions/tandem-l#eop-quick-facts-section).

#### 1.2.3 P-band SAR

The Biomass mission, set to launch in 2024, under the European Space Agency's Earth Explorer program, aiming to provide unprecedented global measurements of forest biomass using P-band SAR (Toan et al., 2018). This mission will be the first to carry a fully polarimetric P-band SAR into space, operating at a frequency of 435 MHz. The P-band's long wavelength allows it to penetrate through dense vegetation and even subsurface layers, making it particularly effective for retrieving data on forest biomass, subsurface geological structures, and soil moisture (Scipal, 2017). The Biomass mission includes a spatial resolution of 50 [m] by 60 [m] and a swath width of approximately 50 [km]. The mission will operate in two phases: the Tomographic (TOM) phase and the Interferometric (INT) phase. The TOM phase will utilize SAR tomography to investigate forest vertical structures by acquiring multiple SAR measurements from different angles, which is crucial for profiling forest canopy and subsurface moisture levels. The INT phase will provide interferometric polarimetric observations, enabling detailed monitoring of surface changes over time (Le Toan, 2014). With a revisit cycle of approximately 16 days, Biomass will ensure frequent and consistent data collection over its five-year mission duration. The mission's ability to penetrate vegetation and surface layers allows it to retrieve soil moisture information at greater depths than shorter-wavelength radars, making it useful for understanding soil moisture dynamics in various environments, including densely forested and arid regions. By providing information into subsurface moisture levels, Biomass is expected to significantly enhance our understanding of the global carbon cycle, forest health, and the impact of climate change on terrestrial ecosystems.

P-band SAR is relatively uncommon in spaceborne missions primarily due to the technical challenges associated with its long wavelength, which requires large antenna systems and is highly susceptible to ionospheric distortions. The ionosphere can significantly affect the P-band signal, introducing errors that are challenging to correct in space-based systems. Moreover, the large antenna required for P-band SAR adds complexity and cost to satellite missions. However, with recent advancements in remote sensing instrument development, P-band sensors have become

more feasible in UAV-based platforms or drones (Moreira et al., 2020). While these UAV-based P-band SAR systems cannot provide the global or operational coverage required for broad applications like soil moisture retrieval, they are highly effective for localized studies. For instance, in precision agriculture and crop water management, UAV-based P-band SAR can have detailed soil moisture profiles over small regions, enabling more accurate and targeted water use strategies. This localized application is particularly valuable for improving agricultural efficiency and sustainability, even if it does not yet scale to the global operational capabilities of spaceborne systems.

#### 1.3 Current and upcoming Microwave Passive mission for soil moisture retrieval

Passive radiometer-based soil moisture retrieval using L-band frequencies is a wellestablished method in Earth observation, known for its high sensitivity to changes in soil moisture content. L-band radiometry, utilized since the 1980s, is particularly effective because of its ability to detect variations in brightness temperature (TB) that correspond to changes in soil moisture. For example, a smooth, bare soil surface can exhibit a TB difference of approximately 90 K between dry (5% water by volume) and wet (35% water by volume) conditions, with modern radiometers achieving a radiometric uncertainty of less than 1K (Das et al., 2016). This high signal-to-noise ratio allows for precise soil moisture estimation, even in challenging conditions. Additionally, Lband radiometry offers advantages such as deeper soil penetration in vegetated areas and reduced sensitivity to factors like surface roughness and soil texture, which can complicate soil moisture retrieval at other frequencies (Njoku and Chan, 2018, 2006). Currently, two prominent missions— NASA's Soil Moisture Active Passive (SMAP) and ESA's Soil Moisture and Ocean Salinity (SMOS)—employ L-band radiometers for global soil moisture retrieval (Entekhabi et al., 2010; Kerr et al., 2012). SMAP, launched in 2015, provides soil moisture data with a gridded data of 9 [km] and a spatial resolution of approximately 33 [km] for its passive product. SMOS, operational since 2009, offers similar spatial resolution at around 40 [km], using radiometer to capture TB across a wide field of view. Both missions have significantly contributed to the global monitoring of soil moisture, though their coarse spatial resolution presents limitations for applications requiring finer detail, such as localized agricultural or hydrological studies.

The upcoming Copernicus Imaging Microwave Radiometer (CIMR) mission, anticipated to launch around 2029-2030, aims to enhance the capabilities of L-band radiometry for soil moisture retrieval. CIMR will feature a multi-frequency radiometer, spanning from L- to Ka-band,

designed to deliver high-resolution observations across a range of environmental parameters, including soil moisture (Ciani et al., 2019; Donlon et al., 2023). The spatial resolution of CIMR's data products will vary depending on the observation frequency, ranging from 2.5 [km] to 36 [km]. The mission is expected to provide global coverage with a swath width of over 1900 [km], facilitating near-daily observations with a focus on polar regions, ocean monitoring and surface soil moisture monitoring. CIMR's inclusion of L-band radiometry will continue to support operational soil moisture measurements by using the frequency's high sensitivity to TB variations, thereby enabling precise soil moisture data collection (Vanin et al., 2020).

Passive radiometers, while effective for capturing large-scale soil moisture patterns, are limited by their coarse spatial resolution and cannot provide the high-resolution soil moisture retrieval needed for many localized applications. However, the radiometer-based soil moisture product plays a crucial role in complementing high-resolution soil moisture retrieval through an active-passive approach. In this method, coarse-scale soil moisture data obtained from passive radiometers can be downscaled by blending it with fine-scale information from SAR data (Das et al., 2019; Lal et al., 2023b). This synergy between passive and active sensors allows for the generation of high-resolution soil moisture maps, which are more suitable for detailed analyses where finer scale information is required.

#### 1.4 Current and upcoming development in climate models for soil moisture

In recent years, climate models have increasingly been recognized as useful tools for providing soil moisture data at a coarse scale. These models simulate various aspects of the Earth's climate system, including soil moisture, by integrating complex interactions between the atmosphere, hydrosphere, biosphere, and geosphere. The outputs from these models are crucial for understanding long-term trends and variability in soil moisture, particularly in the context of global climate change (Lal et al., 2023a). One of the most significant advancements in climate modeling is the integration of satellite datasets through data assimilation techniques (Crow et al., 2023). Data assimilation involves the incorporation of real-time or near-real-time observational data—such as soil moisture measurements from satellites—into climate models to improve their accuracy and predictive capabilities. This process helps to correct model biases and enhance the representation of soil moisture dynamics at various spatial and temporal scales (Fairbairn et al., 2024; Liu and Yang, 2022). The use of satellite data, such as that from radiometers for soil moisture and SAR backscatter as sigma0, in climate models allows for more accurate initial conditions and better

constraining of the model outputs (Wongchuig et al., 2024).

One prominent example is the ECMWF ERA5-Land soil moisture product, developed as part of the Copernicus Climate Change Service (C3S). ERA5-Land is a high-resolution meteorological reanalysis dataset the **ECMWF** provided by (https://cds.climate.copernicus.eu/cdsapp#!/dataset/reanalysis-era5-land?tab=overview). The dataset offers a resolution of approximately 9 [km] and provides multiple surface variables from 1950 to the present, with a temporal resolution of 1 hour. ERA5-Land is essentially a replay of the land component of the ERA5 climate reanalysis, driven by meteorological fields from ERA5. This dataset employs the Tiled ECMWF Scheme for Surface Exchanges over Land (H-TESSEL), which incorporates sophisticated land surface hydrology processes (Muñoz-Sabater et al., 2021). ERA5-Land does not directly assimilate observations; instead, it benefits from the atmospheric forcing and data assimilation carried out in ERA5, where satellite datasets and in-situ observations are assimilated through a 4D-VAR data assimilation system and a Simplified Extended Kalman Filter (Dee et al., 2011; Hersbach et al., 2020; Muñoz-Sabater et al., 2021). The ERA5 reanalysis incorporates a broad range of observational data, including brightness temperature datasets from satellites like NOAA, METOP, and GPM, and backscatter data from sensors such as ERS-1, ERS-2, and ASCAT (https://confluence.ecmwf.int/display/LDAS/LDAS+Home). ECMWF is also now actively developing the next generation of this product, known as ERA6-Land, which is expected be released in the last quarter of 2024 (https://www.ecmwf.int/en/about/mediacentre/focus/2023/fact-sheet-reanalysis). This upcoming reanalysis is expected to incorporate significant improvements, including the direct assimilation of backscatter sigma0 using a machinelearning-based observation operator, which is currently under development. ERA6-Land will also feature data assimilation of surface, snow, and soil moisture observations, leading to more accurate and reliable soil moisture data. In addition to the ECMWF ERA5-Land reanalysis, other major institutions also produce model-based soil moisture products, such as the Global Land Data Assimilation System (GLDAS) and the North American Land Data Assimilation System (NLDAS) developed by NASA (Rodell et al., 2004). These products utilize the Land Information System (LIS), a flexible software framework designed for high-performance land surface modeling and data assimilation (Peters-Lidard et al., 2007).

Climate model data, such as those from ERA5-Land, GLDAS, and NLDAS, cannot be directly used as high-resolution soil moisture products due to their coarse spatial resolution.

However, similar to how radiometer data is utilized, these model outputs can play a crucial role in downscaling algorithms. Downscaling involves combining coarse-resolution data from models with finer-scale information from sources like SAR to enhance spatial detail. For example, as highlighted in the upcoming NISAR mission, climate model data can be integrated into downscaling frameworks to refine soil moisture estimates, allowing these models to contribute to the generation of high-resolution soil moisture products (Lal et al., 2023b). This approach uses the broad-scale accuracy of climate models while compensating for their spatial limitations, making it possible to retrieve fine soil moisture information suitable for precision agriculture, water resource management, and other applications that require high spatial resolution.

#### 1.5 Soil moisture retrieval algorithm using SAR data.

The theory behind microwave remote sensing of soil moisture is based on the significant contrast in the dielectric properties of liquid water ( $\varepsilon \approx 80$ ) and dry soil ( $\varepsilon \approx 6$ ), which creates a strong dependency of the complex dielectric constant on volumetric soil moisture (Ulaby, 1974; Ulaby et al., 1996). This dielectric contrast directly influences the radar backscatter coefficient  $(\sigma^{o})$ , making it possible to estimate soil moisture by analyzing the variations in the backscattered signal (Ulaby, 1974). The backscattering coefficient in microwave remote sensing is influenced by various factors, making soil moisture retrieval a complex process. These factors include soil properties, radar characteristics such as wavelength, polarization, and incidence angle (Ulaby et al., 1986, 1990). The challenge lies in disentangling these influences to accurately assess soil moisture levels, a problem often described as "ill-posed". Among several problems vegetation is a major factor that affects microwave signals (Bindlish and Barros, 2001). It can absorb and scatter microwave radiation, which interferes with the signal's ability to reach and return from the soil surface. The degree of this interference depends on the vegetation's water content and structure. For instance, shorter wavelengths like X-band interact primarily with the upper vegetation layers, while longer wavelengths, such as L-band, can penetrate deeper, providing better soil surface data, and P-band can even penetrate to root zone soil moisture. However, the drier vegetation allows better penetration of C-band data and can have soil moisture information. However, for optimal soil moisture estimation, it is recommended to use longer wavelengths like L-band at low incidence angles, as these reduce the effects of vegetation and surface roughness on the signal (Ulaby et al., 1996, 1981). Surface roughness is another critical factor complicating soil moisture retrieval. Surface roughness can significantly influence the backscatter signal, sometimes even more than

soil moisture itself. Studies have shown that increasing the incidence angle beyond 10° results in more energy being scattered back to the sensor due to increased surface roughness (Brown et al., 2013). Measuring surface roughness accurately is challenging, particularly over large areas, which adds to the difficulty of isolating its effect from that of soil moisture (Lin et al., 2023).

To improve soil moisture retrieval, various radar sensor configurations have been explored. Multi-frequency measurements have been found to provide more accurate soil moisture estimates than single-frequency data (Gao et al., 2020). Using SAR data at both low and high incidence angles has also been shown to improve the accuracy of soil moisture estimates (Srivastava et al., 2024). Low to medium incidence angles are considered optimal for soil moisture retrieval, with specific polarizations like HH and HV offering better sensitivity to soil moisture content (Das and Paul, 2015; Holah et al., 2005). Given the complexities involved, various backscattering models have been developed over the years. These models, categorized into theoretical, empirical, and semi-empirical, aim to interpret radar signals more effectively for soil moisture estimation. Theoretical models are based on physical principles but are often limited by the assumptions they require about surface roughness and other parameters (Gharechelou et al., 2021; Njoku and Chan, 2006; Verhoest et al., 2008). Empirical models, on the other hand, are derived from observational data and may not be universally applicable (Sikdar and Cumming, 2004; Zribi et al., 2008). Semiempirical models have balance by integrating theoretical knowledge with empirical adjustments, making more practical for varying surface conditions (Chen et al., 2012). Apart from the three different backscatter models, there are various retrieval algorithms such as change detection algorithms (Zhu et al., 2022), active-passive disaggregation approaches (Das et al., 2019), and machine learning/artificial intelligence-based soil moisture retrieval methods (Abowarda et al., 2021).

The Theoretical scattering models are crucial for retrieving soil moisture from radar data by simulating the radar backscattering coefficient ( $\sigma^o$ ) based on known soil properties such as dielectric constant and surface roughness (Sikdar and Cumming, 2004). Among the most commonly used models are the Kirchhoff Approximation (KA) and the Small Perturbation Model (SPM). These models apply under specific conditions, with the Geometrical Optics Model (GOM) within KA being suitable for very rough surfaces, the Physical Optics Model (POM) for moderately rough surfaces, and the SPM for smooth surfaces (Ulaby, 1974)). However, these models rely on ancillary information such as surface parameters, including rms height and

correlation length, which are often difficult to measure accurately over large areas. The Integral Equation Model (IEM) extends the applicability of these theoretical models by combining elements from the KA and SPM, making it versatile for a broader range of surface conditions (Fung et al., 1992). The IEM calculates the backscattering coefficient as a function of radar sensor characteristics (e.g., frequency, polarization, incidence angle) and surface properties, enabling more robust soil moisture estimation, particularly over bare soil surfaces (Barrett et al., 2009). However, implementing the IEM in real-world scenarios is complex due to its high data requirements and assumptions of single scattering, limiting its effectiveness in cases of multiple scattering interactions within the soil or vegetation. To address these challenges, various inversion algorithms, such as Look-Up Tables (LUTs), Neural Networks (NN), and Bayesian approaches, have been developed to fit theoretical model predictions to observed radar data. Despite these advancements, achieving accurate soil moisture estimates remains challenging, particularly in vegetated areas or surfaces with complex roughness characteristics.

Soil moisture retrieval through empirical scattering models involves developing statistical relationships between radar backscatter coefficients ( $\sigma^{o}$ ) and *in-situ* soil moisture measurements (Baghdadi et al., 2017). These models often utilize regression analysis or other statistical methodologies to establish correlations, offering a computationally efficient approach (Wickel et al., 2001). However, the application of empirical models is frequently constrained on the specific environmental conditions under which they were derived, such as soil texture, vegetation cover, and radar configuration (Mathieu et al., 2003). This specificity limits the generalizability of empirical models across different regions or under varying environmental conditions. To address the limitations of empirical models, semi-empirical models have been developed that combine physical principles with empirical data. These models offer a compromise between the theoretical rigor of physical models and the simplicity of empirical approaches, making more adaptable and less site-specific (Mathieu et al., 2003). Among the most prominent semi-empirical models are those developed by Oh (Engman and Chauhan, 1995), Dubois (Ma et al., 2021), and Shi (Shi et al., 2021), which are widely used due to retrieval of soil moisture under varying surface roughness conditions. These models typically incorporate simplified assumptions that approximate the complex interactions between radar signals and the soil surface, allowing for practical implementation without the need for extensive parameterization.

The well-used semi-empirical model is the Water Cloud Model (WCM), which is

particularly effective in scenarios involving vegetation cover (Han et al., 2020; Liu et al., 2022). The WCM estimates soil moisture by accounting for both the direct backscatter from the soil and the attenuation and scattering effects of the vegetation layer. The model assumes that the total backscatter is the sum of contributions from the vegetation canopy and the underlying soil, with vegetation acting as a semi-transparent medium that attenuates the signal (Yadav et al., 2019). By incorporating parameters that describe the vegetation structure and water content, the WCM can effectively isolate the soil moisture signal even in the presence of moderate to dense vegetation. Despite its advantages, the model's accuracy can decrease in conditions of very dense vegetation, where the complexity of the interactions between the radar signal, vegetation, and soil becomes more challenging to model (Singh et al., 2023).

Time-series soil moisture retrieval methods represent a more advanced approach that uses the continuous acquisition of SAR data over time to monitor soil moisture dynamics (Kim et al., 2012). Unlike traditional methods that rely on snapshots of radar data, time-series analysis considers the temporal evolution of backscatter, enabling the detection of trends, cycles, and anomalies in soil moisture content (Balenzano et al., 2021; Kim et al., 2012). The development of time-series methods has been driven by the increasing availability of long-term satellite datasets, such as those from the ESA Sentinel-1 mission. Sentinel-1, with its frequent revisit times and consistent radar configurations, has been particularly helpful in time-series soil moisture retrieval (Fan et al., 2022; Zakharov et al., 2020). The use of time-series data allows for the application of more sophisticated analytical techniques, such as harmonic analysis, autoregressive models, and wavelet transforms, which can decompose the radar backscatter signal into its constituent temporal components, isolating the soil moisture signal from noise.

Change detection algorithm is another operational soil moisture retrieval, by taking advantage of the temporal changes in radar backscatter to detect variations in soil moisture content. The fundamental concept behind algorithm is that, assuming constant surface roughness and vegetation cover, any changes observed in the backscatter coefficient ( $\sigma^{o}$ ) between two or more SAR acquisitions can be attributed to changes in soil moisture (Hornacek et al., 2012). This approach has been particularly effective in regions where surface properties remain unchanged over time, allowing for soil moisture retrieval with optimal accuracy.

The earliest forms of change detection in radar remote sensing were relatively simple, focusing on techniques such as image differencing and ratioing. While these methods are

straightforward, they have inherent limitations, particularly the assumption that surface roughness and vegetation conditions remain constant between acquisitions (Bovolo and Bruzzone, 2005; Rignot and van Zyl, 1993). This assumption can often be violated in natural environments, leading to inaccuracies in soil moisture retrieval. For instance, if vegetation cover drastically increases or decreases between the two acquisitions, the change in backscatter may reflect this vegetation change rather than a true change in soil moisture (Notarnicola, 2014). Similarly, changes in surface roughness due to agricultural activities, erosion, or other factors can also complicate the interpretation of the backscatter differences. To address these challenges, researchers have developed more sophisticated change detection algorithms that account for variations in surface conditions. One significant advancement is the Delta Index ( $\Delta$ -index), introduced by (Thoma et al., 2008). The  $\Delta$ -index normalizes the difference in backscatter between wet and dry conditions by the dry reference backscatter, effectively scaling the soil moisture signal. This approach helps mitigate the impact of surface roughness and vegetation changes by focusing on relative rather than absolute differences in backscatter, thereby improving the robustness of the soil moisture retrieval. Over the time, change detection algorithms have been modified as short term change detection (Balenzano et al., 2021) and advanced change detection. The short term change detection algorithm takes advantage of using frequent revisit of the Sentinel 1 SAR data by hypothesizing that the shorter the SAR revisit, the better the assumptions of the algorithm. Further SAR signal at C-band does not always penetrate the vegetation layer and this is resolved by masking those surfaces characterized by volume scattering (Balenzano et al., 2021). Similar to the short term change detection method, the proposed Advanced Change Detection method applies to bare or vegetated soils dominated by attenuated surface scattering (Zhu et al., 2022). Roughness is also assumed to be time-invariant, as it remains relatively stable over a crop season (a few months). However, this method accounts for variations in two-way vegetation attenuation to reflect the effect of temporal changes in vegetation. Additionally, the algorithm uses the full range of soil moisture within a given grid, rather than just the upper and lower bounds, to overcome the tendency to underestimate soil moisture, which often results in most retrievals being near the minimal bound (Zhu et al., 2022). However, with the current temporal resolution of most SAR systems being 12– 14 days, the algorithm may struggle to decouple the effects of surface roughness and vegetation changes accurately, leading to high uncertainty in the retrieved soil moisture. The Advanced Change Detection method relies on auxiliary datasets such as SMAP soil moisture and Moderate

Resolution Imaging Spectroradiometer - based Normalized Difference Vegetation Index (Zhu et al., 2022). Despite these advancements, several challenges remain in the application of change detection algorithms for soil moisture retrieval. One of the primary challenges is the need for accurate and consistent radar data, particularly in regions with complex terrain or heterogeneous land cover. Variations in radar incidence angle, sensor calibration, and environmental conditions can introduce noise into the change detection process, potentially leading to erroneous soil moisture estimates. Moreover, the effectiveness of change detection algorithms can be limited by the temporal resolution of the radar data. In areas with rapid soil moisture dynamics, such as regions subject to frequent rainfall or irrigation, the medium to high temporal gaps between radar acquisitions may result in missed changes or underestimation of soil moisture variability. Further using more ancillary input in the algorithm to retrieve soil moisture may create an additional uncertainty in the soil moisture retrieval.

Looking into the complexities of the soil moisture retrieval using the above mentioned algorithms from SAR, an active-passive disaggregation approach has been proposed by Das et al., (2011). The active-passive disaggregation algorithm developed by Das et al., (2011) is a robust approach that merges L-band radiometer and radar data to improve the spatial resolution of soil moisture retrievals. This method was specifically designed for the NASA SMAP mission, which aims to provide high-resolution soil moisture measurements. The algorithm effectively combines coarse-resolution radiometer data, known for its accuracy in soil moisture retrieval, with fine-scale radar data that captures spatial heterogeneity. This disaggregation process enables soil moisture retrieval at a much finer spatial resolution. Initially developed as a baseline method for the SMAP mission, this algorithm does not require previous satellite overpass observations and provides an absolute measure of soil moisture rather than relative soil moisture change. Later, Das et al., (2014) modified this active-passive disaggregation algorithm to disaggregate brightness temperature using SMAP data. In this method, radar backscatter data were used to downscale the brightness temperature data, from which high-resolution soil moisture was retrieved using a zeroth-order radiative transfer model. However, this method requires high-resolution ancillary data, such as temperature and vegetation water content, for further soil moisture retrieval. Following the failure of the SMAP radar, the active-passive disaggregation approach was used to downscale SMAP brightness temperature by blending it with Sentinel-1 SAR data, enabling soil moisture retrieval at 1 [km] and 3 [km] spatial resolutions (Das et al., 2019). This algorithm has since been used

operationally for SMAP-Sentinel soil moisture retrieval, with validation statistics shows that the ubRMSD is below 0.06 [m³/m³] (Colliander et al., 2022). However, this dataset does not meet the high spatial resolution requirements of some geophysical applications, which requires soil moisture data at 100-200 [m] or even finer scales. The upcoming SAR missions hold great potential for high-resolution soil moisture retrievals, even finer than 100 [m] in spatial resolution. Capitalizing on one of these upcoming missions, specifically the NISAR mission, disaggregation method can potentially be the best algorithm to use. This algorithm disaggregates coarse-resolution soil moisture data, either from climate models or radiometer-based sources, and blends it with fine-scale SAR measurements.

This algorithm aims to retrieve soil moisture at a higher resolution using approximately 10 [m] resolution backscatter measurements from the NISAR mission. The primary objective of proposing this algorithm was to reduce dependency on multiple ancillary parameters related to soil and vegetation, thereby providing an operational high-resolution soil moisture product for the NISAR mission. The multi-scale algorithm is entirely data-driven, relying solely on coarse-resolution soil moisture data and SAR dual-polarization observations, eliminating the need for additional ancillary data. This approach reduces the degree of freedom, allowing for optimal accuracy and low uncertainty. A key advantage of this algorithm is that it can use coarse resolution soil moisture from climate model and does not depend on coarse-resolution inputs from satellite radiometer data. This approach avoids dependencies and uncertainties associated with satellite-based soil moisture products, such as those from the SMAP or SMOS missions. Additionally, using reanalysis soil moisture data ensures a better temporal match with SAR observations, as reanalysis data are typically generated at hourly intervals.

#### 1.6 Discussion

The high-resolution soil moisture retrieval from SAR missions is a critical goal for various geophysical applications, but it comes with several inherent challenges. Traditional soil moisture retrieval algorithms, such as theoretical, empirical, and semi-empirical models, struggle to scale globally and operate effectively due to several factors, including environmental variability, the complexity of radar backscatter signals, and the reliance on ancillary data. These challenges have limited the applicability of these models for global and operational soil moisture retrieval, highlighting the need for innovative approaches. One of the primary challenges with these traditional algorithms is their reliance on ancillary data inputs such as soil texture, vegetation

cover, and surface roughness. Accurate soil moisture estimation requires the effects of these factors from the radar backscatter signal. However, obtaining high-resolution ancillary data at a global scale is immensely difficult, particularly because these variables can vary significantly over small spatial scales and over time. Additionally, each dataset used as ancillary input introduces its own level of uncertainty. Since no dataset is entirely accurate, combining multiple inputs often leads to a cumulative increase in uncertainty, which can compromise the reliability of the soil moisture retrieval. Moreover, the effectiveness of algorithms like theoretical and semi-empirical models depends heavily on the assumptions made regarding surface and vegetation conditions, which may not hold true across different environments and times. For instance, the accuracy of these models can be compromised in areas with dense vegetation or rough terrain, where the radar signal is subject to complex interactions that are difficult to model accurately. In the coming years, the landscape of SAR missions will evolve significantly, with the continuation of the Copernicus Sentinel program and the availability of L-band and C-band SAR data from missions such as ALOS-2, ALOS-4, NISAR, Tandem-L and ROSE-L. This increased availability will reduce temporal resolution limitations and provide more opportunities to apply advanced soil moisture retrieval algorithms. For example, short-term change detection algorithms, which are effective at high temporal resolutions, will become good options with the improved revisit times of these missions. However, the challenges related to the requirement of ancillary data and the potential increase in uncertainty remain.

However, the disaggregation algorithm like active-passive disaggregation approach can potentially be used to achieve optimal accuracy for high-resolution soil moisture retrieval. This algorithm relies on coarse-resolution soil moisture/brightness temperature inputs, which can be sourced from current passive missions like SMAP and SMOS. In the near future, missions such as CIMR may also be explored for the disaggregation of brightness temperature or soil moisture, depending on the frequency of SAR data available. Given the upcoming mission timelines, there will be a substantial availability of C-band and L-band SAR data, including missions from the Copernicus Sentinel Programme, ROSE-L, and NISAR. The disaggregation approach, including active-passive methods and multi-scale algorithms, offers a robust solution to the challenges of high-resolution retrieval by blending the coarse-resolution soil moisture data with high-resolution SAR inputs. These approaches reduce the dependency on ancillary data and minimize the degrees of freedom in the retrieval process, leading to more accurate and less uncertain results. Climate

models, such as ERA5-Land or upcoming ERA6-Land, is a useful source of coarse-resolution inputs, especially given assimilation of satellite data and observation data. The climate model derived soil moisture offer's hourly temporal resolution datasets that can closely match SAR acquisition times. This reduces dependency on satellite-based soil moisture products, which carry uncertainties related to mission lifetimes. By considering climate model inputs, the disaggregation approach also eliminates the need for extensive ancillary data, further reducing uncertainty in soil moisture retrieval. This method can be applied to any upcoming C-band or L-band satellite missions, offering for more accurate and reliable soil moisture retrieval at high spatial resolution < 100 [m], which is particularly beneficial for many geophysical applications like precision agriculture.

In the near future, the introduction of P-band SAR missions, such as the Biomass mission, will be very useful for retrieval of root zone soil moisture. However, the temporal resolution of these missions may not be sufficient for change detection algorithms, which require frequent revisit times. Instead, disaggregation algorithms that use coarse-resolution soil moisture data from climate models could be more effective. The retrieval of high-resolution root zone soil moisture can be useful for understanding deeper soil processes and use in various applications. Additionally, the potential use of UAVSAR or drone-based SAR data offers a unique opportunity to achieve even higher resolution soil moisture retrieval at field scales, around 10 [m]. This could be particularly beneficial for precision agriculture, where fine-scale moisture variability is critical for optimizing irrigation and other water management practices. The combination of drone-based data with passive microwave satellite or climate model data in a disaggregation framework could offer unprecedented detail and accuracy in soil moisture mapping.

#### 1.7 Dissertation Outline

Based on the comprehensive literature review, it is evident that the disaggregation approach holds significant potential for the soil moisture retrieval of upcoming SAR missions. In this thesis, particular emphasis is given for the NISAR mission, which is expected to launch in February 2025. The NISAR mission will provide L-band SAR backscatter measurements with a fine spatial resolution of ~10 [m]. By taking advantage of the availability of NISAR's high-resolution backscatter data, this research aims to develop a robust algorithm for high-resolution soil moisture retrieval, with gridded uncertainty estimates. To accomplish this, the thesis is organized around the following key objectives:

- 1. Understanding the spatiotemporal evolution of long-term patterns of soil moisture at a global extent.
- 2. Assessment of ERA5-Land volumetric soil water layer product using *in-situ* and SMAP soil moisture observations.
- 3. Development of multi-scale algorithm for NISAR mission high resolution soil moisture product.
- 4. Comprehensive validation of the NISAR multi-scale soil moisture retrieval algorithm across various spatial resolutions and landcovers using the ALOS-2 data
- 5. Estimation of uncertainty in high-resolution soil moisture retrieval from SAR observations

Based on the objectives mentioned above, the thesis is organized into seven chapters. Chapter 1, the Introduction, establishes the foundation of the thesis by discussing current and upcoming missions. This chapter provides an overview of various algorithms used in the past, highlighting their advantages and limitations. Additionally, it presents a concise overview of different SAR missions and the potential use of passive radiometer-based soil moisture data, as well as the advantages of incorporating climate data if required by the algorithm.

Chapter 2 explores long-term changes in soil moisture and how these changes are related to various hydrometeorological parameters. This chapter provides a broad overview of soil moisture variations at a coarse resolution of 0.1°, emphasizing the research gap where significant heterogeneity within the coarse resolution data is not captured. It underscores the need for high-resolution soil moisture retrieval, as identified in Chapter 1, where the overview of different algorithms suggests that disaggregation algorithms hold significant potential.

Given the advantages of the disaggregation algorithm and its potential application to the NISAR mission for soil moisture retrieval, the focus shifts to its implementation. The algorithm utilizes coarse resolution soil moisture data (such as that from ECMWF) as an input to disaggregate and retrieve high-resolution soil moisture by incorporating SAR backscatter information. Before employing this coarse resolution soil moisture data in the algorithm, it is crucial to assess the quality of the product using well-established *in-situ* soil moisture networks and satellite products. This assessment is detailed in Chapter 3.

Chapter 4 presents the development and implementation of the "multi-scale algorithm" for

high-resolution soil moisture retrieval. This chapter begins with a detailed discussion of the algorithm's derivation, followed by an explanation of the implementation process. The algorithm is then applied to existing L-band SAR data to retrieve high-resolution soil moisture at a 200 [m] spatial resolution. Finally, the chapter includes a validation of the retrieved soil moisture by comparing it with coinciding *in-situ* measurements, demonstrating the algorithm's effectiveness and accuracy.

Chapter 5 uses the multi-scale algorithm developed in Chapter 4 by applying it to retrieve high-resolution soil moisture at an even finer scale of 100 [m]. This chapter presents the validation of the algorithm across various hydroclimatic zones and land covers, offering a comprehensive assessment of its performance in more complex environments. By testing the algorithm on different land covers, the chapter demonstrates its robustness and evaluates its ability to meet the desired accuracy goals in diverse settings.

Chapter 6 focuses on the uncertainty estimates associated with soil moisture retrieval using the multi-scale algorithm. In this chapter, an analytical solution is derived to estimate the uncertainty in soil moisture retrievals. Traditionally, validation statistics are employed to represent error or uncertainty; however, *in-situ* measurements are only available for a limited number of locations due to the tedious and expensive nature of data collection. These statistics are constrained to specific locations and land covers, and do not adequately represent uncertainties across the full spatial and temporal extent of relevant land surfaces where soil moisture is retrieved. Therefore, this chapter addresses the need for a method to estimate uncertainty for each valid pixel or grid of retrievals, which is important for assessing the quality of high-resolution soil moisture products.

The final chapter, "Conclusion" offers a consolidated summary of the findings from the development and validation of the multi-scale soil moisture retrieval algorithm. It synthesizes all the information from Chapters 2 to 6 and situates them within the broader scope of the research theme, highlighting the importance of high-resolution soil moisture retrieval and its applications in geophysical studies.

# CHAPTER 2: SPATIOTEMPORAL EVOLUTION OF GLOBAL LONG-TERM PATTERNS OF SOIL MOISTURE

This chapter was published as Preet Lal, Ankit Shekhar, Mana Gharun, Narendra N. Das, "Spatiotemporal evolution of global long-term patterns of soil moisture", Science of The Total Environment, Volume 867, 2023, 161470, DOI: 10.1016/j.scitotenv.2023.161470. © 2023 The Authors. Published by Elsevier B.V.

As discussed in the first chapter, the current and upcoming period referred as the "Golden Age of SAR", with endless possibilities for high-resolution soil moisture retrieval using upcoming SAR missions. However, it is important to analyze long-term changes in global soil moisture patterns. Therefore, the primary objective of this chapter is to understand the spatiotemporal evolution of long-term soil moisture patterns on a global scale using the available ERA5-Land reanalysis soil moisture product. This analysis will help determine whether high-resolution soil moisture datasets are necessary in the era of climate change.

#### 2.1 Introduction

Surface soil moisture (SM) is one of the most important state factors for existence of biotic lifeform (Grimm et al., 2013). SM has a major impact on regional climate, hydrology, ecology, and its feedback with atmosphere dominates variability of land carbon uptake by terrestrial ecosystem (Humphrey et al., 2021). Although in the overall global water budget the amount of SM may seem insignificant when compared to the total quantity of water at the global scale, the presence of SM in the thin layer of the Earth crust (i.e., soil surface) controls the success of agriculture, regulates partitioning of solar energy into latent and sensible energy, and precipitation into runoff and infiltration (Feng and Zhang, 2015). Therefore, understanding the long-term spatiotemporal evolution in pattern and trends of SM are of utmost importance for water resource conservation and management and its fate under changing climatic conditions.

The spatiotemporal variability of SM is influenced by many factors, such as precipitation, temperature, topography, land use, vegetation and soil type and depth (Deng et al., 2016, 2018). The change in soil moisture is mainly affected by precipitation as gain (wetting) and temperature/net-radiation as loss (drying) through evapotranspiration which also contributes to land-surface energy balance (Cho and Choi, 2014). Moreover, evapotranspiration is also influenced by wind, humidity, and above-ground vegetation (Wang et al., 2019). Thus, information on SM is critical for understanding the biophysical and geophysical processes that influence its

spatiotemporal evolution.

Given the limitations of using ground-based *in-situ* measurements of SM for understanding global SM variability, much of present research works for long-term (>40 years) SM data focus composite remote-sensing based datasets and/or model simulations (Fakharizadehshirazi et al., 2019; Yang et al., 2011). Presently, researchers employ satellite SM datasets (such as SMAP and SMOS), multi-satellite SWC datasets (such as ESA CCI dataset) and land-surface model-based soil moisture (such as GLDAS and ERA-Interim reanalysis datasets among others) which are well validated based on *in-situ* observations (Albergel et al., 2012b, 2012a; Zeng et al., 2015). The widely used ESA CCI and land-surface model-based SM datasets agree well with in-situ SM with comparable performance. In addition, both ESA CCI and simulated SM (GLDAS-Noah and ERA-Interim) showed consistent global soil drying trend from 1988-2010 (Dorigo et al., 2021). Also, a recent study by (Deng et al., 2020) highlighted that about 36% of the Earth's surface has significantly dried from 1979-2017 mainly in eastern and central Asia, central Europe and Africa, and central North America, mostly comprising of agricultural, urban, grassland and shrublands. However, multi-satellite ESA CCI dataset suffer with serious gaps, especially over its first decade of measurement (from 1978-1990) (Dorigo et al., 2017), thereby limiting its utility in comparison to modelled or reanalysis dataset, which are gap-free, for understanding long-term (>40 years) spatiotemporal trends. Furthermore, recent developments of land surface reanalysis data due to their affordable computational cost and ability to follow the rapid evolutions in land surface models make them a reliable dataset to study global long-term spatiotemporal trends (Boussetta et al., 2021).

The objective of this chapter is to explore the global long-term (40 years) spatiotemporal patterns of SM using the most recent reanalysis data from ECMWF's (European Centre for Medium-range Weather Forecasts) new land component of the fifth generation of European Reanalysis (ERA5-Land) dataset spanning over four decades (1981-2020). We have used spatiotemporal clustering method to highlight regional clusters of prominent long-term trends of SM. To further understand the regional long-term trends, we also performed spatiotemporal clustering of the drivers of SM, i.e., precipitation (P), bare soil evaporation (BSe), vegetation transpiration (VT) and normalized difference vegetation index (NDVI) and segregated these spatiotemporal patterns across different land-cover classes.

#### 2.2 Data and Methods

#### 2.2.1 Datasets

In order to understand the global spatiotemporal patterns of SM, we used long-term (1981-2020) state-of-the-art global ERA5-Land reanalysis (Muñoz-Sabater et al., 2021) dataset and other satellite-based dataset that are primary drivers of SM. The ERA5-Land data is provided by the Copernicus Climate Change Service (C3S). The ERA5-Land is an enhanced global dataset for land applications and provides a better spatial resolution of 9 km compared to 80 km for the older ERA-Interim (Muñoz-Sabater et al., 2021). Furthermore, ERA5-Land has incorporated improvements from 10 years of additional research and development in the use of satellite data as forcings and assimilation of state variables for weather prediction and atmospheric modeling in comparison to ERA-Interim (Hersbach et al., 2020). In comparison to ERA5, ERA5-Land also shows improvements due to non-linear dynamical downscaling with revised thermodynamic input (Muñoz-Sabater et al., 2021).

Table 1: Dataset used in this study. All the datasets span from 1981-2020. All datasets were aggregated yearly for analysis.

Variable	Sub-variable	Spatial Resolution	Source
Volumetric Soil water content (m³/m³) - SM	Depth: 0 - 7 cm	$0.1^{\circ} \times 0.1^{\circ}$	_
	Depth: 7 - 28 cm	$0.1^{\circ} \times 0.1^{\circ}$	
	Depth: 28 - 100 cm	$0.1^{\circ} \times 0.1^{\circ}$	
(III /III ) - SIVI	Depth: 100 - 289 cm	$0.1^{\circ} \times 0.1^{\circ}$	
	Evaporation from bare soil		ERA5 - Land
Evapotranspiration	(BSe)	$0.1^{\circ} \times 0.1^{\circ}$	
<b>(m)</b>	Vegetation transpiration		
	(VT)	$0.1^{\circ} \times 0.1^{\circ}$	
<b>Precipitation (m)</b>	Total Precipitation (P)	$0.1^{\circ} \times 0.1^{\circ}$	
NDVI			NOAA CDR
	NDVI	$0.05^{\circ} \times 0.05^{\circ}$	AVHRR v5

The ERA5-Land reanalysis datasets used in this study were - volumetric soil water content indicating SM for 4 different depths (0-7 [cm], 7-28 [cm], 28-100 [cm] and 100-289 [cm]), evaporation from bare soil, vegetation transpiration, and total precipitation (Table 1). The NDVI was derived from the NOAA Climate Data Record (CDR) of AVHRR (Advanced very-high resolution radiometer) satellite (Vermote et al., 2009) as shown in Table 1. All the datasets were aggregated at  $0.1^{\circ} \times 0.1^{\circ}$  spatial and with yearly means (temporal resolution) to study the

spatiotemporal patterns. In addition, we used the MODIS Landcover data (MCD12C1 v006) of 2020 (Friedl et al., 2010, 2002) to segregate the SM patterns only for different vegetated landcovers (landcovers excluding snow & ice, barren lands and water bodies).

### 2.2.2 Methods

We performed space-time pattern mining (STPM) to detect spatiotemporal patterns of SM. In a nutshell, the STPM does 'spatial clustering' of 'temporal' trends. The STPM allows to detect hotspots and coldspots and their patterns in-terms of 'persistent', 'diminishing' and 'intensifying' trends as shown in Figure 2. The methodology involves the following steps:

- 1. Creation of a space-time cube of the dataset with two spatial dimension and one temporal dimension (see Figure 1). In a space-time cube, each spatial location at any particular time is called a 'bin', whereas the snapshot of all spatial data is called a 'time-slice' (see Figure 1). Each bin also has its timeseries and is called a 'bin time-series'.
- 2. Each bin in a time-slice is assigned to a 'hotspot' or a 'coldspot' cluster based on the Getis Ord Gi\* statistic.
- 3. Hotspot and coldspot cluster represent bins with high and low values, respectively based on a threshold of 0.2 [m³/m³] for the surface soil moisture layer (detected by the Getis Ord Gi\* statistic). The Gi\* statistics considers the feature of neighboring bins (8 neighboring bins 72 [km] used in this study), resulting in a z-score. This z-score is a measure of how strongly a bin belongs to a hotspot or a coldspot cluster. This is repeated for each time-slice, thereby assigning each bin to either of the clusters.
- 4. Then, a non-parametric Mann-Kendall test statistics (MKTS) is performed for the Gi\* statistics of each bin time-series to determine the trend of the spatial clustering (shown in step-3). The MKTS is also a z-score determining any significant trend in Gi\*.
- 5. Thereafter, for values of each bin time-series, a MKTS is also performed to determine the temporal trend over the 40 years (1981-2020). The MKTS indicates if there was a significantly (p<0.05) positive, negative, or no significant trend in the values of a bin time-series. The output is also a z-score for each bin.
- 6. Finally, the z-score from Step-3 and Step-4 are combined to determine the spatiotemporal pattern. The resulting combination of spatiotemporal trends results in various types of spatiotemporal pattern (see Figure 2) which can be seen in for more details.

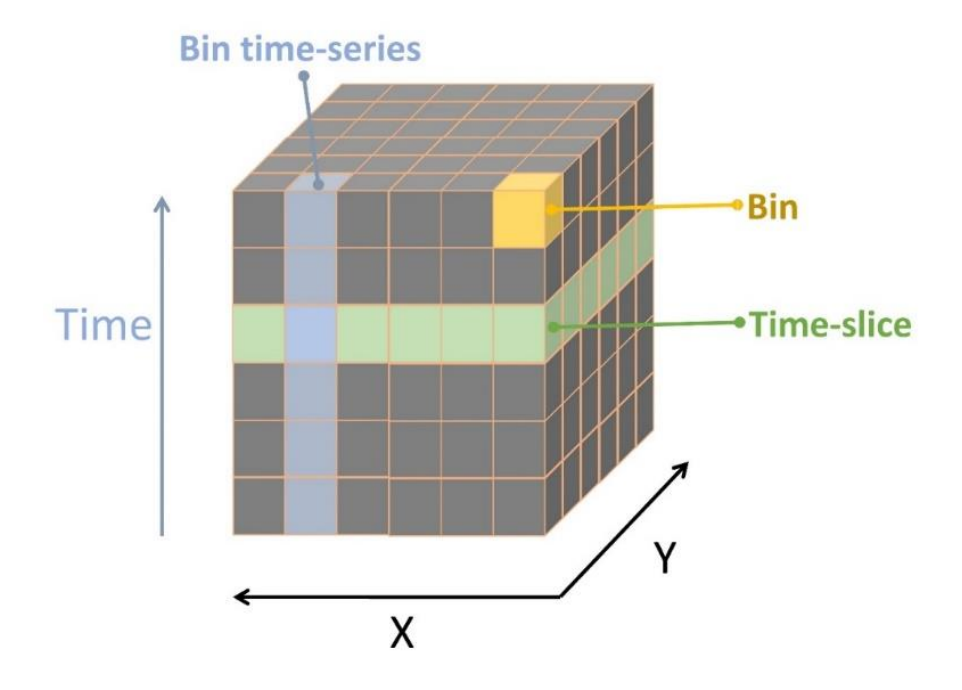


Figure 1: Illustration of space-time cube for the space-time pattern mining (STPM). The space-time cube in a visualization of the dataset in 3-D with two spatial dimension (X and Y) and one temporal dimension (Time). A 'bin' is any spatial point at a particular.

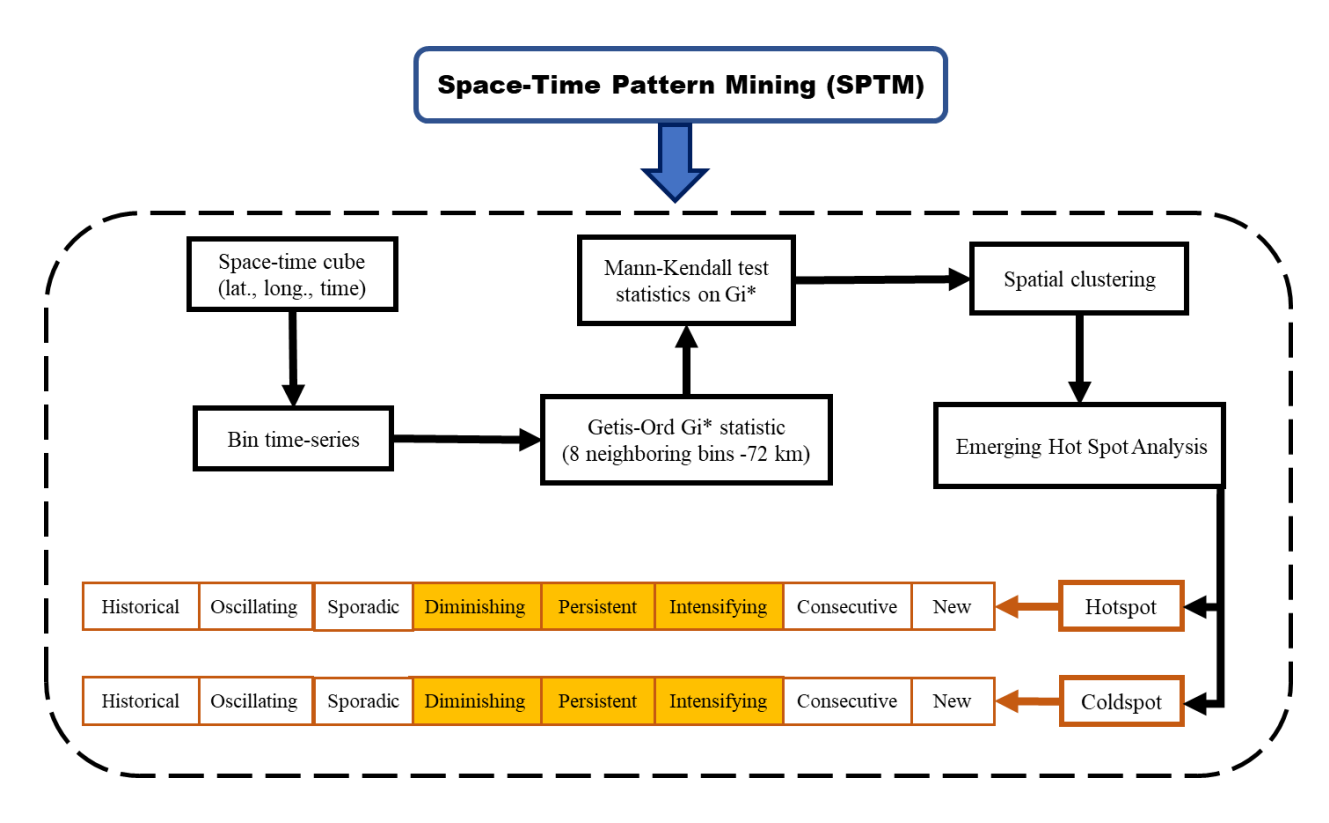


Figure 2: Illustration of space-time pattern mining (STPM) methodology to detect spatiotemporal patterns. The yellow highlighted pattens are focused on this study.

Table 2: The six types of spatiotemporal patterns detected and their definitions.

#	Spatiotemporal pattern	Definition		
1	Diminishing hotspot (DH)	Areas with high values (of the dataset) showing significant (p<0.05) decreasing trend over 40 years.		
2	Diminishing coldspot (DC)	Areas with low values showing significant (p<0.05) increasing trend over 40 years		
3	Intensifying hotspot (IH)	Areas with high values showing significant (p<0.05) increasing trend over 40 years		
4	Intensifying coldspot (IC)	Areas with low values showing significant (p<0.05) decreasing trend over 40 years		
5	Persistent hotspot (PH)	Areas with consistent high values and no significant change over 40 years		
6	Persistent coldspot (PC)	Areas with consistent low values and no significant change over 40 years		

We focused on six types of spatiotemporal patterns in this study i.e., diminishing, intensifying, and persistent hotspots and coldspots (Table 1 and Figure 2). Out of the six types, the diminishing hotspot and intensifying coldspot indicates areas with significant decreasing trend (e.g., soil drying for SM variable), whereas intensifying hotspot and diminishing coldspot indicates areas with significant increasing trend (e.g., soil wetting for SM variable). The persistent patterns indicate areas with consistent values with no significant trend and no short-term trends over the 40 years. We implemented the STPM analysis on all the datasets, i.e., SM, BSe, VT, P and NDVI, to determine areas with the above-mentioned six types of spatiotemporal patterns. We determined regional drivers of SM patterns, based on the corresponding patterns of spatiotemporal evolution of BSe, VT, P and NDVI. The STPM analysis was performed in ArcGIS Pro 2.9 software. The post-processing of the STPM analysis and visualization was conducted with R-software and extended to packages 'dplyr' (Wickham et al., 2020), 'raster' (Hijmans et al., 2015) and 'ggplot2' (Wickham, 2011).

### 2.3 Results and Discussions

## 2.3.1 Soil moisture pattern

Our results indicate that 48.3% of the global vegetated area (GVA) showed significant decreasing trend in surface (0-7 [cm] depth) soil moisture over the 40 years (Figure 3 and Figure S1). This 48.3% of total global vegetated area is further identified and divided into two major

spatiotemporal clusters such as: i) 34.1% of area were under diminishing hotspot pattern, and ii) 14.2% of area were under intensifying coldspot pattern (inset panel in Figure 3). Most of the decreasing SM areas were located in the western part of North America, Europe, South America, Central Africa, and Central Australia as shown in Regions A, C, D, E and H in Figure 3, respectively. Also, about 9% of area of global vegetated area indicated surface soil wetting over the 40 years, with mostly under the intensifying hotspots pattern. The high latitudes and the Indian peninsula regions prominently show soil wetting patterns (Figure 3). The remaining ~30% of the global vegetated areas showed a consistent, no significant trend of soil moisture over 40 years, comprising the eastern and the northern part of North America and the northern part of Asia (Figure 3). The STPM patterns of all the soil layers were largely similar as indicated by high diagonal percentages in Figure 4, indicating most of soil wetting and drying patterns (> 80% of area) were similar across 100 [cm] soil depth. The surface (0-7 [cm]) and 2<sup>nd</sup> soil layer (7-28 [cm]) SM patterns were 90% identical, whereas the similarity between surface and 3<sup>rd</sup> soil layer (28-100 cm) was about 80% (Figures 4a and S2). Furthermore, as much as 45% of the global vegetated area showed soil drying pattern of the deepest soil layer (100-289 [cm]). Our results, especially for surface soil moisture is largely consistent with previous analysis by (Deng et al., 2020; Dorigo et al., 2012). However, few differences (especially in the spatial pattern) were observed, and this might be due to pixel-based analysis by previous research and spatiotemporal clustering in this study. We further analyze the global patterns of evapotranspiration (BSe and VT), precipitation and NDVI to understand the regional drivers of soil moisture pattern. From hereafter we focus only on surface soil moisture patterns.

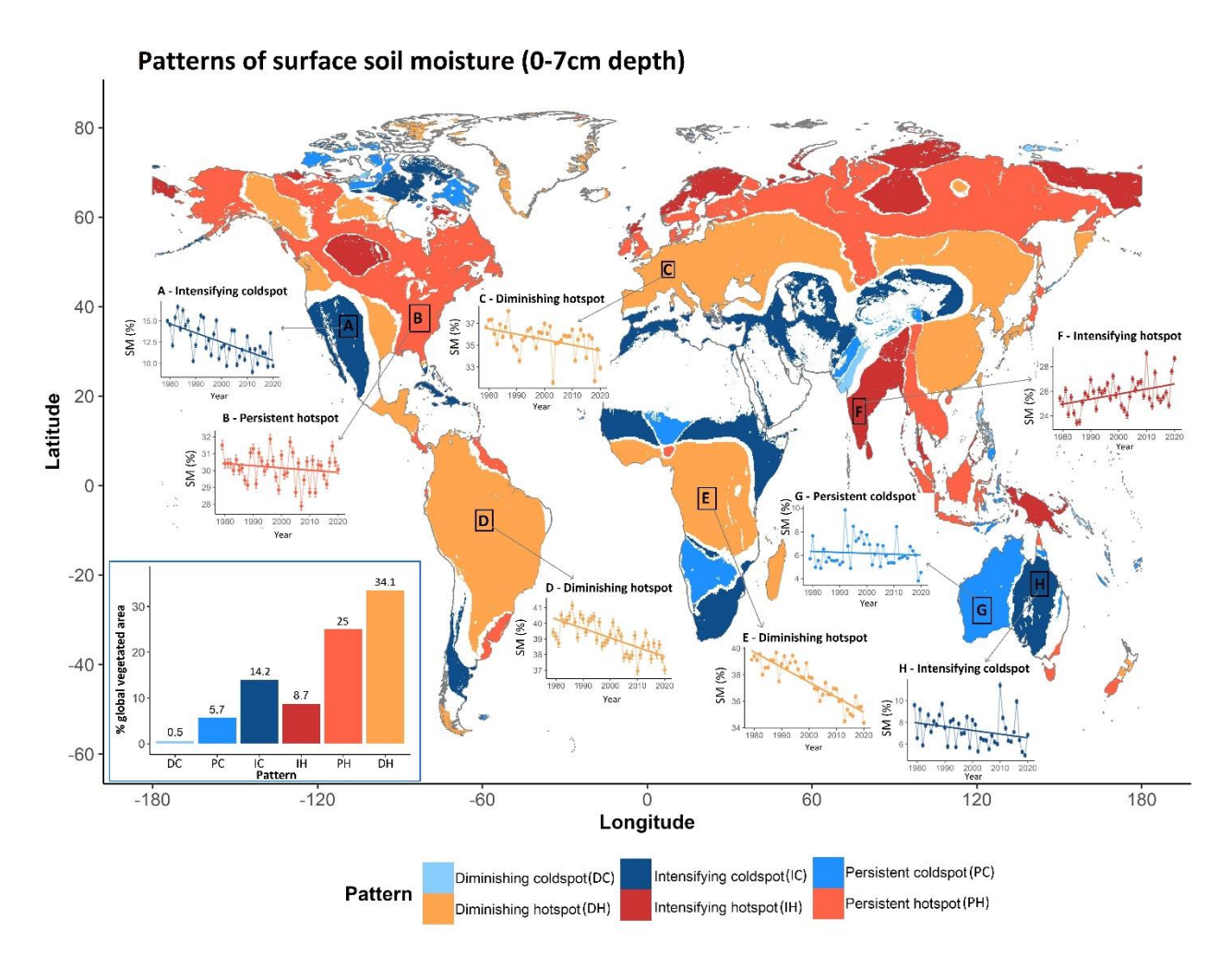


Figure 3: Global patterns surface soil moisture (0-7 cm depth) over global vegetated areas. The inset panel shows the percentage of global vegetated area for each SM pattern. The inset panel shows the percentage of global vegetated area for each SM pattern. The description of the patterns can be found in Table 2.

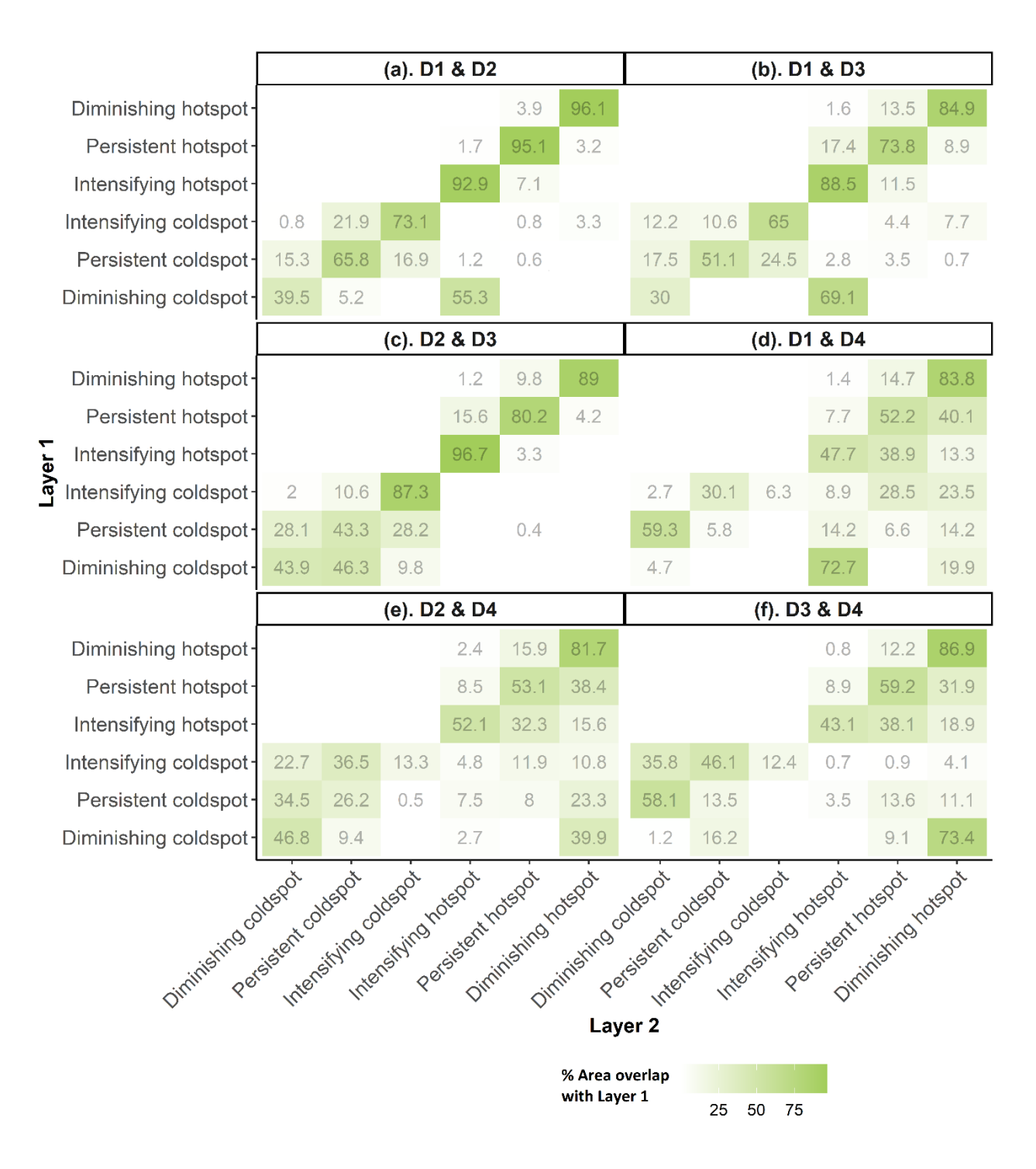


Figure 4: Similarity of spatiotemporal patterns between different layers of soil as a percent of Layer 1. D1, D2, D3 and D4 represents soil layer from depth 1 (0-7 cm), depth 2 (7-28 cm), depth 3 (28-100 cm) and depth 4 (100-289 cm), respectively. Layer 1 represents the first soil layer of the panel label, for example in (a) D1 & D2, the D1 is Layer 1 and D2 is Layer 2.

About 40% and 50% of the global vegetated area showed increasing trend in bare soil evaporation and transpiration over the 40 years period, respectively (as illustrated in Figs. 5b and

5c), with most of them being intensifying hotspots. Also, 16% of global vegetated area showed decreasing trend in bare soil evaporation (belonging to diminishing hotspot class), whereas 16.5% of area showed decreasing vegetation transpiration (Figs. 5c and region F in Figure 6). The precipitation patterns were largely different from patterns of evapotranspiration (BSe + VT) (Figure 5). About 25%, 15%, and 45% of the global vegetated area showed decreasing trend (diminishing hotspot), increasing trend (intensifying hotspot), and consistently no significant trend (persistent hotspot) of precipitation over the 40 years (Figures 5d), respectively. In addition, the vegetation biomass (indicated by NDVI) largely showed increasing trend over 37 % of global area (especially over the northern higher latitudes) and no significant trend over 44% of global area over the 40 years, consistent with observed greening of the Earth (Zhu et al., 2016) (Figure 5e). Only 8% of global vegetated area showed browning patterns (decreasing trend in NDVI) over 40 years, mostly in African and Indonesian rainforest (Figure 5e). This detected browning patterns are largely consistent with results reported by (Winkler et al., 2019) where they observed negative trends in average annual LAI for tropical regions.

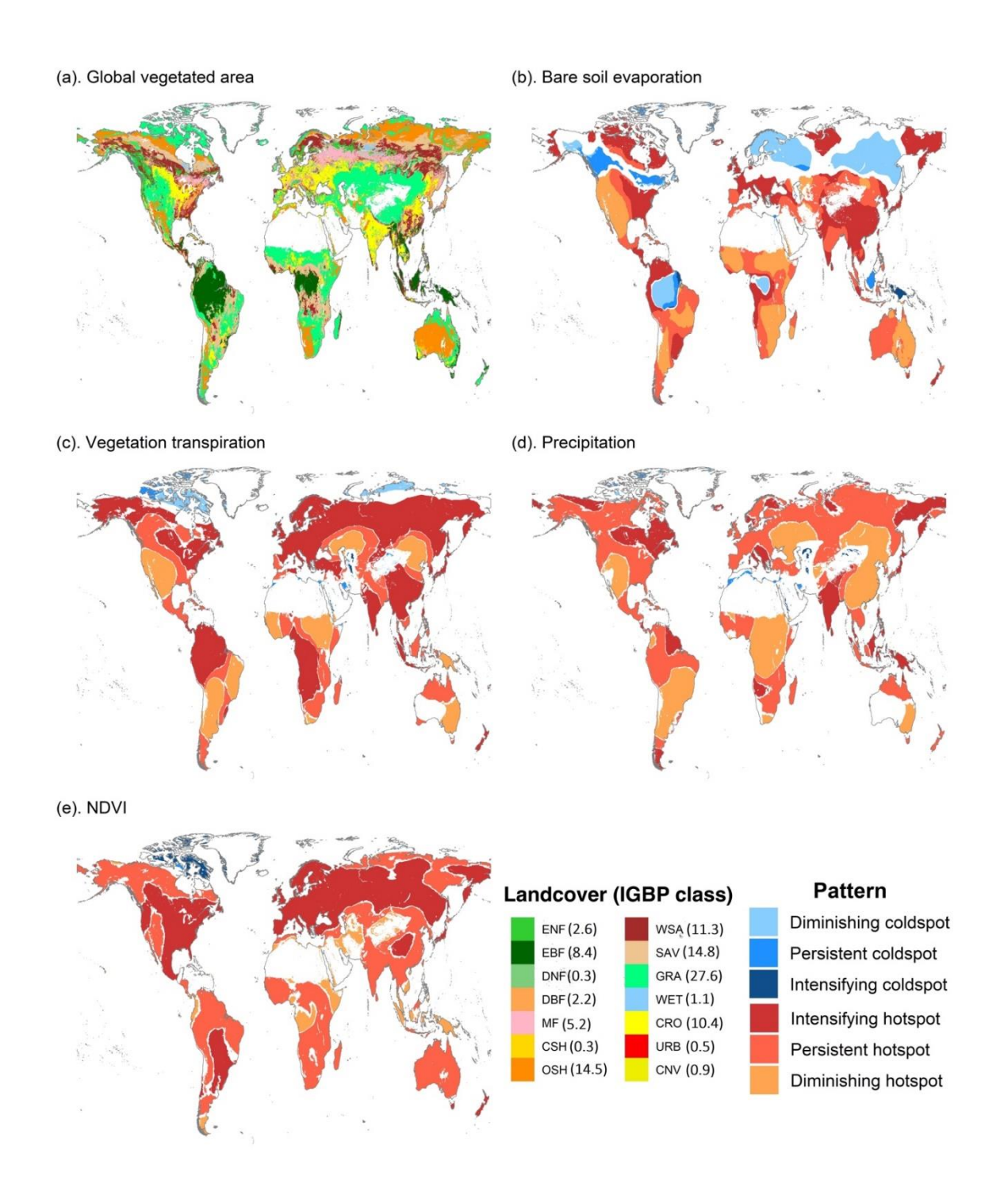


Figure 5: (a) Global vegetated area derived from MODIS landcover data (MCD12C1) and detected spatiotemporal patterns of (b) bare soil evaporation (BSe), (c) vegetation transpiration (VT), (d) precipitation (P) and (e) NDVI. The MODIS landcover data is represented as an IGBP class in 'a'. The number in the brackets outside the IGBP classes represent the % area share of each of the landcover class.

We observed different combinations of evapotranspiration and precipitation (drivers of SM) patterns for different evolution of SM state (Figure 6). For example, the western North America region (region A in Figure 6) witnessed decrease in precipitation resulted in decrease in surface SM eventually resulted in decrease in evapotranspiration over the years (Figure 6). The Congo Rainforest and Basin (region E) witnessed a significant increase in evapotranspiration (BSe + VT) but significant decrease in the precipitation resulting a decrease in soil moisture. On the contrary, the eastern part of Indian Peninsula (region F) witnessed increase in precipitation resulting in increase in SM over the years (Figure 6). About 4.5% of the global vegetated area showed soil wetting (intensifying hotspot or diminishing coldspot) over the 40 years, also showed increasing precipitation (Figure 7). Such regional interactions of precipitation and evapotranspiration affect trends in SM.

## 2.3.3 Spatiotemporal patterns of soil drying

About 80% of the global vegetated areas with drying surface SM patterns over the 40 years also showed areas with combination of decreasing trend in precipitation and/or increasing trend in bare soil evaporation and vegetation transpiration (Figures 7 and 8). Both decreasing precipitation and increasing ET (evapotranspiration) occurred in about 40% each of the soil drying areas (Figures 7 and 8). The western part of North America, the southern part South America, parts of central Africa, parts of South Africa, and the eastern part of Australia are witnessing soil drying because of decreasing trend in precipitation (Figures 3, 6 and 8). The soil drying in the northern South America (most of the Amazonia) region and Europe is primarily characterized by increasing trend in evapotranspiration (in combination of bare soil evaporation and vegetation transpiration) but not due to decreasing trend in precipitation (Figures 3, 6 and 8). The parts of African rainforest and regions in Eastern China witnessed both decreasing trend in precipitation and increasing trend in evapotranspiration, ultimately resulting in decreasing of soil moisture in these areas (Figure 8). However, 20% of the soil drying areas did not show decreasing precipitation or increasing ET, but mainly showed decreasing ET (BSe and/or VT).

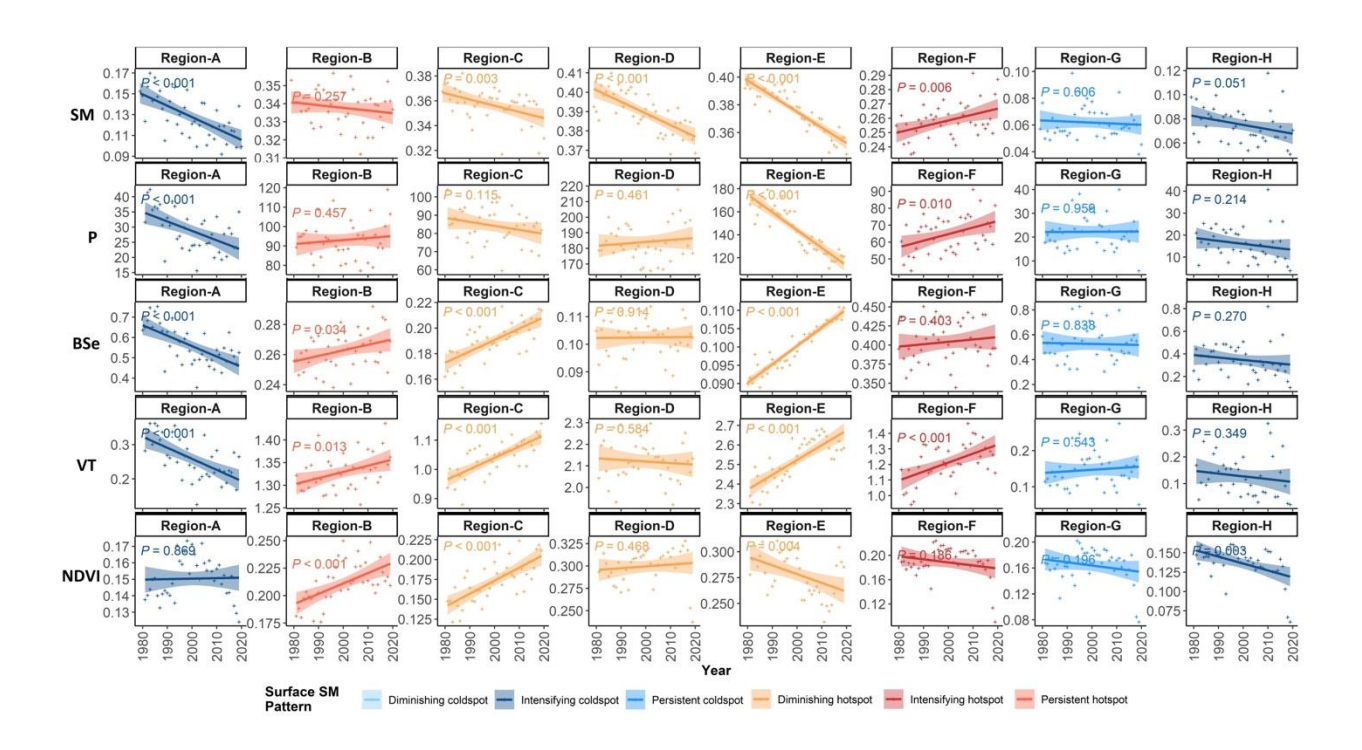


Figure 6: Long-term trends of total precipitation (P; m), bare soil evaporation (BSe; m), transpiration (T, m) and NDVI with surface SM (m³/m³) patterns of the eight regions (A-H) as shown in Figure 3.

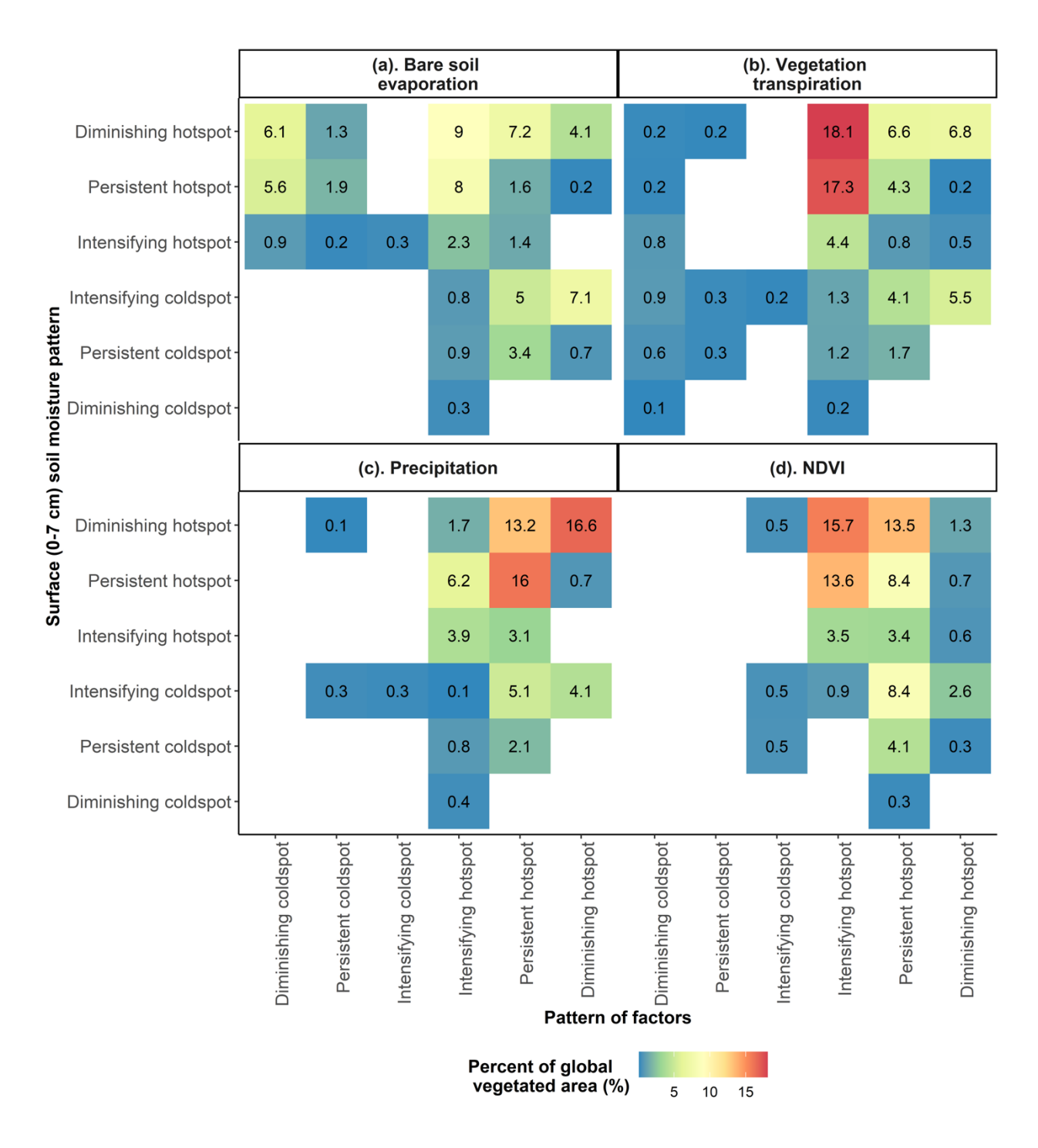


Figure 7: Percent share of global vegetated area with different patterns of soil water content (y-axis) and its drivers – (a) bare soil evaporation, (b) vegetation transpiration, (c) precipitation, (d) NDVI.

Among different landcover classes, more than 50% combined area of the evergreen broadleaf forest (EBF), deciduous broadleaf forest (DBF), grasslands (GRA), croplands (CRO),

urban (URB), and cropland/natural vegetation mosaics (CNV) showed soil drying over the 40 years (Figure 8). Thus, making our food security vulnerable due to soil drying especially in most of the rainfed croplands areas and grasslands. These regionals soil drying will have significant negative implications in future. Deng et al., (2020) showed that the drying trends of SM will most likely continue in the future thereby leading to expansion of global arid areas and widespread increase in drought prone areas (Dai, 2013). Furthermore, present and future soil drying can trigger multiple environmental disaster processes through so-called positive feedback loops. To start with, soil drying will adversely affect soil ecological and microbial health, increase breakdown of soil organic matter resulting in higher carbon loss from soil both in the form of carbon dioxide respiration and soil erosion (Achat et al., 2012). This reduced soil health will reduce crop production and further deteriorate ecosystem health, thereby driving the ecosystem closer to tipping points (Albrich et al., 2020; Seneviratne et al., 2010). Also with soil drying, the local/regional surface energy balance will be affected with increased sensible heat which will further result in increased temperature, thereby creating a positive feedback loop to increased rate of soil drying (Lal et al., 2021, 2022a; Seneviratne et al., 2010). This drying will also result in reduced global photosynthesis, which would ultimately weaken the terrestrial carbon sink and increase the carbon dioxide growth rate in atmosphere (Frank et al., 2015; Liu et al., 2020). Therefore, with future warming and present soil drying, increase in extreme events and land degradation is highly plausible in upcoming future.

The above analysis for global soil moisture pattern and feedback among hydro-meteorological parameters is understood using the ERA5-Land reanalysis datasets. The datasets are developed using multiple forcing of different meteorological observations and then assimilation in the land model. The reanalysis data may not always be the truth as observed. The uncertainty in data product may come from uncertainty and error in observations and during data assimilation, and also how model understand the energy budget of particular regions. However, we have used datasets with the pre-conceived notion that ERA5-Land data is well validated during previous research, and it's one of the best datasets available with high spatiotemporal resolution.

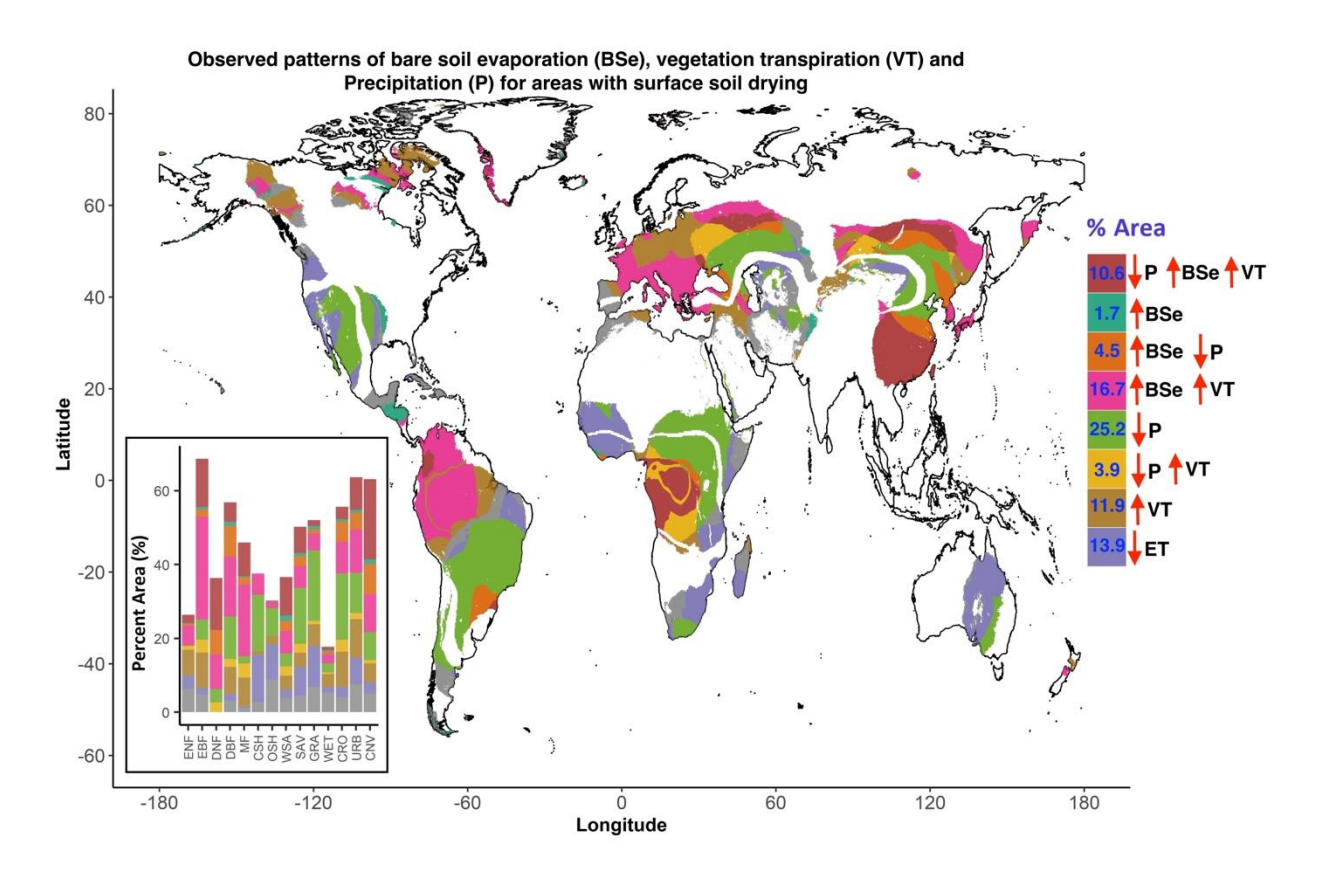


Figure 8: Areas with surface soil drying and pattern of its driver – precipitation (P), vegetation transpiration (VT) and bare soil evaporation (BSe). The upward/downward arrow indicate the increasing/decreasing pattern, with numbers inside the legend representing the % of soil drying areas for each pattern of the driver. The inset plots show the segregation of decreasing SWC area by landcover class. The landcover class is as per the IGBP code. About 80% of the soil drying areas showed decreasing P and increasing ET (BSe + VT).

## 2.4 Conclusions

Applying spatiotemporal clustering algorithm on global reanalysis soil moisture (SM) dataset, we highlighted regions with long-term (40 years) SM patterns in terms of soil drying, soil wetting and nearly steady soil moisture trends. Furthermore, we used long-term datasets of precipitation, evapotranspiration, and NDVI to understand the regional evolution of SM spatial patterns. We observed that about surface (0-7 [cm] depth) of 50% of global vegetated area dried over 40 years mainly accompanied by increased bare soil evaporation and vegetation transpiration and/or decreased precipitation. However, only 9% of global vegetated area showed upward trend in SM over 40 years, largely due to increasing trend in precipitation amount. The regions that showed drying trend are the important ecological regions such as Amazonia and Congo rain forest and agricultural regions in the western part of North America, the South and Central Europe, and

the eastern part of Asia. These SM drying trends will have a negative impact on future biodiversity, carbon cycle and food security. With global warming (with increasing ambient temperature), trends in SM, precipitation, and evapotranspiration and its feedback mechanism probably intensify further. Thus, scientists, stakeholders, and policymakers should focus on slowing down or reversing trends in these detected hotspots of SM regions to mitigate future negative impacts on biodiversity, carbon cycle, and food security.

The above results are indeed interesting as it shows changes and their drivers on a broader scale. However, it falls short in capturing the drivers and feedback on a micro-scale level, where anthropogenic influences can be observed. Consequently, it has become apparent that relying solely on this level of resolution is inadequate. While coarse-scale data offers valuable insights into broad trends and patterns, it fails to capture the intricate complexities present at higher resolutions. Specifically, the heterogeneity in soil moisture, a critical factor in various ecological processes and land management decisions, remains inadequately represented at this scale. High-resolution soil moisture data are essential for understanding localized variations, microclimatic influences, and the dynamic interactions between soil, vegetation, and the atmosphere. Therefore, further exploration and analysis at finer resolutions are necessary to gain a comprehensive understanding of soil moisture dynamics and their implications for ecosystem functioning and resource management.

## CHAPTER 3: ASSESSMENT OF ERA5-LAND SOIL MOISTURE PRODUCT USING IN-SITU AND SMAP SOIL MOISTURE OBSERVATIONS

This chapter was published as Preet Lal, Gurjeet Singh, Narendra N. Das, Andreas Colliander, Dara Entekhabi, "Assessment of ERA5-Land Volumetric Soil Water Layer Product Using In Situ and SMAP Soil Moisture Observations", IEEE Geoscience and Remote Sensing Letters, Volume 19, 2022, DOI: 10.1109/LGRS.2022.322398. Copyright IEEE 2022.

The previous chapter discussed the spatiotemporal pattern changes in soil moisture using ERA5-Land data. The observed patterns were intriguing, as drying trends were identified alongside changes in hydrometeorological drivers. However, these results were captured at a coarse scale of 0.1°, which overlooks the many heterogeneous processes occurring at finer scales. To study these heterogeneous patterns, high-resolution soil moisture datasets are needed, but such datasets are currently unavailable. This gap highlights the urgent need to develop an operational high-resolution soil moisture product.

The literature review in the first chapter highlights the disaggregation approach holding significant potential for high-resolution soil moisture retrieval. As a result, a multi-scale soil moisture algorithm has been developed based on this approach, which has a legacy from SMAP mission algorithm development. This algorithm uses coarse-resolution soil moisture data for high-resolution soil moisture retrieval. But before working on algorithm development, the coarse resolution soil moisture data need to be assessed with the *in-situ* and validated satellite based soil moisture product. Therefore, the objective of this chapter is to assess the ERA5-Land volumetric soil water layer product using *in-situ* and SMAP soil moisture observations.

## 3.1 Introduction

Soil moisture can be obtained using *in-situ* instruments, remote sensing satellites, and modeling by assimilating the data from multiple sources. Usually, *in-situ* soil moisture measurement is considered the most reliable measurement that also helps to validate the satellite-based or modeled-based product. However, *in-situ* instruments have a very local spatial support and cannot provide soil moisture at a large spatial extent (Singh et al., 2019b). On the other hand, satellite-based microwave remote sensing has the potential to provide soil moisture for large spatial extents, with passive microwave observations at the coarse resolution (30-40 km) and enhanced grid resolution ~9 [km] (Chan et al., 2018), and with active microwave observations at a finer resolution (~100 [m]) (Huang et al., 2022). The SMAP mission provides a soil moisture product

combining the active and passive measurements at a spatial resolution of ~3 [km] with an accuracy of ubRMSE ~0.049 [m³/m³] (Das et al., 2019). The temporal resolution of the satellite-based soil moisture products varies from 1.5 to 12 days depending upon the satellite acquisition mode and orbit configuration. To overcome the limited temporal resolution and lifetime of satellite sensors, simulated/reanalysis soil moisture datasets are generated at hourly to daily time scales by various models that also assimilate the satellite-based observations (Muñoz-Sabater et al., 2021).

The soil moisture product developed through modeling needs validation to report error/uncertainty involved in the product. The validation is usually conducted by comparing the soil moisture product against *in-situ* measurements or by remotely sensed retrievals (Muñoz-Sabater et al., 2021). However, optimal number of sampling locations are required to upscale the *in-situ* soil moisture measurements over a large spatial domain (Colliander et al., 2022; Singh et al., 2019b). The core validation sites (CVS) used by the SMAP mission represent such measurement configurations. However, the spatial scale of satellite-based soil moisture products may be similar to that of the modeled soil moisture product over a global extent allowing direct or almost direct grid-to-grid comparisons. Various modeled and satellite-based soil moisture products at a coarser resolution (≥ 0.25°) have been extensively validated globally with *in-situ* measurements. Xu et al., (2021) found that among eight different modeled/satellite products, ERA5 has better performance relative to other datasets, with lowest bias -0.05 [m³/m³] to 0.1 [m³/m³] and ubRMSE ~0.04 [m³/m³]. Deng et al., (2020) reveals that ERA-Interim and ESA CCI products has lowest bias as compared to the other three modeled/satellite products.

This chapter evaluates the ERA5-Land soil moisture product at 0.10° against the SMAP-enhanced radiometer soil moisture product and the CVS *in-situ* soil moisture measurements for nearly six years (March 31, 2015, to October 26, 2021). Muñoz-Sabater et al., (2021) validated the ERA5-Land soil moisture product using *in-situ* soil moisture data and reported a global wet bias between 0.08 [m³/m³] and 0.12 [m³/m³]. However, the systematic validation and comparison of ERA5-Land soil moisture product against the SMAP soil moisture retrievals and the CVS *in-situ* measurements are not conducted so far, and hence needed investigation. Our motivation to conduct such an investigation is driven by one of the soil moisture retrieval algorithms of the upcoming NISAR mission that uses coarse resolution ECMWF soil moisture (~9 [km]) as an input to generate a very high-resolution (200 [m]) soil moisture product at a global extent.

### 3.2 Overview of Soil Moisture Datasets

#### 3.2.1 ECMWF ERA5-Land

ERA5-Land is a meteorological reanalysis dataset developed by the European Centre for Medium-Range Weather Forecasts (ECMWF) as part of the Copernicus Climate Change Service (C3S) (Muñoz-Sabater et al., 2021). It provides multiple surface variable data sources at a resolution of 0.01° from the period of 1950 to the present, with a 1-hour temporal resolution. ERA5-Land is a replay of the land component of the ERA5 climate reanalysis, driven by meteorological fields from ERA5 (Muñoz-Sabater et al., 2021a). The core of ERA5-Land is the Tiled ECMWF Scheme for Surface Exchanges over Land, incorporating land surface hydrology (H-TESSEL). ERA5-Land does not directly assimilate observations. Instead, these components come from ERA5 reanalysis datasets, which assimilate multiple satellite datasets and in-situ observations. As observations indirectly influence the simulation through the atmospheric forcing of ERA5. This forcing drives the ERA5-Land single simulation, which has been obtained by assimilating observations through a 4D-VAR data assimilation system and a Simplified Extended Kalman Filter (SEKF). The ERA5 reanalysis datasets assimilate observational data such as satellite data, in-situ observations, and snow data. For example, brightness temperature datasets come mainly from NOAA-15/16/17/18/19, AQUA, METOP-A/B (ASCAT), NPP, GPM, and Aqua. Backscatter sigma0 and soil moisture observation data come from ERS-1, ERS-2, METOP-A/B, OCEANSAT-2, and QUICKSAT. For soil moisture assimilation, ECMWF uses a change detection approach and then apply a CDF-matching to match to the model climatology (Muñoz-Sabater et al., 2021). The model also assimilates *in-situ* observations for surface temperature and humidity from land stations, as well as wind and pressure data from buoys and radiosondes. Apart from the above, a large number of datasets are being assimilated to produce overall very reliable datasets for in various geophysical applications use (https://confluence.ecmwf.int/display/CKB/ERA5%3A+data+documentation).

## 3.2.2 SMAP Core-Validation Sites (CVS) in-situ Soil Moisture

*In-situ* measurements are required to evaluate soil moisture retrievals and outputs from satellites and models, respectively. In recent years massive efforts have been made to make available such observations in contrasting biomes and climate conditions with various types of networks (Colliander et al., 2022). The *in-situ* data collected for validation and comparison of the ERA5-Land datasets are from the CVS, which are also used to validate the SMAP soil moisture

product (Colliander et al., 2022, 2017). A total of 22 CVS (Table 1; Figure 48) provide reference data in the 9 [km] grid across North America, South America, Europe, Africa, and Australia (Colliander et al., 2022). The measurement sites are characterized by various land cover types (i.e., croplands, grasslands, woody savannas, open shrubland, and barren/sparse).

## 3.2.3 SMAP Enhanced Radiometer Soil Moisture (L3\_SM\_P\_E)

The SMAP L3\_SM\_P\_E (single channel algorithm vertical - version 5) product has a native resolution of 33 [km] and it is gridded on a 9 [km] second-generation Equal-Area Scalable Earth (EASE2) grid (Chan et al., 2018). The SMAP satellite acquires data at approximately 0600 hrs. local solar time (descending overpass) and 1800 hrs. (ascending overpass), and provides top ~5 cm surface measurement (Entekhabi et al., 2010). This study considers both descending (AM) and ascending (PM) pass data (Hornbuckle and England, 2005). Previous studies have shown that the SMAP L3\_SM\_P\_E soil moisture product meets the accuracy level of ~0.04 [m³/m³] ubRMSE when validated against CVS, excluding surfaces with ice and snow, urban areas, and vegetated regions with higher vegetation water content (Colliander et al., 2022). Even though the native resolution of the product is 33 [km] it has been shown to correspond well to the 9 [km] scale, especially over CVS (Colliander et al., 2017).

## 3.3 Methodology

The comparison and validation were conducted with close attention to some limiting factors, such as the quality flags, matching overpass time difference, and resolving the projection difference. First, ERA5-Land soil moisture is re-gridded to the SMAP EASE2 (O'Neill et al., 2021) grid to spatially match with L3\_SM\_P\_E using the Delaunay triangulation interpolation approach (Correc and Chapuis, 1987). Second, SMAP has different acquisition times for each spatial grid, and ERA5-Land data is available at an hourly temporal scale with uniform time across the globe. Taking an advantage of the availability of hourly temporal resolution datasets from the ERA5-Land data, the closest acquisition hours soil moisture value of each grid based on the SMAP overpass time, was used for comparison. This nearly removes the time difference between two different products before comparison. For the validation of ERA5-Land soil moisture data against the CVS data, a closest UTC hour is selected to choose the *in-situ* measurements evaluating ERA5-Land product.

Three different validation matrices are used for *in-situ* validation i.e., root-mean-square-error (RMSE), bias, and unbiased RMSE (ubRMSE). For comparison from the SMAP satellite

product, correlation (R), root-mean-square-difference (RMSD), and mean difference (MD) is computed. The detail about different error metrics is provided in Appendix. Apart from the above validation matrices, seasonal anomaly correlation and mean seasonal amplitude also calculated for both datasets. The seasonal anomaly and mean seasonal amplitude are calculated by applying the 91-day moving window average over the time series. The seasonal amplitude is the difference between the peak and trough of the volumetric time-series after the moving window average is applied.

## 3.4 Soil Moisture Intercomparison

### 3.4.1 Validation with CVS *in-situ* measurements

Table 3 and Figure 9 show the validation results for the ERA5-Land soil moisture against the in-situ 0-5 [cm] soil moisture measurements from CVS data for 22 different locations across the globe. Overall, the ERA5-Land has a substantial wet bias except for one station of Walnut Gulch, Arizona site which has a dry bias. In North America, validation matrices show that bias varies from -0.1441 [m<sup>3</sup>/m<sup>3</sup>] to 0.0047 [m<sup>3</sup>/m<sup>3</sup>], with the least bias in Walnut Gulch, Arizona, and the highest bias with poor correlation (0.49) in South Fork, Iowa. The ubRMSE is  $\sim 0.045 \, [\text{m}^3/\text{m}^3]$ but the bias and RMSE values are slightly higher for all the sites. The average wet bias of around 0.05 [m<sup>3</sup>/m<sup>3</sup>] was observed over Tonzi Ranch and Walnut Gulch with low ubRMSE (~0.040 [m<sup>3</sup>/m<sup>3</sup>]) and high correlation (> 0.80) because those regions are semi-arid and covered mostly with open shrubland, and the ERA5-Land model captures that variability reasonably well due to the land surface scheme and precipitation forcing used in the model (Martens et al., 2020). However, high biases in the ERA5-Land product show that some of the forcing used does not capture the local variability in precipitation and ambient temperature. Another reason for high biases, e.g., in the Little River site is due the cropland receiving regular irrigation, and the ERA5-Land model has no way to capture the heterogenous irrigation practices. Another example is in the CVS site South Fork region, the agricultural fields are equipped with tiles to improve the drainage system and with a huge change in vegetation water content, this together complicates the ERA5 modeling of soil moisture as local variability is not considered in the modeling (Reichle et al., 2017).

The sole South American site showed high RMSE (0.0801  $[m^3/m^3]$ ) with ubRMSE of 0.0651  $[m^3/m^3]$  but low bias (-0.0361  $[m^3/m^3]$ ) and moderate correlation (0.65). For the European sites, the ERA5-Land has the lowest bias in Denmark (-0.0032  $[m^3/m^3]$ ) with low RMSE and

ubRMSE (0.0487 [m³/m³]; 0.0486 [m³/m³]), but the REMEDHUS site from Spain have a high wet bias with high RMSE (0.12 [m³/m³]), high correlation (0.83) and average ubRMSE (0.055 [m³/m³]). In Australia, the two available stations are in the cropland/grassland, and the ERA5-Land soil moisture has better performance with low wet bias (-0.0361 [m³/m³] and -0.0451 [m³/m³]) with low ubRMSE (0.0368 [m³/m³] and 0.051 [m³/m³]), high correlation (>0.85) and RMSE (0.515 [m³/m³] and 0.0681 [m³/m³]). A similar finding was observed for the ERA5-Land model output validation but at a coarser resolution (~0.25°) (Xu et al., 2021). The Canadian sites (Kenaston and Carman) are located in the croplands and have a higher overestimation of soil moisture leading to high wet bias with moderate correlation (~0.68) and RMSE with values >0.089 m³/m³ and >0.10 m³/m³, although ubRMSE is low with moderate correlation (~0.62) for the Kenaston site but high for the Carman site. The Benin site in Africa, located in the Sahel, has the highest ubRMSE with high correlation (0.88), and wet bias compared to all other sites, but the site in Niger (Africa), located in grassland, has very low wet bias and average RMSE. It should be noted that the number of sites used for validation of the ERA5-Land is limited, and the validated result does not represent the entire land surface but is limited to the validated regions only.

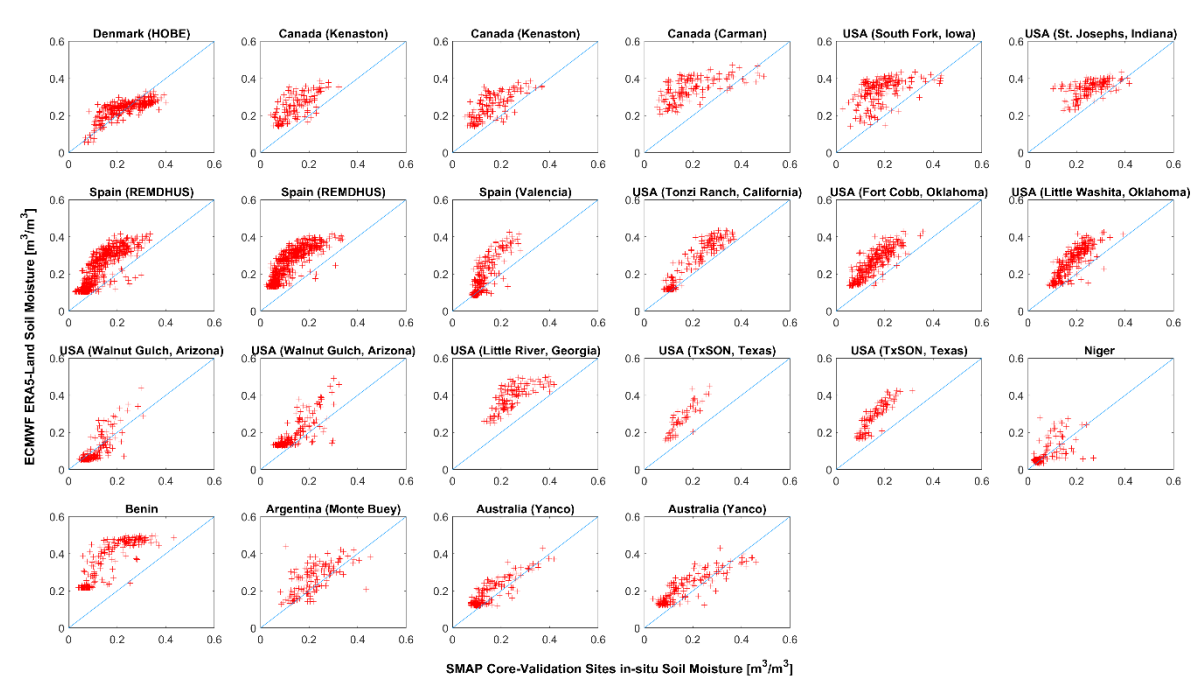


Figure 9: Scatter plots for the comparison between the SMAP CVS soil moisture measurements and the ERA5-Land soil moisture product.

Table 3: The ERA5-Land soil moisture validation metrics for the different SMAP CVS.

		Mean		Correlation	No. of
Location	<b>RMSE</b>	difference	ubRMSE	[R]	<b>Points</b>
Denmark (HOBE)	0.0487	0.0032	0.0486	0.77	303
Canada (Kenaston)	0.1173	0.1059	0.0505	0.68	128
Canada (Kenaston)	0.1041	0.0899	0.0524	0.70	128
Canada (Carman)	0.1688	0.1495	0.0785	0.61	145
USA (South Fork, Iowa)	0.1614	0.1441	0.0728	0.49	183
USA (St. Josephs, Indiana)	0.1018	0.0878	0.0514	0.61	145
Spain (REMEDHUS)	0.1105	0.956	0.0554	0.83	558
Spain (REMEDHUS)	0.1383	0.1298	0.0478	0.84	541
Spain (Valencia)	0.0843	0.0556	0.0633	0.82	212
USA (Tonzi Ranch, California)	0.0677	0.0521	0.0432	0.95	200
USA (Fort Cobb, Oklahoma)	0.1113	0.1032	0.0417	0.83	263
USA (Little Washita,					237
Oklahoma)	0.0956	0.0849	0.0439	0.83	
USA (Walnut Gulch, Arizona)	0.0459	-0.0047	0.0457	0.83	162
USA (Walnut Gulch, Arizona)	0.0708	0.0526	0.0474	0.80	193
USA (Little River, Georgia)	0.1495	0.1415	0.0484	0.73	113
USA (TxSON, Texas)	0.1215	0.1135	0.0435	0.88	55
USA (TxSON, Texas)	0.1307	0.1242	0.0405	0.89	103
Niger	0.0506	0.0133	0.0489	0.62	143
Benin	0.1958	0.1875	0.0567	0.87	227
Argentina (Monte Buey)	0.0801	0.0467	0.0651	0.65	128
Australia (Yanco)	0.0515	0.0361	0.0368	0.88	144
Australia (Yanco)	0.0681	0.0451	0.051	0.87	152

## 3.4.2 Comparison with SMAP L3\_SM\_P\_E

Statistics such as R, MD, and RMSD are calculated using six years (2015-2021) of SMAP L3\_SM\_P\_E and matching the ERA5-Land datasets. Figure 10 shows the soil moisture correlation between the ERA5-Land and the L3\_SM\_P\_E and is ~0.70 in most parts of the world, and a similar spatial pattern has been observed for PM and AM-PM combined observations (Figure 50). The seasonal anomaly correlation also exhibits a similar correlations pattern. However, over northern latitudes (Alaska, Russia, and Tundra regions), densely forested regions (Amazon basin, Congo basin, and Himalayan region), and areas where L-band microwave is impacted by radio frequency interference (RFI) such as over Japan, the R values are lower.

In comparison between the ERA5-Land and the L3\_SM\_P\_E data, the Canadian and the Russian regions have a relatively high MD of  $\pm \sim 0.20$  [m<sup>3</sup>/m<sup>3</sup>] with relatively high RMSD of  $\sim 0.18$ 

[m³/m³] (Figure 49), which is likely due to high soil organic carbon content. The L3\_SM\_P\_E retrieval algorithm does not use soil organic carbon content and can result in such high RMSD. On the other hand, hydrologic modeling in highly organic soil is also challenging. Such anomaly in the L3\_SM\_P\_E and the ERA5-Land data can explain the high RMSD in the arctic regions of Canada and Russia. The potential reason for the poor correlation in the northern hemisphere might be the short time-series (~17.26 % of dataset) of L3\_SM\_P\_E observations due to snow cover during November to April in the northern hemisphere.

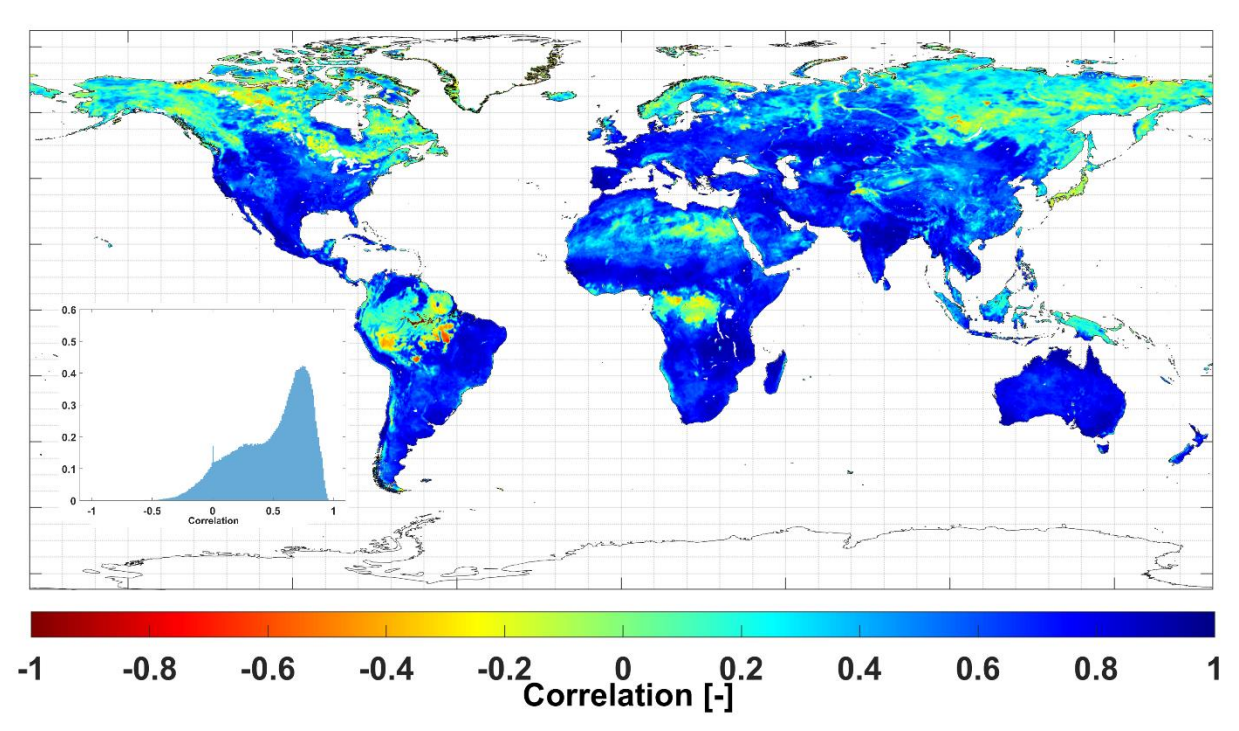


Figure 10: Correlation between SMAP enhanced radiometer soil moisture (L3\_SM\_P\_E) and ERA5-Land soil moisture.

Figure 10 shows that for the bare soil regions e.g., the Sahara has poor correlation (vary between -0.10 to 0.10) but found to have relatively low MD of ~0.01 [m³/m³] and RMSD of ~0.03 [m³/m³] (Figure 49). The potential reason for the low correlation over bare soil region is desert-like biomes, which exhibits a very small dynamic range of soil moisture. Dense forested regions (Amazon basin, Central Africa, and Indonesia) exhibit low (R ~0.10) correlation with moderate wet bias and high RMSD. In those regions, ERA5-Land soil moisture might have better performance than the L3\_SM\_P\_E. The L3\_SM\_P\_E algorithm underperforms over high vegetation-water-content (VWC > 5 kg/m²) because the heavy vegetation reduces the L-band microwave emissions from the soil and the algorithm has not been calibrated for forests yet

(Colliander et al., 2022). In absence of calibrated forest soil moisture retrieval algorithm, the ERA5-Land performance is expected to be better than the current L3\_SM\_P\_E over the dense vegetated surface because it uses relevant forcing and parameters in the hydrologic modeling. However, over the forested regions, the data from both ERA5 and SMAP are not well validated due to the unavailability of *in-situ* soil moisture.

Correlation (R) is relatively high over the grassland, cropland, sparsely vegetated, shrubland, and savannah region with relatively low to moderate wet MD and moderate RMSD. MD shows that the ERA5-Land slightly overestimates soil moisture in comparison to the L3\_SM\_P\_E. Among these land cover types, the lowest MD was observed in the agricultural-dominated region of India, followed by the western part of Australia and South America, Europe, and North America. Monthly MD shows that observed MD is high in India and South America regions (~0.08 [m³/m³]) from July to September (Figure 51). Generally, in India, from July to September, most of the parts are covered with surface water and frequent flood-like situations due to the summer monsoon. Whereas, from October to March (5-year mean), bias is high in North America. Bias in Europe remains constant over time and does not have much variability (Figure 51).

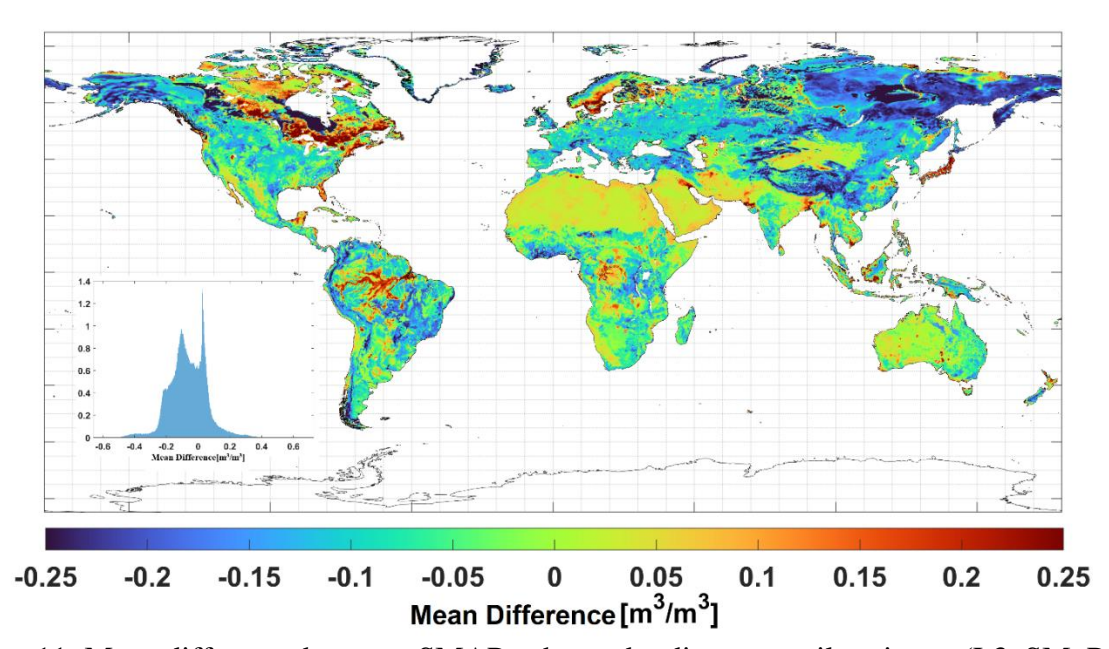


Figure 11: Mean difference between SMAP enhanced radiometer soil moisture (L3\_SM\_P\_E) and ERA5-Land soil moisture.

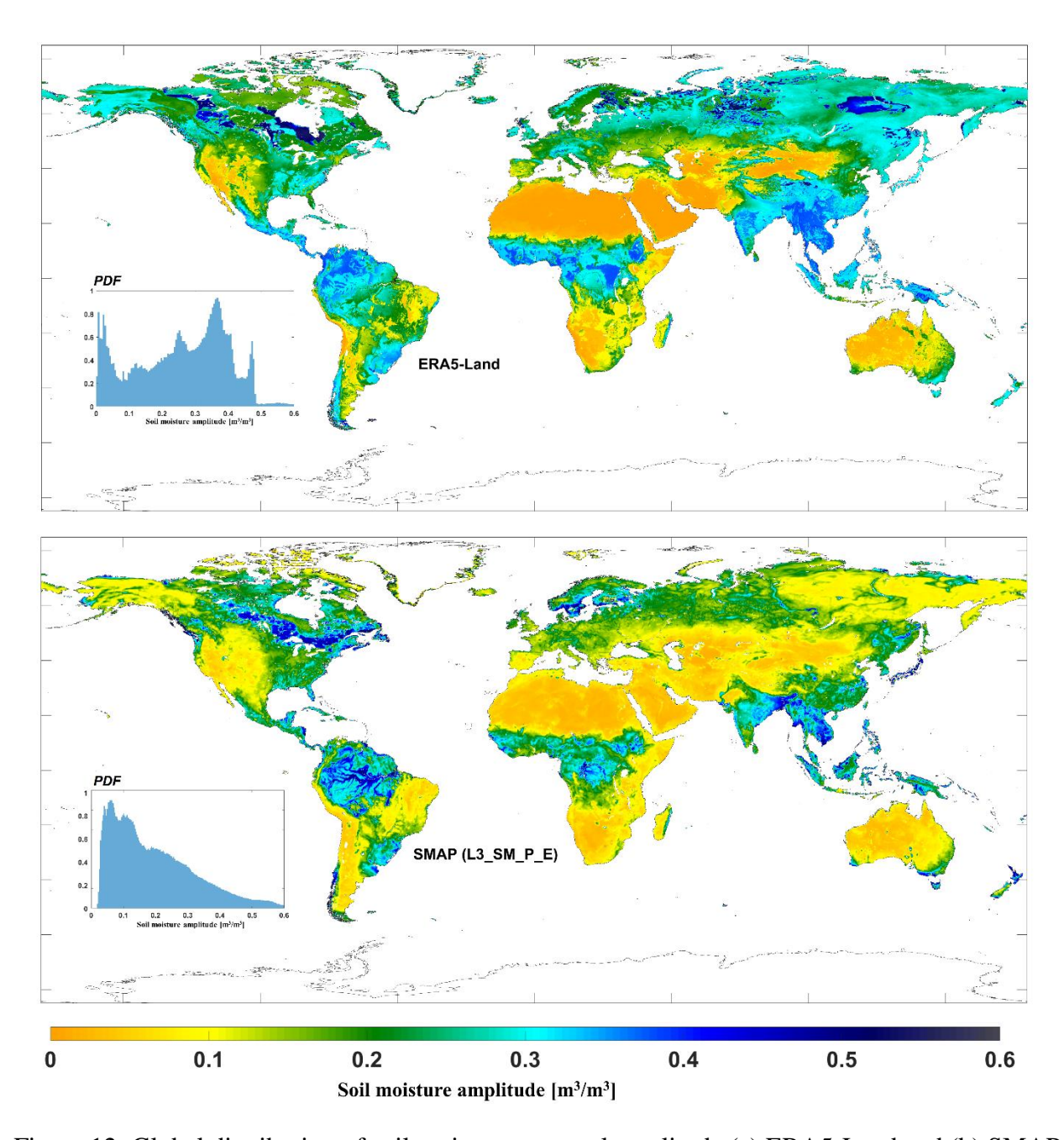


Figure 12: Global distribution of soil moisture seasonal amplitude (a) ERA5-Land and (b) SMAP L3\_SM\_P\_E.

For further analyzing soil moisture the differences between L3\_SM\_P\_E and ERA5-Land, a mean seasonal amplitude has been estimated (Figure 12). The soil moisture amplitude appears to be highest in the Canadian region, Amazon Forest, south-east Asian countries, savannah forest of Africa for the L3\_SM\_P\_E. However, the ERA5-Land has an overall similar pattern, but slightly high amplitude especially over the Tibet region, the Indian sub-continent, and the northern

latitudes, which represents a slight wet bias of ERA5-Land soil moisture. The histogram of amplitude shows a slope with an increase in soil moisture amplitude value for the L3\_SM\_P\_E, but the ERA5-Land histogram shows distributed pattern representing more pixels with higher values.

Data from the ERA5-Land and the SMAP L3\_SM\_P\_E have their advantages and disadvantages over different regions due to the different methods used for generating soil moisture products. The differences in the spatial and temporal pattern are attributed to these different approaches, such as the algorithm used to retrieves L3\_SM\_P\_E soil moisture is the Tau-Omega model, and the ERA5-Land generates product is obtained from modeling and data assimilation method. In the L3\_SM\_P\_E retrieval algorithm from brightness temperatures to soil moisture, the uncertainties primarily come from errors in first-order inputs ancillary data (VWC and surface temperature) and algorithm parameters related to soil roughness, albedo, and vegetation. Whereas the modeled soil moisture from ERA5-Land has errors due to model nonlinear physics and uncertainties in forcing and data for assimilation

## 3.5 Conclusion

In summary, validation with *in-situ* measurements indicates that the ERA5-Land product has mostly reasonable ubRMSE (~0.050 [m<sup>3</sup>/m<sup>3</sup>]) globally but found to have a relatively high bias (~0.10 [m<sup>3</sup>/m<sup>3</sup>]) and RMSE (>0.07 [m<sup>3</sup>/m<sup>3</sup>]) specifically over cropland in North America and medium bias (~0.055 [m<sup>3</sup>/m<sup>3</sup>]) in Europe. Whereas in comparison with the SMAP enhanced soil moisture globally, the ERA5-Land has a reasonable correlation (R> 0.7) and RMSD (~0.055 [m<sup>3</sup>/m<sup>3</sup>]) with medium MD (~0.05 [m<sup>3</sup>/m<sup>3</sup>]) and similar pattern of mean seasonal soil moisture amplitude in the tropical and temperate regions. Although poor correlation (R ~0.1) with high MD (~0.15 [m<sup>3</sup>/m<sup>3</sup>]) exists over dense vegetated regions and polar regions at least partly because the L3\_SM\_P\_E soil moisture retrieval has not been calibrated for forests. Whereas in some of the agricultural-dominated regions, the ERA5-Land does not capture the local heterogeneity due to irrigation practices. However, this does not point to any superiority of one product over another. The study also reveals a good correlation between the ERA5-Land and the L3\_SM\_P\_E, but the ERA5-Land soil moisture is slightly wetter than SMAP enhanced L3 SM P E soil moisture product. The mismatch between the SMAP and the ERA5-Land data are higher where soil moisture retrievals are susceptible to the presence of high organic layer and high vegetated region such as an evergreen forest.

The positive MD (wet bias) may be explained by the fact that *in-situ* sensors, satellites, and modeled soil moisture products represent the soil moisture of different soil layers (Rondinelli et al., 2015). *In-situ* sensors at CVS are buried at 5 cm and do not directly measure the soil moisture immediately at the surface that most influences the L-band brightness temperature. Consequently, SMAP soil moisture initially decreases faster than *in-situ* measurements following rainfall (Shellito et al., 2016). Drier soil within the L-band emitting depth of 3-5 [cm] would cause the modeled soil moisture product to be wetter than *in-situ* and SMAP observations. Overall, the ERA5-Land represents soil moisture values and fluctuations reasonably in most regions globally and can be used in different geophysical applications.

As the soil moisture algorithms of the upcoming NISAR mission is going to use the ERA5-Land as coarse resolution soil moisture input in the algorithm. The statistics shown in this study reveal the possibilities and caveats of applying it as input to the soil moisture algorithm.

# CHAPTER 4: DEVELOPMENT OF MULTI-SCALE ALGORITHM FOR NISAR MISSION HIGH RESOLUTION SOIL MOISTURE PRODUCT

This chapter was published as Preet Lal, Gurjeet Singh, Narendra N. Das, Dara Entekhabi, Rowena Lohman, Andreas Colliander, Dharmendra Kumar Pandey, R.K. Setia, "A multi-scale algorithm for the NISAR mission high-resolution soil moisture product", Remote Sensing of Environment, Volume 295, 2023, 113667, DOI:10.1016/j.rse.2023.113667. © 2023 Elsevier Inc.

In the previous chapter, the coarse-resolution ERA5-Land soil moisture was assessed and compared with *in-situ* measurements and SMAP L3\_SM\_P\_E observations. The statistical analysis showed that ERA5-Land soil moisture is well correlated globally with both *in-situ* and SMAP observations, but it exhibits a wet bias. It is recommended to address this wet bias. Considering this finding, the current focus shifts to the development of the multi-scale algorithm for the NISAR mission's high-resolution soil moisture product.

### 4.1 Introduction

Surface soil moisture (~ 5 [cm]) is one of the essential state variables for hydrology and agriculture (Martínez-Fernández et al., 2019). Having an optimal spatiotemporal measure of soil moisture is important for many geophysical applications. For example, the spatiotemporal dynamics of soil moisture helps to determine evapotranspiration (Koster et al., 2018, 2004), climate forecasting (Peng et al., 2021), flood forecasting (Rahman et al., 2019), drought monitoring (Mishra et al., 2020), irrigation detection (Kwon et al., 2022; Lawston et al., 2017), and water-demand mapping in agricultural regions (Singh and Das, 2022). Apart from the hydrological and agricultural applications, high-resolution soil moisture also plays a significant role in plant ecology and the carbon cycle. It is increasingly considered a valuable ecohydrological natural resource (Humphrey et al., 2021; Lal et al., 2023a).

Soil moisture can be obtained using various sources, such as *in-situ* measurement, satellite-based retrieval, and modeling/reanalysis. *In-situ* soil moisture observations are considered the most reliable measurement source and usually provide high-temporal resolution datasets but cover a very small spatial domain, i.e., a few square meters around the *in-situ* location. Despite being a reliable source of measurement, *in-situ* soil moisture has limitations in providing measurements over a large area. Maintaining a dense *in-situ* soil moisture measurement network is challenging due to the high costs and manhours involved (Singh et al., 2019b). On the other hand, remote sensing data acquired in the microwave domain, particularly in longer (> 5 [cm])

wavelengths/lower frequencies, can measure soil moisture over a large spatial extent (hundreds of km) at various spatial resolutions with regular temporal sampling and an acceptable level of uncertainties within a given set of surface and climatic conditions (Das et al., 2016; Singh et al., 2019a). Numerous efforts have been devoted to monitoring soil moisture globally, using passive as well as active microwave remote sensing techniques. The current remotely sensed soil moisture measurements come from various satellites, i.e., Advanced Microwave Scanning Radiometer (AMSR-2) by Japan Aerospace Exploration Agency (JAXA) (Kawanishi et al., 2003; Njoku and Chan, 2006), Soil Moisture Ocean Salinity (SMOS) by European Space Agency (ESA) (Kerr et al., 2010), and Soil Moisture Active Passive (SMAP) by NASA (Das et al., 2018, 2011; Entekhabi et al., 2010) which use passive microwave sensors for measurement. The current passive microwave observations provide soil moisture at a coarse spatial resolution of >30 [km] (Entekhabi et al., 2010). However, the active-passive approach that combines radiometer and SAR observations has shown its potential to provide soil moisture at a spatial resolution of 3 [km] and 1 [km] using disaggregated brightness temperature (Das et al., 2019).

There are several other algorithms available in the scientific literature to estimate highresolution soil moisture at different spatial resolutions using SAR data, such as model-based polarimetric decomposition (Wang et al., 2018), empirical and semi-empirical models (Hoskera et al., 2020; Zribi et al., 2008; Zribi and Dechambre, 2003), time-series approach (Kim et al., 2012) short-term change detection approach (Balenzano et al., 2021), and data-driven physical models using machine learning and artificial intelligence approaches (Chaudhary et al., 2022). However, these algorithms/models have certain limitations in terms of their data requirements and operational implementation. Such as short-term change detection approach uses VV-pol observation and decouples the effect of soil moisture from that of other parameters, such as roughness or vegetation (Balenzano et al., 2021). However, in the current scenarios, the temporal resolution of most of the SAR is 12-14 days, and the algorithm may not be able to decouple the effect of surface roughness and vegetation change properly. Eventually, this will lead to high uncertainty in the retrieved soil moisture. Whereas the extended approach of this algorithm, i.e., the advanced change detection method, is dependent on the auxiliary data sets such as SMAP soil moisture and Moderate Resolution Imaging Spectroradiometer (MODIS) based Normalized Difference Vegetation Index (NDVI) (Zhu et al., 2022). In the case of the polarimetric decomposition model, there is a need of quad polarimetric datasets, whereas most SAR platforms

do not frequently provide quad pol data because it is cost prohibitive, technologically demanding, and involves much larger amounts of data. Besides the quad pol datasets requirement, the polarimetric decomposition algorithm uses the scattering component for retrieving the surface parameters. If inaccurate ground scattering is estimated, soil moisture varies significantly, resulting in either underestimation or overestimation. On the other hand, empirical and semi-empirical models require pre-collected *in-situ* soil moisture measurements to calibrate the empirical coefficients of the model (Hoskera et al., 2020). These algorithms/models for soil moisture estimates also require other ancillary datasets such as soil parameters (surface roughness, soil texture), and vegetation parameters (NDVI/ Radar Vegetation Index (RVI), VWC) (Hoskera et al., 2020). Certain algorithms like polarimetric decomposition and empirical models are very tedious and computationally very intensive when used to estimate soil moisture on a high spatiotemporal resolution at a global extent. The limited availability of ancillary datasets at high-resolution and the unavailability of required observations at a high spatiotemporal resolution to fulfill the requirement of algorithms/models to retrieve the high-resolution (<=200 [m]) soil moisture at a global extent using the above-explained algorithms are very challenging.

Currently, none of the satellite missions provide soil moisture retrievals that meet all the requirements including high spatial resolution (<=200 [m]) in all weather conditions at a global extent with optimal accuracy over low to moderate vegetation (<=5 [kg/m²] VWC) conditions (Park et al., 2021), which is also a focus of Satellite Needs Working Group. The aim of this study was to show that these requirements can be achieved through the NISAR mission's very high-resolution (~10 [m]) L-band observations. The NISAR mission will observe the global landmass using microwave L-band (1.25 [GHz], 24 [cm] wavelength) frequency. The NISAR mission's L-band SAR observations will have a temporal resolution of a 12-day repeat (6-day with combined ascending and descending) and will help to observe geophysical processes and state variable changes (Kellogg et al., 2020). The NISAR L-band SAR will be capable of a 242 [km] swath width in single, dual, and quad polarimetric modes (Kellogg et al., 2020). Most of the Earth's land cover surfaces will be observed using a 20 [MHz] bandwidth, and hence, once projected onto the ground, will have ~10 [m] resolution in range and azimuth.

The NISAR L-band backscatter observations can be used to estimate the state variables, such as soil moisture, with a single overpass and changes in soil moisture over time with repeat overpasses. The unique capabilities of the NISAR mission (Rosen et al., 2015) motivate the

production of field-scale (200 [m]) surface soil moisture products. The high-resolution soil moisture from the NISAR mission is likely to be provided weekly (at an interval of every 6 days) by combining the ascending and the descending passes. The NISAR soil moisture product is expected to have a data latency of 72 hours (3 days) because the NISAR Level-2 (L2) backscatter product has a data latency of 48 hours, with an additional 24 hours needed for soil moisture algorithm implementation. The NISAR soil moisture product has an accuracy goal of 0.06 [m³/m³] (especially over areas with vegetation water content <=5 [kg/m²]). Soil moisture estimates will be provided over areas with dense vegetation (VWC greater than 5 [kg/m²]) but will be flagged during the retrieval process. Areas with high topography will also be flagged, and no soil moisture retrieval data will be available over areas with active precipitation, frozen ground, snow, urban areas, or water bodies.

To achieve this NISAR high-resolution soil moisture product, we propose a multi-scale algorithm (presented in the subsequent section) which has a legacy from the SMAP mission algorithm development (Das et al., 2011). The key approach of this multi-scale algorithm is to reduce the degrees of freedom (reducing the dependency of multiple ancillary information of vegetation and soil parameters) while retrieving high-resolution soil moisture. The proposed algorithm eliminates any complex modeling or dependence on multiple ancillary data and performs the soil moisture retrieval at ~200 [m] by blending the coarse resolution (~9 [km]) soil moisture with very-high-resolution SAR backscatter (~10 [m]) datasets. The NISAR soil moisture product spatial resolution of 200 m product is based on the user requirement suggested by the NASA, Satellite Needs Working Group after interacting with users.

Das et al., (2011) used a multi-scale algorithm for the SMAP mission to merge the radiometer soil-moisture retrievals (~36 [km]) with SAR observations (<3 [km]) to retrieve soil moisture at 9 [km]. However, the algorithm by Das et al., (2011) doesn't account for heterogeneity on the land surface, and also the algorithm has not been tested on very high-resolution SAR datasets (~10 [m]) and modeled/reanalysis soil moisture products. For retrieving high-resolution soil moisture, this multi-scale algorithm has been modified to accept model/reanalysis-based (such as ECMWF) coarse-scale soil moisture at 0.1-degree (~10 [km]) resolution as input. This is to avoid any dependencies and uncertainty associated with satellite missions based on soil moisture products such as from the SMAP or the SMOS missions. Thus, the satellite radiometer-based soil moisture is replaced with reanalysis/operational soil moisture in the proposed multi-scale

algorithm. Another advantage of using the reanalysis soil moisture dataset is that it results in the best temporal match with the SAR observations (reanalysis data are generally generated at hourly temporal resolution). Since coarse-scale soil moisture is the most critical input in the proposed multi-scale algorithm, selecting the best available soil moisture product is important. In the past, various modeled and satellite-based soil moisture products available globally with a coarser resolution (≥0.25°) have been extensively validated using *in-situ* measurements. On comparing eight different modeled/satellite products by Xu et al., (2021), ECMWF's ERA5 product was found to have a better performance relative to other datasets, with the lowest bias of −0.05 to 0.1 m³/m³ and ubRMSE ~0.04 m³/m³. The validation of the ECMWF ERA5-Land soil moisture product from previous chapter shows that product has error statistics that compare favorably with the SMAP global soil moisture product (L2\_SM\_P\_E) gridded at 9 [km]. The study also reveals that the comparable performance of ERA5-Land soil moisture product is attributed to the use of satellite-based observations as forcing and assimilation for state variables. Thus, ERA5-Land reanalysis land product is used for the proposed NISAR soil moisture multi-scale algorithm.

Higher-level NISAR data products are not expected to be available until May 2025. Hence, for this study, as a replacement for the NISAR data, we used existing SAR L-band datasets from the UAVSAR and the ALOS-2 platform. The objective of this study is to evaluate the capability of the proposed multi-scale algorithm to retrieve high-resolution volumetric soil moisture (200 [m]) using the L-band SAR observations and the ERA5-Land reanalysis of soil moisture in a diverse set of agricultural and hydro-climatic regimes.

## 4.2 Algorithm for high-resolution soil moisture retrievals

The proposed soil moisture multi-scale algorithm takes advantage of ERA5-Land coarser resolution soil moisture products (native resolution  $0.1^{\circ}$ , gridded to 9 [km] global EASE2 projection), which has a ubRMSE of about ~0.05 [m³/m³] and a wet bias of about 0.05 [m³/m³] - 0.1 [m³/m³], and L-band SAR observations (~10 [m]) that carry a distinct signature of soil moisture at very high-resolution. Although SAR backscatter observations have the capability to distinguish soil moisture heterogeneity at a very high resolution, at a native resolution of ~10 [m], it is characterized by speckles. Aggregating SAR observations (i.e.,  $\sigma_{HH}$ ,  $\sigma_{HV}$ ) to 200 [m] reduces the effect of speckle noise by nearly ~20 times  $(1/\sqrt{n})$ , where n is the total number of single looks (in this ideal case, it is 400, based on the ~10 [m] resolution of one single look). The algorithm is elaborated in the next few paragraphs.

For clear illustration, we first define general grid topologies, math operators, and terms used in the mathematical algorithm formulation. Figure 13 explains the topology of the coarse-resolution (9 [km]) and high-resolution (200 [m]) grids that are perfectly nested due to EASE2 projection. For the sake of convenience and to mathematically formulate the algorithm, the naming convention of coarse-resolution (9 [km]) grid cells as 'C' (coarse) and high-resolution 200 [m] grid cells as 'F' (fine) are followed throughout the rest of this section. The linear operators used in the mathematical formulation are defined as Space-Average operators: $\langle x \rangle = \frac{1}{M} \sum x \, dm$ , where M is the area of a larger pixel and m is the area of a smaller pixel within M, and the spatial anomaly operator as  $\delta x = x - \langle x \rangle$ .

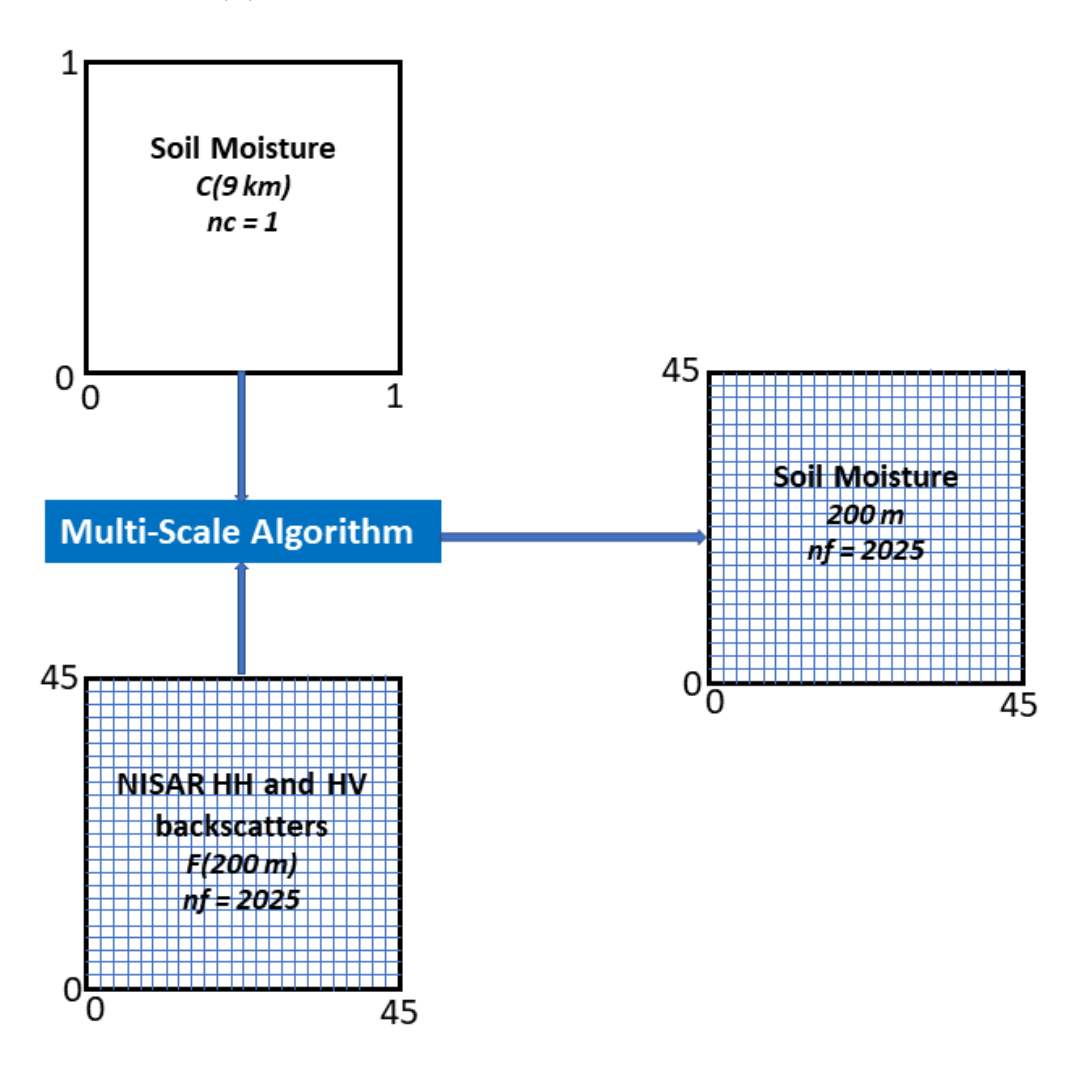


Figure 13: EASE2 grid topology to be used in the proposed NISAR soil moisture algorithm.

The relationship between SAR co-pol backscatter ( $\sigma_{hh}$  at L-band) and volumetric soil moisture was reported by Kim and van Zyl, (2009), who found a nearly linear relationship between the two during the Washita 92 field experiment. Another study by Piles et al., (2009) also reported a similar observation, i.e., a linear relationship between  $\sigma_{HH}$  of L-band and volumetric soil moisture during the SMEX02 campaign. The formulation of the NISAR soil moisture multi-scale algorithm is based on a linear relationship between SAR backscatter and volumetric soil moisture as shown in Figure 14.

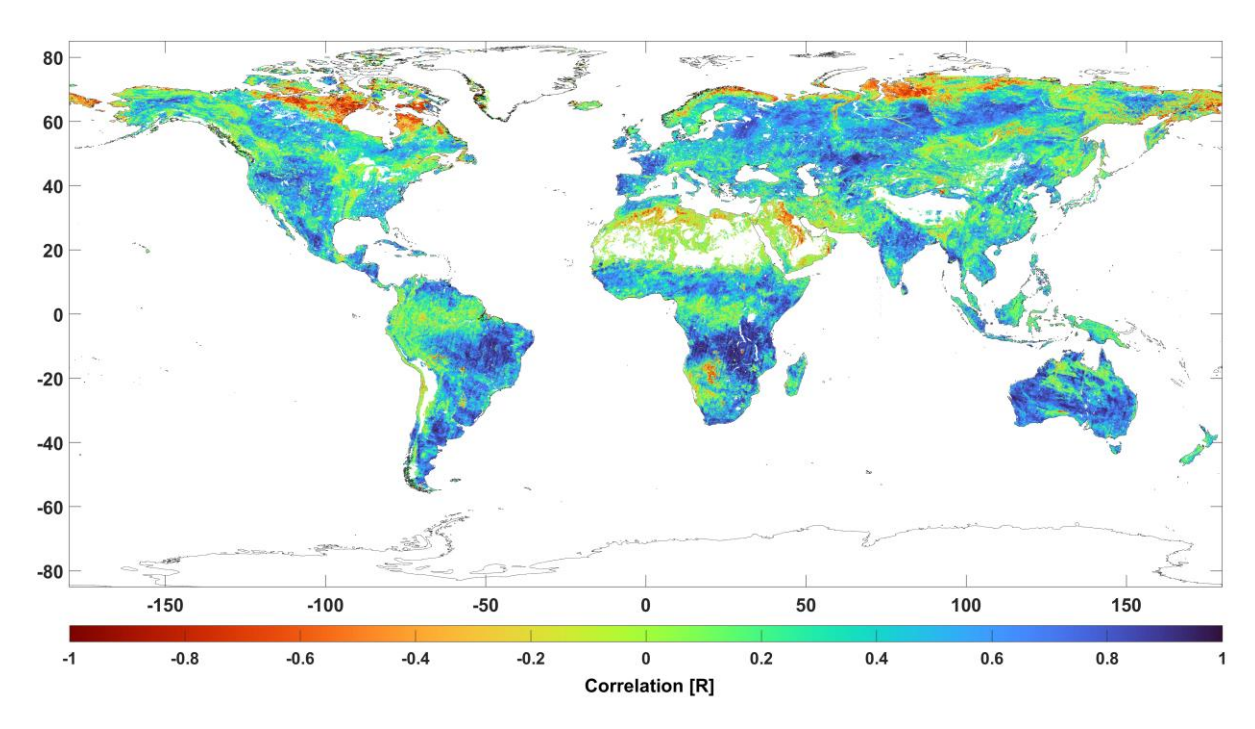


Figure 14: Correlation coefficient (R) between ECMWF ERA5-Land Soil Moisture and SMAP co-polarized backscatter (in dB unit) for 84 days. \*White-colored pixels over land show a null value.

Based on the above correlations as illustrated in Figure 14, we hypothesize that the volumetric soil moisture and co-polarized SAR backscatter ( $\sigma_{hh}$ ) are linearly correlated through an equation of the form:

$$SM(t) = \alpha + \beta . log[\sigma_{HH}(t)] \tag{1}$$

In this section, log represents  $10.log_{10}$ . At a given scale (C or F), in (1),  $\alpha$  and  $\beta$  are parameters depend on the land use, vegetation cover types, surface roughness, and incidence angle of  $\sigma_{HH}(t)$ . For the formulation of Eq. 1, all the backscatter observations over a particular grid cell have the same incidence angle. The parameters  $\alpha$  and  $\beta$ , especially  $\beta$ , vary seasonally and can be

estimated at scale C using the coarse-resolution soil moisture observations and aggregated NISAR  $\sigma_{HH}$  time-series as regression and regressors, respectively, as in

$$SM(C,t) = \alpha(C) + \beta(C).\log\langle [\sigma_{HH}(F_n,t)\rangle$$
 (2)

Here  $\sigma_{HH}(F_n, t)$  is co-polarized radar backscatter at a fine spatial scale, SM(C, t) is volumetric soil moisture at a coarse spatial scale. The parameters  $\alpha(C)$  and  $\beta(C)$  can be obtained by time-series regression of SM(C, t) and  $log([\sigma_{HH}(F_n, t))$ . The formulation of the multi-scale algorithm begins with the hypothesized linear relationship between volumetric soil moisture and co-polarized radar backscatter at a fine (F) spatial scale so that (1) can be written as

$$SM(F_n, t) = \alpha(F_n) + \beta(F_n) \cdot \log(\sigma_{HH}(F_n, t))$$
(3)

where  $\alpha(F_n)$  and  $\beta(F_n)$  are the algorithm parameters at a fine (F) spatial scale, and  $SM(F_n,t)$  is a soil moisture value at a fine spatial scale and at time t for a particular F grid within C.  $SM(F_n,t)$  is the primary target variable that we estimate through this algorithm. By subtracting Eq. 2 from Eq. 3, we get

$$SM(F_n, t) - SM(C, t) = \alpha(F_n) + \beta(F_n) \cdot \log(\sigma_{HH}(F_n, t)) - \alpha(C) - \beta(C) \cdot \log([\sigma_{HH}(F_n, t)])$$

$$(4)$$

Because  $SM(F_n,t)$  is not available, the parameters  $\alpha(F_n)$  and  $\beta(F_n)$  cannot be estimated in the manner that was followed at scale C. To incorporate the effects of the variations of these parameters at scale F with respect to the coarser scale C begins with algebraically rewriting (4) by substituting  $\sigma_{hh}(C,t) = log\langle [\sigma_{HH}(F_n,t)] \rangle$  and  $\sigma_{HH}(F_n,t) = log(\sigma_{HH}(F_n,t))$ ,

$$SM(F_n, t)$$
  
=  $SM(C, t)$  + RHS Term I  
 $\{\beta(C) \cdot [\sigma_{HH}(F_n, t) - \sigma_{HH}(C)]\}$  RHS Term II  
+ $\{[\alpha(F_n) - \alpha(C)] + [\beta(F_n) - \beta(C)] \cdot \sigma_{HH}(F_n, t)\}$  RHS Term III (5)

 $SM(F_n, t)$  is the final output variable of the algorithm, *i.e.*, the high-resolution soil moisture at 200 m. The first term on the right-hand side (RHS Term I), SM(C, t), is the coarse resolution soil moisture from ERA5-Land at scale C (9 km).

The RHS Term II,  $\{\beta(C) \cdot [\sigma_{HH}(F_n, t) - \sigma_{HH}(C)]\}$ , can be calculated based on the regression slope parameter  $\beta(C)$  that is estimated through the time series regression between SM(C,t) from ERA5-Land and NISAR observation aggregated  $\sigma_{HH}(C)$  to scale C. The remainder of this second RHS term  $([\sigma_{HH}(F_n) - \sigma_{HH}(C)])$  is also based on the NISAR observations at scales F and C.

The RHS Term III,  $\{[\alpha(F_n) - \alpha(C)] + [\beta(F_n) - \beta(C)] \cdot \sigma_{HH}(F_n, t)\}$ , accounts for the variations of the parameters  $\alpha$  and  $\beta$  within the grid cell C. The term  $\{[\alpha(F_n) - \alpha(C)] + [\beta(F_n) - \beta(C)] \cdot \sigma_{HH}(F_n, t)\}$  is in units of volumetric soil moisture and represents sub-grid scale (relative to C) heterogeneity effects. The algorithm parameters  $\alpha$  and  $\beta$  depend on surface roughness and vegetation. For a perfectly homogeneous region, the parameters  $\alpha(F_n) = \alpha(C)$  and  $\beta(F_n) = \beta(C)$ , and the subgrid heterogeneity term becomes zero. However, in nature, homogeneity within C rarely exists.

NISAR can provide high-resolution cross-polarization radar backscatter measurements at scale F, which will be highly sensitive to vegetation and surface characteristics such as surface roughness, sensitivity to moisture, and topography change (Kellogg et al., 2020). The sub-grid deviation/heterogeneity patterns in vegetation and roughness are captured by the cross-polarization backscatter at scale  $F_n$  as  $[\sigma_{HV}(C) - \sigma_{HV}(F_n)]$ . Further, the cross-polarization derived heterogeneity patterns are converted to variations in co-polarization backscatter ( $\sigma_{HH}$ ) space to balance the mathematical formulation by multiplying a heterogeneity parameter as  $\Gamma$ .  $\left[\sigma_{HV}(C) - \sigma_{HV}(F_j)\right]$ , where  $\Gamma \equiv \left[\frac{\partial \sigma_{HH}(F_n)}{\partial \sigma_{HV}(F_n)}\right]_C$  (Das et al., 2019, 2014; Singh et al., 2021). The  $\Gamma$ parameter is specific to a particular grid cell C and specific for each day. It is estimated using Fscale  $\sigma_{HH}$  and  $\sigma_{HV}$  observation within each grid cell of C scale using equation  $\Gamma \equiv \left[\frac{\partial \sigma_{HH}(F_n)}{\partial \sigma_{HV}(F_n)}\right]_c$ . These variations are due to the heterogeneity in parameters  $\alpha$  and  $\beta$  in the radar co-polarization space. It can be converted to soil moisture volumetric units for use in Eq. 5 through multiplication by  $\beta(C)$ , the particular coarse grid-scale C conversion factor relating co-polarization backscatter variations to soil moisture variations. Thus, the product  $\beta(C) \cdot \Gamma \cdot [\sigma_{HV}(C) - \sigma_{HV}(F_j)]$  is the contribution of sub-grid (sub-grid to scale C) variations in  $\alpha$  and  $\beta$  to the soil moisture at scale F. The NISAR soil moisture multi-scale algorithm is completed by substituting the term  $\beta(\mathcal{C}) \cdot \Gamma$ .  $[\sigma_{HV}(C) - \sigma_{HV}(F_i)]$  to RHS Term III in Eq. 5,

$$SM(F_n,t) = SM(C,t) + \{\beta(C) \cdot [\sigma_{HH}(F_n,t) - \sigma_{HH}(C)]\} + \beta(C) \cdot \Gamma \cdot [\sigma_{HV}(C) - \sigma_{HV}(F_i)]$$

$$(6)$$

which can be written more compactly as:

$$SM(F_n,t) = SM(C,t) + \beta(C) \cdot \{ [\sigma_{HH}(F_n,t) - \sigma_{HH}(C,t)] + \Gamma \cdot [\sigma_{HV}(C,t) - \sigma_{HV}(F_n,t)] \}$$

$$(7)$$

### 4.3 Test sites and Datasets

### 4.3.1 Test sites

The potential of the proposed NISAR multi-scale algorithm (Eq. 7) is demonstrated over four different hydroclimatic regions of the world: (a) North India (region including Punjab, Uttarakhand, Haryana, Rajasthan, and Uttar Pradesh), located around 30.73°N, 76.77°E, primarily dominated by agriculture, and including mostly forested foothills of the Himalayan range and the Thar desert, respectively, in the north-eastern (tropical climate) and south-western (semi-arid) regions. This region has a continental monsoonal type of climate and receives rainfall from the south-west monsoon winds between July and September. In terms of agriculture, this region has three different cropping seasons (Kharif, Rabi, and Zaid) with combined rainfed and irrigation practices. During the selected date of retrieval (October 13, 2020), the dominating agricultural crop is Paddy at the mature stage; (b) Southern California, USA, centered on 40.19°N, 122.20°W, a hot, arid region encompassing agricultural landscapes of the San Joaquin Valley nestled between mountain ranges. The satellite footprint of the region shows the mountains on the east and west sides and agricultural sites in the center with diverse local climatic conditions. The dominant crops include grapes, tomatoes, hay, sugar beets, nuts, cotton, and a multitude of other fruits and vegetables, with dominating irrigation practices because rain is infrequent. The selected AOI gives the interest to measure a large range of soil moisture with dry conditions on the east and west mountains and moderately wet condition in the valley; (c) South Central Canada, Carman, located around 49.40°N, 98.01°W, a site within the Canadian Red River watershed in Manitoba, primarily dominated with the agricultural region and with soil texture varying across the region from heavy clay to loamy fine sand, and with a humid continental climate. The agricultural site consists of dominant annual crops composed of cereals (32.2% of the area), canola (13.2%), corn (7.0%), and soybean (6.7%). The selected site is also covered with a mix of forest (deciduous tree cover) and grasslands; (d) Hoshangabad (Central India), located around 22.75°N, 77.72°E, can be characterized by a tropical climate and rain-fed agriculture, with rugged terrain in the north and south with dense forest cover (deciduous broadleaf forest) and cropland in the center. The agriculture of the region is primarily cereals crops and consists of both rainfed and irrigation agricultural practices. These four test sites were selected based on the availability of L-band SAR datasets and coinciding *in-situ* measurements across different hydroclimatic regions. However, the in-situ soil moisture measurements required for evaluating the performance of the proposed

algorithm are available only for the three test sites (a) North India, (b) California, and (c) Carman, Manitoba, Canada. For the other site, validation has not been carried out due to the unavailability of the ALOS-2 time series and coinciding *in-situ* time series, and results are just used for qualitative analysis of the spatial soil moisture features in the heterogenous landscape produced by the algorithm. Further details of datasets for the different study areas are shown in Table 4.

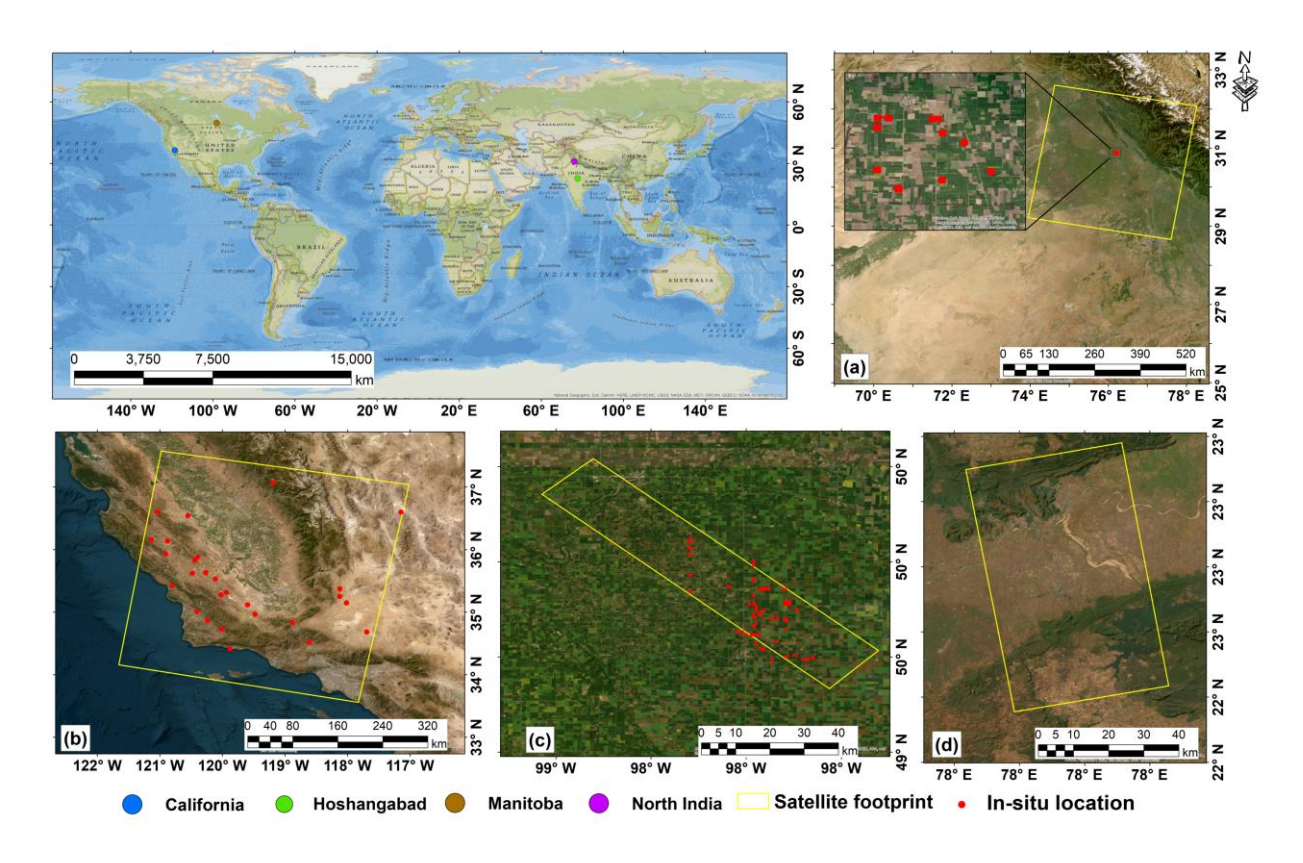


Figure 15: Test sites: (a) North India (ScanSAR mode), (b) California, USA (ScanSAR mode), (c) Carman, Manitoba, Canada (UAVSAR) and, (d) Hoshangabad (Fine mode). Base map service layer credits: Source: Esri, Maxar, GeoEye, Earthstar Geographics, CNES/Airbus DS, USDA, USGS, AeroGRID, IGN, and the GIS User Community; National Geographic, Esri, Garmin, HERE, UNEP-WCMC, USGS, NASA, ESA, METI, NRCAN, GEBCO, NOAA, and increment P Corp.

## 4.3.2 Datasets

# 4.3.2.1 SMAP L3\_SM\_A

The SMAP satellite is equipped with two microwave instruments - a L-band radar (VV, HH, and HV polarizations) and a L-band radiometer (V and H polarizations) that enable the

accurate mapping of soil moisture and freeze-thaw state (Entekhabi et al., 2010). Both instruments share a single feedhorn and reflector, and the deployable mesh reflector, which is offset from the nadir and rotates at a speed of 14.6 rpm, provides a conical scanning antenna beam with a surface incidence angle of 40°. This unique scan geometry ensures a constant incidence angle for repeat pass measurements, which in turn aids in the precise estimation of soil moisture without the need for reprocessing the level 1 dataset. The SAR dataset's range and azimuth resolution are determined by the antenna's scan geometry. The single-look SAR data is averaged onto fixed 1km grid pixels to create the L1C\_S0\_HiRes data product, although the spatial resolution varies across the swath. The processed 1 km L1C\_S0\_HiRes data is highly accurate, with an uncertainty of 1.0 dB or less (1-sigma) from all sources for HH and VV data, defined at a 3-km spatial resolution and for surfaces of radar cross-section greater than -25 dB. The HV data have an uncertainty of 1.5 dB or less from all sources (excluding rain) defined at a 3-km spatial resolution and for surfaces of HV radar cross-section greater than -30 dB (Entekhabi et al., 2010). This study utilizes the available 84 days of 3-km spatial resolution HH polarization datasets from the SMAP radar to generate the algorithm parameters  $\beta(C)$ , given that the radar failed after only 84 days of launch.

## 4.3.2.2 ALOS-2

The ALOS-2 is a global leading fully polarimetric Phased Array L-band SAR-2 (PALSAR-2) satellite from Japan Aerospace Exploration Agency (JAXA) launched in May 2014 (Rosenqvist et al., 2014). The satellite operates on a 1.2 GHz band at different acquisition modes (single, dual, and quad pol) and resolutions, combining different polarization at incidence angles between 20° to 40°. The ALOS-2 satellite has five different acquisition modes (a) High Sensitive Polarimetric mode acquires data on quad pol (HH, HV, VH, VV) at 6 [m] resolution and (b) ScanSAR Dual 5-scan mode (HH and HV) acquire data at 100 [m] resolution (Rosenqvist et al., 2014). The evaluation of radiometric accuracy by JAXA shows that noise-equivalent sigma zero (NESZ) of the PALSAR-2 strip map varies from -36.6 [dB] to -49.9 [dB] with a calibration factor of ~-83 [dB] (Shimada et al., 2009).

#### 4.3.2.3 UAVSAR-SMAPVEX12

UAVSAR datasets were collected during the SMAPVEX-12 campaign at Carman, Manitoba, Canada site. During the campaign, NASA's UAVSAR acquired quad polarization of L band (1.26 GHz) datasets (Table 4). The UAVSAR looks to the left of the flight direction and

collects data over a nominal swath of 21 [km] and incidence angles between 25° and 65°. The spatial resolution of data is 1.66 [m] range resolution and 0.8 [m] azimuth resolution in SLC mode. UAVSAR has a noise-equivalent sigma zero of -45 [dB] (McNairn et al., 2015). Apart from SAR data acquisition, various other measurements were carried out, such as *in-situ* soil moisture measurement, precipitation, crop type, soil and crop temperature, and crop height from 55 different agricultural fields (McNairn et al., 2015). The retrieval algorithm was applied to a version of the UAVSAR data that had been simulated to closely match the expected characteristics of NISAR (e.g., spatial resolution, noise) and using only the incidence angle range between 30° to 50°. The detail about the field campaign and soil moisture measurement, crop type and attribute, and soil datasets of SMAPVEX12 is available at https://smapvex12.espaceweb.usherbrooke.ca/.

## 4.3.2.4 *In-situ* soil moisture

The *in-situ* soil moisture datasets are used for the validation of retrieved high-resolution soil moisture at 200m spatial resolution. In the current study, three different test sites have been validated using the *in-situ* soil moisture measurements:

Table 4: Detail of SAR data used for retrieval of high-resolution soil moisture.

Test Site	Acquisition Date	Acquisitio n mode	Available Polarizations	Source	Weblink of data availability
Hoshangabad	3/30/2016	Fine	HH, HV,VH,VV		
North India	10/13/2020	ScanSAR	HH, HV	ALOS-2	https://alos-pasco.com/en/
Southern California, USA	7/30/2017   ScanSAD   HH HV				
	06/17/2012 (DOY 169)		HH, HV,VH,VV		https://smapvex12.espaceweb .usherbrooke.ca/ https://nsidc.org/data/sv12ub k/versions/1
Carman, Manitoba, Canada	06/19/2012 (DOY 171)		HH, HV,VH,VV	UAVSAR SAMPVEX-12	
	06/22/2012 (DOY 174)		HH, HV,VH,VV		
	06/23/2012 (DOY 175)	1	HH, HV,VH,VV		
	06/25/2012 (DOY 177)		HH, HV,VH,VV		
	06/27/2012 (DOY 179)		HH, HV,VH,VV		
	06/29/2012 (DOY 181)	-	HH, HV,VH,VV		
	07/03/2012 (DOY 185)		HH, HV,VH,VV		
	07/05/2012 (DOY 187)		HH, HV,VH,VV		
	07/08/2012 (DOY 190)		HH, HV,VH,VV		
	07/10/2012 (DOY 192)		HH, HV,VH,VV		
	07/13/2012 (DOY 195)		HH, HV,VH,VV		
	07/14/2012 (DOY 196)		HH, HV,VH,VV		
	07/17/2012 (DOY 199)		HH, HV,VH,VV		

(a) In the North India test site, the in-situ soil moisture measurements (0 – 5 cm) were carried out in 13 agricultural fields (~ 200 m grid-cell) of Ludhiana, Punjab (Location on in-situ points shown in Figure 15). The in-situ soil moisture measurements were taken using Stevens Hydra Probe during morning hours coinciding with the ALOS-2 overpass on October 13, 2020. The soil condition during field measurement is moist, and the surface roughness was smooth. To capture the spatial variability of soil moisture within the 200 m grid cell, each agricultural field consisted of five sampling locations, and three HydraProbe measurements were taken at each sampling location within  $1m \times 1m$  area. A total of 15 HydraProbe measurements within each field were used to upscale the in-situ soil moisture measurements at 200 m grid resolution of soil moisture retrievals for reasonable and reliable validation.

Table 5: Detail of Ancillary input required in the multi-scale soil moisture algorithm.

Dataset	Duration	Purpose	Data source	Weblink of data availability
SMAP SAR	13 April – 07 July 2015	Generating $\beta(C)$	SMAP	https://nsidc.org/data/spl3sma/versions/3
Land cover	Static	Selecting $\beta(C)$ in retrieval algorithm	SMAP Ancillary files	https://smap.jpl.nasa.gov/documents/
Soil Moisture		Input in Algorithm		
Precipitation	Vary with L-	Flagging and Masking	ECMWF ERA5- Land [09 km]	https://cds.climate.copernicus.eu/cdsapp#!/dataset/reanalysis- era5-land?tab=overview
Surface Temperature	Band SAR input			
Snow Depth				
Urban Mask	Static		ESA land cover [10 m]	https://esa-worldcover.org/en

- (b) In the southern California test site, 28 points of *in-situ* soil moisture data (0 − 5 cm) were collected from the International Soil Moisture Network (https://ismn.geo.tuwien.ac.at/) for July 30, 2017. Since time-series data of retrieved soil moisture were not available, three different networks/stations (PBO H2O, SCAN, and URSCAN) were combined to validate the retrieved soil moisture datasets.
- (c) For the Carman, Manitoba, Canada test site, the *in-situ* soil moisture was collected as a part of the SMAPVEX-12 campaign. The soil moisture measurements were collected at near-surface depth (0 6 cm) over 55 agricultural fields. The measurements were conducted over multiple locations in each selected agricultural field to capture the soil moisture variability. In each field, data was collected along the two transact at a distance of 200 m, and each transect has eight

measurement sites at 75 [m] apart. At each measurement location, 3 Hydra probe readings at 0 - 6 cm depth were taken. The detail about the *in-situ* soil moisture sampling strategy is available at https://smapvex12.espaceweb.usherbrooke.ca/.

## 4.4 Algorithm implementation

## 4.4.1 SAR processing

In this study, two different acquisition modes of the ALOS-2 were used, i.e., the ScanSAR Dual-5 scan mode and the Fine mode, for three different test sites and UAVSAR L-band data for one test site (Table 4) as a substitute for the NISAR L-band datasets. The original resolution of SLC ALOS-2 ScanSAR and Fine mode with  $\sigma_{HH}$  (co-polarized) and  $\sigma_{HV}$  (cross-polarized) are 100 [m] and 10 [m], respectively. The high-resolution SLC SAR data is processed with the conversion of slant range to ground range, radiometric calibration, and terrain correction (with Copernicus 30 [m] DEM) using the ESA-Sentinel toolbox (SNAP). The UAVSAR datasets are multi-look GRD terrain-corrected products with ~8 [m] spatial resolution. The incidence angle of ALOS-2 SAR and UAVSAR varies with the acquisition. The incidence angle normalization of  $40^{\circ}$  ( $\theta_{ref}$ ) applied to all the co-pol and cross-pol observations using the equation provided by Mladenova et al., (2013). Before aggregation of  $\sigma_{HH}$  and  $\sigma_{HV}$  from fine to coarse resolution, a hybrid spatial filtering approach was implemented to remove the effect of urban and artificial structures on the aggregated backscatter observations. The advantage of using a hybrid spatial filter tool (Figure 16) developed by Das et al., (2019) is that it preserves the information and suppresses or removes the unwanted backscatter measurement mostly due to urban built-up or water bodies (Figure 18). The spatial hybrid filter approach is implemented as follows: (a) For each 200 m<sup>2</sup> grid cell based on the ALOS-2, the mean  $(m_i)$  and standard deviation  $(s_i)$  were calculated.  $i = 1 \dots N_f$  where  $N_f$  is the number of grid cells in the 200 m<sup>2</sup> SAR datasets, (b) Then mean standard deviation (SMD) computed over all  $s_i$ ,  $i = 1 \dots N_f$ . (c) For all the 200 m<sup>2</sup> grid cells with  $s_i > SMD$ , a moving window filter was applied. (d) For all 200 m<sup>2</sup> grid cells with  $s_i \leq SMD$ , all ALOS-2 and UAVSAR backscatter values out of range  $[m_i - SMD: m_i + SMD]$  were eliminated. Further, SAR backscatter datasets were masked with urban fraction > 20%, water body fraction > 20%, surface temperature below freezing > 0°C, and high precipitation > 5 mm/hr. (Table 4). Further the spatial filter significantly reduces the speckle noise, as visible in Figure 18.

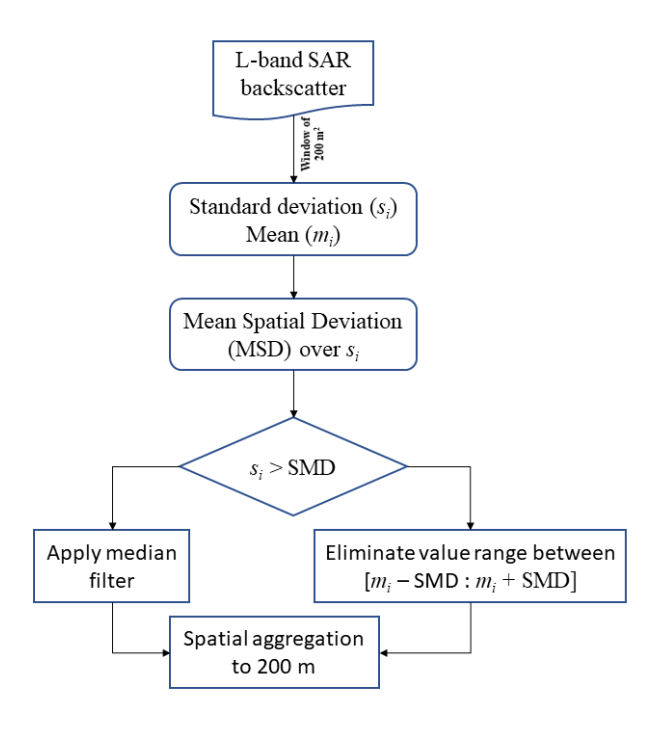


Figure 16: Methodology flowchart for spatial filter used in the soil moisture algorithm.

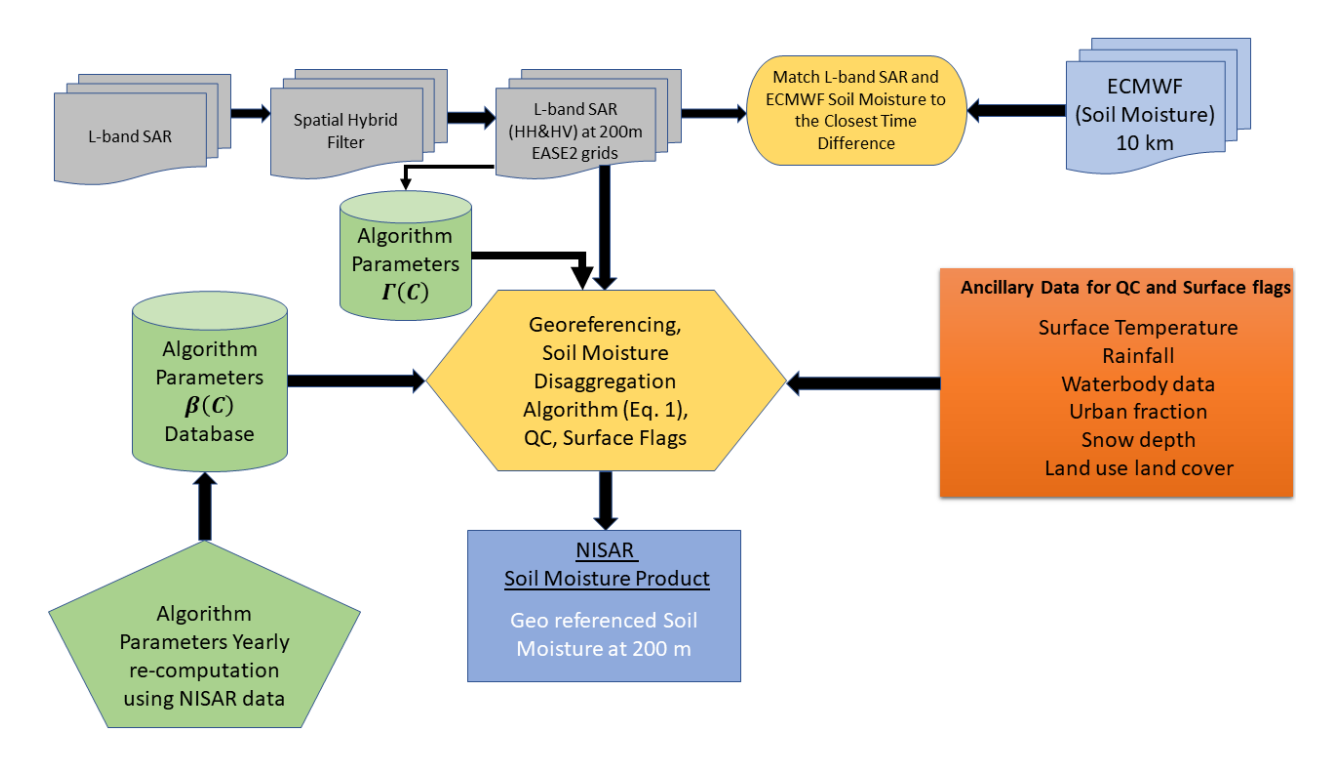


Figure 17: Methodology flowchart for retrieving high-resolution soil moisture using a multi-scale soil moisture algorithm.

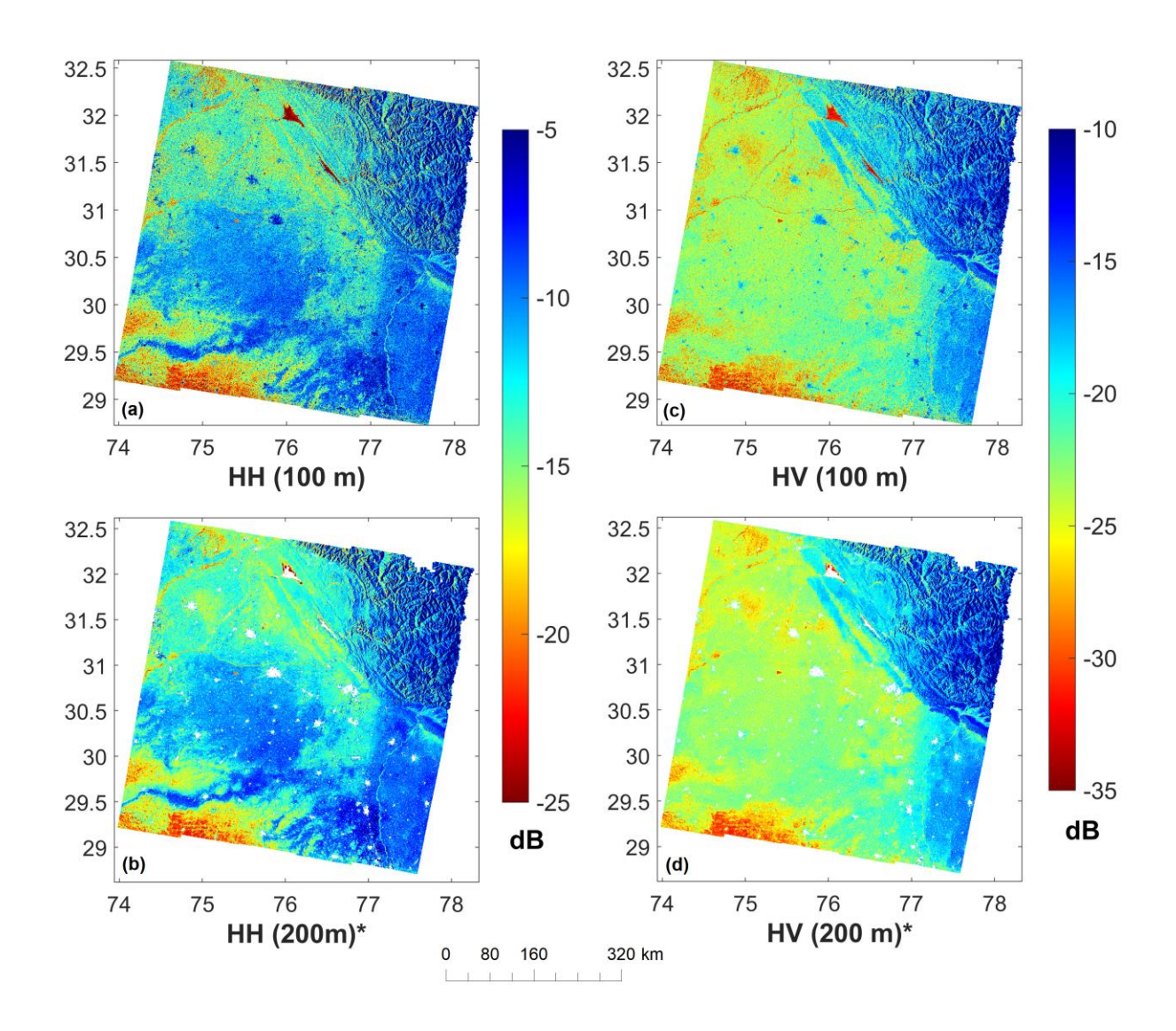


Figure 18: ALOS-2 ScanSAR acquisition mode granule over North India (October 13, 2020). (a & c)  $\sigma_{HH}$  and  $\sigma_{HV}$  unprocessed data (radiometrically calibrated, terrain corrected but without aggregation and filtering); and (b & d)  $\sigma_{HH}$  and  $\sigma_{HV}$  data after filtering and aggregation to 200 [m]. \*White-colored pixels in the map correspond to inapplicable land cover types for soil moisture estimation as water bodies, built-up and permanent snow.

## 4.4.2 Algorithm parameter estimation

# 4.4.2.1 **β** Parameter

The algorithm parameter  $\beta(C)$  preliminary database was developed using time-series regression between ECMWF ERA5-Land based soil moisture at 9 [km] and  $\sigma_{HH}(C)$  from SMAP\_L3\_A of available 84 days between 13 April to 07 July 2015 for each 9 [km] coarse-scale

grid as shown in Figure 19. SMAP\_L3\_A L-band radar dataset was used because of its global coverage; no other L-band SAR satellite has archived data with such a high temporal resolution (approx. a 3-day revisit). Though the L-band ALOS-2 has 14 days of revisit time, datasets are acquired based on the windows of opportunity. Consequently, ALOS-2 datasets lack global coverage with the same data mode of acquisition (e.g., spotlight/fine/ScanSAR). Thus, estimation of  $\beta$  parameter was not possible using ERA5-land soil moisture and ALOS-2 SAR backscatter datasets.

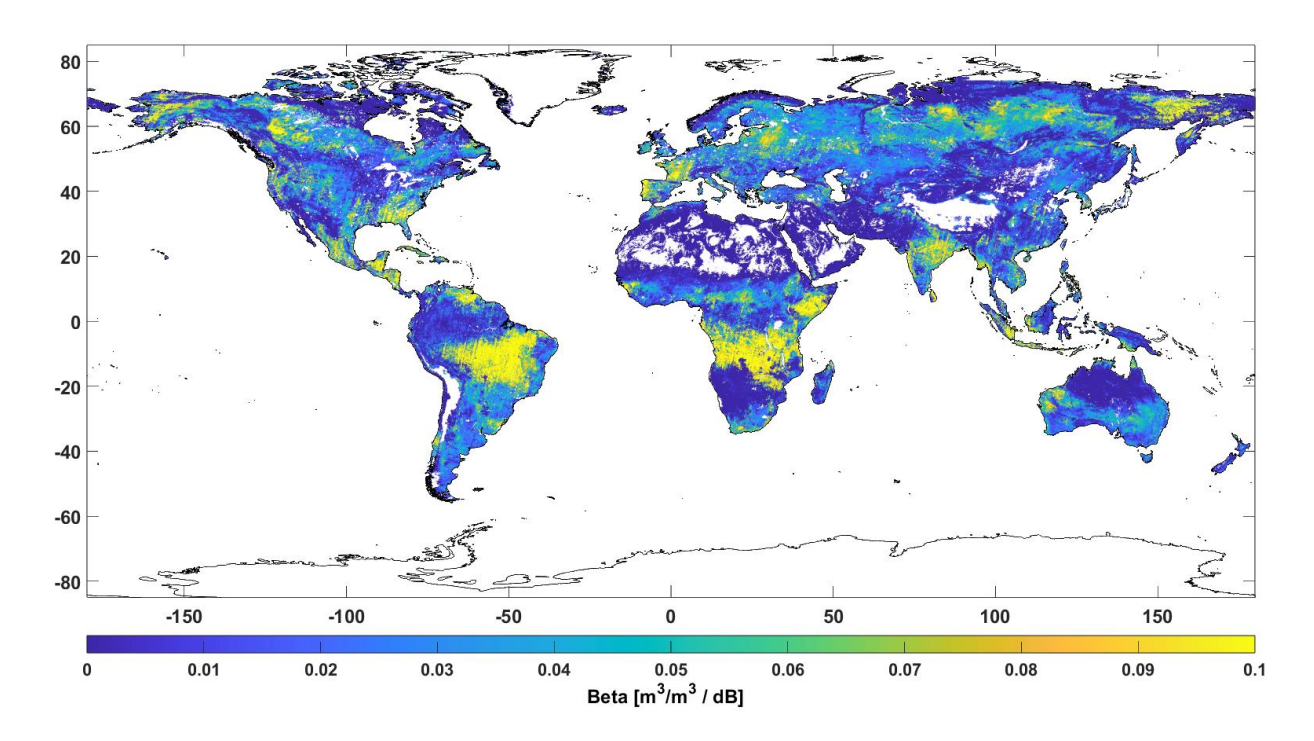


Figure 19:  $\beta(C)$  parameter developed using ~3 months of SMAP L-band SAR ( $\sigma_{HH}$  dB unit) and ECMWF ERA5-Land volumetric soil moisture data (84 days). \*White-colored pixels over land show a null value.

The spatial evolution sensitivity parameter  $\beta$  looks reasonable in Figure 19. The magnitude of  $\beta(C)$  (Figure 19) mostly depends on the soil moisture dynamics, vegetation density and surface roughness conditions (Das et al., 2011). The magnitude of  $\beta(C)$  decreases with an increase in vegetation water content and vice versa (Das et al., 2019c). In most of the regions, a high correlation (>0.6) is observed (Figure 14), primarily in the cropland and grassland cover and  $\beta(C)$  is also following similar pattern as of correlation *i.e.*, high value except southern part of Australia (which is semi-arid region), USA and northern latitude (Figure 19). The high correlation value over agricultural land is primarily due to high temporal variability of soil moisture. In the dense

forested regions such as Amazon, East Asia, and the Southern African continent  $\beta(C)$  is low (~0.02) with correlation value ~0.2 because of dense canopy or canopy closure and also if aboveground biomass exceeds ~150 - 300 Mg/ha L-band signal saturates (Lal et al., 2022b; Vittucci et al., 2023) leading to backscatter mostly with information of vegetation instead of soil parameters as the heavy vegetation canopy is almost opaque to L-band microwave emissions from the soil (Njoku and Entekhabi, 1996). Also, the backscatter of radar is prone to saturation in such conditions because of the densely vegetated regions (Attema and Ulaby, 1978; Ulaby, 1974; Zeng et al., 2022). In contrast, very low  $\beta(C)$  and correlation values were observed over the dryland region across the Sahara, parts of the Middle East, Central Asia, regions in a northern latitude, and Oceania (Figure 14) because the region does not have enough soil moisture variability in those selected three months. In these regions, the dynamic of soil moisture is very limited, and the dry soil often causes surface and weak sub-surface scattering for microwave signals (Wagner et al., 2022). Due to the low temporal variability of soil moisture in a region with no or very low vegetation covers show negative correlation in some regions. Fundamentally it should not exist, but due to complex phenomenon of surface and sub-surface scattering it happens. The negative correlation observed in Figure 14 has nearly similar observations with the Wagner et al., (2022) pearson correlation coefficient that's calculated using the three years of ERA5-Land soil moisture and Advanced Scatterometer (ASCAT) C-band backscatter datasets. This phenomenon particularly explains that regions with low temporal variability of soil moisture or lower soil moisture gives anomalous backscatter or wide sub-surface scattering. Examples of such regions include temperate climatic regions (during dry spells) or where rocks laying near the soil surface (Wagner et al., 2022). However, a detailed study requires on the L-band how scattering or anomalous scattering occur with high variability in soil moisture. The upcoming NISAR L-band SAR data can help in such analysis once sufficient number of temporal datasets are archived.

For the NISAR mission prelaunch soil moisture algorithm, we created a look-up table (LUT) for different International Geosphere-Biosphere Programme (IGBP) land cover types. Currently, only those grid-cells were used to create a look-up table (LUT) for  $\beta(C)$  parameter, which has valid correlation (R) values (> 0.4). Using valid grid cells  $\beta(C)$  values, a land coverwise global  $\beta(C)$  parameter was calculated to create LUT, which is a median  $\beta(C)$  value of all the valid grid-cells in a specific land cover class. Figure 20 shows the box plot of  $\beta(C)$  parameter for different land cover classes to represent the spatial variability of  $\beta(C)$  across the globe. The global

 $\beta(C)$  parameter has been further used in the algorithm to retrieve soil moisture. We assume that the global  $\beta(C)$  substitution in the soil moisture retrieval algorithm may incur small errors, but those are encapsulated in the random error. Since the global  $\beta(C)$  parameter is derived using correlated grid-cells (R>0.4) which cover most land regions of the world, reliable accuracy in soil moisture retrieval is expected on those regions having a correlation value < 0.4, between ERA5-Land soil moisture and SMAP HH polarization. Notably, the correlation value < 0.4 was observed in a region having low soil moisture temporal variability, such as deserts, dense canopy forests (primarily tropical forests), and tundra regions.

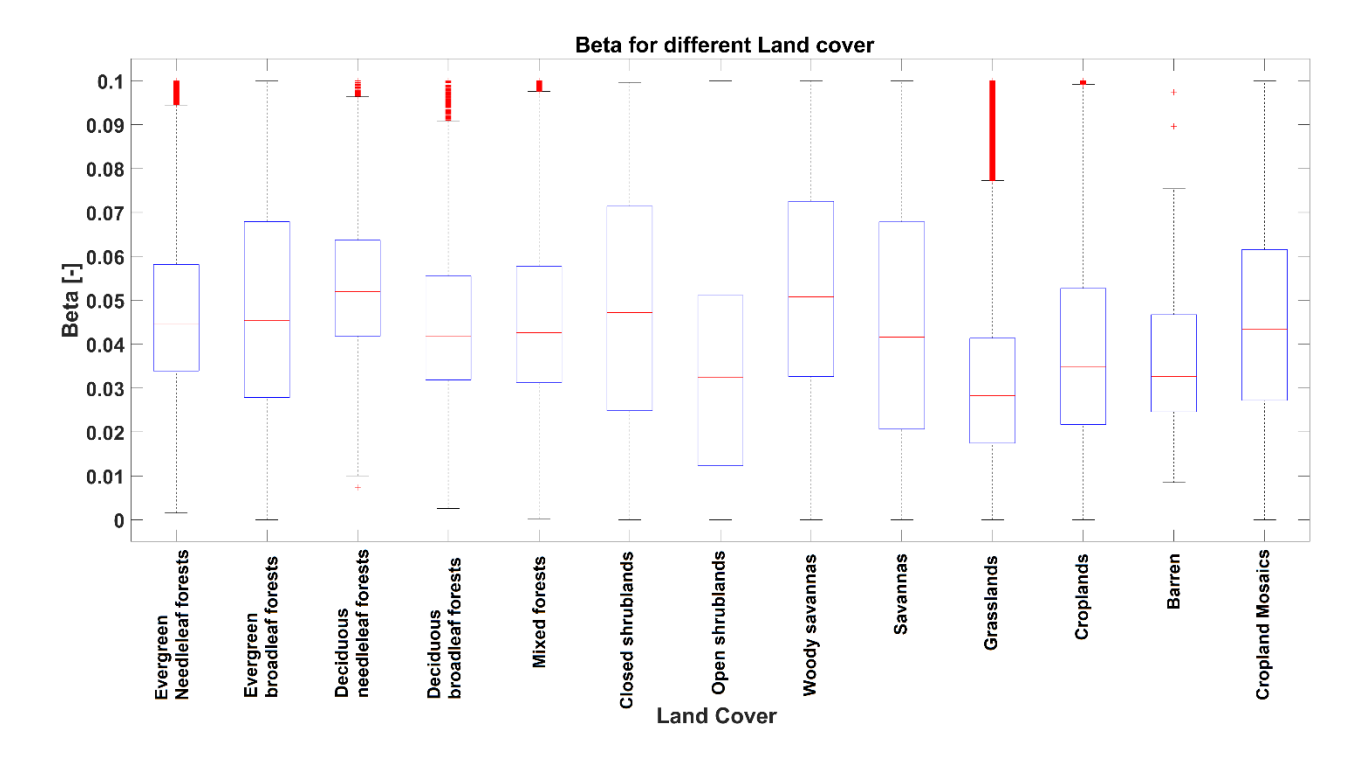


Figure 20:  $\beta(C)$  estimates for each land cover created from the ECMWF ERA5-Land Soil Moisture and SMAP L-band SAR  $\sigma_{HH}$ .

# 4.4.2.2 **Γ** parameter

The parameter  $\Gamma(C)$  is a heterogeneity parameter that is calculated statistically from the SAR backscatter ([dB] scale) for  $\sigma_{HH}$  and  $\sigma_{HV}$  at the finest resolution of 200 m, which is used to estimate the downscaled soil moisture bounds within the 9 km (C) grid cell. Unlike  $\beta(C)$ , the calculation of parameter  $\Gamma(C)$  doesn't require any time series, and it is computed statistically for any specific overpass using the F scale backscatters ( $\sigma_{HH}^{\circ}$  and  $\sigma_{HV}^{\circ}$ ) within a particular grid cell

of C as  $\Gamma \equiv \left[\frac{\partial \sigma_{HH}(F_n)}{\partial \sigma_{HV}(F_n)}\right]_C$  (Das et al., 2019). In this study,  $\Gamma(C)$  is estimated using the  $\sigma_{HH}$  and  $\sigma_{HV}$  SAR backscatter at the finest resolution of 200 [m] within each grid 9 [km] (C) grid cell.  $\Gamma$  is unique for an overpass of the satellite, which projects the spatial variation in  $\sigma_{HV}$  in the space of  $\sigma_{HH}$ . In an ideal condition, there will be 2025 combinations of  $\sigma_{HH}(F_n)$  and  $\sigma_{HV}(F_n)$  to enable robust estimation of the  $\Gamma$  parameter.

# 4.5 High-resolution soil moisture retrievals and validation

In this study, from Eq (7), the term  $[\sigma_{HH}(F_n,t) - \sigma_{HH}(C,t)]$  was calculated by considering the  $\sigma_{HH}$  upscaled to 200 [m] resolution as  $\sigma_{HH}(F_n,t)$  and the average of  $\sigma_{HH}$  for the coarser-resolution 9 [km] grid (*C*-scale) as  $\sigma_{HH}(C,t)$ . The term  $[\sigma_{HV}(C,t) - \sigma_{HV}(F_n,t)]$  was also calculated using the average of  $\sigma_{HV}$  at coarse resolution as  $\sigma_{HV}(C,t)$  and the upscaled high-resolution  $\sigma_{HV}$  as  $\sigma_{HV}(F_n,t)$  for each *C*-scale grid. Then 9 [km] coarse resolution soil moisture from ERA5-Land soil moisture (*C*, *t*) was disaggregated to 200 [m] using Eq. 7. Further, the retrieved soil moisture datasets were validated against *in-situ* measurements. The validation metrices used for *in-situ* validations are root mean square error (RMSE), bias, correlation coefficient (R), and unbiased RMSE (ubRMSE), following Colliander et al., (2022). The equation for the validation metrices is given in the appendix.

## **4.5.1 Test site 1 (Hoshangabad):**

ERA5-Land soil moisture was disaggregated to soil moisture at 200 [m] spatial resolution using the above-discussed multi-scale soil moisture retrieval algorithm. Figure 21 shows soil moisture for the Hoshangabad region for March 30, 2016. The southern and northern part of the test site is covered with undulated terrain and dense deciduous broadleaf forest. The soil moisture at 200 [m] captures (Figure 21) the details otherwise not visible in the ERA5-Land soil moisture at 9 [km]. The central part of the test site is covered with cropland, and most parts have a similar pattern to ERA5-Land soil moisture (SM: 0.2 m³/m³ – 0.4 m³/m³). This test site doesn't have *insitu* measurement and is just used to demonstrate the capability of the multi-scale algorithm on the heterogeneous landscape. The white areas in Figure 21b is due to the rivers, large water bodies, and urban areas.

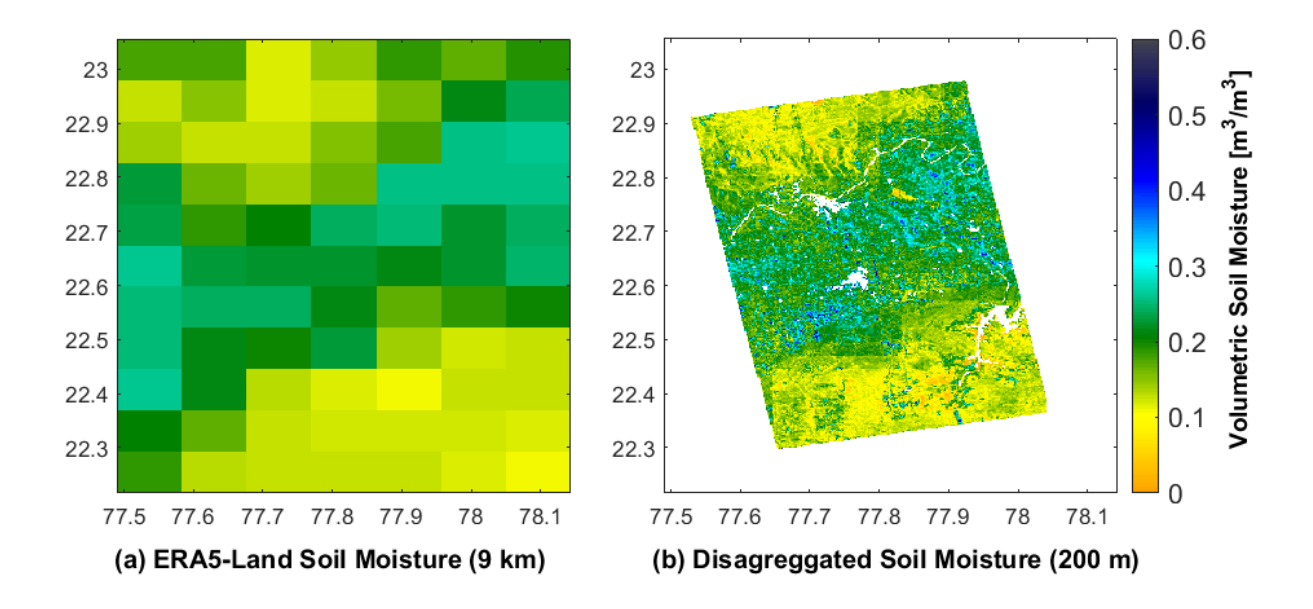


Figure 21: Soil Moisture maps over the Central India region for March 30, 2016. (a) ERA5-Land coarse resolution (~9 km) soil moisture product, (b) high-resolution (200 [m]) soil moisture retrievals using the proposed algorithm (March 30, 2016). White-colored pixels in the high-resolution maps correspond to inapplicable land cover types for soil moisture retrievals, such as water bodies, built-up urban areas, and permanent snow.

## 4.5.2 Test site-2 (North India)

This test site is located in the northern part of India, covering different land cover types, *i.e.*, cropland, barren land, forest cover, and snow cover. Figure 22 shows that North India has moderate dry to wet soil moisture conditions (~0.25 m³/m³) in the agricultural region (central part of AOI), wet conditions (~0.4 m³/m³) in the north-eastern region (upper right), and arid condition (< 0.1 m³/m³) in the south-western parts (lower left) which is a desert region. Null value pixels in the high-resolution maps correspond to inapplicable land cover types for soil moisture retrievals, such as water bodies, built-up urban areas, and permanent snow. The test site did not receive any precipitation a week before the acquisition of ALOS-2. Overall, the high-resolution soil moisture at 200 [m] (Figure 22) has a similar pattern to coarse-scale soil moisture as the algorithm nearly aggregates to its spatial mean to coarse-scale soil moisture.

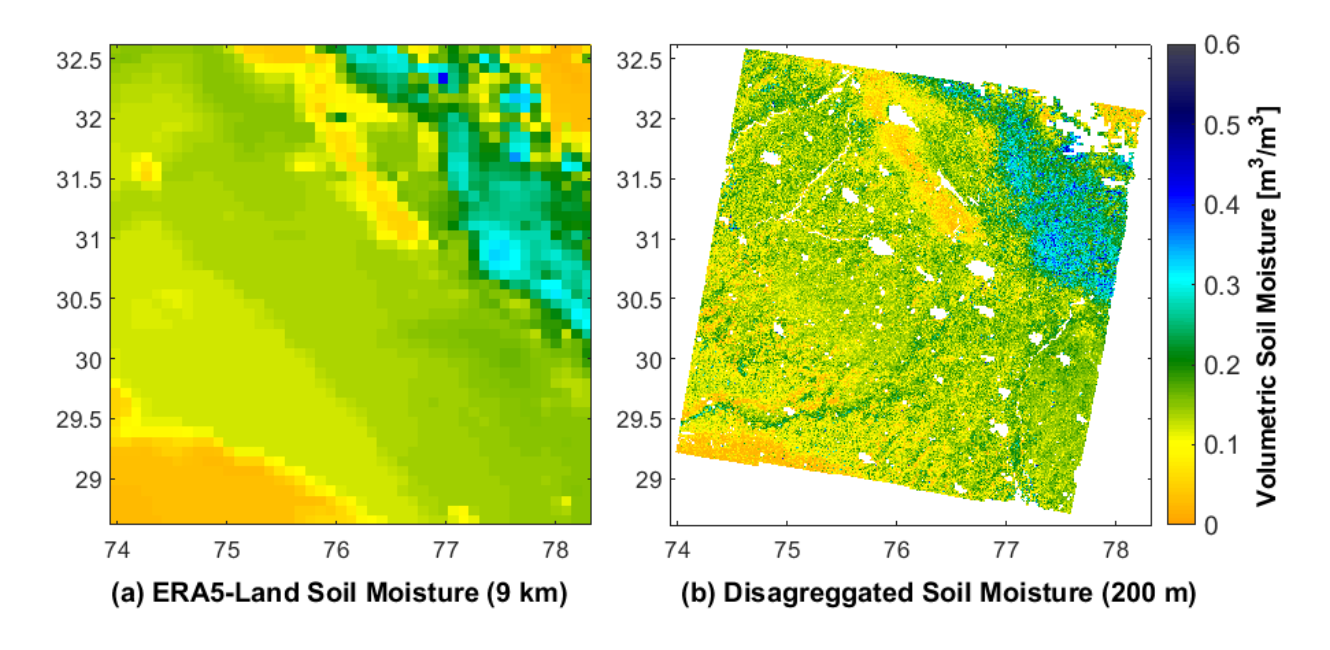


Figure 22: (a) ERA5-Land soil moisture at a coarse resolution of ~9 km (b) high-resolution (200 m) soil moisture retrievals for North India (October 13, 2020). White-colored pixels in the high-resolution maps correspond to inapplicable land cover types for soil moisture retrievals, such as water bodies, built-up urban areas, and permanent snow.

Due to only one day overlap between soil moisture retrievals and *in-situ* measurements, we could not perform a time-series approach for validation. An ergodic substitution of space for time is adopted for validation as per Singh et al., (2019a), assuming that all the agricultural fields are nearby and are almost similar. Thus, the spatially distributed *in-situ* and retrieved soil moisture represent a time series with a range of soil moisture conditions. The comparison shown in Figure 23 demonstrated an encouraging result with a low ubRMSE value of 0.036 m<sup>3</sup>/m<sup>3</sup> that is within the accuracy goals (volumetric soil moisture: 0.06 m<sup>3</sup>/m<sup>3</sup>) for the NISAR-based soil moisture product. However, for this site, a moderate correlation with dry bias has been observed, and this may be attributed to the bias in coarse-scale ERA5-Land soil moisture and, advanced phenological stage of plants and fruit development. This caused a saturation effect in SAR as most of the paddy fields were in the mature stage leading to moderate error in soil moisture retrievals. A more robust validation will be conducted to analyze the variability and error in soil moisture in similar conditions after the launch of the NISAR mission.

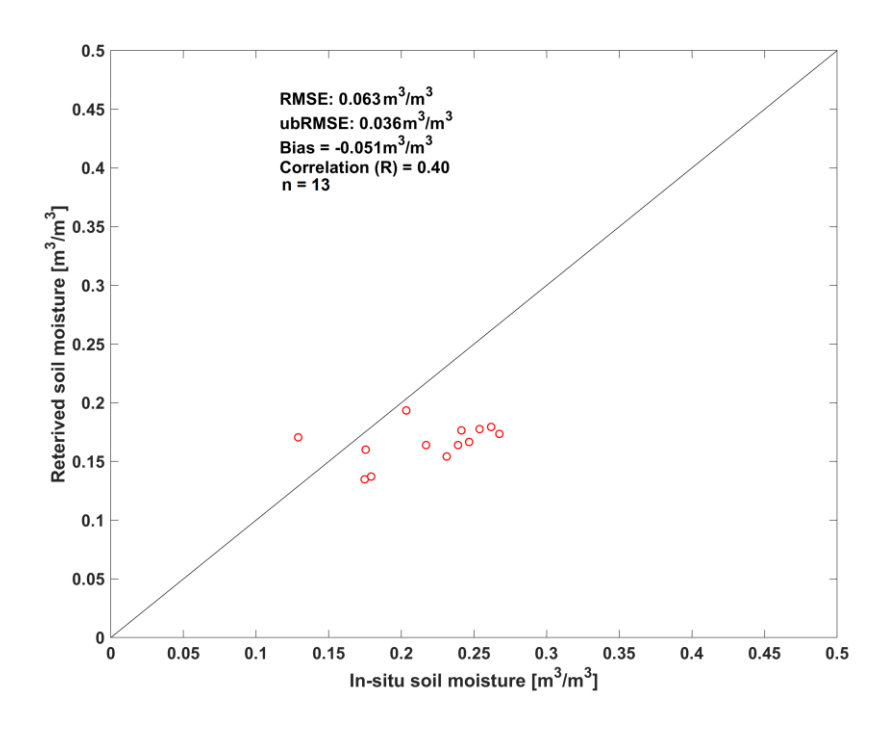


Figure 23: A comparison between high-resolution (200 m) soil moisture retrievals using the ALOS-2 SAR dataset and *in-situ* soil moisture measurements (upscaled at 200 m grid resolution) over 13 agricultural fields in Ludhiana, Punjab, India, for October 13, 2020.

## 4.5.3 Test site 3 (California)

This section analyzes the retrieval of high-resolution (200 [m]) soil moisture with ALOS-2 datasets acquired on July 30, 2017, over Southern California. The region is located within the agricultural landscapes of San Joaquin Valley, nestled between the Sierra and the Coastal Mountain ranges. The eastern part of the test site is covered with an arid region with little vegetation, and dry condition (< 0.1 [m³/m³]) is observed on both coarse resolution and high-resolution soil moisture with a similar spatial pattern (Figure 24). The central-eastern part of the test site is covered with a dense broadleaf forest canopy, and soil moisture range from 0.15 m³/m³ to 0.25 m³/m³. The central part of the test site is covered with agricultural land and urban area. Due to the unavailability of the ALOS-2 time series, it is hard to differentiate between crops in the harvesting stage or initial stage, which are both possible during the summer season (Zhong et al., 2011). The estimated soil moisture for the agricultural fields ranges from ~0.1 [m³/m³] – 0.2 [m³/m³]. Overall, the algorithm demonstrates that high-resolution features are successfully captured and can be monitored. For example, soil moisture at a resolution of 200 [m] can be useful for many agricultural applications related to irrigation and the determination of water demand in

the San Joaquin Valley.

The retrieved soil moisture is validated with limited *in-situ* measurements (~28 points) over southern California. The *in-situ* points were ergodically substituted of space for time, assuming that all the land covers are nearby and are almost similar. Thus, the spatially distributed *in-situ* and retrieved soil moisture represent a time series with a range of soil moisture conditions. The comparison shown in Figure 25 demonstrates that the variability of both *in-situ* and retrieved soil moisture is dry to moderate dry (0.05 m³/m³ – 0.17 m³/m³) with low ubRMSE of 0.0271 m³/m³, a low bias of 0.0163 m³/m³ and high correlation (R) of 0.88. The retrieved soil moisture accuracy shows that it's with in the NISAR soil moisture product accuracy goals (volumetric soil moisture: 0.06 m³/m³).

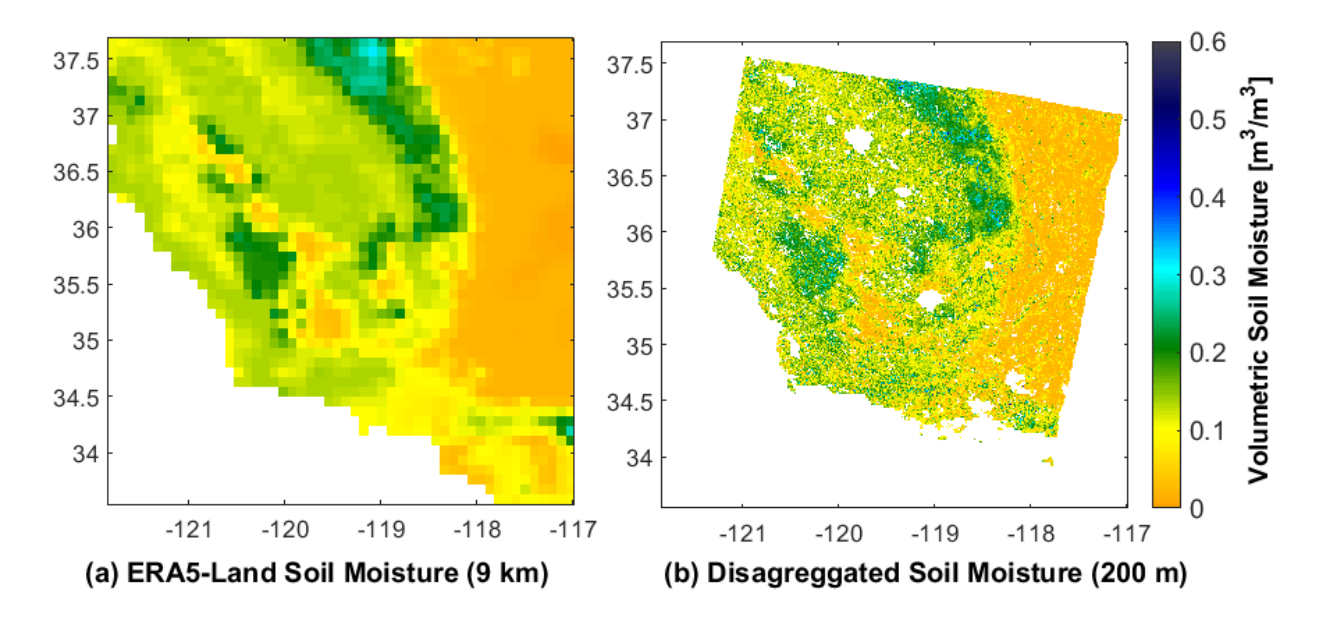


Figure 24: (a) ERA5-Land soil moisture at a coarse resolution of ~9 [km], (b) high-resolution (200 [m]) soil moisture retrievals for the Southern California region (July 30, 2017). White-colored pixels in the high-resolution maps correspond to inapplicable land cover types for soil moisture retrievals, such as water bodies, built-up urban areas, and permanent snow.

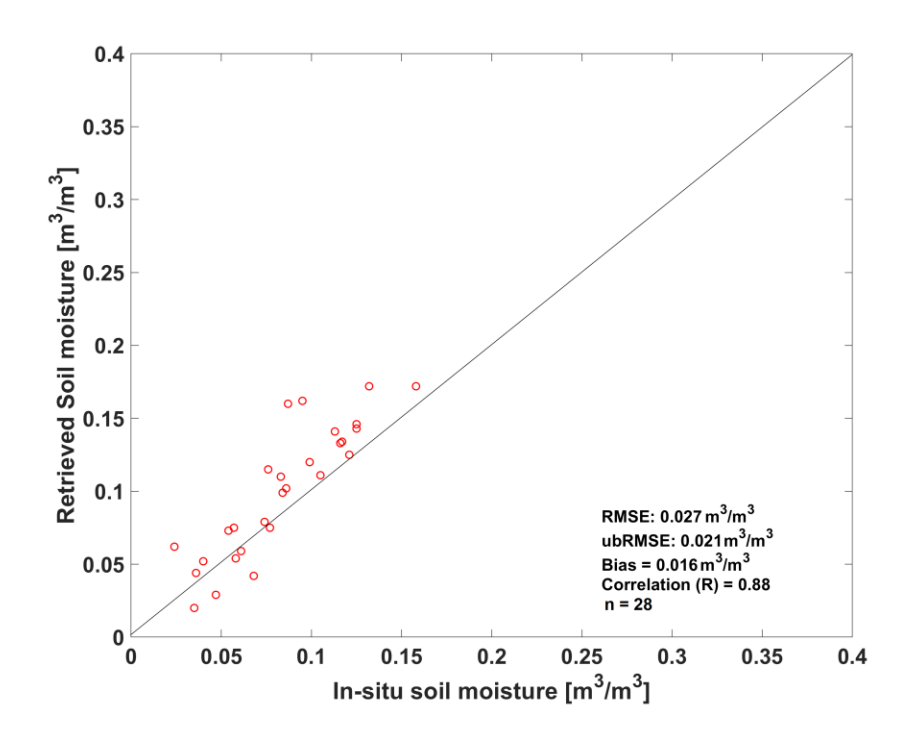


Figure 25: A comparison between high-resolution (200 m) soil moisture retrievals using the ALOS-2 SAR dataset and *in-situ* soil moisture measurements over 28 *in-situ* locations in Southern California, USA, for July 30, 2017.

# 4.5.4 Test site 4 (Carman, Manitoba, Canada)

The high-resolution (200 [m]) soil moisture at this site was retrieved by using UAVSAR L-band  $\sigma_{HH}(F_n)$  and  $\sigma_{HV}(F_n)$  datasets (Flight lines 31606 and 31604) over the SMAPVEX 2012 field campaign domain in Carman, Manitoba, Canada, and validated for eight crop types. As illustrated in Figure 26, a total of 14 UAVSAR scenes (flight line 31606) from a one-month period (June 17 – July 17, 2012) were downscaled using the algorithm. During the one-month period, a long dry down with a growth of vegetation (Figure 59) and a wetting event were observed. The detailed description and methodology used for measuring crop growth stages are shown on the SMAPVEX12 campaign portal (https://smapvex12.espaceweb.usherbrooke.ca/site\_agri.php). The algorithm successfully captured the evolution of soil moisture at 200 [m] resolution during the dry-down and subsequent wetting events.

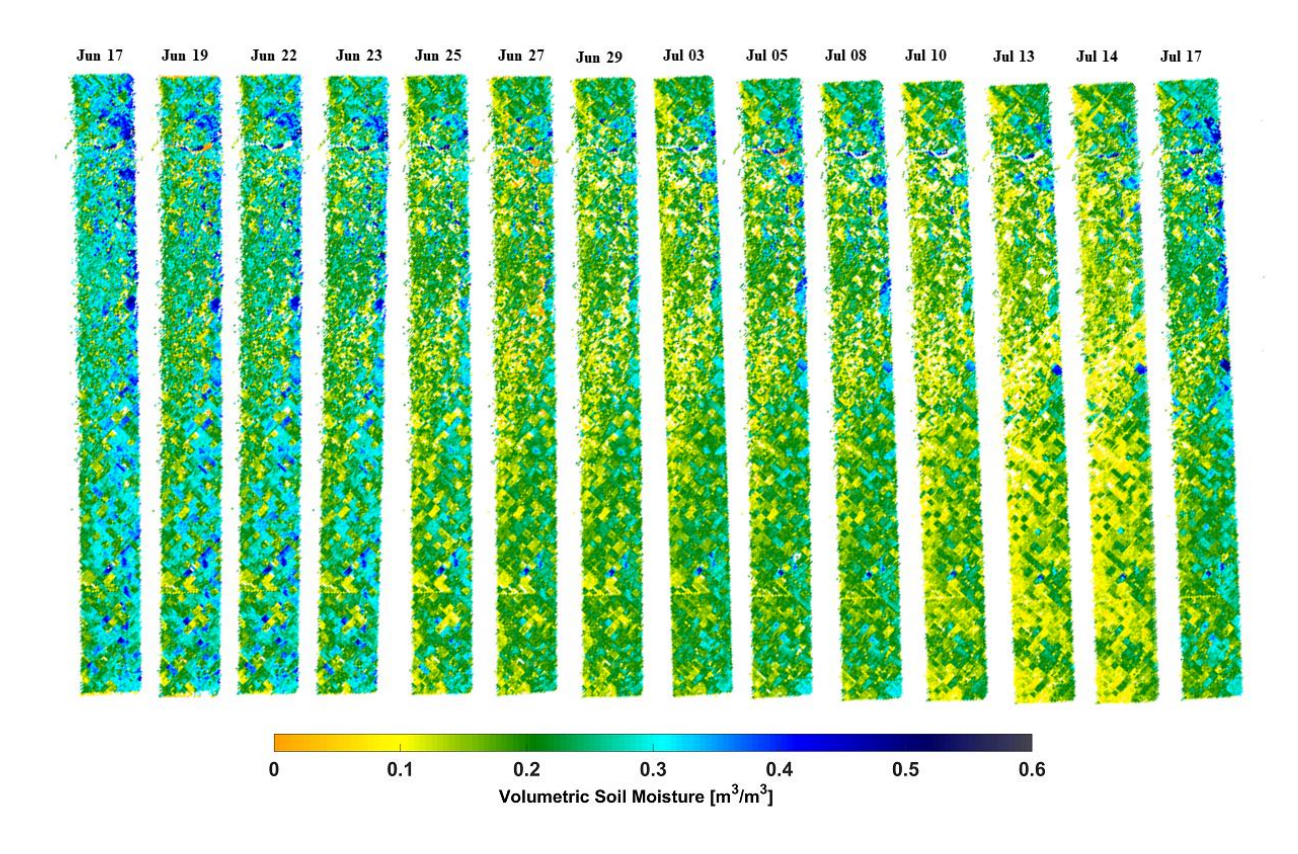


Figure 26: Spatiotemporal variation of high-resolution soil moisture at 200 [m] resolution retrievals using UAVSAR data from SMAPVEX12 campaign over Carman, Manitoba test site between June 17 to July 17, 2012, for the UAVSAR flight line (31606).

The test of the algorithm at this site is of particular importance as the UAVSAR observations cover agricultural fields with tremendous heterogeneity in crop types (soybean, maize, sunflower, oats, canola, wheat, and forage). Thus, in the NISAR prelaunch phase, the SMAPVEX 2012 is considered a major site for testing algorithm performance within agricultural landscapes. We extensively validated the retrieved high-resolution soil moisture against the measured *in-situ* soil moisture over various agricultural fields with different crop types. A more detailed soil moisture map of a part of UAVSAR flight line 31606 is shown in Figure 26. The two scenarios show dry and wet conditions and how the multi-scale algorithm captures the variability in soil moisture as visible in different fields. The variability in high-resolution surface soil moisture is primarily due to various crop covers, diversity in crop density, variability in soil types, and difference in vegetation-water-content, and these attributes are captured by the L-band SAR  $\sigma_{HH}(F_n)$  and  $\sigma_{HV}(F_n)$  observations. The north-south aligned agricultural fields are clearly seen

because of different soil moisture conditions. Such high-resolution soil moisture products will enable the monitoring of individual agricultural fields.

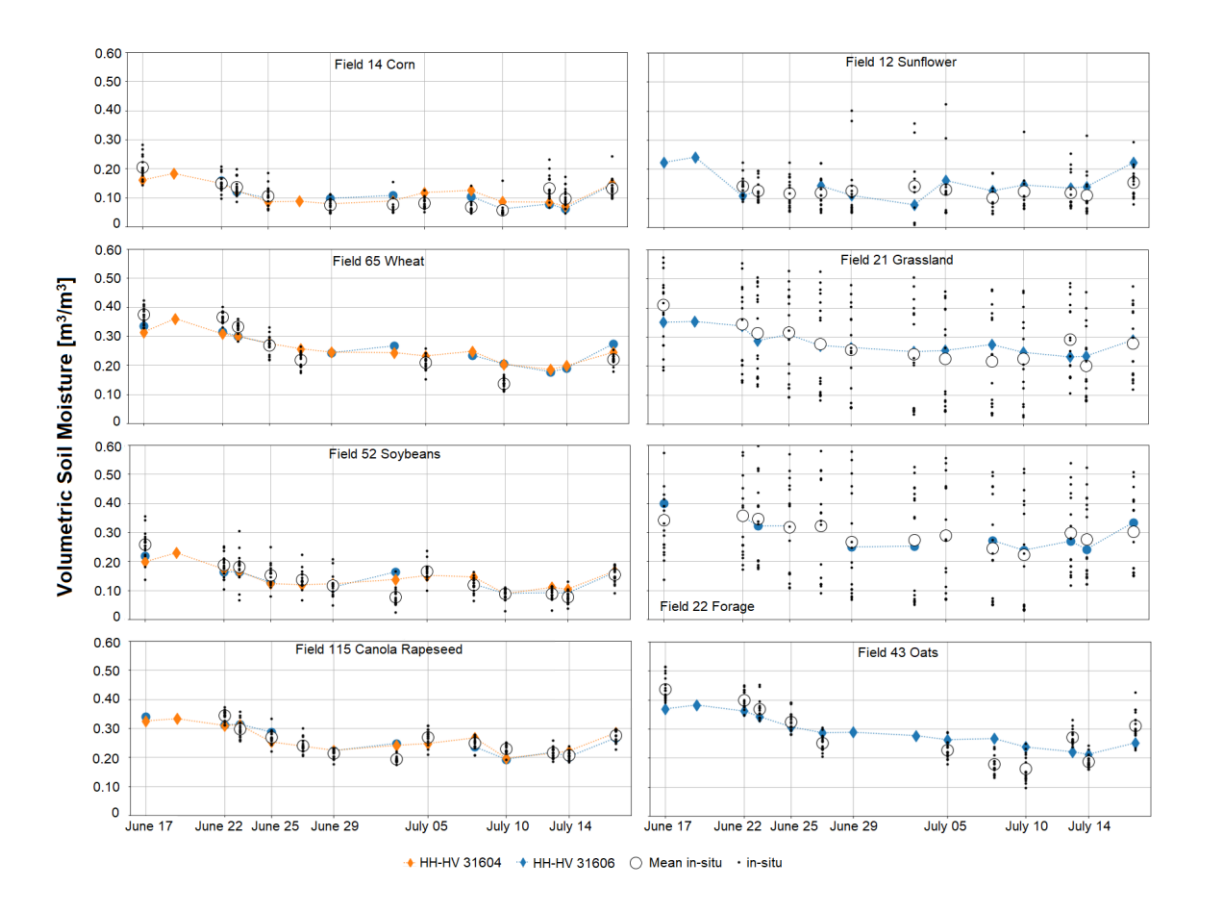


Figure 27: Time series of high-resolution (200 [m]) soil moisture retrievals from two different UAVSAR flight lines (31604 and 31606) over agricultural fields with different crops. Orange and blue symbols show the retrievals from line 31604 and 31606, respectively, and black open circles and small dots show the mean of *in-situ* observations for a given field and the total of all observations for that field.

Figure 27 shows the high-resolution (200 [m]) soil moisture time series over fields (randomly selected, but all the fields have similar soil moisture variability) with different crop covers. The most important aspect to notice in Figure 27 is that the high-resolution (200 [m]) soil moisture retrievals closely follow and match the mean of the field *in-situ* measurements for all the days. The retrieved soil moisture even matched closely with the mean of the *in-situ* soil moisture where the variability is high, such as the agricultural fields that have sunflower, forage, and grassland. Figure 27 also demonstrates another aspect of the algorithm, the retrieved high-resolution soil moisture time series from two different flight lines (31604 and 31606) are almost

similar. This shows that the algorithm is quite capable of retrieving almost the same values of soil moisture irrespective of the difference in the incidence angle of the SAR observation geometry. Time series plots from various other fields with different land cover were also analyzed and have similar matching characteristics and results, as shown in Figure 27.

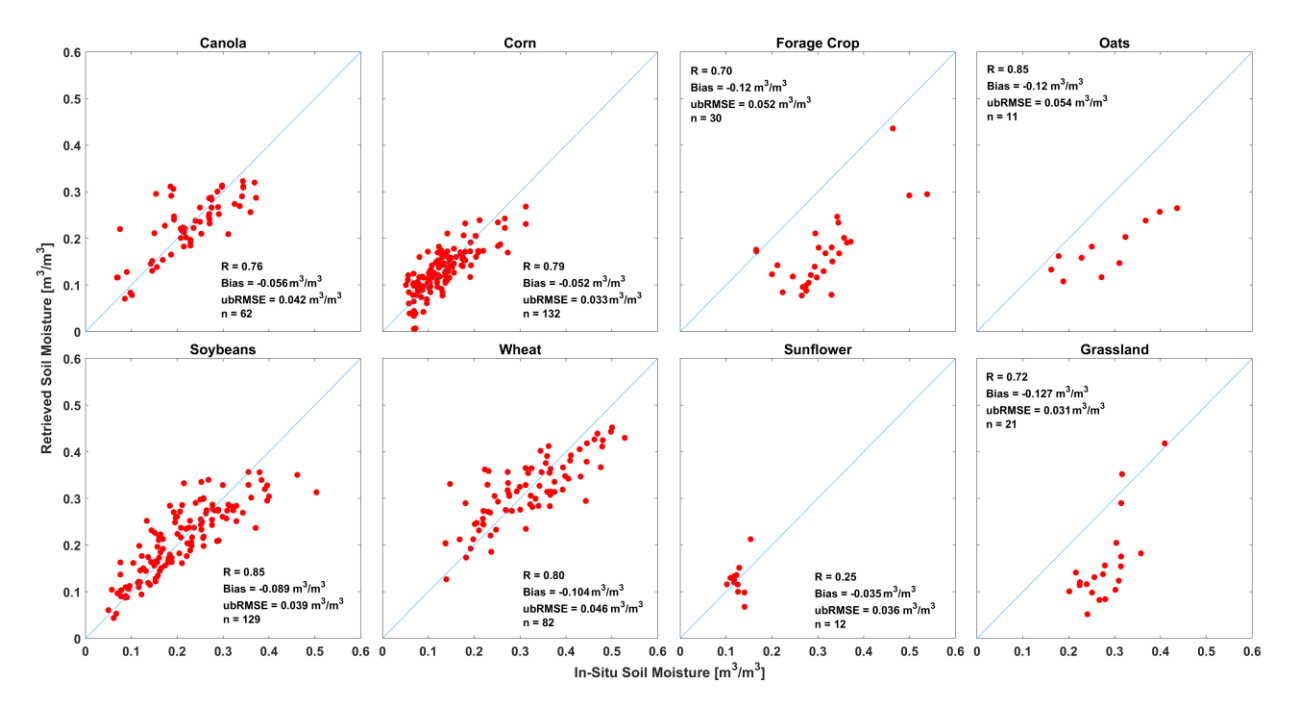


Figure 28: A comparison between high-resolution (200 m) soil moisture retrievals using the SAMPVEX12 UAVSAR dataset and *in-situ* soil moisture measurements for different crops. Note that some of the crops, such as oats, forage, and broadleaf, had fewer than 3 fields.

Figure 28 illustrates the statistics for soil moisture retrievals obtained from UAVSAR flight line 31606 (similar statistics were obtained for flight line 31604, not shown here). The statistics come from all the fields of a certain crop cover. The ubRMSE of the high-resolution (200 [m]) soil moisture retrievals are below the NISAR science goal of 0.06 m<sup>3</sup>/m<sup>3</sup>. As expected, the biases on fields with some crop cover, such as forage and oats, are on the higher side (> 0.10 m<sup>3</sup>/m<sup>3</sup>). These high bias in the retrieved soil moisture can be attributed to bias in ERA5-Land coarse resolution soil moisture and a lesser number of observations, and also, it should be noted that some of the crops had fewer than three fields' samples. Another reason to moderate to high bias may be attributed to the plant structure, e.g., the Soybean plant has a pianophiles canopy structure (horizontally oriented leaf structure) during the flowering and pod initiation stage, and the chance of attenuation of HH pol is high. This leads to saturation of HH pol backscatters. However, the

ubRMSE numbers (Figure 28) over all the fields impart more credence to the multi-scale algorithm as they were calculated under a range of soil conditions (dry to wet) and with crop growth (i.e., increasing vegetation-water-content).

#### 4.6 Discussion

The proposed NISAR soil moisture multi-scale algorithm developed as Eq. 7 was tested on different hydroclimatic domains and validated in limited conditions over various airborne- and satellite-based SAR L-band observations. Primarily data from UAVSAR and ALOS-2 are used for testing the algorithm, as other L-band SAR data such as from the SACOM platform are not available to the public. Although the SAR data from UAVSAR and ALOS-2 do not have the matching L-band instrument characteristics of NISAR, these datasets do provide L-band SAR  $\sigma_{HH}(F_n)$  and  $\sigma_{HV}(F_n)$  backscatter data over a large geographic extent with a wide range of land use/land cover and climate characteristics. The UAVSAR L-band data from the SMAPVEX12 campaign and ALOS-2 were preprocessed to add noise to make it nearly similar to the noise characteristics of the expected NISAR observations. The SAR data as single-look-complex (SLC) (~10 [m] resolution) is not used as input to the algorithm, it is further aggregated to ~200 [m] spatial resolution. This aggregation step greatly reduces the speckle by averaging ~400 SLC values to obtain SAR  $\sigma_{HH}(F_n)$  and  $\sigma_{HV}(F_n)$  backscatter observations at 200 [m] spatial resolution. The aggregation step also greatly reduces the uncertainty due to speckle and makes the difference in backscatter noise characteristics very less at 200 [m] resolution between the expected NISAR data and other SAR data from ALOS-2 and UAVSAR data used for the study.

A key input to the NISAR soil moisture multi-scale algorithm is the coarse resolution (9 [km]) soil moisture from ECMWF land product. This imparts a tremendous reduction in the degrees of freedom for the algorithm, as the direct dependence on other satellite missions is eliminated. Moreover, the algorithm does not depend on other ancillary data to produce high-resolution soil moisture retrievals. The input soil moisture from ERA5-Land is available at hourly timesteps, enabling the algorithm to closely match the NISAR overpass time. The study by Lal et al., (2022b) has demonstrated that the ECMWF ERA5-Land based soil moisture data have almost similar error characteristics as the SMAP retrieved soil moisture. This is due to the fact that ECMWF uses many microwaves satellite-based soil moisture products as model forcings and also assimilates the state variables. Thus, using reanalysis data from an ECMWF as input for coarse-resolution soil moisture in the algorithm eliminates dependence on radiometer-based soil moisture

product. This approach significantly reduces the risk of implementation as an operational algorithm for generating the soil moisture product through the NISAR mission science data system.

The coarse-resolution ECMWF ERA5-Land soil moisture data and SAR HH-pol backscatter data are used to estimate the algorithm (Eq. 7) sensitivity parameter  $\beta$ . In the NISAR prelaunch phase, the sensitivity parameter  $\beta$  is derived using the legacy SMAP SAR HH-pol data and ERA5-Land soil moisture data at 9 [km] to build a prior database. This is possible because the SMAP SAR HH-pol backscatter can be aggregated to 9 [km] from its native resolution of ~1 [km]. Our analysis and the validation results demonstrated that the algorithm sensitivity parameter  $\beta$ developed for the prior database performed satisfactorily. However, this prior database of  $\beta$  has significant scope of improvement after the NISAR launch. The improvement will come from acquisition of longer time series of NISAR HH-pol SAR data. The longer time series will enable to capture variable land surface conditions (such as higher variability in soil moisture state) and seasonality. The prior database of sensitivity parameter  $\beta$  is based on categorization of land cover type, however, postlaunch and with acquisition of longer time series NISAR observations, evaluation will be performed to maintain the  $\beta$  database according to land cover or create  $\beta$ parameter for every 9 [km] grid cell. The ideal way is the grid-based  $\beta$  estimates, as it can improve the algorithm accuracy significantly. The is because the  $\beta$  parameter is expected to be unique for any given grid cell due to the surface characteristics. However, in the real-world operational scenario, the significance level of derived  $\beta$  from time series for a particular 9 [km] grid cell may not be optimal due to non-presence of soil moisture dynamic range, thus, we expect a mix of gridbased and land cover based  $\beta$  estimates used in the algorithm implementation. In case of the other algorithm parameter i.e., the heterogeneity parameter  $\Gamma$ , various studies and our analysis shows that this parameter is very stable and can be computed on the fly when implementing the algorithm. The  $\Gamma$  parameter experiences very less variability during algorithm implementation for any given 9 [km] grid cell. The heterogeneity parameter  $\Gamma$  normally has a standard deviation of 0.02 for a grid cell and ranges between 0.7 and 0.9 spatially.

The testing and implementation of the algorithm was conducted over three sites using L-band airborne UAVSAR data and satellite-based ALOS-2 data. The eligibility of these sites is due to the availability of coinciding *in-situ* soil moisture measurements. The results showed that the algorithm successfully retrieved/disaggregated the coarse-resolution soil moisture to 200 [m]. For

the SMAPVEX12 site (Figure 26), the spatial variability in soil moisture space was captured at 200 [m] resolution and it clearly shows the field-specific impact of crop covers, open fields, and forested regions. The retrieved soil moisture validation against the field-specific averaged *in-situ* soil moisture shows that the algorithm can meet the NISAR mission goal of 0.06 m³/m³ ubRMSE for the high-resolution (200 [m]) soil moisture product. The extensive validation conducted especially over the SMAPVEX12 site imparts credibility to the results because it is very challenging to achieve retrieval accuracy over the agricultural land cover due to dynamic and complex nature of the landscape as compared to other natural land covers such as grassland and shrubland. It is commonly accepted that a soil moisture product meeting the accuracy level over agricultural land cover normally can meet accuracy goals over other valid land covers except forested regions. However, postlaunch we expect more comprehensive validation of the NISAR high-resolution soil moisture product over different land covers at a global extent using sparse network sites (such as SCAN, Mesonet, and International Soil Moisture Network *in-situ* data) and planned dedicated field campaigns to be conducted in CONUS and India.

Overall, the multiscale fusion algorithm captured the soil moisture spatial geophysical distribution as observed by the SAR backscatter at high-resolution (200 [m]). The science and application communities need such unprecedented high-resolution soil moisture data applications in the field of agriculture, drought monitoring, carbon-related studies, and watershed management. The high-resolution soil moisture, particularly at the field scale, can help in (a) detecting irrigation signals (Jalilvand et al., 2023; Kwon et al., 2022); (b) identifying how hydroclimatic phenomenon is driven at a local scale (Vergopolan et al., 2022); (c) drought forecasting as it's highly spatially variable due to differences in vegetation composition and cover; (d) improvement of flood forecasting with data assimilation; (e) identifying the role of soil moisture for heat wave persistence at regional scale (Dubey et al., 2021).

#### 4.7 Conclusion

The study presented a robust multiscale soil moisture algorithm for the upcoming NISAR mission. The algorithm function purely in a snapshot manner and does not require any time series of NISAR observations and ancillary data except coarse-resolution soil moisture estimates. However, off algorithm implementation NISAR observations time series are required to estimate the primary algorithm parameter. These attributes make the multiscale soil moisture algorithm operationally very feasible. The testing and validation using limited L-band airborne and satellite-

based SAR datasets demonstrated that the algorithm is capable to meet the NISAR mission goal of 0.06 m³/m³ ubRMSE except for the forested regions. Postlaunch, the multiscale soil moisture algorithm has potential to perform better due to expected further improvement in the algorithm parameter-associated uncertainty. This unprecedented high-resolution (200 [m]) weekly (~6-days) NISAR mission soil moisture product will have tremendous value in geophysical applications for societal benefits. It is expected that the NISAR high-resolution (200 [m]) soil moisture data will be available to the public from ~August 2025 through one of the NASA Distributed Active Archive Centers (DAAC, the Alaska SAR Facility).

# CHAPTER 5: COMPREHENSIVE VALIDATION OF THE NISAR MULTI-SCALE SOIL MOISTURE RETRIEVAL ALGORITHM ACROSS VARIOUS SPATIAL RESOLUTIONS AND LANDCOVERS USING THE ALOS-2 DATA

In the previous chapter, a multi-scale soil moisture algorithm was developed for the upcoming NISAR mission. Due to the unavailability of NISAR data, similar data from UAVSAR and ALOS-2 L-band SAR were used as substitutes. The soil moisture was retrieved at a 200 [m] spatial resolution and validated on agricultural test sites. However, given the algorithm's multi-scale nature, it is essential to assess its performance at higher spatial resolutions and across land cover types. Therefore, this chapter aims to comprehensively validate the NISAR multi-scale soil moisture retrieval algorithm across varying spatial resolutions and land cover types using ALOS-2 data.

#### 5.1 Introduction

Soil moisture, the water content held within soil pores, is a fundamental variable that influences a wide range of environmental processes. It plays a critical role in hydrological studies (Nanda et al., 2024), directly impacting the partitioning of precipitation into infiltration and runoff. Soil moisture also regulates land-atmosphere interactions and is crucial for plant growth and ecosystem productivity. From an ecological perspective, soil moisture levels determine the availability of water for plant uptake, influencing species distribution, biodiversity, and overall ecosystem health (Lal et al., 2022a). Additionally, the coupling between soil moisture and the atmosphere, along with the role of vegetation, can directly impact the climate system. The resolution at which soil moisture data is being observed has significant implications in various applications. While coarse-resolution observations provide insights into large-scale soil moisture patterns (Lal et al., 2023a), high-resolution soil moisture is essential for applications like precision agriculture (de Lara et al., 2019), water-demand mapping in agricultural regions (Singh and Das, 2022), localized flood risk assessment (Wanders et al., 2014), and detailed ecosystem modeling (Hu et al., 2018). Improving the spatial resolution of soil moisture data collection is crucial for better understanding complex land surface interactions at smaller scale. Thus, higher-resolution data can provide more detailed insights into local-scale soil moisture dynamics, enabling better management and decision-making in various geophysical applications. Despite the clear advantages of high-resolution soil moisture data, its widespread availability and measurement remain limited. Although the use of electronic sensors with automatic data-logging devices for

continuous *in-situ* soil moisture measurement has the potential to provide high-resolution data, it is expensive to maintain a sufficiently large sensor network for regional to global scale monitoring.

However, remote sensing offers a potential alternative to costly in-situ soil moisture measurements with broader coverage at multiple spatial and temporal resolutions. Over the past two decades, space agencies and the scientific community have devoted numerous efforts to monitor soil moisture globally using passive and active microwave remote sensing techniques with an acceptable level of uncertainties within a given set of surface and climatic conditions (Das et al., 2016). The current operational soil moisture products are primarily derived from the radiometer-based passive remote sensing satellite such as i.e. Advanced Microwave Scanning Radiometer (AMSR-2) by Japan Aerospace Exploration Agency (JAXA), Soil Moisture Ocean Salinity (SMOS) by European Space Agency (ESA), and Soil Moisture Active Passive (SMAP) by NASA. The satellite soil moisture observations coming from these radiometer satellite missions have a spatial resolution of ~30-50 [km] and a temporal resolution of 2-3 days. While useful for large-scale monitoring, this resolution is often too coarse for many hydrometeorological and agricultural applications (de Lara et al., 2019; Vergopolan et al., 2020). To address this limitation, active microwave remote sensing observations based on Synthetic Aperture Radar (SAR) have shown significant potential for high-resolution soil moisture retrieval. The SAR systems transmit microwave signals and measure the backscatter energy, which is also influenced by a soil dielectric constant (i.e., soil moisture content). Unlike radiometers, SAR can provide detailed spatial information primarily influenced by soil moisture, vegetation, and soil roughness, making it valuable for different applications. Despite having the capability of high-resolution soil moisture retrieval, it often poses challenges due to the inherent complexity of radar backscatter signals and the inverse problem of backscattering models (Mattia et al., 2006). The backscattered signal is highly sensitive to vegetation cover, in presence of thick vegetation cover the soil moisture and surface roughness signals can severely attenuated/masked, which introduces variability and complexity to the measurements. To address these issues, several sophisticated algorithms have been developed, such as empirical and semi-empirical models (D'Urso and Minacapilli, 2006; Ettalbi et al., 2023; Hoskera et al., 2020), model-based polarimetric decomposition (Wang et al., 2018), inversion methods which include change detection, linear and non-linear interpolation and look-up-table inversion (Balenzano et al., 2021), and data-driven physical models using machine learning and artificial intelligence and fuzzy logic approaches (Chaudhary et al., 2022; Moosavi

et al., 2016). These algorithms are often difficult to implement in operational product generation due to the involvement of different levels of complexities in each algorithm and requirement of many ancillary inputs at high spatio-temporal resolution. The limitations of the above algorithms for operational implementation have been well discussed in detail by Lal et al., (2023b). Further, an active-passive approach for soil moisture retrieval has been developed to address these limitations for operational high-resolution soil moisture retrieval (Das et al., 2019, 2018). The active-passive algorithm disaggregates the coarse-resolution SMAP brightness temperature (~ 36 [km]) to resolutions of 9 [km], 3 [km], and 1 [km] using the SAR backscatter observations (Das et al., 2018). The disaggregated brightness temperature is used to retrieve soil moisture using the tau-omega radiative transfer model. However, the tau-omega models for retrieving soil moisture require other ancillary datasets at high resolution, such as soil and vegetation parameters (Das et al., 2018), and often, these ancillary parameters have uncertainty associated with it to match the required resolution (Das et al., 2016). Thus, these factors usually make operational high-resolution soil moisture retrievals very challenging.

In the last chapter, a multi-scale algorithm has been proposed for the operational highresolution soil moisture product with reasonable error/uncertainty at ~ 200 [m] resolution for the upcoming NISAR mission. The multi-scale algorithm is developed based on the SMAP mission algorithm based on Das et al., (2011). This multi-scale algorithm proposes to retrieve 200 [m] resolution soil moisture using ~ 10 [m] resolution backscatter measurements from the NISAR mission. The major aim of proposing the multi-scale algorithm was to reduce the algorithm's dependency on multiple ancillary parameters of soil and vegetation to provide the NISAR mission's operational high-resolution soil moisture product. The multi-scale algorithm is totally data-driven by the coarse resolution soil moisture data and the SAR dual-pol observations and needs no other ancillary data, thus, reduces the degree of freedom to achieve optimal accuracy and low uncertainty. A detailed description of the multi-scale algorithm can be found in the previous chapter (section 4.2). Given the nature of this algorithm as "multi-scale", it has the potential to retrieve soil moisture at different scales or even higher resolution, given favorable L-band SAR observations. However, the proposed multi-scale algorithm was not tested for spatial resolutions higher than 200 [m], and validation was limited to cropland only due to the unavailability of coinciding L-band SAR observations and *in-situ* measurements. Therefore, the objective of this chapter is to investigate and validate the multi-scale algorithm's soil moisture retrieval capabilities

at both 100 [m] and 200 [m] resolutions across five diverse test sites. These sites are characterized by different land covers (forest, shrubland, cropland, and grassland) and varying hydrometeorological conditions, ranging from arid to polar regions. Since the NISAR L-band SAR observations are not available currently due to its delayed launch until February 2025, this study utilizes existing L-band SAR datasets from the ALOS-2 platform as a substitute to test the multiscale algorithm. This allows algorithm validation on a wider range of spatial resolution and field conditions before the availability of NISAR products.

## **5.2 Test Sites**

To evaluate the performance of multi-scale algorithm for high-resolution soil moisture retrieval (at resolutions of 100 [m] and 200 [m]), we selected five diverse sites having *in-situ* measurements of soil moisture. These sites were selected based on their distinct land covers, which include forested areas, shrublands, croplands, and grasslands. Moreover, these sites have a wide range of hydrometeorological conditions, ranging from arid to polar regions. An overview of these test sites is presented in Figure 29, with detailed information provided in the subsequent sections.

## **5.2.1 Delta Junction**

The Delta Junction (DEJU) NEON site in Alaska has a subarctic climate with long intensely cold winters and short mild summers. This climate profoundly influences the dominant soil types within the region. The soils are predominantly eluvial deposits created by the weathering of the underlying glacial till and outwash, often covered with a thin layer of loess (wind-blown silt). These soils are characteristically well-drained with gravelly textures. The harsh winters lead to the development of permafrost in some areas, adding a layer of complexity to the soil profile. Despite the challenging climate, the Delta Junction site supports a mix of vegetation, including resilient spruce and aspen forests adapted to the short growing seasons and unique soil conditions.

## 5.2.2 Caddo-Lyndon B. Johnson National Grasslands

The Caddo-Lyndon B. Johnson National Grasslands (CLBJ) NEON site, located in the Great Plains region of north-central Texas, experiences a climate typical of the region – hot, humid summers and cool, windy winters. The grassland's climate patterns, with periods of rainfall and dry spells, influence the soil types found on site. The soils are classified as Udic Paleustalfs, formed from weathered sandstone, siltstone, and some limestone. These soils often have a significant clay component, which can moderate moisture retention and drainage. However, areas with particularly

high clay content can hinder tree growth due to reduced permeability. This soil composition contributes to the landscape being dominated by diverse grasses that are well-adapted to these conditions.

# 5.2.3 University of Kansas Field Station

The University of Kansas Field Station (UKFS) is located in eastern Kansas. Its continental climate features warm, wet summers, cold, dry winters, and occasional intense storms. The soil of UKFS classified as fertile Mollisols, supports a mix of mixed hardwood forests and tallgrass prairie remnants. The site drains into the Kansas River Basin and provides a habitat for wildlife, including deer, small mammals, and numerous bird species. Historically, it is a transition zone between forest and prairie. Currently, the Field Station balances its agricultural legacy with a focus on research, education, and conservation.

## 5.2.4 Walnut Gulch

Located in southeastern Arizona, Walnut Gulch experiences a semi-arid climate. Summers are hot, winters are mild, and rainfall comes mostly from summer monsoons. The hot, dry conditions shape the region's soils, which are typically well-drained and often gravelly. In some areas, a layer of calcium carbonate, known as "caliche," below the surface is present. Soil types can be sandy loams or have more clay content, depending on elevation and the underlying rock types. Walnut Gulch is home to shrublands and grasslands, specifically adapted to the region's unique climate and soil conditions.

## 5.2.5 Little River

Little River watershed, Georgia, experiences a humid subtropical climate characterized by hot, humid summers and mild winters. This climate, along with the region's geology, shapes the dominant soil types. The soils in Little River are primarily loamy sands – a mixture of sand, silt, and clay that allows for good drainage. These well-drained soils support diverse vegetation, including woodlands, row crops, and pastureland.

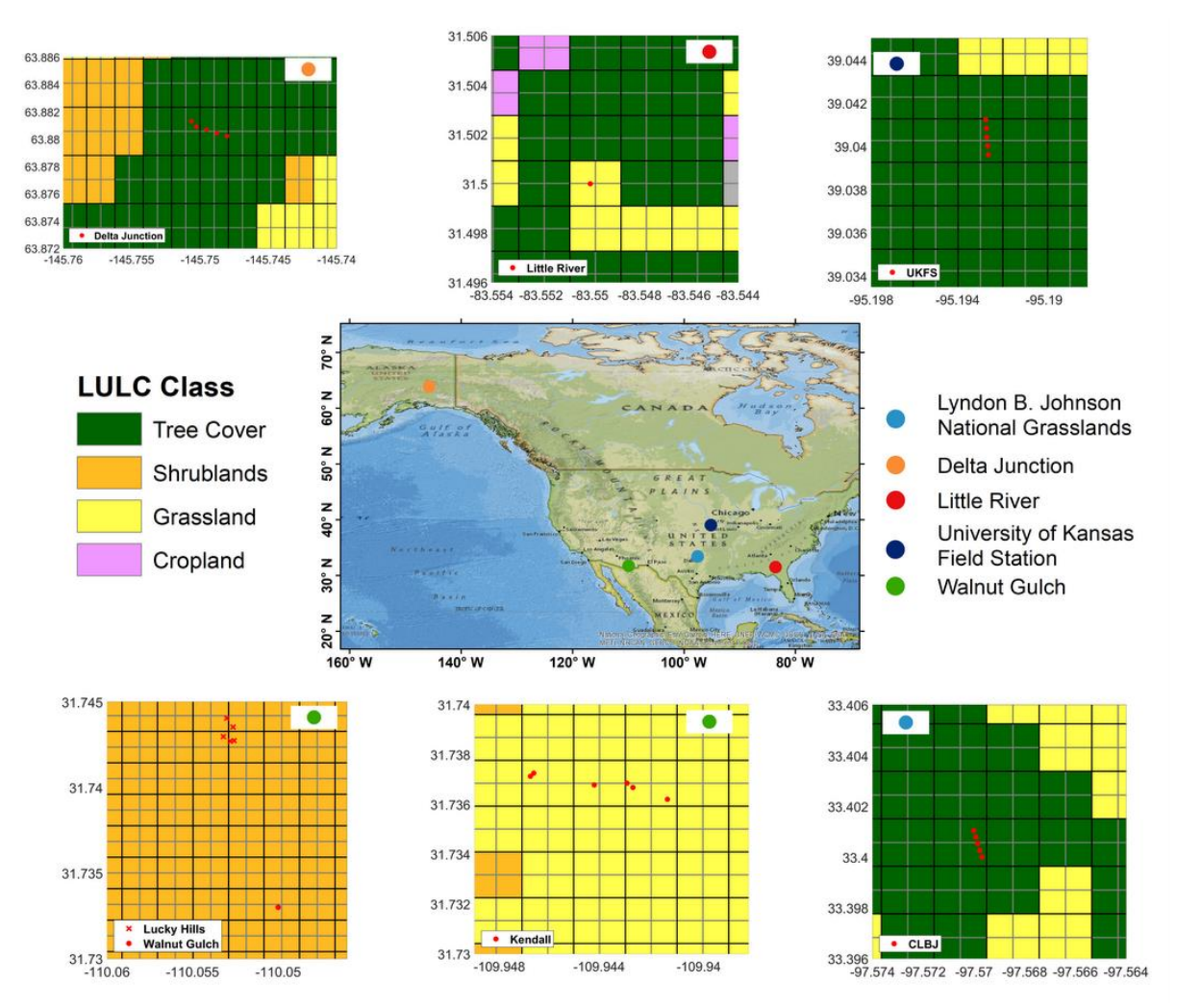


Figure 29: Overview of the test site showing the EASE-2 grid-cells at a spatial resolution of 200 [m] (black line) and 100 [m] (grey line), along with land cover class and the locations of *in-situ* measurements of soil moisture.

## 5.3 Data Used

For high-resolution soil moisture retrieval, L-band SAR data from ALOS-2 and ECMWF ERA5-Land data have been utilized. A detailed description of ECMWF ERA5-Land can be found in Section 3.2.1, and description for ALOS-2 SAR is provided in 4.3.2.2. *In-situ* soil moisture has been used for the validation of the retrieved soil moisture and precipitation data has been used to analyze the temporal change in soil moisture. The detail about the *in-situ* measurements and precipitation data is given below.

#### 5.3.1 *In-situ* soil moisture

The soil moisture retrievals of the multi-scale algorithm are validated against *in-situ* soil moisture measurements. In this study, we have used *in-situ* measurements from the International Soil Moisture Network (ISMN), Soil Moisture Sensing Controller And OPtimal Estimator (SoilSCAPE), and National Ecological Observatory Network (NEON).

The ISMN is a collaborative global initiative dedicated to collecting, standardizing, and distributing *in-situ* soil moisture data. ISMN has more than 35 international soil moisture networks, which include ~1500 stations (Dorigo et al., 2021, 2011). The ISMN data from the various SM networks were downloaded from https://ismn.earth/en/. The datasets available as *in-situ* are for single points in a given grid.

Table 6: Details of the selected test sites for soil moisture retrieval and *in-situ* locations used for validation.

Sl. No.	Test site*	Name of the <i>insitu</i> locations within the test site*	Source of <i>in-situ</i> soil moisture	Data source
1.	Delta Junction	Delta Junction	NEON	https://data.neonscience.org/data- products/DP1.00094.001
2.	Caddo-Lyndon B. Johnson National Grasslands	Caddo-Lyndon B. Johnson National Grasslands	NEON	https://data.neonscience.org/data-products/DP1.00094.001
3.	University of Kansas Field Station	University of Kansas Field Station	NEON	https://data.neonscience.org/data- products/DP1.00094.001
4.		Walnut Gulch	ISMN	https://ismn.earth/en/
	Walnut Gulch	Lucky Hills	SoilSCAPE	https://soilscape.usc.edu/sites- and-data/
		Kendall	SoilSCAPE	https://soilscape.usc.edu/sites- and-data/
5.	Little River	Little River	ISMN	https://ismn.earth/en/

SoilSCAPE is a network of field sites distributed across the United States and New Zealand. The SoilSCAPE is a soil moisture network with high-density nodes, and the SM sensors are clustered in groups within a relatively small area (1 [km²]) (Moghaddam et al., 2010). The SoilSCAPE *in-situ* soil moisture data for two different stations were downloaded from https://soilscape.usc.edu/sites-and-data/.

NEON collects *in-situ* soil moisture data across its various field sites using a robust sensor network. These sensors provide valuable ground-based measurements to complement and validate satellite-derived soil moisture estimates. NEON installs an array of five soil plots within or near the flux tower's footprint and in the locally dominant soil type of each terrestrial field site. NEON employs Sentek - EnviroSCAN TriSCAN soil sensors to measure soil moisture across its array of five soil plots (Kao et al., 2012; Metzger et al., 2019). These are strategically placed near the flux tower's footprint. These plots are typically spaced between 25 [m] to 40 [m] apart to capture diverse soil conditions accurately and provide a high temporal resolution of one minute (https://data.neonscience.org/data-products/DP1.00094.001). Details of the *in-situ* soil moisture locations within the test sites are provided in Table 6.

## **5.3.2 Precipitation Data**

Precipitation data is utilized to analyze the spatial patterns of soil moisture retrievals by the multi-scale algorithm under various precipitation events. We used precipitation data from two sources: the Precipitation-elevation Regressions on Independent Slopes Model (PRISM) and the Integrated Multi-satellitE Retrievals for GPM (IMERG). Specifically, IMERG data were used solely for the Delta Junction site due to the unavailability of PRISM precipitation data over Alaska.

IMERG, a product of the US GPM Science Team, utilizes a multi-satellite data approach and incorporates various sources including precipitation gauge. It provides a spatial resolution of 0.10° and temporal resolution of half-hour intervals, starting from January 1, 2001. We utilized the "Final run" product, which is well-calibrated with rain gauge data, ensuring reliable rainfall estimates (Huffman, 2015; Huffman et al., 2014).

The PRISM dataset is a widely used precipitation data in the United States, developed by the PRISM Climate Group at Oregon State University. PRISM does not rely on satellite or radar data. Instead, it uses a digital elevation model (DEM) to estimate the "orographic" elevations of precipitation stations, which helps to account for the influence of topography on precipitation. The methodology involves a windowing technique that groups stations onto individual topographic facets, allowing for more accurate regional precipitation estimates. PRISM precipitation data development involves rigorous validation processes to ensure reliability (Daly et al., 2008, 1994). The PRISM dataset is available in two different resolutions i.e., 800 [m] and 4 [km] data. In this study, we have used 4 [km] data to analyze the precipitation events between dry to wet events observed in soil moisture retrieval.

## **5.4.** Methodology

# **5.4.1 Retrieval Approach**

The multi-scale algorithm is one of the algorithms under upcoming NISAR missions to provide high-resolution (200 [m]) soil moisture retrieval. The NISAR mission multi-scale soil moisture algorithm uses the coarse resolution soil moisture (either from reanalysis datasets or radiometer-derived product) with the NISAR fine resolution L-band SAR co-pol (HH) and cross-pol (HV) backscatter observations. The fine-scale backscatter measurements represent the spatial pattern of landscape characteristics within the coarse-resolution grid cell. The current NISAR mission plan is to use a 6-hourly soil moisture dataset of the ECMWF (similar to the ERA5-Land) as the coarse resolution (~9 [km]) soil moisture input in the multi-scale algorithm. This will help in minimizing the potential mismatch between input SAR backscatter and input coarse resolution soil moisture. The detail about the algorithm is discussed in the previous chapter (section 4.2).

In this chapter, we used ALOS-2 stripmap mode dual pol (HH and HV) SAR data as a substitute for upcoming NISAR L-band measurements. The ALOS-2 data was simulated to closely match the expected characteristics of NISAR measurements (e.g., spatial resolution, noise, etc.). The spatial resolution of the ALOS-2 data is 4.29 [m] × 3.38 [m] (range × azimuth resolution) in single look complex (SLC) mode. The SLC SAR data is processed with the following steps using the ESA-Sentinel toolbox (SNAP): conversion of slant range to ground range, radiometric calibration, and terrain correction (with Copernicus 30 [m] DEM). SAR data usually contains some systemic and random noise, encapsulated as speckles. To mitigate the effects of speckles, with urban and artificial structures on backscatter observations (especially those land cover is not used in the soil moisture retrieval), a spatial hybrid filter is applied. The calibrated GRD SAR backscatter observations are aggregated to 100 [m] and 200 [m] resolutions after filtering. These aggregated SAR data, along with other necessary inputs such as ECMWF soil moisture and algorithm parameters, are used in the multi-scale algorithm to retrieve high-resolution soil moisture at 100 [m] and 200 [m] resolutions. The process flow for high-resolution soil moisture retrieval and validation is provided in Figure 30.

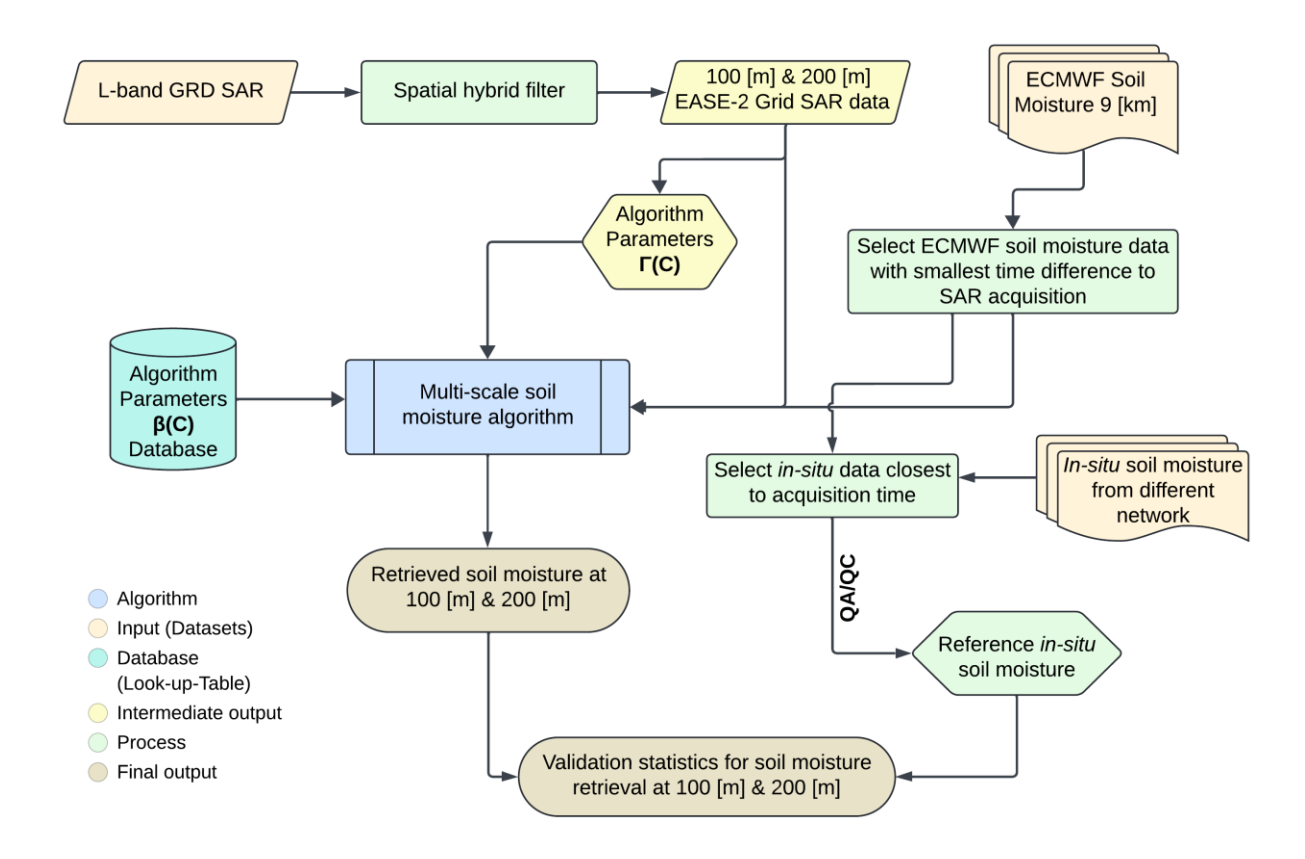


Figure 30: Methodology flowchart for high-resolution soil moisture retrieval and validation.

#### **5.4.2 Validation Approach**

The multi-scale algorithm-based soil moisture retrievals at both 100 [m] and 200 [m] spatial resolutions were validated using *in-situ* soil moisture measurements across various land cover classes and hydrometeorological conditions. Performance metrics such as Mean Difference (MD), Root Mean Square Difference (RMSD), unbiased RMSD (ubRMSD), and correlation (R) are used to assess the accuracy of the soil moisture retrieval. Prior to applying the performance metrics, careful attention was given to filtering out unreliable data points. Subsequently, the one-minute (NEON) and thirty-minute (SCAN and SoilSCAPE) data is aggregated into hourly intervals to align with ECMWF soil moisture and SAR acquisition times. Given the coverage, the collected data can be spatially aligned with 1 to 3 grids based on the EASE-2 Grid systems for both 100 [m] and 200 [m] spatial resolutions. If multiple *in-situ* points fall within the spatial extent of a single EASE-2 grid, the mean value has been calculated and used as a reference for validation to ensure consistency and accuracy, similar to the approach used by Colliander et al., (2022) for

SMAP soil moisture validation.

#### 5.5 Result and Discussion

# 5.5.1 Multi-scale algorithm soil moisture retrieval at multiple resolutions

The multi-scale algorithm-based high-resolution soil moisture retrieval demonstrates significant potential for capturing spatial heterogeneity in soil moisture patterns across various landcover classes. While the overall patterns of soil moisture observed at both 100 [m] and 200 [m] resolutions are similar, the 100 [m] results exhibit much finer details. For example, in Figure 31, the retrieved soil moisture at 100 [m] within a desert area of the Walnut Gulch Watershed in southern Arizona shows a more detailed depiction of farms irrigated with pivot systems, capturing small to medium-sized farmlands interspersed. Soil moisture retrieval at the 100 [m] resolution over pivot farmland appears nearly circular, closely reflecting the actual shapes observed in USGS Earth imagery (Figure 31). In contrast, the 200 [m] resolution soil moisture retrievals tend to provide generalized (i.e., averaged) values, over larger areas, which do not capture such fine details. This discrepancy can lead to inaccuracies in soil moisture retrievals when agricultural farms are small and non-uniform, highlighting the importance of 100 [m] soil moisture retrievals for precise agricultural monitoring.

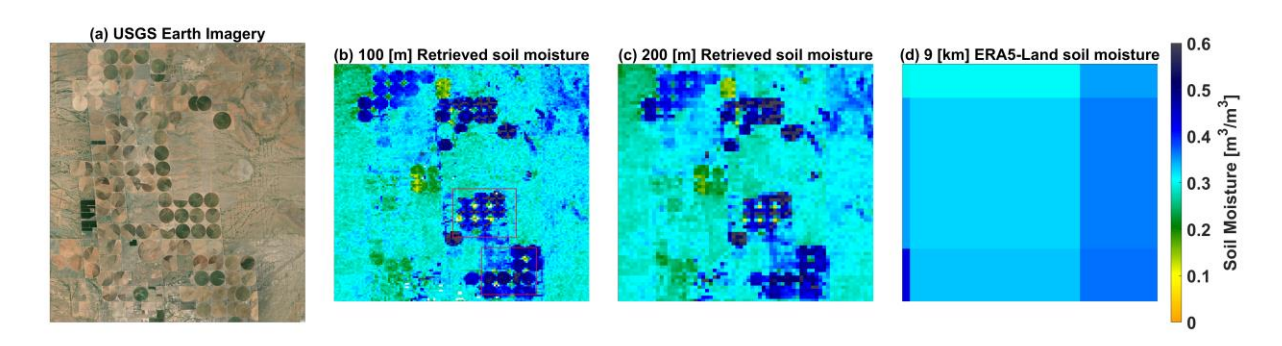


Figure 31: (a) USGS Earth imagery showing a pivot agricultural farm in the Southern Arizona desert, (b) retrieved soil moisture at 100 [m] spatial resolution, (c) retrieved soil moisture at 200 [m] spatial resolution, (d) ECMWF ERA5-Land soil moisture grid.

There are several advantages of soil moisture retrieval at 100 [m] resolutions compared to 200 [m] resolutions. For instance, in Figure 31b, the area of interest (AOI) in the southern region (indicated by a dotted box) shows low soil moisture retrievals between pivot fields. This low soil moisture corresponds to the dry barren land between four circular pivot fields (refer to Figure 31a).

Notably, this dry soil condition is better captured in the soil moisture retrievals at 100 [m] than at 200 [m]. This difference is due to the resolution effect, as one 200 [m] grid contains four 100 [m] grids. Similarly, the 100 [m] retrieval demonstrates the potential to capture the soil moisture gradient (ranging from dry to moderately wet) across pivot fields in the central part of the AOI (Figure 31a), whereas the 200 [m] retrieval shows an average wetness condition (moderate soil moisture) within the 200 [m] grid cell. Furthermore, Figure 32 shows that over farmland with a row/column structure, the 100 [m] soil moisture retrievals capture a better soil moisture gradient than the 200 [m] resolution retrievals. A significant difference observed between the soil moisture retrievals at the two resolutions in Figure 32 is that the 100 [m] retrieval helps mask grids with artifacts caused by man-made structures, effectively identified by a hybrid filter used in the multiscale algorithm. These grids remain intact in the 200 [m] retrieval due to their diminished prominence at the larger spatial scale.

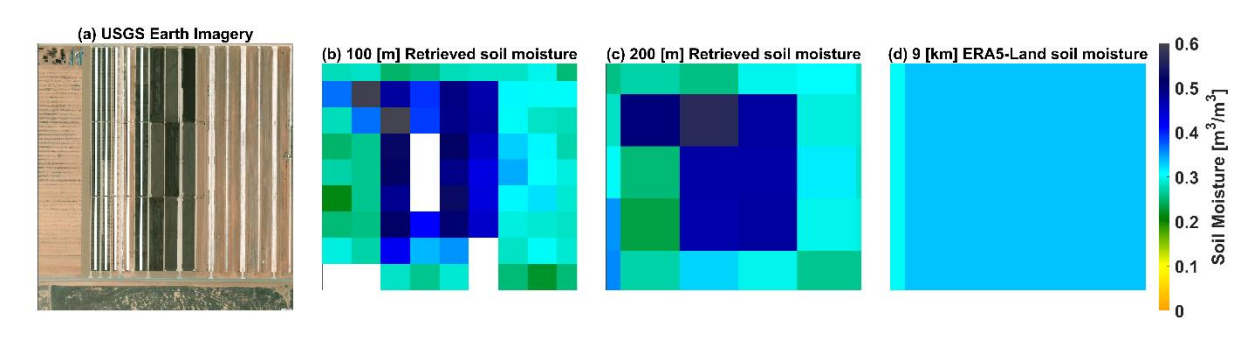


Figure 32: (a) USGS Earth imagery showing the column structured agricultural farm in Southern Arizona, USA, (b) soil moisture retrievals at resolution of 100 [m], (c) soil moisture retrievals at resolution of 200 [m], (d) corresponding ECMWF ERA5-Land soil moisture grid-cells.

These results show that the multi-scale algorithm has great potential to provide reliable soil moisture gradients at high resolutions of 100 [m], identifying small man-made structures and masking them in soil moisture retrievals. In contrast, at the 200 [m] resolution, these structures are not masked, leading to an average value of soil moisture. The results highlight the potential of high-resolution soil moisture retrievals (i.e., 200 [m] and 100 [m]) through a multi-scale algorithm, especially in agricultural applications such as crop water management (Singh and Das, 2022) and irrigation planning (Brocca et al., 2017). This potential stands in contrast to coarse-resolution soil moisture products, which fail to capture such features, as shown in the ~ 9 [km] ECMWF soil moisture product (Figure 31 and Figure 32). A very high-resolution soil moisture retrievals at 100 [m] can provide significantly more detailed information on soil moisture dynamics for these

applications, especially in small farm landscapes such as farms irrigated with pivot systems within arid environments (refer to Figure 31b), where fine-scale mapping is essential. This 100 [m] soil moisture dynamic can enable more reliable estimate of irrigation water requirement, supporting the optimization of water usage and the improvement of agricultural productivity.

However, these high-resolution soil moisture retrievals need to be validated for accuracy before being used in various applications. Therefore, several test sites were selected across various land cover classes and hydrometeorological conditions, as detailed in section 2.2.2, for validation. The multi-scale algorithm-based soil moisture retrievals at both 100 [m] and 200 [m] spatial resolutions were validated and compared against *in-situ* measurements. The spatial patterns of the soil moisture retrievals at 100 [m] resolution over the test sites for selected days with different soil wetness conditions, along with the validation statistics, are presented in the subsequent section.

# 5.5.2 Performance of Multi-Scale Algorithm at Test Sites

#### 5.5.2.1 Delta Junction

The Delta Junction site is an ideal location to demonstrate the robustness of multi-scale algorithms for high-resolution soil moisture retrieval and validation in the polar region. Its polar setting highlights the critical importance of high-resolution soil moisture data. Here, soil moisture plays a key role in permafrost dynamics, influencing thaw-freeze cycles with implications for carbon release and greenhouse gas emissions. Additionally, high-resolution soil moisture data can enhance the hydrological modeling of complex polar environments, improving our understanding of water fluxes, flood risk, and ecosystem responses to changing precipitation patterns.

Figure 33 shows the spatial pattern of the multi-scale algorithm-based soil moisture retrievals at a 100 [m] resolution across the Delta Junction for four different days from June 14, 2023, to July 26, 2023. These spatial patterns are provided at 14-day intervals, corresponding to the ALOS-2 SAR exact repeat overpass. Additionally, the daily average precipitation pattern over the Delta Junction test site is shown in Figure 33, offering a better understanding of the changes in soil wetness spatial patterns during each 14-day interval. A range of spatial patterns of soil moisture retrievals (~24 days) at 100 [m] resolution. The temporal variations in high-resolution soil moisture retrievals effectively capture characteristic events of the polar region. For example, August has peak vegetation growth, reflected in lower soil moisture due to evapotranspiration. Conversely, in April/May, glaciers and snowmelt increase soil moisture, which decreases due to plant water uptake and evapotranspiration. The changes in soil dryness and wetness closely follow

the precipitation trends, as this site received approximately 50 mm of precipitation before July 26<sup>th</sup>, resulting in high soil moisture values (Figure 33). However, despite receiving small amounts of precipitation on other selected days, a drying pattern of soil moisture has still been observed. These drying patterns can be attributed to the soil type, which consists of gravelly glacial till and outwash covered by a thin layer of loess. Typically, these soils have less water retention properties, which, together with plant-water uptake and evapotranspiration, might lead to drying soil patterns.

Spatially, the selected AOI exhibits a gradient in soil moisture. The northern riparian zone has the highest moisture content, while downstream areas also have high soil moisture (~0.40 [m³/m³]) due to the release of meltwater from the snow-covered southern mountains (masked as unsuitable for soil moisture retrieval). These high-resolution soil moisture retrievals can enable monitoring vegetation responses to variations in water availability, providing insights into potential shifts in polar plant community composition due to climate-driven changes.

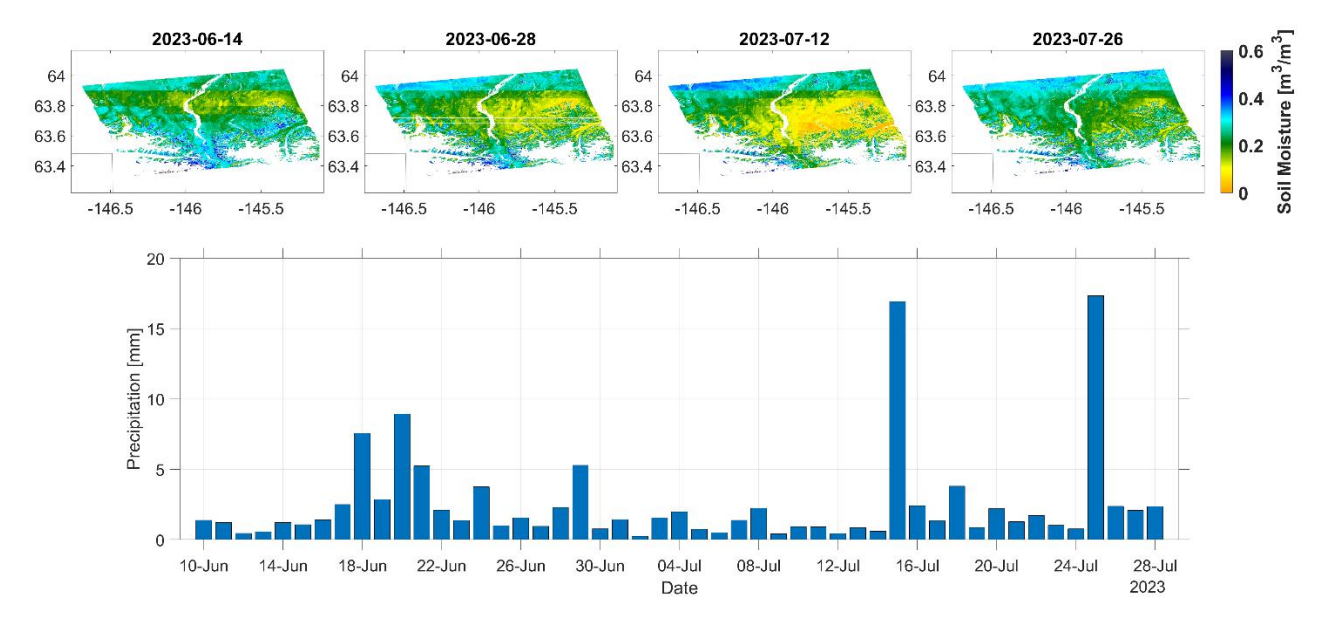


Figure 33: Spatio-temporal distribution of retrieved soil moisture (100 [m]) using a multi-scale algorithm over the Delta Junction site located in Alaska (top panel) and corresponding precipitation variability over the same period (bottom panel).

#### 5.5.2.2 Caddo-Lyndon B. Johnson National Grasslands

Soil moisture spatiotemporal variability in the CLBJ is a multifaceted phenomenon shaped by various environmental factors. Seasonal changes, driven by fluctuations in precipitation and temperature, significantly impact soil moisture content. Texas, where the CLBJ Grasslands are situated, experiences distinct wet and dry seasons, leading to dynamic shifts in soil moisture content over time.

Figure 34 shows the spatial patterns of the 100 [m] soil moisture retrievals across the CLBJ at 14-day intervals between April 30, 2023, and June 25, 2023, alongside the daily average precipitation time series for the AOI. The retrieved soil moisture closely follows the varying precipitation regimes. For instance, the period from May 1 to May 14, which had high precipitation events (approximately 70 [mm]), significantly impacted the soil moisture pattern retrieved on May 14. During this period, high soil moisture values (> 0.04 [m³/m³]) were observed in the eastern part of the AOI. Following the wet period after May 14, a drying pattern in soil moisture was observed, which can be attributed to the very low precipitation events over the selected AOI. This drying trend highlights the influence of precipitation on soil moisture dynamics. The CLBJ area, known for its high clay content, might have good water retention and drainage properties, contributing to a slower rate of soil moisture depletion. Generally, the clay soil retains moisture for a longer period, allowing a gradual decrease in soil moisture levels (i.e., a slow dry-down). In contrast, the above disused Delta Junction test site, characterized by glacier till and outwash with poor water retention properties, experiences a rapid drying pattern, with soil moisture dropping significantly in almost 14 days. However, in the case of CLBJ, due to the high clay content, the soil drying patterns are much slower, which has been efficiently captured by the multi-scale algorithm. Over a period of 28 days, the soil moisture in CLBJ decreased from 0.45 [m³/m³] to 0.30 [m³/m³]. Seasonal dynamics shows how soil moisture decreases during the months of September and October due to low or no precipitation and increasing evapotranspiration. Therefore, it enhances moisture loss from the soil and vegetation. Conversely, precipitation primarily falls from mid-April to late June and can increase the soil moisture, and those are well captured in the highresolution retrieval. Moreover, the composition of soils within the grassland sites, characterized by Udic Paleustalfs with considerable clay content, significantly impacts moisture retention and release patterns. Clay soils possess high water-holding capacity but are prone to compaction, affecting both infiltration rates and drainage. This phenomenon with precipitation dynamics (in Figure 34) has been very well captured in high-resolution soil moisture retrieval, as it shows the variability across the grids. This variability underscores the effectiveness of high-resolution soil moisture data in capturing soil moisture dynamics within the grassland ecosystem.

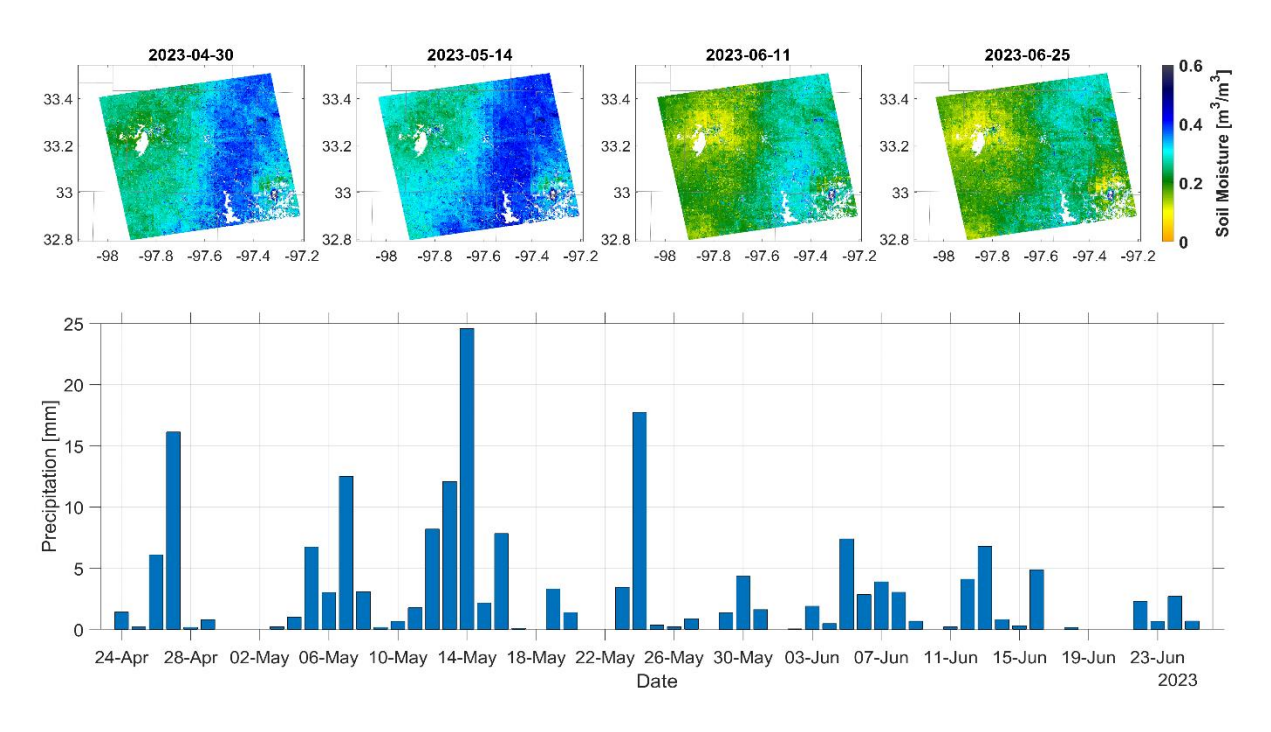


Figure 34: Spatio-temporal distribution of retrieved soil moisture (100 [m]) using a multi-scale algorithm over the Caddo-Lyndon B. Johnson National Grasslands site located in Texas (top panel) and corresponding precipitation variability over the same period (bottom panel).

## 5.5.2.3 University of Kansas Field Station

Soil moisture spatiotemporal variability near UKFS is influenced by a combination of factors reflecting the diverse landscape characteristics across the satellite swath. Encompassing a broader agricultural landscape, the transitions from pasture-dominated regions in the east to a mix of grassland and deciduous forest in the central areas. The spatial distribution of vegetation types, topography, and proximity to water bodies, such as the Lawrence River, all contribute to the observed patterns of soil moisture (Figure 35). High soil moisture values are consistently observed near the Lawrence River, which is expected given its proximity to a water source. Temporally, soil moisture dynamics exhibit distinct seasonal patterns that follow the precipitation distribution (refer to Figure 35), with high values predominantly occurring between April and July. Figure 35 exemplifies this condition, as the soil moisture pattern follows the precipitation trend. For both the 10<sup>th</sup> and 24<sup>th</sup> of June retrievals, the UKFS region received cumulative precipitation of approximately 25 [mm], with a small change in soil moisture value in retrieval. In contrast, the 8<sup>th</sup> and 22<sup>nd</sup> of July retrievals show higher soil moisture (~0.03 [m³/m³]), closely following the precipitation pattern, as the UKFS received a cumulative precipitation of ~50 mm before these retrievals. However, the change in the soil moisture pattern is not as pronounced compared to other

sites (i.e., CLBJ and Delta Junction) because the UKFS regions have residuum, till, colluvium, and local alluvium as parent materials, and the soil order is Mollisol. These soil types give the region moderate water retention capacity, which limits significant variations in drying and wetting patterns. Additionally, a two-year temporal pattern shows that soil moisture aligns closely with the seasonal precipitation pattern, as approximately 70% of the annual precipitation falls between April and September (Rahmani et al., 2014). Following this precipitation period, a drying trend is observed until October, showing the seasonal shift towards drier conditions. This seasonal variability in soil moisture is well captured in the high-resolution soil moisture retrieval using the multi-scale algorithm.

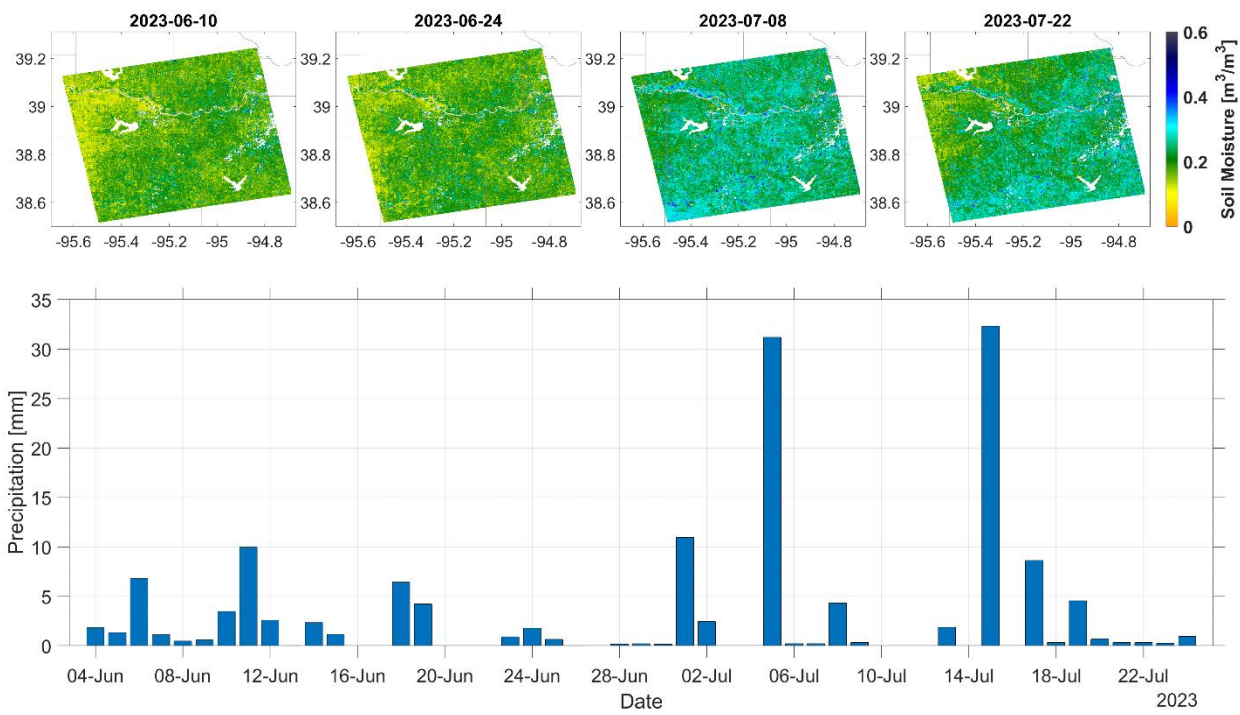


Figure 35: Spatio-temporal distribution of retrieved soil moisture (100 [m]) using a multi-scale algorithm over the University of Kansas Field Station site located in Kansas (top panel) and corresponding precipitation variability over the same period (bottom panel).

### 5.5.2.4 Little River

The spatiotemporal variability of soil moisture within the Little River watershed presents a dynamic picture influenced by various factors specific to the region. Among all the selected sites, the Little River watershed stands out for having the most available data on a temporal scale. The region selected for this site is predominantly characterized by agricultural land interspersed with patches of grassland and tree cover. The soils within the watershed are primarily sandy loam,

featuring well-drained surface layers and relatively high permeability (Bosch et al., 2006; Choi et al., 2008). This soil composition is typical for agricultural regions, particularly for crops like cotton and peanuts, which have typical growing seasons from May to October.

Figure 36 shows the spatial pattern of soil moisture retrieval at a 100 [m] resolution for selected days between July and August. The temporal variability in soil moisture closely follows the cropping and precipitation patterns within the watershed. Figure 36 exemplifies this relationship, as soil moisture values increase following high precipitation events on the day of retrieval. For instance, on 11th July, high precipitation resulted in a high value of soil moisture (~0.4 [m³/m³]) retrieval, while on 25<sup>th</sup> July, although there were high precipitation events two days prior, the soil was slightly drier due to well-drained surface/low water holding capacity. On 8<sup>th</sup> August and 22<sup>nd</sup> August, despite receiving cumulative precipitation of ~30 [mm], a drying pattern was observed due to the sandy loam soil's poor water retention capacity. This indicates that whenever there is precipitation on the day or one day before retrieval, this region has high soil moisture in the retrieval. This highlights the multi-scale algorithm's potential to capture small changes based on soil types. Furthermore, long-term features persist, such as a consistently wet area in the southeastern part (dotted box in Figure 36) of the AOI near a lake, demonstrating the algorithm's reliability at 100 [m] resolution in capturing such small features. Furthermore, our long-term analysis from high-resolution soil moisture retrieval shows that during the initial phenological stage of crops, typically around April-May, high soil moisture values are observed. This is likely due to irrigation practices applied to the fields. During the initial phenological stage of crops, typically occurring around April-May, high soil moisture values are observed, likely due to irrigation practices applied to the fields (Figure 36). Further, as the crops progress to the advanced phenological stage, particularly from September to November, soil moisture values tend to decrease. Overall, soil moisture retrieval for this site tends to indicate a relatively wetter condition (discussed in the subsequent validation section). The wet condition observed during December to March may be primarily attributed to the precipitation as region receive considerable amount of precipitation in that period (Bosch et al., 2021).

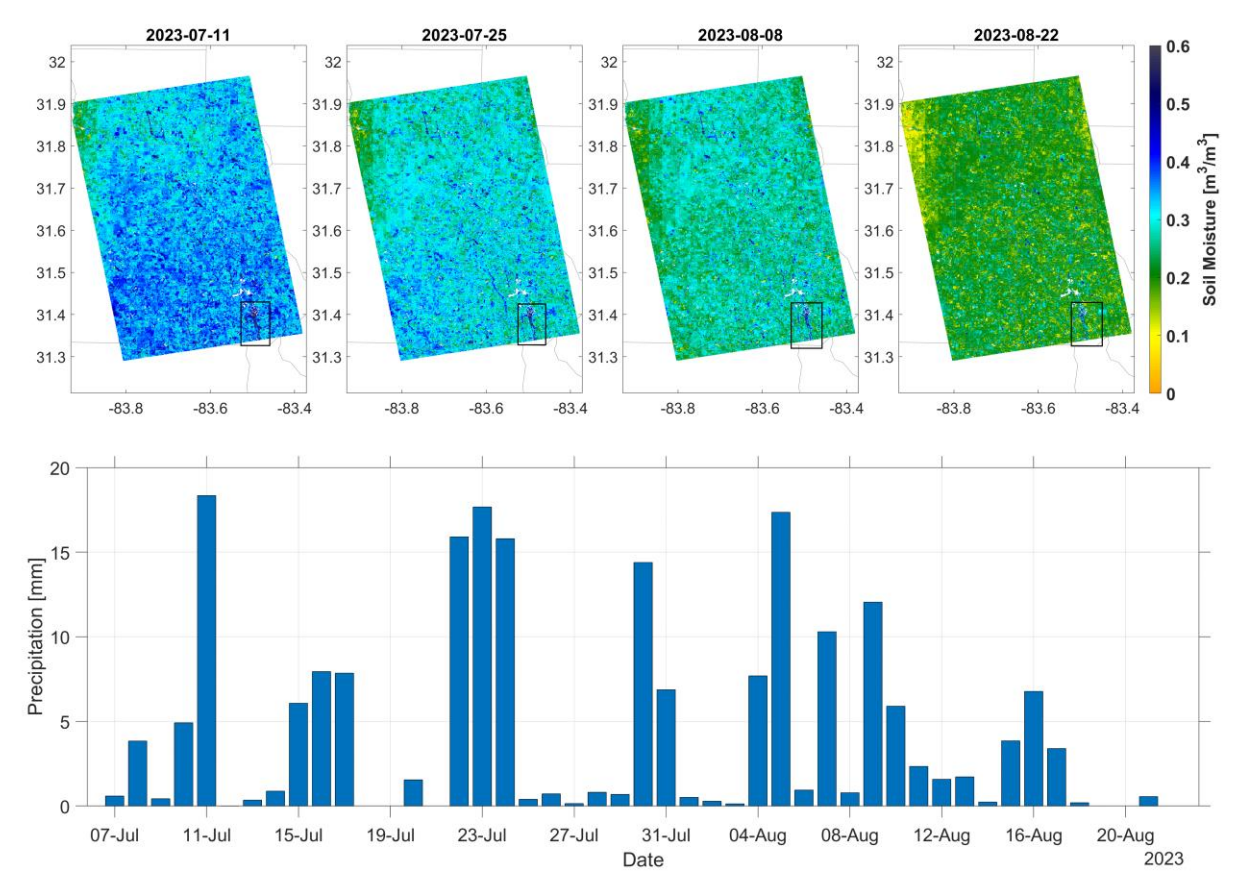


Figure 36: Spatio-temporal distribution of retrieved soil moisture (100 [m]) using a multi-scale algorithm over the Little River, Tifton site located in Georgia (top panel) and corresponding precipitation variability over the same period (bottom panel).

#### 5.5.2.5 Walnut Gulch

At the Walnut Gulch site located in the Walnut Gulch watershed, the soil type predominates as sandy, gravelly loams, contributing to the unique characteristics of the area. The sandy, gravelly loams of Walnut Gulch exhibit relatively low water-holding capacity due to their coarse texture and high permeability. These soil types have rapid drainage, reducing the likelihood of prolonged water saturation. This soil composition supports two primary vegetation: "shrub-dominated" and "grass-dominated" landscapes. These vegetation types are concentrated in the eastern portion of the AOI.

High-resolution soil moisture retrievals show a consistent drying pattern across the region following precipitation events. As shown in Figure 37, the AOI received approximately 20 [mm] of precipitation before 26<sup>th</sup> February retrieval, leading to high soil moisture values. However, subsequent precipitation was minimal, and due to the coarse texture and high permeability of the

dominant sandy, gravelly loams in this region, its impact on soil moisture wetness was negligible. This is evidenced by the decrease in soil moisture values observed in the high-resolution retrievals. This rapid drying pattern highlights the poor water holding capacity of these soils. The observed drying pattern was primarily concentrated in the northern and central parts of the AOI. In contrast, the eastern region exhibited a much slower drying pattern. This can be attributed to the dominance of grasslands in this area, and soil has better water holding capacity compared to other regions. This characteristic is effectively captured by the multi-scale soil moisture algorithm. This site shares similar properties with the Little River site, including good drainage and poor water holding capacity. This is very well captured in the retrieved soil moisture data for both locations. Notably, if the region doesn't receive precipitation, soil moisture decreases within 2-3 days. This contrasts with other sites like UKFS and CLBJ, which possess good water holding capacity (slow drying patterns), and this is also captured by the retrieved soil moisture using the multi-scale algorithm. Throughout the selected time period, soil moisture levels remain consistently dry, with values ranging from 0.05 m<sup>3</sup>/m<sup>3</sup> to a maximum of 0.3 m<sup>3</sup>/m<sup>3</sup>. The region experiences lower soil moisture variability due to prevailing dry weather patterns. Notably, the east side of the region, characterized by grasslands, exhibits comparatively higher soil moisture levels compared to the drier west and central parts (Figure 37).

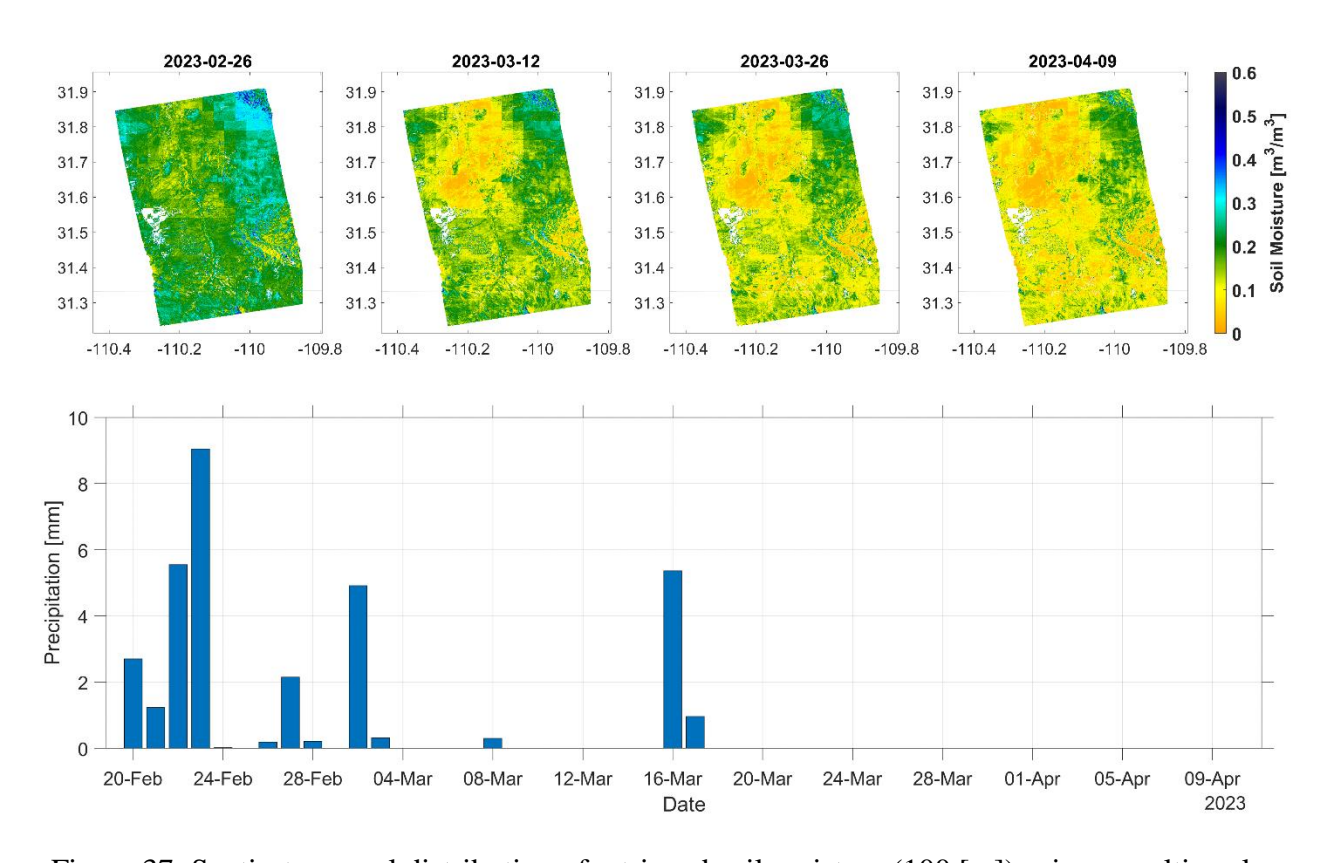


Figure 37: Spatio-temporal distribution of retrieved soil moisture (100 [m]) using a multi-scale algorithm over the region of Walnut Gulch watershed located in Southern Arizona (top panel) and corresponding precipitation variability over the same period (bottom panel).

# 5.5.3 Validation of multi-scale algorithm's soil moisture retrievals with *in-situ* measurements

The *in-situ* measurements of soil moisture for validation were collected from different test sites as discussed in Section 5.2 and shown in Figure 29. These selected test sites have been widely used to validate the various satellite soil moisture products, including SMAP mission products (Colliander et al., 2022). Figure 38 present performance metrics comparing high-resolution soil moisture retrieval against *in-situ* measurements for each site, at both 100 [m] and 200 [m] spatial resolutions. Though the ISMN *in-situ* measurements contain only one station per 200 [m] or 100 [m] grid, we have assumed a homogeneous landcover within each reference grid for comparisons at both resolutions. The validation statistics shown in Table 7 demonstrate a strong correlation between the retrieved soil moisture (at both spatial resolutions) and the *in-situ* measurements across all sites, with mostly R values ranging between 0.70 and 0.89. The negative MD values (bias) indicate a wet bias in the retrieval for most sites, potentially stemming from a similar wet bias within the ECMWF ERA5-Land soil moisture model. The relatively higher wet bias for the Little River site can also be attributed to factors such as how the ECMWF model incorporates soil

texture and other input forcings. The previous validation study indicates a ~0.14 [m<sup>3</sup>/m<sup>3</sup>] wet bias at the Little River site (Lal et al., 2022c), which carries over in the high-resolution soil moisture retrieval. Despite this, the wet bias is on the lower side in comparison to the coarser resolution soil moisture product, likely due to SAR's ability to capture heterogeneous anthropogenic practices as shown in (Figure 37). Interestingly, validation statistics demonstrate superior performance at sites with tree cover (UKFS, Delta Junction, and CLBJ). The ubRMSD for these sites are relatively lower (~0.040 [m<sup>3</sup>/m<sup>3</sup>]) except as Delta Junction, it has relatively high ubRMSD for both spatial resolutions i.e.,  $0.058 \text{ [m}^3/\text{m}^3]$  for 200 [m] and  $0.069 \text{ [m}^3/\text{m}^3]$  for 100 [m] retrieval. The high ubRMSD value may be attributed to the presence of organic soil and the region's fluctuating thawfreeze state (Bakian-Dogaheh et al., 2022). However, even with this higher ubRMSD, the 200 [m] retrievals remain within the NISAR mission accuracy goals. Further analysis of the southern Arizona sites (Walnut Gulch, Lucky Hills, and Kendall) within the Walnut Gulch watershed shows favorable validation statistics across all three locations for both 100 [m] and 200 [m] soil moisture retrievals. In Walnut Gulch, the ubRMSD values remain below 0.046 [m<sup>3</sup>/m<sup>3</sup>] (which is under the NISAR mission goal) with low bias  $<0.049 \text{ [m}^3/\text{m}^3]$  and good correlation (R  $\sim 0.75$ ). Among the three sites of southern Arizona, Walnut Gulch and Lucky Hills are relatively drier than Kendall sites, located in a semi-arid region with shrubland land cover. In contrast, the Kendall site, with grassland land cover, has comparatively higher soil moisture with dry to wet extent ( $\sim 0.4 \, [\text{m}^3/\text{m}^3]$ ). Since the contrasting shrubland and grassland land cover types represent a spectrum of soil moisture conditions (from dry to wet), the retrieved soil moisture data effectively captures the full range of moisture levels across both environments (Figure 38).

The overall validation statistics for different landcovers shows that multi-scale soil moisture algorithm performs well, achieving accuracy within the NISAR mission accuracy goal of 0.06 [m³/m³]. Additionally, the algorithm effectively captures the dry to wet range of soil moisture very well in retrieval. The high accuracy of soil moisture retrieval in forests and grasslands with high canopy density is directly related to the penetration capability of L-band SAR. This penetration allows for the capture of detailed surface heterogeneity across different land cover types, enabling accurate soil moisture retrieval at the sub-kilometer scale. However, challenges persist in certain conditions, such as the distinct cold climate with transitional frozen and unfrozen seasons found at the Delta Junction site. The presence of organic soil can complicate retrieval, leading to ubRMSD values exceeding 0.06 [m³/m³]. This also highlights the need for further

research to optimize retrieval in these challenging scenarios. Despite these complexities, the difference in validation statistics between 100 [m] and 200 [m] retrieval is minimal (± 0.005 [m³/m³]), with almost similar correlation values. This demonstrates the multi-scale soil moisture algorithm's strong performance across the selected regions. The algorithm can potentially retrieve high-resolution soil moisture at 100 [m] and 200 [m] scales, meeting NISAR mission accuracy goals. However, it should be noted that the number of sites for validating retrieved high-resolution soil moisture is limited. A comprehensive post-launch validation of NISAR-retrieved soil moisture is necessary to identify areas for more potential improvement.

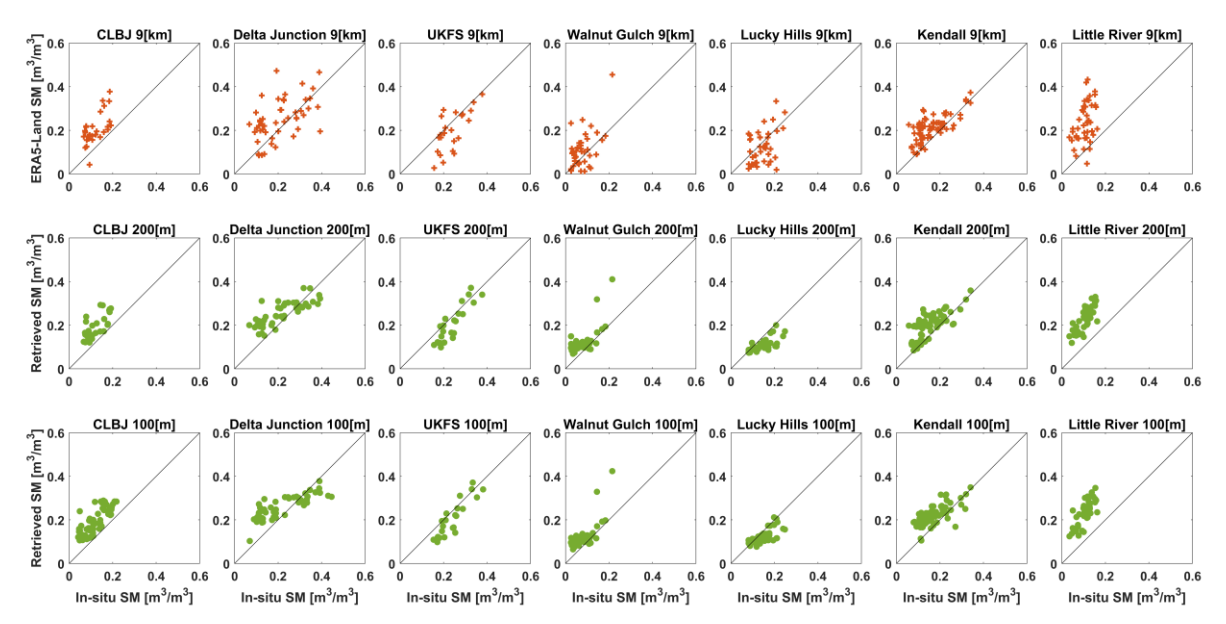


Figure 38: Scatter plots comparing input EMCWF ERA5-Land soil moisture at 9 [km] and, multi-scale algorithm-based high-resolution soil moisture retrievals at 200 [m] and 100 [m] resolutions with in-situ measurements from different test sites. The first row presents scatter plots for 9 [km] input soil moisture, second row represent 200 [m] soil moisture retrievals, and the third row presents scatter plots for 100 [m] soil moisture retrieval. The solid line represents the 1:1 line.

To accurately assess the impact of SAR data on high-resolution soil moisture retrieval, a baseline level of accuracy i.e., minimum performance has been demonstrated. This is demonstrated by comparing the high-resolution retrieval with in-situ and similarly the input ERA5-Land soil moisture with the same in-situ measurement. The validation statistics show that ERA5-Land generally has higher RMSE, ubRMSE, and more bias, as seen in sites like Delta Junction, Little River, and CLBJ, which exhibit poor correlation and elevated ubRMSD and RMSD (Fig. 11 and Table 1). However, the 200 [m] retrieval shows significant improvements, achieving accuracy

within the NISAR mission's goals. In contrast, arid sites such as Walnut Gulch, Kendall, and Lucky Hills show less improvement due to the lack of spatial heterogeneity, which leads to coarser-resolution soil moisture information being transferred to the higher resolution. Despite this, some improvements in correlation are observed, as these sites, located in shrubland areas with vegetation, capture the spatial variability well. Overall, the inclusion of SAR co-pol and cross-pol data in the multi-scale algorithm improved the correlation with MD by providing high-resolution backscatter information and spatial heterogeneity, which the algorithm effectively captures. For example, at Delta Junction, a polar site with vegetation during the selected time-period, soil moisture variations driven by glacial melt and changes in evapotranspiration. These are well captured in the high-resolution retrieval. The overall results show that high-resolution soil moisture retrievals exhibit better RMSE and ubRMSE, with reductions of 18.34% and 34.53%, respectively, and a 36% improvement in temporal correlation. However, a noticeable MD remains in both high-resolution retrievals and the input coarse-resolution soil moisture, as the wet bias from the coarse-resolution data carries over, as discussed in previous sections.

Further, it's important to acknowledge the caveat of this study, that it has been validated with limited *in-situ* measurements coinciding with the ALOS-2 SAR data. As an exception, some of the sites have single *in-situ* points in a grid for validation for both 100 [m] and 200 [m] soil moisture datasets. Sometimes, these single-point observations may be biased compared to the weighted area average and may not represent the spatial representation of soil moisture in each grid. However, the grid size is typically 100 [m] or 200 [m], and it is assumed that within each grid cell, the land cover does not change drastically. Therefore, a single *in-situ* measurement is considered sufficient to represent the soil moisture value for the entire grid cell. This contrasts with previous operational missions like SMAP, where soil moisture was retrieved at larger grid sizes ranging from 1 [km] to 9 [km] (Colliander et al., 2022; Das et al., 2019, 2018). In those cases, multiple *in-situ* observations are required for arithmetic averaging of the soil moisture measurements to match the scale of the satellite grid-cell. This is due to potential variations in land cover within the larger grid sizes. Thus, the advantage of high-resolution soil moisture retrievals lies in their ability to be validated effectively using single *in-situ* measurements.

Table 7: Performance metrics of high-resolution soil moisture retrievals for the test sites.

In-situ	ERA5-Land 9 [km] soil moisture				200 [m] soil moisture retrieval				100 [m] soil moisture retrieval			
locations	MD	RMSD	ubRMSD	R	MD	RMSD	ubRMSD	R	MD	RMSD	ubRMSD	R
	$(m^3/m^3)$	$(m^3/m^3)$	$(m^3/m^3)$		$(m^3/m^3)$	$(m^3/m^3)$	$(m^3/m^3)$		$(m^3/m^3)$	$(m^3/m^3)$	$(m^3/m^3)$	
CLBJ	-0.084	0.099	0.054	0.63	-0.070	0.080	0.039	0.710	-0.071	0.081	0.037	0.770
Delta	-0.043	0.100	0.090	0.51	-0.043	0.072	0.058	0.810	-0.036	0.078	0.069	0.810
Junction												
UKFS	0.043	0.078	0.065	0.69	0.034	0.052	0.040	0.890	0.036	0.053	0.038	0.890
Walnut	-0.044	0.067	0.049	0.54	-0.044	0.061	0.043	0.710	-0.043	0.061	0.044	0.740
Gulch												
Lucky Hills	0.036	0.056	0.058	0.45	0.035	0.047	0.032	0.730	0.024	0.038	0.030	0.710
Kendall	-0.051	0.070	0.049	0.71	-0.049	0.067	0.046	0.750	-0.054	0.069	0.043	0.720
Little River	-0.128	0.151	0.081	0.43	-0.123	0.128	0.034	0.780	-0.126	0.131	0.037	0.780

#### 5.6 Conclusion

This study expanded the validation of the multi-scale algorithm to provide soil moisture retrievals at a 200 [m] resolution for the upcoming NISAR mission. The focus was on evaluating its performance against in-situ observations across different land covers and hydroclimatic conditions. Additionally, one of the main objectives was to test the algorithm's capability as "multiscale" by retrieving even higher resolution soil moisture, i.e., 100 [m] under favorable L-band SAR observations. The soil moisture retrievals are investigated across multiple test sites with different climatic conditions and soil types, each possessing distinct physical properties. These sites' soil physical properties vary between the gravelly glacial till of Delta Junction to the clay-rich soils of CLBJ and the sandy loam of Walnut Gulch. The multi-scale algorithm found to be effectively captured finer-scale information and wetting and drying patterns induced by precipitation events. Despite the varying water retention and drainage capacities of each site, the algorithm consistently followed precipitation trends, highlighting the robustness of high-resolution soil moisture retrieval. This consistent performance across different soil types and regions underscores the algorithm's ability to provide reliable soil moisture data. Furthermore, the retrieved soil moisture was rigorously validated with coinciding in-situ measurements from five CONUS sites, representing diverse land covers (forest, shrubland, and grassland) and hydroclimatic zones (from polar to arid). The high-resolution soil moisture retrievals demonstrate that while the overall patterns observed at 100 [m] and 200 [m] are similar, the 100 [m] resolution provides finer-scale information. The validation across both resolutions and all sites indicates that the ubRMSE remains below 0.06 m<sup>3</sup>/m<sup>3</sup>, meeting the NISAR mission accuracy goal. The performance of multi-scale algorithm, even in forested regions with dense canopies, presents the robustness of the algorithm. This is because the L-band SAR frequency has higher penetration and shows sensitivity for soil moisture under forest canopy, allowing the acquisition of soil moisture information. Considering the algorithm's ability to meet the accuracy goals in challenging environments, the expectation is that the NISAR mission goal can be achieved across a wide range of environments and land covers. Post-launch, with anticipated improvements in the algorithm parameter-associated uncertainty, the multi-scale soil moisture algorithm has the potential to retrieve high-resolution soil moisture with even better performance. The retrieval quality demonstrated in this study makes the retrieval of highresolution soil moisture using multi-scale algorithm very useful for monitoring and managing hydrological processes in diverse landscapes. This high-resolution soil moisture can be beneficial

for multiple geophysical applications. For instance, fine-scale soil moisture information can improve flood forecasting accuracy by providing insights into moisture conditions at the watershed level. Similarly, it aids in ecological studies by elucidating soil moisture dynamics in heterogeneous landscapes, informing habitat suitability assessments and biodiversity conservation efforts. Furthermore, high-resolution soil moisture data serve as valuable inputs for validating and refining hydrological and climatic models, enhancing our understanding of water cycle dynamics and their implications for regional and global water resources management.

# CHAPTER 6: UNCERTAINTY ESTIMATES IN THE NISAR HIGH-RESOLUTION SOIL MOISTURE RETRIEVALS FROM MULTI-SCALE ALGORITHM

This chapter was published as Preet Lal, Gurjeet Singh, Narendra N. Das, Dara Entekhabi, Rowena B. Lohman, Andreas Colliander, "Uncertainty estimates in the NISAR high-resolution soil moisture retrievals from multi-scale algorithm", Remote Sensing of Environment, Volume 311, 2024, 114288, DOI:10.1016/j.rse.2024.114288. © 2024 Elsevier Inc.

The previous two chapters discussed high-resolution soil moisture retrieval and its validation with *in-situ* measurements. This validation provides a reliable estimate of the error and uncertainty in soil moisture retrievals. However, *in-situ* measurements are available only at limited locations, as they are typically tedious and expensive to obtain. Therefore, an approach is needed to estimate uncertainty for each grid of soil moisture retrievals. Moreover, NASA mandates that gridded uncertainty be provided for all derived products. To address this, the primary objective of this chapter is the estimation of uncertainty in high-resolution soil moisture retrievals from SAR observations.

#### **6.1 Introduction**

The NASA-ISRO Synthetic Aperture Radar (NISAR) mission is a joint space mission between the National Aeronautics and Space Administration (NASA) and the Indian Space Research Organization (ISRO), scheduled to launch in February 2025. NISAR will be the first satellite mission to carry Synthetic Aperture Radar (SAR) sensors at two different microwave frequencies, at L-band (1.25 GHz) and S-band (3.20 GHz), to measure changes in our planet's surface ranging from ecosystem disturbances and dynamics to behavior of the solid earth and cryosphere. To achieve this the NISAR mission is designed for fine spatial resolution measurements (~10 [m] range resolution and ~8 [m] azimuth resolution) with a temporal resolution of 12 days (6 days when ascending and descending passes are combined) (Kellogg et al., 2020). NISAR will enable numerous key applications, including high-resolution soil moisture retrieval.

High-resolution soil moisture products like those that will be available from NISAR can be utilized in various hydrological and agricultural applications. In past studies, through multiple methods/approaches have been used to retrieve high-resolution soil moisture from SAR observations, including model-based polarimetric decomposition (Han et al., 2020), empirical and semi-empirical models (Hoskera et al., 2020), time-series approach (Zhu et al., 2022), active-passive approach (Das et al., 2019, 2016, 2014, 2011) and data-driven physical models coupled

with machine learning and artificial intelligence approaches (Skulovich and Gentine, 2023). However, each of these algorithms requires multiple ancillary datasets and these datasets has some extent of errors, thus introducing additional error and uncertainty in soil moisture retrievals. In the context of operational high-resolution soil moisture products, there are several limitations and advantages of different soil moisture algorithms and the limited availability of ancillary datasets at high resolution. To address operational limitations and reduce error and uncertainty in high-resolution soil moisture products, we proposed a multi-scale algorithm for a global, operational soil moisture product at ~ 200 [m] resolution under the NISAR mission (discussed in chapter 5). The major goal of the multi-scale algorithm is to remove dependencies on any complex modelling/steps and reduce the degrees of freedom (reducing the dependency on multiple ancillary data needs of vegetation and soil parameters) while retrieving high-resolution soil moisture to achieve optimal accuracy and low uncertainty.

The NISAR multi-scale algorithm blends a coarse-resolution soil moisture product (either from reanalysis datasets or radiometer-derived product) with the NISAR fine resolution L-band SAR co-pol (HH) and cross-pol (HV) backscatter measurements. The current NISAR mission plan is to use a 6-hourly or 1-hourly soil moisture dataset (Muñoz-Sabater et al., 2021) of the European Centre for Medium-Range Weather Forecast (ECMWF) as the coarse resolution (~9 [km]) soil moisture input in the multi-scale algorithm. The use of ECMWF's operational dataset in the NISAR multi-scale algorithm will enable the selection of the soil moisture data from ECMWF at the closest time with respect to satellite overpass. This might help in minimizing potential errors/uncertainties in soil moisture retrievals due to temporal mismatch of the coarse-resolution soil moisture input and SAR backscatter measurements (Lal et al., 2022c). However, other sources of uncertainty in the high-resolution soil moisture retrievals include errors in the input datasets (e.g., coarse-resolution soil moisture and SAR instrument errors) and algorithm parameters. The multi-scale soil moisture algorithm has two parameters namely  $\beta$  and  $\Gamma$ . The algorithm parameter  $\beta$  is sensitive parameter which indicates the soil moisture change to the co-pol backscatter observations (Leroux et al., 2016). Whereas the algorithm parameter  $\Gamma$  represent the heterogeneity in the grid cell and it change with time as soil condition and vegetation condition change (Das et al., 2014). The errors in the multi-scale algorithm parameters  $\beta$  and  $\Gamma$  arise due to surface/vegetation conditions, soil texture and landscape heterogeneity. The detail about the algorithm parameter  $\beta$  and  $\Gamma$  and contribution in the error sources has been discussed in the

subsequent section.

In the past, SAR-based high-resolution soil moisture products (1 km and 3 km) have shown great potential in various hydrological and agricultural applications such as flood forecasting (Komma et al., 2008; Massari et al., 2018), weather forecast modelling (Taylor et al., 2012), crop water demand and irrigation mapping (Jin et al., 2022; Singh and Das, 2022). It is expected that the NISAR multi-scale algorithm based on 200 [m] resolution soil moisture products will be very useful for applications that need a very high-resolution soil moisture (<1 [km]) dataset. However, these geophysical applications are effective only when good-quality soil moisture products with known estimates of uncertainty are used. Thus, there is a need to quantify uncertainty in highresolution soil moisture retrievals for their effective utilization in various geophysical applications. Traditionally, validation statistics (e.g., ubRMSE) computed using in-situ soil moisture measurements at a few calibration/validation sites are used to express the error/uncertainty in soil moisture retrievals. However, these statistics are limited to specific locations/land cover and do not represent the uncertainties across the entire space and time of relevant land surfaces where soil moisture is retrieved. Therefore, many studies have used the comparison of retrieved soil moisture data with the well-validated products such as ERA5, GLDAS and ESA-CCI soil moisture product (Escorihuela et al., 2018; Holgate et al., 2016; Kim et al., 2015) as a current standard practice. If reference data on similar resolution is not available, the retrieved soil moisture can be upscaled to match the resolution of the reference data, and validation statistics can be calculated accordingly (Gruber et al., 2019). This comparison, while useful for spatial validation, cannot calculate temporal error/uncertainty. Further if a similar resolution reference data is not available, the dataset needs to be aggregated/upscaled for error calculation, precluding the estimation of error/uncertainty for individual high-resolution grids. Thus, we require an approach to estimate uncertainty for each valid pixel/grid of retrievals to better describe the quality of soil moisture, especially for the upcoming NISAR mission's high-resolution soil moisture product, which is expected to be used for various geophysical applications. One of the classical ways to estimate soil moisture uncertainties is to propagate known sources of uncertainty through the Monte-Carlo approach (Gruber et al., 2019). Das et al., (2016) demonstrated that this approach does provide an estimate of uncertainties in soil moisture retrievals. However, this method is very computationally expensive, and therefore, not feasible to implement for the operational high-resolution NISAR soil moisture product with its large number of grid-cells globally (i.e., 73080 × 173520 grids). Hence,

a time-efficient and reliable method is required to estimate uncertainty in the operational NISAR soil moisture product.

Keeping a view of the above-mentioned facts, the major aim of this chapter is to develop a reliable and operationally feasible approach for quantitative estimation of the uncertainty in soil moisture retrievals. In this chapter, an approach has been developed to quantify uncertainty in NISAR operational soil moisture products that vary in space and time for each 200 [m] grid cell. The approach for uncertainty estimation in high-resolution soil moisture retrievals through the NISAR multi-scale algorithm presented here has a legacy from Das et al., (2016) analytical approach for uncertainty estimation in brightness temperature disaggregation using the SMAP active-passive algorithm. In this chapter, a detailed sensitivity analysis over NISAR multi-scale algorithm parameters and input datasets was carried out using an analytical approach for uncertainty analysis in high-resolution soil moisture retrievals. Further, the implementation of an analytical approach for the NISAR mission is also demonstrated on available L-band UAVSAR data from the SMAPVEX-12 campaign. Finally, the uncertainty estimates were compared with the validation statistics (i.e., ubRMSE) of soil moisture retrievals derived using *in-situ* measurements.

## 6.2 Summary of NISAR multi-scale soil moisture algorithm and its uncertainties

The NISAR multi-scale soil moisture retrieval algorithm proposed in previous chapters disaggregates the coarse resolution (~9 [km]) ECMWF ERA5-Land reanalysis soil moisture product with the help of fine resolution (~10 [m]) L-band SAR backscatter observation representing the spatial pattern of landscape characteristics within the coarse resolution grid cell. The proposed algorithm was tested using a version of the UAVSAR L-band data time-series that had been simulated to closely match the expected characteristics of NISAR (e.g., spatial resolution, noise). The spatial pattern of SAR depends on the spatial pattern of cross-sectional sensitivity to soil moisture variability and density of vegetation cover. The algorithm parameters ( $\beta$  and  $\Gamma$ ) derived at the coarse resolution grid-cell scale and implemented in the algorithm to retrieve high-resolution soil moisture. The  $\beta$  parameter was determined by establishing a linear temporal relationship between the 9 [km] soil moisture dataset and upscaled SAR measurements at 9 [km] resolution using data observations acquired over an 84-day period (from 13 April to 7 July 2015). The  $\Gamma$  parameter was estimated for any specific overpass through a linear regression using high-resolution SAR measurements. The NISAR multi-scale soil moisture algorithm can be described as:

$$SM(F_n,t) = SM(C,t) + \beta(C) * \{ [\sigma_{HH}(F_n,t) - \sigma_{HH}(C,t)] + \Gamma \cdot [\sigma_{HV}(C,t) - \sigma_{HV}(F_n,t)] \}$$

$$(8)$$

where  $SM(F_n,t)$  is the target fine/high-resolution  $(F_n)$  soil moisture product at 200 m, and SM(C,t) is the input coarse resolution (C) soil moisture product of ECMWF at ~9 [km].  $\beta(C)$  is an algorithm parameter at coarse resolution grid cell. The term  $\sigma_{HH}(F_n,t)$  and  $\sigma_{HV}(F_n,t)$  are high-resolution (~200 [m]) co-pol and cross-pol backscatter datasets, respectively, derived using fine-scale (~ 10 [m]) L-band SAR measurements. The term  $\sigma_{HH}(C,t)$  and  $\sigma_{HV}(C,t)$  are the upscaled backscatter dataset at 9 [km] by averaging  $\sigma_{HH}(F_n,t)$  and  $\sigma_{HV}(F_n,t)$  within C resolution grid-cell. The algorithm parameter  $\Gamma$  is estimated through a linear regression between the F resolution (200 [m]) co-pol  $(\sigma_{HH})$  and cross-pol  $(\sigma_{HV})$  backscatter within each C resolution grid-cell  $\Gamma \equiv \left[\frac{\partial \sigma_{HH}(F_n)}{\partial \sigma_{HV}(F_n)}\right]_C$ . The  $\Gamma$  parameter of each grid-cell and specific overpass represents the spatial heterogeneity effects due to variability in vegetation and surface conditions within C resolution.

The multi-scale soil moisture algorithm in Eq. 8 relies directly on the ECMWF model, which might contain errors of its own. The SAR input data used in Eq. 8 might also have error/uncertainty due to the radar instrument noise. In addition, uncertainty also arises in the estimation of algorithm parameters  $\beta(C)$  and  $\Gamma(C)$ , which play a key role in high-resolution soil moisture retrievals. For example, during  $\beta(C)$  estimation, the need for a linear regression between soil moisture and SAR co-pol backscatter may introduce errors when there are too few SAR overpasses, or when a suboptimal temporal window size in establishing linear regression coefficient for  $\beta$  parameter. Similarly, low variability in soil moisture during the time period used to estimate the  $\beta$  parameter could result in higher levels of uncertainty. During estimation of  $\Gamma$ , the ideal condition is to have a total of 2025 (45×45 grid) SAR grid-cells of 200 [m] within C resolution (~ 9 [km]) to establish a linear regression. However, in some cases, many SAR grid cells get masked out because of land cover classes which are not useful for soil moisture retrieval such as urban, snow/ice and water body. These results in fewer data points for the regression and adding a larger uncertainty in  $\Gamma$  estimation. Finally, the presence of diverse land cover conditions at the coarse spatial scale of estimation introduces heterogeneity, further adding to the overall uncertainty in estimating  $\beta$  and  $\Gamma$ .

To quantify uncertainty in high-resolution soil moisture retrievals  $SM(F_n, t)$  that arises due to input datasets and algorithm parameters, an analytical solution/approach is proposed in this

study. The purpose of developing an analytical solution is to facilitate a computationally inexpensive approach to estimate uncertainty in soil moisture retrievals that vary in space and time in operational NISAR multi-scale algorithm-based soil moisture products.

#### 6.3 Analytical approach for uncertainty estimation in high-resolution soil moisture

Uncertainty estimation is a critical part of any algorithm development process. We propose an approach to estimate total uncertainty in  $SM(F_n,t)$  of NISAR soil moisture multi-scale algorithm (Eq. 9). The total uncertainty in  $SM(F_n,t)$  is divided into two parts: i) errors in the input datasets such as SM(C,t),  $\sigma_{HH}(F_n)$ , and  $\sigma_{HV}(F_n)$ , and ii) errors in the algorithm parameters  $\beta$  and  $\Gamma$ . The details of formulation that quantifies the total uncertainty in  $SM(F_n,t)$  is presented in the following sub-sections.

## 6.3.1 Uncertainty due to input datasets

Expanding Eq. 9, we get:

$$SM(F_n, t) = SM(C, t) + \beta(C) * \sigma_{HH}(F_n, t) - \beta(C) * \sigma_{HH}(C, t) + \beta(C) * \Gamma *$$

$$\sigma_{HV}(C, t) - \beta(C) * \Gamma * \sigma_{HV}(F_n, t)$$
(9)

To estimate uncertainty in  $SM(F_n, t)$  due to input datasets, we take the variance of the NISAR multi-scale algorithm (Eq. 9), keeping all parameters constant except for the NISAR observations and input coarse resolution soil moisture, allowing them to have statistically independent errors.

$$var[SM(F_n,t)] = var[SM(C,t)] + var[\beta(C) * \sigma_{HH}(F_n,t)] + var[-\beta(C) * \sigma_{HH}(C,t) + var[\beta(C) * \Gamma * \sigma_{HV}(C,t)] + var[-\beta(C) * \Gamma * \sigma_{HV}(F_n,t)]$$

$$var[SM(F_n,t)] = var[SM(C,t)] + \beta(C)^2 var[\sigma_{HH}(F_n,t)] +$$

$$(10)$$

$$(-1)^{2}\beta(C)^{2}var[\sigma_{HH}(C,t)] + \beta(C)^{2}\Gamma^{2}var[\sigma_{HV}(C,t)] + (-1)^{2}\beta(C)^{2}\Gamma^{2}var[\sigma_{HV}(F_{n},t)]$$
(11)
$$var[SM(F_{n},t)] = \beta(C)^{2}\{var[SM(C,t)] + var[\sigma_{HH}(F_{n},t)] + var[\sigma_{HH}(C,t)] + v$$

$$\Gamma^{2}var[\sigma_{HV}(C,t)] + \Gamma^{2}var[\sigma_{HV}(F_{n},t)]$$
(12)

$$var[SM(F_n,t)] = \beta(C)^2 \{var[SM(C,t)] + var[\sigma_{HH}(F_n,t)] + var[\sigma_{HH}(C,t)] + var[\sigma_{$$

$$\Gamma^{2}(var[\sigma_{HV}(C,t)] + var[\sigma_{HV}(F_{n},t)])\}$$
(13)

$$var[SM(F_n,t)] = var[SM(C,t)] + \beta(C)^2 \{var[\sigma_{HH}(F_n,t)] + var[\sigma_{HH}(C,t)] + \Gamma^2(var[\sigma_{HV}(C,t)] + var[\sigma_{HV}(F_n,t)])\}$$

$$(14)$$

Since  $\sigma_{HH}(C)$  and  $\sigma_{HV}(C)$  can be expressed as an average of high-resolution values within C resolution grid-cell  $<\sigma_{HH}(F_n)>$ , and  $<\sigma_{HV}(F_n)>$ , respectively, Eq. 14 gives:

$$var[SM(F_n,t)] = var[SM(C,t)] + \beta(C)^2 \{var[\sigma_{HH}(F_n,t)] + var[\langle \sigma_{HH}(F_n) \rangle] + \Gamma^2(var[\langle \sigma_{HV}(F_n) \rangle] + var[\sigma_{HV}(F_n)])\}$$

$$(15)$$

With the statistical assumption that the variance of an average value approaches zero as the number of measurements becomes large (Casella and Berger, 2002; Hogg et al., 2019), we simplified Eq. 15 further by substituting  $var[<\sigma_{HH}(F_n)>]=0$  and  $var[<\sigma_{HV}(F_n)>]=0$ .

$$var[SM(F_n, t)] = var[SM(C, t)] + \beta(C)^2 \{var[\sigma_{HH}(F_n, t)] + \Gamma^2(var[\sigma_{HV}(F_n)])\}$$
(16)

Since  $\sigma_{HH}$  is in dB unit in Eq. 16, we substituted it in a linear unit as 10log10 (1 +  $\omega KpC$ ), where KpC is the speckle noise and  $\omega$  is Gaussian noise with zero mean and a standard deviation of 1. For the sake of notational simplicity  $\sigma_{HH}(F_n)$ ,  $\sigma_{HV}(F_n)$ , and  $\beta(C)$  were expressed hereafter as  $\sigma_{HH}$ ,  $\sigma_{HV}$ , and  $\beta$ , respectively, and substituted in Eq. 10, which can then be written as:

$$var[SM(F_n)] = var[SM(C)] + \beta^2 \begin{cases} var[10log10(\sigma_{HH} * (1 + \omega KpC_{HH}))] \\ + \Gamma^2 var[10log10(\sigma_{HV} * (1 + \omega KpC_{HV}))] \end{cases}$$
(17)

Further, a relationship  $var[log(\sigma_{HH} * (\omega KpC_{HH}))] = (10/ln10)^2 KpC_{HH}^2)$ , where ln is natural log (derivation of the relationship is given in Appendix), was used for simplifying Eq. 17, which results in:

$$var[SM(F_n)] = var[SM(C)] + \beta^2 * \begin{cases} (10/ln10)^2 KpC_{HH}^2 + \\ \Gamma^2 * (10/ln10)^2 * KpC_{HV}^2 \end{cases}$$
(18)

and

$$var[SM(F_n)]_{input} = var[SM(C)] + \beta^2 * (10/ln10)^2 \{ KpC_{HH}^2 + \Gamma^2 * KpC_{HV}^2 \}$$
 (19)

Eq. 19 describes the variance/uncertainty in high-resolution soil moisture retrievals  $SM(F_n)$  due to errors in the input dataset.

#### **6.3.2** Uncertainty due to algorithm parameters

The NISAR multi-scale soil moisture algorithm parameters  $\beta$  and  $\Gamma$  are influenced by variations in surface/vegetation characteristics and heterogeneity across different land covers. The uncertainties in the estimation of algorithm parameters ( $\beta$  and  $\Gamma$ ) might arise due to two basic sources: i) errors in the input coarse resolution soil moisture, SM(C), and speckle noise in  $\sigma_{HH}$  and  $\sigma_{HV}$  measurements, and ii) errors in the linear regression for each term due to the finite number of data points. The mathematical equations and notations are as follows:

$$SM(F_n) = SM(C) + \beta \{\delta_{HH} + \delta_{HV} * \Gamma\}$$
(20)

where 
$$\delta_{HH}=[\sigma_{HH}(F_n)-<\sigma_{HH}(F_n)>]$$
 and  $\delta_{HV}=[\sigma_{HV}(F_n)-<\sigma_{HV}(F_n)>]$  are the

deviation of SAR observations in each F resolution grid-cell of 200 [m],  $\sigma_{HH}(F_n)$  and  $\sigma_{HV}(F_n)$ , from their average value within the C resolution grid-cell of 9 [km],  $<\sigma_{HH}(F_n)>$  and  $<\sigma_{HV}(F_n)>$ , respectively. Expanding the parameters as mean values (i.e.,  $\underline{\beta}$ ) and independent perturbations (i.e.,  $\beta'$ ) result in:

$$SM(F_n) = SM(C) + \left(\underline{\beta} + \beta'\right) \left\{ \delta_{HH} + \delta_{HV} \left(\underline{\Gamma} + \Gamma''\right) \right\}$$
 (21)

Rearranging the terms in Eq. 21 gives:

$$SM(F_n) = SM(C) + \underline{\beta}\delta_{HH} + \underline{\beta}\underline{\Gamma}\delta_{HV} + \underline{\beta}\Gamma'\delta_{HV} + \beta'\delta_{HH} + \beta'\underline{\Gamma}\delta_{HV} + \beta'\Gamma'\delta_{HV}$$
 (22)

Taking the variance of Eq. 22 results in:

$$var[SM(F_n)] = var[SM(C)] + var\left[\underline{\beta}\,\delta_{HH}\right] + var\left[\underline{\beta}\,\underline{\Gamma}\delta_{HV}\right] + var\left[\underline{\beta}\,\Gamma'\delta_{HV}\right] + var\left[\beta'\,\delta_{HV}\right] + var\left[\beta'\,\underline{\Gamma}\,\delta_{HV}\right] + var\left[\beta'\,\Gamma'\delta_{HV}\right]$$
(23)

The constant terms in Eq. 23 have null variance, i.e.,  $var[SM(C)] \approx 0$ ,  $var\left[\underline{\beta}\delta_{HH}\right] \approx 0$ , and  $var\left[\underline{\beta}\underline{\Gamma}\delta_{HV}\right] \approx 0$ . Because the perturbation terms  $\beta'$  and  $\Gamma'$  are independent, the  $var[\beta'\Gamma'\delta_{HV}]$  term in Eq. 23 has an expectation of zero. Based on these conditions, Eq. 23 can be expressed as:

$$var[SM(F_n)] = var \left[\beta \Gamma' \delta_{HV}\right] + var[\beta' \delta_{HH}] + var[\beta' \underline{\Gamma} \delta_{HV}]$$
 (24)

or

$$var[SM(F_n)] = \underline{\beta}^2 \delta_{HV}^2 var[\Gamma'] + \delta_{HH}^2 var[\beta'] + \underline{\Gamma}^2 \delta_{HV}^2 var[\beta']$$
 (25)

Eq. 24 can be rearranged further as:

$$var[SM(F_n)]_{param} = \delta_{HH}^2 var[\beta'] + \delta_{HV}^2 \left\{ \beta^2 var[\Gamma'] + \underline{\Gamma}^2 var[\beta'] \right\}$$
 (26)

Eq. 26 captures the expected variance contribution due to uncertainties in parameters  $\beta$  and  $\Gamma$ . The term  $\beta'$  and  $\Gamma'$  can be calculated individually as they are obtained from regression coefficients. Errors in  $\beta$  depend on characteristics of the time series of SM(C) and  $\sigma_{HH}(C)$ , and the errors in  $\Gamma$  depend on the spatial variability of  $\sigma_{HH}(F_n)$  and  $\sigma_{HV}(F_n)$ . The linear regression coefficient model for  $var[\beta']$  and  $var[\Gamma']$  is described in Appendix.

Finally, the total uncertainty in high-resolution soil moisture retrievals,  $SM(F_n)$ , is obtained by combining Eq. 19 and Eq. 26 as:

$$Std[SM(F_n)]_{total} = sqrt(var[SM(F_n)]_{input} + var[SM(F_n)]_{param})$$
(27)

#### 6.4 Data Used

The UAVSAR datasets used for implementing the uncertainty equation collected during the SMAPVEX-12 field campaign at the Carman, Manitoba, Canada site. This campaign data has been considered to test the analytical approach because it's assumed that if validation statistics meet accuracy goals over agriculture land, it can also meet accuracy goals over other land covers. Additionally, this campaign provides a valuable time series dataset coinciding with in-situ measurements. This presents a significant advantage over other L-band data sources like ALOS-2, which lack the same temporal frequency and co-inciding in-situ measurements. During the campaign, UAVSAR acquired quad polarized L-band (1.26 GHz) datasets with a spatial resolution of 1.66 [m] in range resolution and 0.8 [m] in azimuth resolution with single look complex (SLC) mode (McNairn et al., 2015). The L-band UAVSAR data has been simulated to closely match the characteristics of NISAR data such as ~10 [m] spatial resolution in ground range detected (GRD) mode, ~40 dB of noise-equivalent sigma zero (NESZ) and using backscatter value with incidence angle ranging between 30° to 50°. To accurately simulate the characteristics expected from NISAR data, multiplicative noise following a Gamma distribution was applied to the UAVSAR data. This type of noise mimics the speckle effect inherent in SAR images, where noise intensity scales with the signal strength. Using the Gamma distribution allows for control over the speckle severity, helping to match UAVSAR data to the anticipated speckle patterns of NISAR.

In addition to the UAVSAR L-band data acquisition, various other measurements were carried out such as soil moisture, vegetation attributes and soil attributes for each selected field. The *in-situ* soil moisture measurements were measured at multiple sampling points for each field, with three replicate measurements at each sample points. The detail about the field campaign and soil moisture measurement, crop type and attribute, and soil datasets of SMAPVEX12 is available at <a href="https://smapvex12.espaceweb.usherbrooke.ca/">https://smapvex12.espaceweb.usherbrooke.ca/</a>. Further, this study does not directly use ECMWF ERA5-Land data as an input in the uncertainty equation. This is already incorporated during the soil moisture retrieval process using the multi-scale algorithm. Instead, the uncertainty equations rely on error values established in the previous validation studies by Muñoz-Sabater et al., (2021).

## 6.5 Methodology

The impact of individual sources of error in soil moisture retrievals of the NISAR multiscale algorithm has been analyzed by performing a sensitivity analysis using the proposed solution, as discussed in Section 6.3. Firstly, a detailed sensitivity analysis of input datasets such as SM(C), high-resolution  $\sigma_{HH}$  and  $\sigma_{HV}$ , and algorithm parameters were carried out using Eq. 19, 26, and 27 to quantify the total uncertainty in  $SM(F_n)$ . In addition, we also demonstrated the feasibility of this implementation of an analytical solution for estimating total uncertainty (Eq. 27) in  $SM(F_n)$  and compared the uncertainty estimates with the *in-situ* measurements-based error/validation statistics of soil moisture retrievals to test performance.

## 6.6 Implementation of the analytical approach

The proposed solution for uncertainty estimation in  $SM(F_n)$  has been implemented and coded in the science software of the NISAR multi-scale soil moisture algorithm. This implementation provides the uncertainty in the NISAR high-resolution soil moisture product of the multi-scale algorithm for each valid grid-cell of ~200 [m] over land. As discussed above, the parameters and datasets required in Eqs. 19, 26, and 27 primarily come from the inputs to the multi-scale algorithm or are constants (e.g.,  $KpC_{HH}^2$  and  $KpC_{HV}^2$ ). The input of var[SM(C)] can be generated from a lookup table (LUT) based either on longitudinal/latitudinal zone or LULC type or a combination of both. As an initial guess for the pre-launch phase, we used var[SM(C)] = 0.04 [m³/m³] (ubRMSE value of ~0.04 [m³/m³] for cropland, shrubland and grassland). However, these values will be adjusted for different land cover classes during the post-launch algorithm cal/val activities. The uncertainty in the NISAR high-resolution soil moisture retrieval as calculated here will be specifically used for quality control and flagging of grid cells that exceed the NISAR mission accuracy goal of 0.06 [m³/m³]. The flowchart in Figure 39 illustrates our approach for estimating the uncertainty of the operational NISAR soil moisture product for the multi-scale algorithm.

In this study, we demonstrated the implementation of the proposed approach with a version of the UAVSAR L-band data time series that had been simulated to closely match the expected characteristics of the NISAR. In this study, we used  $\sigma_{HH}$  and  $\sigma_{HV}$  backscatter from UAVSAR L-band data, to calculate the uncertainty in the retrieved soil moisture. The GRD SAR data from UAVSAR data is processed with the following steps, radiometric calibration, and terrain correction (with Copernicus 30 [m] DEM). SAR data usually contain some systemic and random noise, encapsulated as speckle noise. To mitigate the effects of speckle noise, with urban and artificial structures on backscatter observations, a spatial hybrid filter is applied. During the soil moisture retrieval process using the multi-scale algorithm, LULC data is used to mask land cover

types that are not relevant to the retrieval, such as water bodies, snow/ice, and urban areas. Following filtering and masking, the calibrated GRD SAR backscatter observations are aggregated to 200 [m] resolutions, and used for the uncertainty estimation. Finally, a comparison was carried out between soil moisture uncertainty estimates based on the proposed approach and the error/validation statistics (i.e., ubRMSE) of soil moisture retrievals derived using *in-situ* measurements of the SMAPVEX-12 experiment.

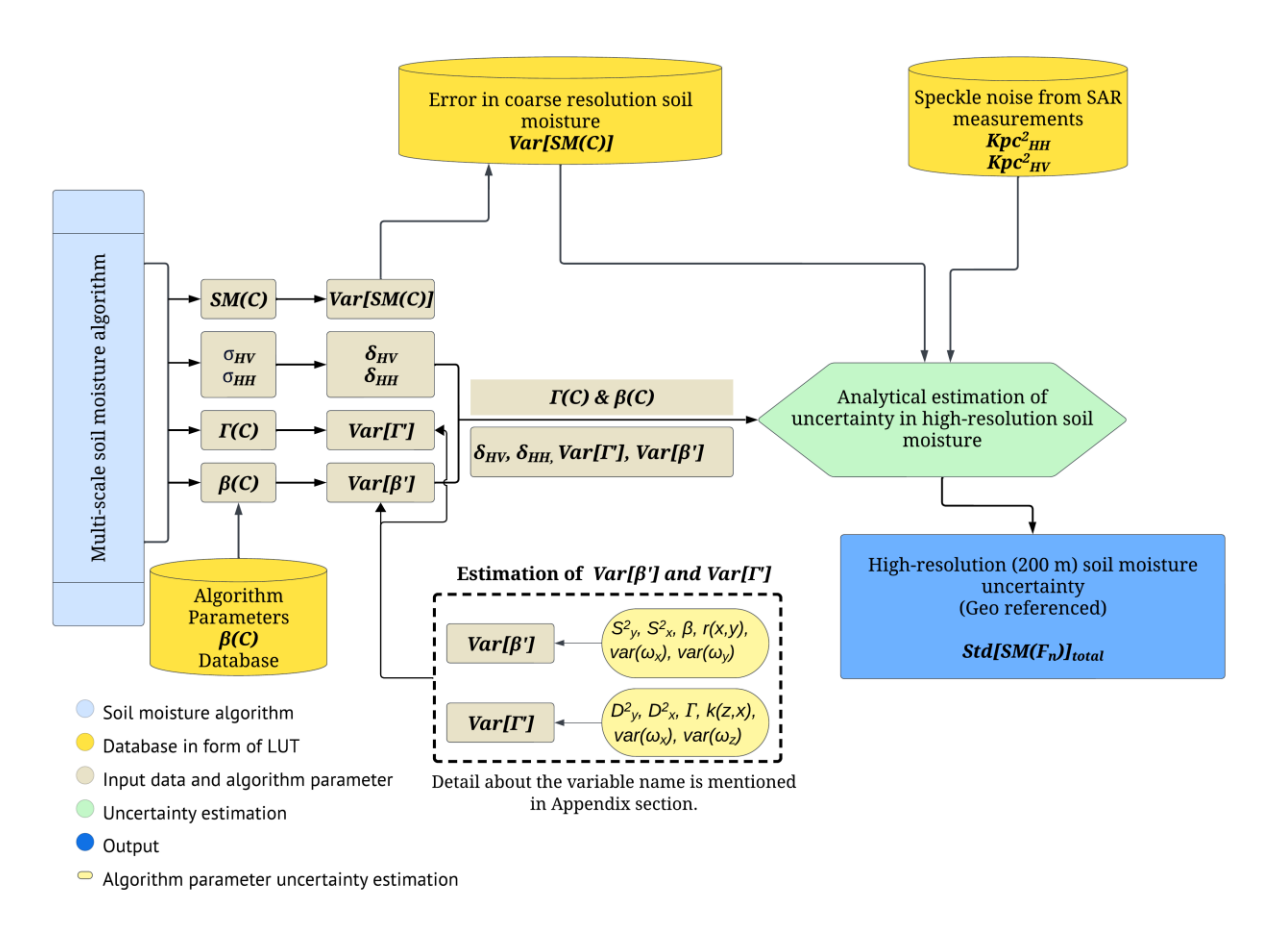


Figure 39: Methodology flowchart of analytical approach-based uncertainty estimation in the NISAR high-resolution soil moisture products under the multi-scale algorithm.

#### 6.7 Results

## 6.7.1 Sensitivity analysis of the uncertainty estimation in the high-resolution soil moisture

We carried out sensitivity analysis for each error source using the proposed equations (Eq. 19, 26, and 27), as discussed in Section 6.3. We first analyze the sensitivity to errors in the input

datasets, SM(C) and SAR observations ( $\sigma_{HH}$  and  $\sigma_{HV}$ ). Then we present the sensitivity analysis of total uncertainties in  $SM(F_n)$  due to the error in multi-scale algorithm parameters ( $\beta$  and  $\Gamma$ ).

## **6.7.2** Input data uncertainty

It is evident from the multi-scale soil moisture algorithm (Eq. 15) that with  $\beta = 0$ , (i.e., almost no contribution from the SAR measurements ( $\sigma_{HH}$  and  $\sigma_{HV}$ ) the uncertainty in  $SM(F_n)$  is entirely due to an error from the input coarse-resolution soil moisture product SM(C). This condition occurs mostly over homogeneous dense forests, where  $\sigma_{HH}$  and  $\sigma_{HV}$  are isometric in nature, and soil moisture exhibits a small standard deviation due to low variability. This condition occurs mostly over homogeneous dense forests, where  $\sigma_{HH}$  and  $\sigma_{HV}$  are isometric in nature, and soil moisture exhibits a small standard deviation due to low temporal variability. On the other end of the backscattering characteristics is the dry desert because it can be very specular in nature and thus exhibits very low backscatter. Furthermore, desert environments can also exhibit some spatial variability in backscatter measurements, particularly due to factors such as sub-surface scattering effects in very dry sandy soils (Morrison and Wagner, 2020). It is also possible that for a given region of desert due to very dry soil there is no temporal variability in soil moisture and this scenario can also lead to very low magnitude  $\beta \sim 0$  value. These factors can introduce variability into the backscatter signal across different regions and contribute to variability of  $\beta$  the parameter. Fig.3 shows the global map of the  $\beta$  parameter derived for the NISAR multi-scale algorithm. It shows that  $\beta$  usually ranges between 0 and 0.1 globally. It was also observed that low  $\beta$  (~ 0.01) value was found to be mostly over dense tropical forests (e.g., Amazon Forest, Congo Rainforest, and North-eastern parts of the Indian sub-continent). See Figure 58 for more details. The very low estimated  $\beta$  values are due to the use of a dataset with a low temporal dynamic either in SM(C) or  $\sigma_{HH}$ . As discussed above, in the regions having very low  $\beta$ , the uncertainty in the  $SM(F_n)$  of the NISAR multi-scale soil moisture algorithm mainly stems from the error in the input dataset, SM(C). Figure 19 also exhibit that for land covers other than forests and deserts/barren land, most areas exhibit moderate  $\beta$  values (0.02 to 0.06) to high  $\beta$  values (i.e., > 0.06). In cases with larger  $\beta$  values, the total uncertainty in  $SM(F_n)$  increases due to the multiplicative relationship between SAR measurement noise and the  $\beta$  values in Eq. 19. In this chapter, we used nominal values of SAR measurement noise in co-pol ( $KpC_{HH} = 0.15 \text{ dB}$ ) and cross-pol ( $KpC_{HV} = 0.25 \text{ dB}$ ) along with the value for error in the input SM(C) of ECMWF as described above (var[SM(C)] = 0.04)

 $[m^3/m^3]$ ).

Figure 40 presents an analysis of the uncertainty in  $SM(F_n)$  as a function of  $\beta$  (between 0 to 0.1) and with different error values in the input ECMWF SM(C) (in the range of 0 to 0.06  $[m^3/m^3]$ ). The overall uncertainty in  $SM(F_n)$  increases both with the increase of error in SM(C)(Figure 40a) and with algorithm parameter  $\beta$  (Figure 40b). As discussed earlier, the error in ECMWF soil moisture product var[SM(C)] might differ from what is used here due to the involvement of complex nonlinear physics and uncertainties in the forcing and assimilated dataset. The high  $\beta$  values can occur in regions/grid-cells with characteristics such as 1) extreme seasonal variability that leads to frequent wetting and drying of soil and vegetation conditions (Singh et al., 2019a); 2) seasonal flooding and saturated fields (i.e., paddy landscapes) experiencing very wet conditions (Singh et al., 2021), and 3) presence of heterogeneous land cover conditions within the C resolution grid-cell. For example, tropical regions in the monsoon season undergo changes from very dry to very wet soil over short timescales. Similarly, croplands and croplands mixed with natural vegetation also experience high temporal variation in soil moisture and non-isometric backscatter due to drying and wetting events and changes in crop phenology. For such challenging geophysical and land cover conditions, it is crucial to select the optimal temporal window size for estimating the  $\beta$  parameter reliably.

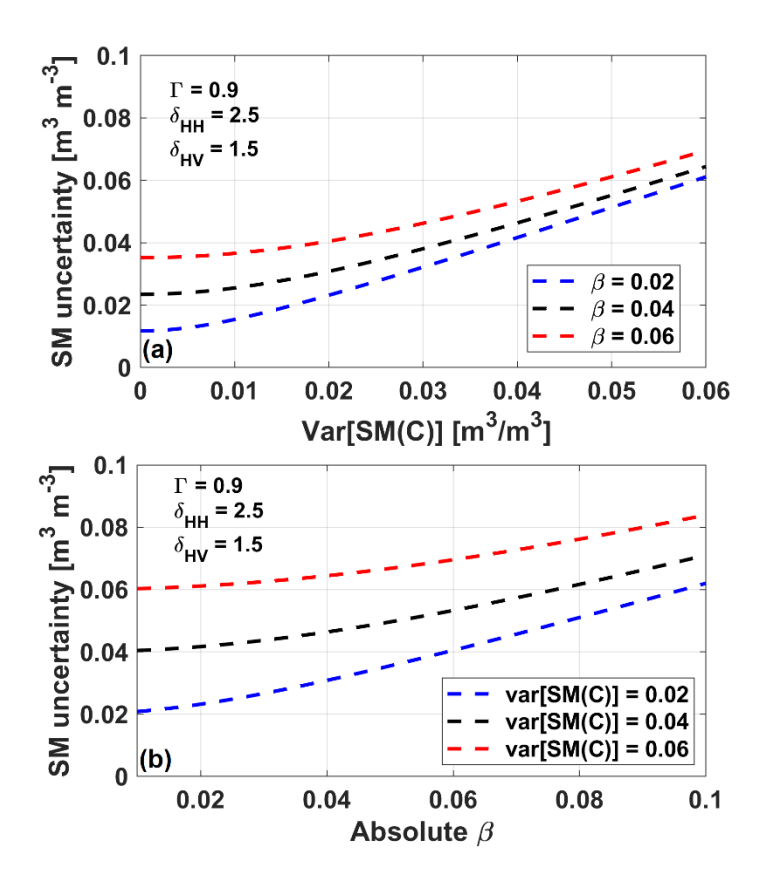


Figure 40: Uncertainty analysis in the high-resolution soil moisture retrievals (a) with different error values in the input ECMWF coarse resolution soil moisture product at a few typical  $\beta$  values of 0.02, 0.04, and 0.06, and (b) with an increase in  $\beta$  values at typical error in ECMWF soil moisture product ( $\pm 0.02$  [m<sup>3</sup>/m<sup>3</sup>] of the nominal value 0.04 [m<sup>3</sup>/m<sup>3</sup>]).

## **6.7.3** Algorithm parameter uncertainty

The NISAR multi-scale soil moisture algorithm's parameters  $\beta$ , and  $\Gamma$ , vary in space and time due to changes in geophysical conditions, vegetation characteristics, and landcover heterogeneity. Though errors in both  $\beta$  and  $\Gamma$  are major sources of uncertainty in  $SM(F_n)$ , error in parameter  $\beta$  is a particularly large contributor to the total uncertainty in many areas of the world. As discussed in the above sections, there are various reasons for the error in  $\beta$  estimation. In this chapter, we specifically focused on analyzing the sensitivity of different temporal window sizes under varying land cover conditions. In the past, Leroux et al., (2016), investigated the effect of different temporal window sizes on the estimation of the  $\beta$  parameter, aiming to improve the soil moisture retrievals for the SMAP active-passive algorithm. They emphasized that optimizing the temporal window size for estimating  $\beta$  helped enhance the soil moisture retrieval accuracy and

reduce uncertainty. They also noted that the correlation between brightness temperature/soil moisture and SAR backscatter decreases as vegetation water content exceeds 5 [kg/m<sup>2</sup>], impacting the  $\beta$  parameter estimation as well as high-resolution soil moisture retrievals.

We conducted a sensitivity analysis to examine the impact of different temporal window sizes (i.e., number of overpasses) on the error in  $\beta$  estimation using Eq. A20. We assumed two different correlation coefficient values (R = 0.5 and R = 0.75) between SM(C) and up-scaled copol SAR backscatter measurements  $\sigma_{HH}(C)$ . Two simulations were performed with two typical  $\beta$ values (moderate  $\beta = 0.04$  and high  $\beta = 0.08$ ) with two different correlation coefficient values . The first simulation focused on croplands, undergoing rapid changes in vegetation density due to varying stages of crop growth over 3 to 4 months. For these cropland scenarios, we used relatively low standard deviations in  $\sigma_{HH}(C)$  and SM(C), with  $S_x$  (variance of  $\sigma_{HH}(C)$  in a C resolution grid – cell) 2.5 and  $S_{\nu}(variance\ of\ SM(C)\ in\ a\ C\ resolution\ grid-cell)=0.20\ [m^3/m^3]$ . The optimal temporal window size for a crop growth period will typically range between 12 to 16 overpasses, considering the NISAR overpass repeat interval of 6 days (combining the ascending and descending overpasses). Thus, we fixed the maximum window size to 20 overpasses. Simulations are presented in Figure 41a and Figure 41b. The second simulation is for the land cover other than cropland, such as a bare surface and surface with moderate dense vegetation conditions that usually experience minimal changes on physical surface conditions. In such land cover conditions, standard deviations of SM(C) and  $\sigma_{HH}(C)$  are relatively high due to varying soil moisture dynamics and SAR backscatter measurements. Thus, in such scenarios, high standard deviations in  $\sigma_{HH}(C)$  and SM(C) were assumed ( $S_x = 5.0$  dB and  $S_y = 0.40$  [m<sup>3</sup>/m<sup>3</sup>], respectively) and simulations are presented in Figure 41c and Figure 41d. Additionally, simulations with different correlation (R) values were considered, as in real-world scenarios, R values may vary from low to high due to different conditions. For instance, R values may be low in forested and barren where there is low soil moisture variability. In contrast, grid cells with higher soil moisture variability may exhibit high R values, and these differences may impact the soil moisture uncertainty.

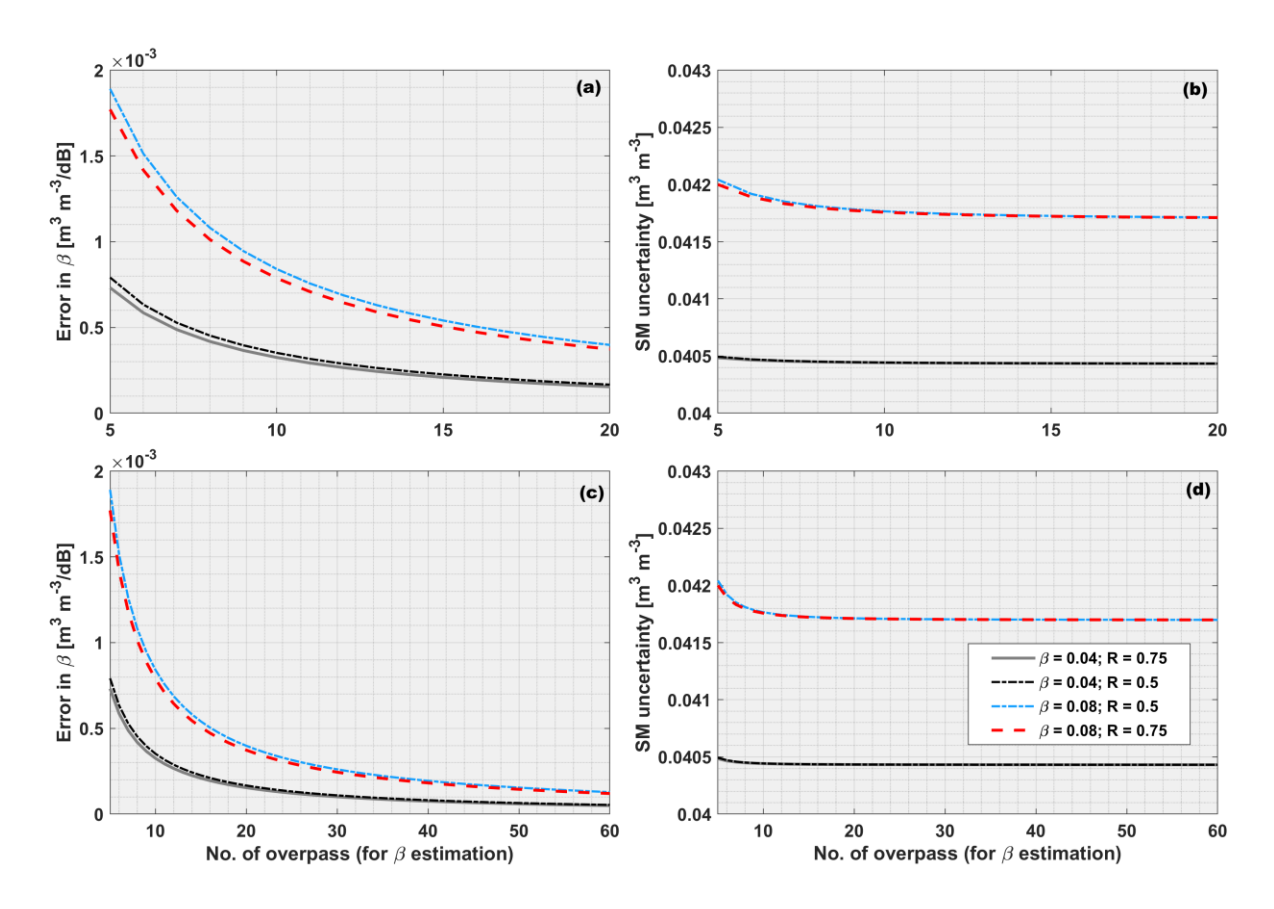


Figure 41: Expected error in the algorithm parameter  $\beta$  (left panel) and total uncertainty in  $SM(F_n)$  (right panel): (a) and (b) when having shorter overpass or temporal window size with the maximum window size of 20, whereas (c) and (d) when having larger overpass or temporal window size with the maximum window size of 60. A moderate correlation (R = 0.75 and R= 0.5) between  $\sigma_{HH}(C)$  and SM(C) and typical  $\beta$  values of 0.04 and 0.08 were used in all the analyses. The equation used to create plot is given in Appendix A2.

Analyzing both scenarios in Figure 41, it was observed that, though the standard deviations of  $\sigma_{HH}(C)$  and SM(C) were assumed low in cropland scenarios, a higher total uncertainty was found in  $SM(F_n)$  as compared to the scenario with high standard deviations in  $\sigma_{HH}(C)$  and SM(C). In addition, Figure 41a and Figure 41b exemplifies that total uncertainty in  $SM(F_n)$  decreases exponentially with an increase in the number of overpasses from 5 to 10 in  $\beta$  estimation. It was also found in Figure 41a that selecting 20 overpasses (~ 4-month period) over cropland, the magnitude of error in  $\beta$  decreases by ~55% in the case of high  $\beta$  of 0.08 and ~30% in the case of moderate  $\beta$  of 0.04. In the case of the shorter temporal window (~10), the soil moisture uncertainty difference was ~0.22% and ~8% less error in  $\beta$ , when compared with the just 5 overpasses. However, for longer temporal window (~20), the soil moisture uncertainty reduces to ~0.14% and the error in  $\beta$  reduces to ~4.6%, when compared with short overpass of ~10. Though the error in

 $\beta$  significantly impacts the overall uncertainty, the above analysis shows that the overall soil moisture retrieval uncertainty is below ~0.0420 [m³/m³] ( $\beta$  = 0.08) and ~0.0405 [m³/m³] ( $\beta$  = 0.04) for the scenarios explored in this chapter. In real-world situations, it is not recommended to rely on long time-series data in  $\beta$  estimation for land cover types like i) croplands and (ii) croplands mixed with natural vegetation. This is because these two land covers undergo rapid changes with the different crop phenological stages in a growing season, where shorter time series may be necessary to capture the seasonality in optimal  $\beta$  estimation. Based on the real-world considerations and the analysis presented in Figure 41a and Figure 41b, suggests that more work is needed in order to select the optimal temporal window size for estimating a robust  $\beta$  parameter over croplands for the NISAR multi-scale algorithm's soil moisture retrievals.

In contrast, the scenario of the second simulation resulted in a more robust estimation of the  $\beta$  parameter with lower uncertainty. Figure 41 shows a simulation of this situation, using high standard deviations in  $\sigma_{HH}(C)$  and SM(C), and shows that the use of more than 30 overpasses (~ 6 months) for  $\beta$  estimation reduces the overall uncertainty to less than 0.0418 [m³/m³] (at  $\beta$  = 0.08) and 0.0403 [m³/m³] (at  $\beta$  = 0.04). Also, using two different correlation values, the analysis shows that the difference in overall uncertainty is minimal (difference observed ~0.01%) when a larger number of overpasses was used for estimating  $\beta$ . Furthermore, the analysis shows that the overall uncertainty is reduced by approximately 1.5% in both  $\beta$  values scenarios, with ~33% less contribution of error in the  $\beta$  parameter compared to the conditions with shorter overpasses for  $\beta$  estimation (see Figure 41c and Figure 41d).

To achieve an overall retrieved soil moisture uncertainty of  $< 0.0418 \text{ [m}^3/\text{m}^3]$  for regions having high standard deviation in soil moisture and backscatter, a longer time series of NISAR datasets is required, spanning at least 5 to 12 months (Figure 41b). However, the selection of the number of overpasses for  $\beta$  parameter estimation depends on the land use type and the accuracy of soil moisture retrievals when compared with *in-situ* measurements. Following the launch of NISAR and the availability of data for a timeframe of at least 5-6 months, a comprehensive study will be conducted to optimize the number of overpasses required for the  $\beta$  parameter estimation, aiming to minimize uncertainty and achieving high accuracy in high-resolution soil moisture when compared with *in-situ* measurements.

Furthermore, the use of a number of grid cells in estimating NISAR multi-scale algorithm parameters also impact the soil moisture retrieval accuracy. If an insufficient number of 200 [m]

grid cells are used in aggregating SAR measurements to a coarser resolution of 9 [km]. In that case, the error increases in estimating algorithm parameters, leading to high soil moisture uncertainty. This happens because, during the disaggregation process, the algorithm will encounter masked grid cells that are not valid/appropriate for soil moisture retrievals, such as snow and ice, frozen ground, urban and water bodies. This reduction of the grid cell number also impacts the  $\Gamma$ parameter calculation and leads to higher uncertainty in the high-resolution soil moisture products. A sensitivity analysis was conducted by varying the number of grids available for  $\Gamma$  estimation. Figure 42 shows the simulated result by keeping all the values constant, such as  $\beta = 0.04$  and,  $\Gamma =$ 0.9 and R (co-pol, cross-pol) = 0.8 (however,  $\Gamma$  and R (co-pol, cross-pol) will vary based on the number of 200 [m] grid used, but for the current simulation it's kept as constant). The simulation shows that when the number of grids is less in number, i.e., ~100, the magnitude of uncertainty is expected to exceed 0.12 dB/dB (Figure 42a). Whereas when the maximum grids (> 1900) are available, the magnitude of error in  $\Gamma$  is < 0.04 dB/dB with an overall decrease of ~65% error in  $\Gamma$ value (Figure 42a). The output soil moisture uncertainty also decreases overall from 0.041 [m<sup>3</sup>/m<sup>3</sup>] to 0.0401 [m<sup>3</sup>/m<sup>3</sup>] when the maximum grids are available to use (Figure 42b). However, it has minimal impact on the overall soil moisture uncertainty.

Apart from the error in  $\Gamma$  parameter, the number of available grids might also impact the spatial deviation of backscatter, which is considered in the proposed equation as  $\delta_{HH}$  and  $\delta_{HV}$ . During the algorithm implementation, the spatial deviation of backscatter in dB increases primarily for two different reasons: (a) the 9 km grid has a heterogeneous land cover, and (b) partial rainfall or a high amount of variability in rainfall within 9 [km] coarser grid  $\Gamma$ . In both cases, if the spatial deviation increases, the soil moisture uncertainty increases. Figure 43 represents such trends as the spatial deviation trends in backscatter increase the uncertainty in the retrieved soil moisture increases. However,  $\delta_{HH}$  and  $\delta_{HV}$  have very minimal impact on the  $Std[SM(F_n)]_{total}$  in comparison to  $var[\Gamma']$  and var[S'] and var[SM(C)].

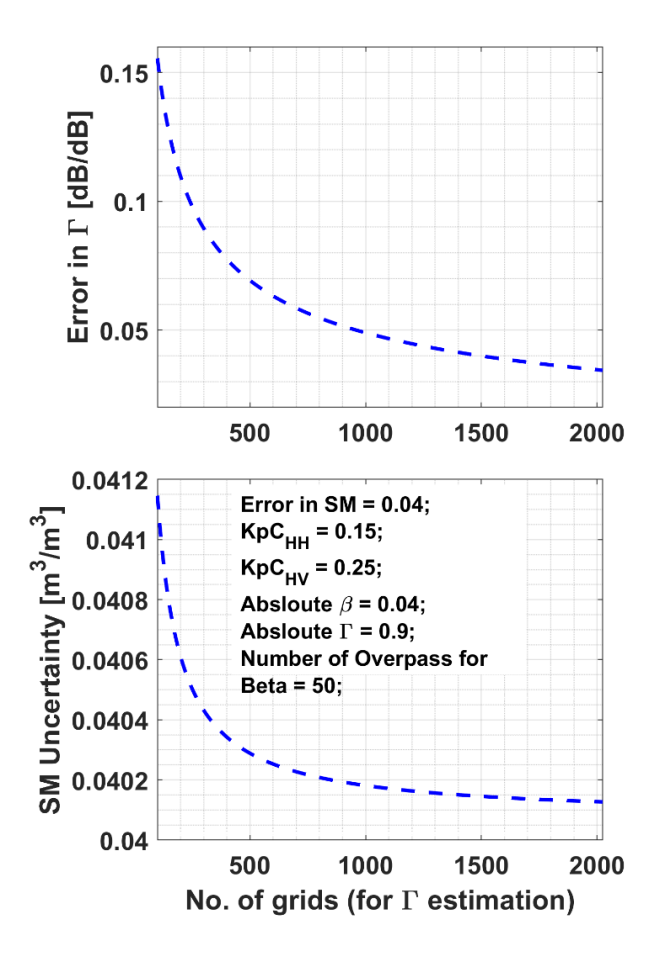


Figure 42: (a) Expected error in  $\Gamma$  parameter for different numbers of grids, (b) total uncertainty in soil moisture due to different numbers of grids used to estimate  $\Gamma$  parameter.

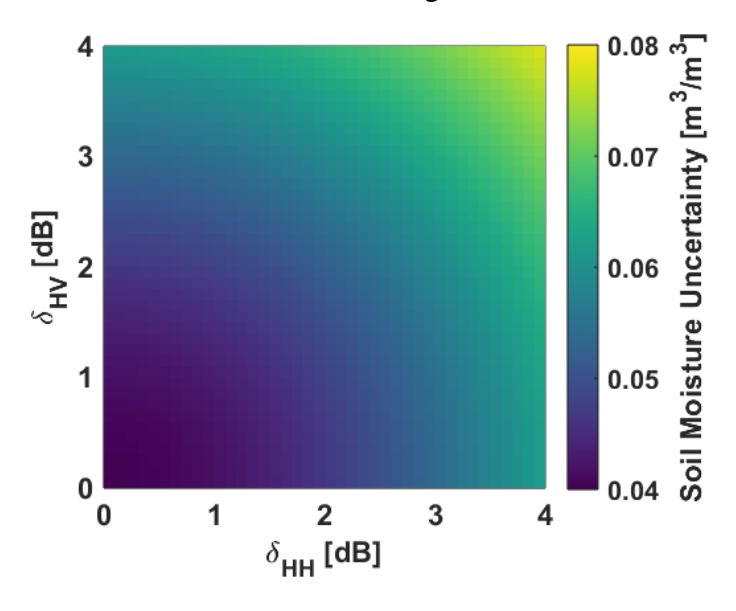


Figure 43: Uncertainty in high-resolution soil moisture due to spatial deviation in backscatter (in dB unit) of SAR data.

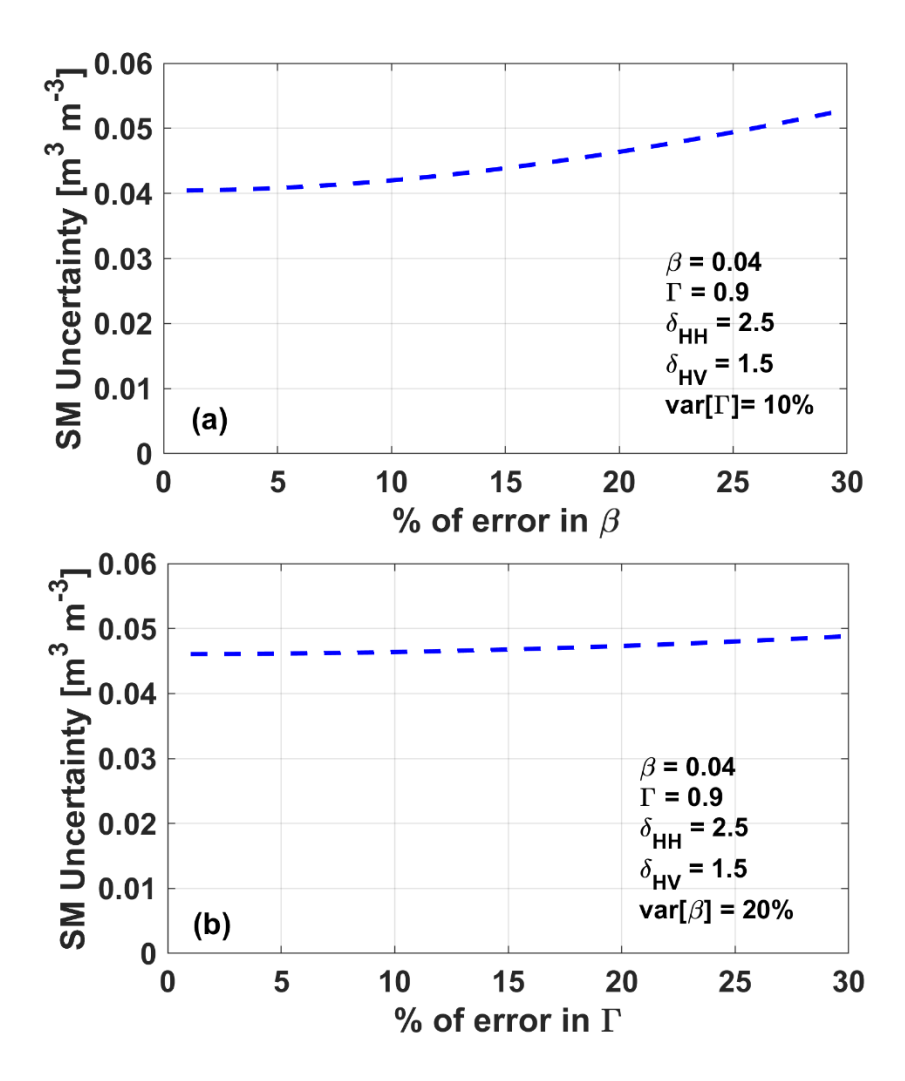


Figure 44: Uncertainty in soil moisture due to percentage error in algorithm parameters  $\beta$  and  $\Gamma$  by considering 0.04 as  $\beta$  value and 0.9 as  $\Gamma$  value.

Besides solving the errors in  $\beta$  and  $\Gamma$  based on the input in these parameters, another approach can be used as injecting the value of the percentage of error in the  $\beta$  and  $\Gamma$ . For sensitivity analysis, different percentages of error in  $\beta$  and  $\Gamma$  are injected into the proposed approach to determine the level of impact on the soil moisture uncertainty. Figure 44 illustrates the uncertainty in soil moisture resulting from varying levels of uncertainty in the  $\beta$  and  $\Gamma$  parameters. The simulation with different levels of uncertainty in  $\beta$  and  $\Gamma$  parameters shows that the error in the  $\beta$  parameter has a greater impact on output soil moisture uncertainty due to its magnitude and its multiplication with the standard deviation of co-pol and cross-pol observations from SAR, as derived in Eq. 26. When error in the  $\beta$  parameter exceeds 20%, the uncertainty in soil moisture increases to 0.05 [m³/m³]. On the other hand, when there is more than 30% error in  $\Gamma$ , the soil

moisture retrievals uncertainty reaches  $0.05~\text{m}^3/\text{m}^3$ . When both the  $\beta$  and  $\Gamma$  parameters have a combined error of ~ 20%, the uncertainty in soil moisture is less than  $0.045~\text{[m}^3/\text{m}^3]$ , with minimal impact on the disaggregation algorithm. Figure 45 presents a combined data cube showing the errors in soil moisture, as well as the percentages of error in the  $\beta$  and  $\Gamma$  parameters. The data cube also indicates that, apart from the error in soil moisture, the  $\beta$  parameter has a greater impact on the overall uncertainty of soil moisture compared to the  $\Gamma$  parameter. The level of uncertainty in  $\Gamma$  primarily affects the overall soil moisture uncertainty when the uncertainty level of the  $\beta$  parameter is too low. This situation may occur when there are fewer 200 [m] high-resolution SAR grids within a 9 km coarse resolution grid cell or when the underlying 9 [km] resolution grids have heterogeneous land cover, leading to increased uncertainty in the  $\Gamma$  parameter. However, the impact of uncertainty varies under different conditions due to the dynamics of soil moisture and backscatter over various land cover types and regions. Sometimes, both algorithm parameters may exceed 20% uncertainty, resulting in high uncertainty in the output soil moisture, while vice versa can also occur. Therefore, it is important to quantify and test the level of uncertainty in the algorithm parameters across different scenarios.

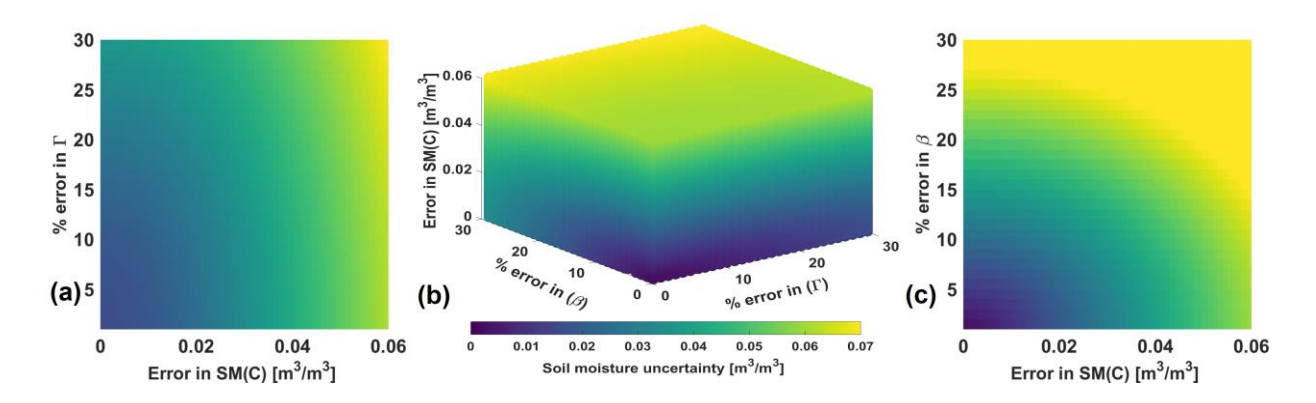


Figure 45: (a) Uncertainty in high-resolution soil moisture due to percentage error in  $\Gamma$  and error in input soil moisture, with constant relative error of 10% in  $\beta$ ; (b) Data cube representing expected uncertainty in high-resolution soil moisture due to three different sources: (i) error in input soil moisture, (ii) percentage error in  $\beta$ , and (iii) percentage error in  $\Gamma$ ; (c) Uncertainty in high-resolution soil moisture due to percentage error in  $\beta$  and error in input soil moisture, with constant relative error of 12% in  $\Gamma$ .

#### 6.7.4 Uncertainty in NISAR soil moisture product

The proposed approach for estimating total uncertainty in high-resolution soil moisture using Eq. 19, 26, and 27) was implemented on a version of the UAVSAR L-band data time series

(collected during the SMAPVEX-12 field campaign) that had been simulated to closely match the expected characteristics of NISAR (e.g., spatial resolution, noise) with incidence angle ranges between 30° to 50°.

SMAPVEX-12 campaign encompasses agricultural fields with diverse crop types, such as soybean, maize, sunflower, oats, canola, wheat, and forage (see Figure 57). The presence of these crops, which undergo a complete phenological cycle involving drying down and subsequent wetting events, makes it suitable for testing the algorithm's performance and calculating errors and uncertainties. The high-resolution soil moisture was retrieved using the NISAR multi-scale algorithm (Lal et. al 2023) on 14 UAVSAR scenes for one month between Jun 17 – Jul 17, 2012. The soil moisture retrievals of 14 UAVSAR scenes (Figure 27). Soil moisture retrievals given in Figure 27 were found to meet the accuracy goal of the NISAR mission (0.06 [m³/m³]) in comparison with *in-situ* soil moisture measurements during SMAPVEX-12.

Figure 27 shows retrieved soil moisture at a 200 [m] spatial resolution using L-band UAVSAR data, whereas Figure 46 illustrates the corresponding uncertainty in soil moisture. The retrieved soil moisture data exhibits two distinct conditions over one month. Initially, during the first 3-4 observations, the soil moisture range was relatively high, exceeding 0.35 [m³/m³]. As the phenological stage of the crop progresses, the soil moisture gradually decreases, indicating a shift towards drier conditions. The variation in soil moisture throughout the month can be attributed to a multitude of factors, encompassing variations in crop cover, diverse crop types, the heterogeneity of soil types, and changes in vegetation water content (VWC) corresponding to different phenological stages of plant growth. In terms of quantifiable uncertainty, the calculated range extends from approximately 0.04 [m³/m³] to 0.06 [m³/m³], with an assumed error of 0.04 [m³/m³] in the coarse-resolution soil moisture input.

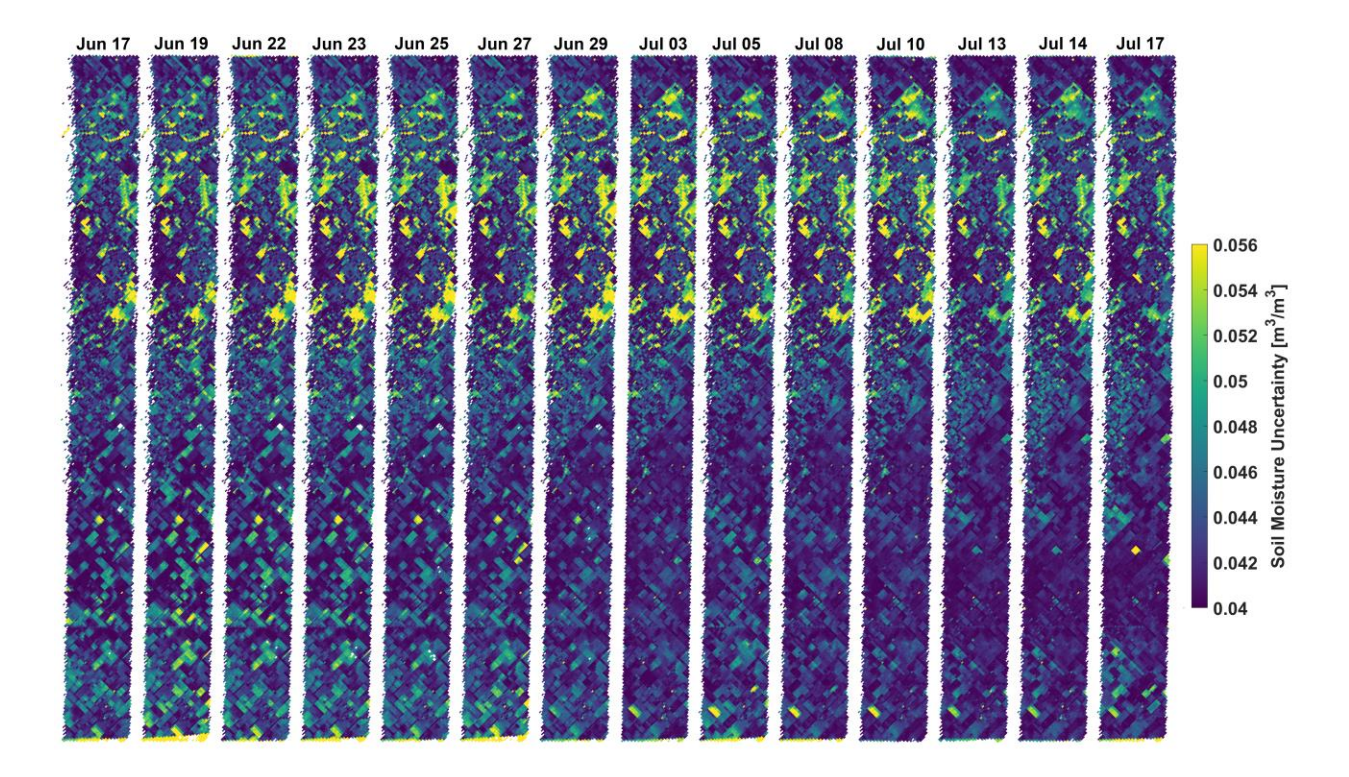


Figure 46: Spatiotemporal variation of uncertainty in high-resolution soil moisture at 200 [m] resolution retrievals using UAVSAR data from SMAPVEX12 campaign over Carman, Manitoba test site between June 17 to July 17, 2012, for the UAVSAR flight line (31606).

The spatio-temporal variability of soil moisture uncertainty is similar to the wetting and drying pattern in the 200 [m] retrieved soil moisture. During the first few observations, the high soil moisture values are > 0.35 [m³/m³]; similarly, for most fields, the uncertainty values are also high, i.e., > 0.046 [m³/m³]. As the crops advance in maturity, the soil moisture starts decreasing similarly, the uncertainty also starts decreasing, and the overall uncertainty is < 0.044 [m³/m³]. The possible reasons for high uncertainty in some parts of the test site are as follows: (a)  $\delta_{HH}$  and  $\delta_{HV}$  are on the higher side, which leads to higher uncertainty (Figure 43 exemplifies this); (b) the UAVSAR L-band data have a smaller swath width for all the selected dates, which makes the high uncertainty in the  $var[\Gamma']$ . In an ideal condition, there will be a 2025 combination of co-pol and cross-pol measurements for calculating the  $\Gamma$  parameter, but due to the small swath width, the magnitude of  $var[\Gamma']$  is higher, contributing to high uncertainty in the retrieved soil moisture. Most crop types were at the leaf development stage during the first few observations (McNairn et al., 2015), and the surface roughness was high. This will directly impact the standard deviation of

co-pol and cross-pol backscatters, which is of high value in this case. During the sensitivity analysis experiment, Figure 43 explains such conditions, i.e., high standard deviation in the co-pol and cross-pol backscatter, which increases the soil moisture uncertainty.

Further, the analytical solution-derived uncertainty has been compared with the ubRMSE between retrieved soil moisture and *in-situ* measurements for different crop types. For comparison, the average of standard deviation for each crop type is used, and it's calculated as  $\sqrt{\text{((Sum of squares of uncertainty) / total count)}}$ . It's observed that ubRMSE is lower than the soil moisture uncertainty for most of the crop types, whereas both statistics show that error and uncertainty of retrieved soil moisture is below the NISAR mission goal of 0.06 [m<sup>3</sup>/m<sup>3</sup>] (Figure 47) This also shows that the multi-scale algorithm is capable of meeting NISAR mission goals despite simulating the soil moisture uncertainty with constant value of 0.04 [m<sup>3</sup>/m<sup>3</sup>] as var[SM(C)].

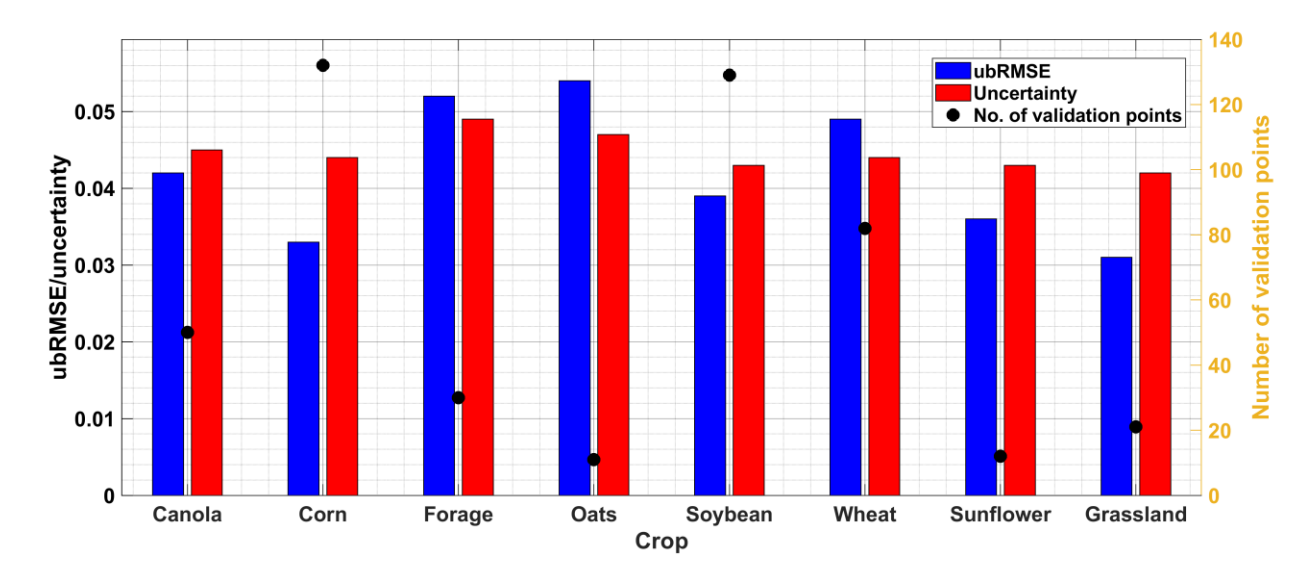


Figure 47: A comparison between ubRMSE of high-resolution soil moisture retrievals and soil moisture uncertainty using the SAMPVEX12 UAVSAR dataset.

## 6.8 Discussion and Conclusion

The NISAR mission will provide high-resolution soil moisture at 200 [m] spatial scale and ~6 days temporal scale (with combined ascending and descending pass) using the multi-scale algorithm in conjunction with two other algorithms. In the multi-scale algorithm, the coarse-resolution soil moisture from passive microwave observation/reanalysis/modelled product is

disaggregated to high-resolution soil moisture with the help of high-resolution SAR co-pol and cross-pol backscatter datasets. In the multi-scale algorithm soil moisture retrieval approach, the retrieved soil moisture at high resolution has uncertainty distribution around the mean error at 9 [km] coarse-scale soil moisture. This is because of error/uncertainty in the input parameters and model assumptions, i.e., the standard deviation in the estimated parameters due to vegetation conditions, landscape heterogeneity, and satellite instrument errors. Traditionally, the error in retrieved soil moisture is assessed against *in-situ* soil moisture data over very limited sites/pixels. However, geophysical applications that use high-resolution soil moisture need quality assessment (uncertainty estimates) over all the valid retrieved 200 [m] grid cells. Therefore, an analytical solution/approach is developed (Eq. 27) to calculate uncertainty in the retrieved high-resolution soil moisture. This proposed approach provides an option to quantify uncertainties of the spatiotemporal high-resolution soil moisture retrievals over all the valid 200 [m] grid cells without using in-situ as reference data and is very straightforward to implement on the multi-scale soil moisture algorithm. A key input to the analytical solution is error and standard deviation of input and parameters used for retrieving soil moisture. Such as errors in input coarse resolution soil moisture, spatial deviation in SAR backscatter ( $\delta_{HH}$  and  $\delta_{HV}$ ) within the coarse resolution grid cells, speckle noise and error in the algorithm parameter ( $\beta$  and  $\Gamma$ ).

The sensitivity analysis conducted for soil moisture uncertainty by injecting a different level of error source in all the input parameters of the algorithm to identify the thresholds for the data quality flags. From the above sensitivity analysis, it is observed that the retrieved soil moisture has error/uncertainty due to the multiple parameters but primarily influenced by the error in the input coarse-resolution soil moisture i.e.,  $var[SM(F_n)]_{input}$ . The error in the input coarse resolution soil moisture can arise due to model physics, parameterizations, and uncertainties in the forcing and assimilated data. Since the multi-scale algorithm depend significantly on the input coarse-resolution soil moisture, determining the error source for this data is crucial. This error source can be identified based on validation statistics (ubRMSE) derived from *in-situ* measurements. In the current chapter, we have used Lal et al., (2022c) statistics as a reference for the error in the var[SM(C)]. For the pre-launch and algorithm sensitivity test, we have considered  $var[SM(C)] = 0.04 \, [m^3/m^3]$ , based on the ubRMSE of cropland. However, during post-launch, var[SM(C)] value can be used based on LULC type, longitudinal/latitudinal zone, or a combination of all. Beside var[SM(C)] for  $var[SM(F_n)]_{input}$ , in the Eq. 19 speckle noise comes

from the NISAR instrument characteristics which will be a constant value,  $\beta$  and  $\Gamma$  can be used in a similar way as implemented in the multi-scale algorithm.

The algorithm parameter ( $\beta$  and  $\Gamma$ ) also contains an error, and this is encapsulated in the  $var[SM(F_n)]_{param}$ . The  $var[SM(F_n)]_{param}$  describes the uncertainty in the soil moisture specifically due to the algorithm parameters  $\beta$  and  $\Gamma$ , and spatial deviation in the backscatter. The uncertainty in the  $\beta$  parameter varies with space and time due to the low standard deviation in soil moisture and SAR backscatter. Furthermore, not selecting an optimal window size for calculating the regression coefficient between soil moisture and backscatter also leads to high uncertainty in soil moisture. During the sensitivity analysis, it's observed that uncertainty in  $\beta$  is low if the absolute  $\beta$  value is low. The lower  $\beta$  values demonstrate that a particular grid or land cover doesn't have much variability, and SAR backscatter can be isometric in nature. However, the high  $\beta$  value can have high uncertainty in the soil moisture retrieval, but this depends on the multiple factors considered in the analytical approach. Besides low to high  $\beta$  value, the uncertainty in  $\beta$  is highly dependent on the no. of overpass selected for calculating the regression coefficient. For low uncertainty in the  $\beta$  value, the no. of overpass should be more than 30 (~5-6 months for NISAR), as the magnitude of error in  $\beta$  decreases by ~55% ( $\beta$  = 0.08) and ~30% ( $\beta$  = 0.04) when using > 30 overpass in comparison to 8-10 overpass. However, selecting the number of overpasses also depends on the LULC type as cropland experiences wetting and drying of soil moisture over a shorter period, and the phenological cycle has a shorter time scale. It's essential to limit the window size for calculating the  $\beta$  parameter for cropland and similar land cover having shorter vegetation phenological cycles. In contrast, other land cover types, such as over forest cover or sparse vegetation (such as grassland and shrubland) and bare soil undergo minimal ground condition changes due to its very slowly changing physical nature. For such land cover, the standard deviation of soil moisture and backscatter value is high due to the range of values over the period. This can also result in the robust estimation of  $\beta$  value. The selection of number of overpasses for different land cover will be tested during post-launch calibration and validation of a multi-scale algorithm for more accurate soil moisture retrievals.

In the case of the other algorithm parameter i.e., the heterogeneity parameter  $\Gamma$  is more stable than  $\beta$  parameter and experiences much less variability and can be calculated on the fly during the algorithm implementation. The uncertainty in the heterogeneity parameter  $\Gamma$  arises primarily due to the number of grids available in the coarser resolution grid. For the NISAR

mission, ideally, there should be 2025 grids of 200 [m] resolution in the 9 [km] coarser resolution grid. But in the real-world scenario each coarse resolution grid has some missing 200 [m] grids because the algorithm will encounter masked grid cells that are not appropriate for soil moisture retrievals, such as snow and ice, frozen ground, urban and water bodies. The availability of a lesser number of 200 [m] grid cells in the 9 [km] grid impacts the gamma calculation and leads to higher uncertainty to the high-resolution soil moisture products. Other conditions, such as the 9 [km] grid has heterogeneous landcover, then the  $\delta_{HH}$  and  $\delta_{HV}$  values will be on the higher side, increasing the uncertainty in the high-resolution soil moisture. However, the uncertainty in the  $\beta$  parameter has a high impact on the uncertainty in comparison  $\Gamma$  and other inputs except for error in input coarse resolution soil moisture. The higher impact of uncertainty of the  $\beta$  parameter to the retrieved high-resolution soil moisture comes due to the magnitude and multiplication of deviation of copol and cross-pol measurements.

The testing and implementation of proposed approach for estimating high-resolution soil moisture uncertainty was conducted over the SMAPVEX-12 field campaign using the L-band UAVSAR data for one month between Jun 17 to Jul 17, 2012. The quantifiable terms of soil moisture uncertainty are ~0.042 [m<sup>3</sup>/m<sup>3</sup>] to 0.055 [m<sup>3</sup>/m<sup>3</sup>] using UAVSAR data, which is below the NISAR mission goal of 0.06 [m<sup>3</sup>/m<sup>3</sup>]. When compared with the *in-situ* ubRMSE value for different crops, the calculated soil moisture uncertainty values are a slightly higher but below the NISAR mission goal. Since the difference between both values is very minimal, the testing of the derived uncertainty estimates proves that it can be used to calculate the uncertainty in soil moisture in near real-time with qualitative value. The uncertainty in high-resolution soil moisture retrievals will be used as thresholds for quality control and flagging the retrieved soil moisture. However, postlaunch, we expect a more comprehensive comparison with validation statistics over different land covers and hydroclimatic zones to adjust the threshold value and make the proposed approach more robust. This will eliminate the doubt over the credibility of retrieved soil moisture using multi-scale algorithm, where the *in-situ* soil moisture is not available to validate. The formulation described here accounts for error and uncertainty based on the input data, parameters, and algorithm structure. However, there can be an unpredictable error related to the algorithm not being sufficient to replicate the conditions of the real system. The current uncertainty approach calculates temporal uncertainty for each individual pixel. However, it does not directly address spatial uncertainty, which is not considered in this chapter. We assume that spatial heterogeneity is

adequately captured by combining the SAR co-polarization and cross-polarization backscatters (accounted in the algorithm) with coarse resolution soil moisture values. This allows us to retrieve high-resolution soil moisture data that reflects the variability within individual SAR grids. On any given day, spatial uncertainty is estimated by considering the uncertainties of all grid cells, assuming spatial independence since each pixel is treated individually. The high-resolution soil moisture uncertainty data will be available for each grid globally within the NISAR high-resolution soil moisture HDF5 package from one of the NASA Distributed Active Archive Centers (DAAC, likely the Alaska SAR facility) from ~August 2025.

## **CHAPTER 7: CONCLUSION**

Understanding long-term changes in soil moisture is essential for several reasons. Soil moisture plays a critical role in the Earth's hydrological cycle, influencing not only the plant-water availability but also broader environmental processes such as carbon cycling, weather patterns, and climate regulation. Given the ongoing changes in global climate patterns, including shifts in temperature and precipitation, it is increasingly important to monitor and understand how soil moisture is evolving over time. Long-term trends in soil moisture provide insights into the impact of climate change on terrestrial ecosystems, the sustainability of agricultural practices, and the availability of water resources. These trends can also help identify regions that are becoming more vulnerable to extreme weather events and inform strategies for mitigation and adaptation.

To detect spatiotemporal patterns in soil moisture over a 40-year period, a space-time pattern mining approach was used. The space-time pattern mining involves creating a space-time cube, where each spatial location and its temporal progression were analyzed to identify 'hotspots' and 'coldspots' of soil moisture using the Getis Ord Gi\* statistic. A non-parametric Mann-Kendall test was then performed to assess the trends in these spatial clusters, as well as the temporal trends within each spatial bin. The combination of these analyses allowed for the categorization of regions into six distinct (a total of sixteen patterns were created but only six were considered based on the significance level) spatiotemporal patterns: diminishing, intensifying, and persistent hotspots and coldspots. These patterns highlight areas experiencing significant drying or wetting trends, as well as regions with stable soil moisture conditions over time. The space-time pattern mining analysis shows that approximately 50% of the global vegetated area has experienced surface soil drying, primarily driven by increased bare soil evaporation, vegetation transpiration, and/or decreased precipitation. Conversely, only 9% of the global vegetated area showed an increasing trend in soil moisture, largely attributed to a rise in precipitation levels. The regions identified with drying trends are particularly concerning, as they include critical ecological zones such as the Amazon and Congo rainforests, as well as vital agricultural regions in North America, Europe, and Asia. The implications of these drying trends are severe, with potential threats to biodiversity, disrupting the carbon cycle, and food security.

While these results are interesting in understanding broad-scale changes, it also underscores the limitations of coarse-resolution data in capturing localized variations and the drivers of soil moisture change at finer scales. The heterogeneity of soil moisture, which is

important for understanding various ecological processes and making informed land management decisions and remains inadequately represented in broad-scale analyses. This research gap led to the second major focus of this thesis: the development of a high-resolution soil moisture retrieval algorithm with uncertainty estimates, specifically for L-band satellite missions like NISAR.

High-resolution soil moisture retrieval at 100 [m] and 200 [m] resolutions can be achieved using upcoming SAR missions, with several missions scheduled to launch in the next 5-8 years. Among these, the NISAR mission is focused on this thesis. Using this upcoming SAR mission's multiple algorithms, including empirical, semi-empirical, time-series, change detection, and disaggregation approaches, can be used for high-resolution soil moisture retrieval. Notably, the disaggregation approach holds a distinct advantage for high-resolution soil moisture retrieval and can be used for NISAR mission. The advantages and limitations of the different algorithms are discussed in detail in Chapter 1.

Considering the base of disaggregation approach, a multi-scale soil moisture algorithm has been developed. This approach has its legacy from the SMAP mission algorithm development. The developed algorithm takes advantage of coarse-resolution soil moisture data. In this approach coarse-resolution soil moisture is used to retrieve high-resolution soil moisture with the help of SAR backscatter measurements. The input coarse resolution soil moisture can be either from satellite observations such as from SMAP and SMOS, or from climate model such as from ECMWF. Here for the NISAR mission soil moisture algorithm development, EMCWF ERA5-Land soil moisture available at 9 [km] were used. The ECMWF model assimilates multiple satellite and *in-situ* observations. The assimilation of satellite information includes soil moisture from ASCAT, or backscatter information from SAR to produce reliable soil moisture data. As shown in Chapter 3, ERA5-Land soil moisture exhibits strong correlation with SMAP soil moisture observations and in-situ measurements. However, exceptions exist in regions where SMAP calibration is less robust, such as tundra, dense forests, and areas with organic soil. In these regions, ERA5-Land soil moisture may outperform SMAP, but the accuracy ultimately depends on the model's physics. Further comparison with SMAP observations and *in-situ* measurements reveals that ERA5-Land tends to have a wet bias, overestimating soil moisture.

Since the coarse input soil moisture is almost similar to SMAP observation with consideration of wet bias, it can be used in the multi-scale algorithm for high-resolution soil moisture retrieval. The key approach of this multi-scale algorithm is to reduce the degrees of

freedom (reducing the dependency of multiple ancillary information of vegetation and soil parameters) while retrieving high-resolution soil moisture. The proposed multi-scale algorithm eliminates any complex modeling or dependence on multiple ancillary data and performs the soil moisture retrieval at ~200 [m] by blending the coarse resolution (~9 [km]) soil moisture with very-high-resolution SAR backscatter (~10 [m]) datasets. This algorithm was initially tested on three agricultural sites using L-band UAVSAR data from the SMAPVEX-12 campaign and ALOS-2 SAR data. The results showed that the algorithm successfully retrieved the high-resolution soil moisture at 200 [m] with field-specific impact of crop covers, open fields, and forested regions. Furthermore, validation of the retrieved soil moisture against field-specific averaged *in-situ* measurements demonstrated that the algorithm meets the NISAR mission's goal of achieving an ubRMSE of 0.06 m³/m³ for high-resolution (200 m) soil moisture products.

Since the validation statistics over agricultural sites demonstrates that the algorithm meets the NISAR accuracy goal, it is also important to retrieve and validate it across other land covers with more complex hydrometeorological settings. Further given the algorithm has multi-scale in nature and SAR backscatter information is available at much finer scale i.e., 10 [m], the soil moisture has been retrieved at even higher resolution soil moisture, i.e., 100 [m]. The soil moisture retrievals are validated across multiple test sites with various hydroclimatic conditions and different soil types and land cover, each possessing distinct physical properties. These sites' hydroclimatic condition varies from polar to arid region and soil physical properties vary between the gravelly glacial till to the clay-rich soils and the sandy loam. For this retrieval and validation activity, time-series of ALOS-2 L-band SAR data has been used on five different sites. Further for the comparison and analysis, precipitation data has been used to check the consistency of pattern observed in the soil moisture retrieval. The multi-scale algorithm found to be effectively captured finer-scale information and wetting and drying patterns induced by precipitation events. Despite the varying water retention and drainage capacities of each site, the algorithm consistently followed precipitation trends, highlighting the robustness of high-resolution soil moisture retrieval. This consistent performance across different soil types and regions underscores the algorithm's ability to provide reliable soil moisture data. The high-resolution soil moisture retrievals also demonstrate that while the overall patterns observed at 100 [m] and 200 [m] are similar, the 100 [m] resolution provides finer-scale information. Furthermore, the retrieved soil moisture has been rigorously validated with coinciding in-situ measurements from five CONUS sites, representing

diverse land covers and hydroclimatic zones. The validation across both resolutions and all sites indicates that the ubRMSE remains below  $0.06 \, \text{m}^3/\text{m}^3$ , meeting the NISAR mission accuracy goal. The performance of the multi-scale algorithm, even in forested regions with dense canopies, presents the robustness of the algorithm. This is attributed to the L-band SAR frequency which has higher penetration capabilities. Considering the algorithm's ability to meet the accuracy goals in challenging environments, the expectation is that the NISAR mission goal can be achieved across a wide range of environments and land covers.

In the previous chapters, the high-resolution soil moisture retrieved using the multi-scale algorithm was validated against *in-situ* measurements across selected sites. The validation statistics demonstrated that the retrieval meets the NISAR mission's accuracy goals. *In-situ* measurements are considered reliable estimates of error and uncertainty in the retrieved soil moisture products. However, these measurements are only available for limited locations due to the tedious and expensive nature of data collection. Therefore, it's crucial to estimate the error or uncertainty for each valid grid of soil moisture retrieval, especially in areas where *in-situ* validation is not possible. Moreover, NASA mandates that gridded uncertainty be provided for each retrieved product.

To address these mandates and the limitations of traditional error/uncertainty calculations, an analytical approach has been proposed. This approach estimates uncertainty for each valid grid of retrieval by accounting for errors in the input datasets and algorithm parameters. Sensitivity analysis was first conducted to assess soil moisture uncertainty by introducing different levels of error into all the algorithm's input parameters, identifying critical thresholds. From the sensitivity analysis, it's observed that the retrieved soil moisture has error/uncertainty due to the multiple parameters but primarily influenced by the error in the input coarse resolution soil moisture. The proposed analytical approach was then implemented using UAVSAR L-band data from the SMAPVEX-12 campaign and validated against the ubRMSE values calculated for different crop types. The quantified soil moisture uncertainty was found to range from approximately 0.042 m³/m³ to 0.055 m³/m³ using UAVSAR data, which is below the NISAR mission's goal of 0.06 m³/m³. When compared with the *in-situ* ubRMSE value for different crops, the calculated soil moisture uncertainty values are slightly higher but below the NISAR mission goal. Since the difference between both values is very minimal, the testing of the derived uncertainty estimates proves that it can be used to calculate the uncertainty in soil moisture in near real-time with

qualitative value. These uncertainty estimates in high-resolution soil moisture retrievals will serve as thresholds for quality control and flagging of the retrieved soil moisture data, ensuring that the final products meet the required standards.

## **CHAPTER 8: LIMITATIONS AND FUTURE DIRECTIONS**

The multi-scale soil moisture retrieval algorithm is developed based on the disaggregation approach, which uses coarse-resolution soil moisture as input data. This input is then blended with fine-scale SAR measurements to retrieve high-resolution soil moisture. In the case of the multi-scale algorithm, the coarse-resolution data is derived from the ECMWF climate model, which provides reanalysis of soil moisture products. The ECMWF model assimilates a wide range of observations, including satellite-based measurements and *in-situ* data. It assimilates satellite observations such as backscatter measurements from SAR, along with other relevant atmospheric and land surface parameters, including air temperature, precipitation, vegetation characteristics, soil temperature, and humidity. *In-situ* measurements from various ground-based networks are also assimilated in a similar manner to satellite data. This data assimilation framework enhances the model's capacity to reliably estimate various hydrometeorological parameters, including soil moisture.

However, the process of assimilating such diverse datasets introduces significant challenges. One key issue is the heterogeneity in satellite data characteristics across different sensor generations. Older satellites have different spatial, temporal, and spectral resolutions compared to newer satellites. For example, vegetation indices may be derived using different central wavelengths or spatial footprints depending on the satellite platform. This variability can cause inconsistencies when such data is assimilated into the model, potentially leading to disparities in the estimation of land surface parameters. Similarly, in-situ measurements have their own challenges. Measurement instruments in the field may vary in calibration protocols and operational capabilities across different time periods. Older instruments may have lower precision or fewer calibration points, while newer instruments tend to provide more accurate and reliable data due to advancements in sensor technology. This variability adds to the complexity when insitu data is integrated into the ECMWF model. Another challenge is related to missing satellite data. For instance, technical issues in satellite, data transmission problems, or quality-control measures that flag low-quality retrievals can result in gaps in the available geophysical parameters. The ECMWF model assimilates all available data, but when key parameters are missing or flagged as unreliable, this can introduce noise and uncertainty in the hydrometeorological estimates, including soil moisture.

The errors in these hydrometeorological parameters, including soil moisture, are typically evaluated using limited *in-situ* measurements from different ground networks. However, these error estimates are spatially sparse and do not provide a full representation of uncertainty across every grid cell. The current study uses these limited error values to compute the uncertainty in the high-resolution soil moisture products retrieved by the multi-scale algorithm. In particular, the error estimates are classified according to different land cover types, which are then used in the analytical solution for calculating the uncertainty of the soil moisture product at higher resolutions. Given these challenges, it is recommended that the ECMWF model includes an additional uncertainty layer as part of its gridded hydrometeorological data products. This layer would provide spatially resolved estimates of uncertainty across the entire grid, allowing users to better identify grid cells that may be unreliable or should be flagged for specific geophysical applications. By incorporating a continuous source of uncertainty information can make more informed decisions when using ECMWF products in various environmental, agricultural, and hydrological models.

It is essential to acknowledge the limitations of this research work. Validation has been conducted with a limited set of in-situ measurements, particularly coinciding with ALOS-2 SAR and UAVSAR data, and in some cases, single in-situ points were used to validate both 100 [m] and 200 [m] soil moisture datasets. While these single-point measurements are assumed to represent the soil moisture for the entire grid cell, especially where land cover remains relatively consistent within the grid, some level of bias may still be introduced. This bias becomes more apparent when comparing the results to a more spatially representative area average. However, the grid size is typically 100 [m] or 200 [m], and it is assumed that within each grid cell, the land cover does not change. Therefore, a single in-situ measurement is considered sufficient to represent the soil moisture value for the entire grid cell and can have more number of points for validations in comparison to current operational soil moisture products. Furthermore, to improve the validation of the high-resolution soil moisture retrievals, there is a need for denser in-situ measurement networks to provide more spatially representative error estimates. The denser *in-situ* measurement and sparse *in-situ* measurements will be used to validate the high-resolution soil moisture retrieval from NISAR mission post-launch cal/val activities. Together with both types of in-situ measurement can help in improving accuracy of retrieval. In the post-launch cal/val activities the algorithm sensitivity parameter β, currently derived from SMAP SAR data and ERA5-Land soil

moisture, is expected to undergo significant improvement with the acquisition of a time-series of NISAR HH-pol SAR data, capturing a range of land surface conditions and enhancing the algorithm's performance. Post-launch, with anticipated improvements in the algorithm parameter-associated uncertainty, the multi-scale soil moisture algorithm has the potential to retrieve high-resolution soil moisture with even better performance.

## **BIBLIOGRAPHY**

- Abowarda, A.S., Bai, L., Zhang, C., Long, D., Li, X., Huang, Q., Sun, Z., 2021. Generating surface soil moisture at 30 m spatial resolution using both data fusion and machine learning toward better water resources management at the field scale. Remote Sens. Environ. 255, 112301. https://doi.org/10.1016/j.rse.2021.112301
- Achat, D.L., Augusto, L., Gallet-Budynek, A., Bakker, M.R., 2012. Drying-induced changes in phosphorus status of soils with contrasting soil organic matter contents Implications for laboratory approaches. Geoderma 187–188, 41–48. https://doi.org/10.1016/j.geoderma.2012.04.014
- Ahmad, S., Kalra, A., Stephen, H., 2010. Estimating soil moisture using remote sensing data: A machine learning approach. Adv. Water Resour. 33, 69–80. https://doi.org/10.1016/j.advwatres.2009.10.008
- Albergel, C., Balsamo, G., de Rosnay, P., Muñoz-Sabater, J., Boussetta, S., 2012a. A bare ground evaporation revision in the ECMWF land-surface scheme: evaluation of its impact using ground soil moisture and satellite microwave data. Hydrol. Earth Syst. Sci. 16, 3607–3620. https://doi.org/10.5194/hess-16-3607-2012
- Albergel, C., Rosnay, P. de, Balsamo, G., Isaksen, L., Muñoz-Sabater, J., 2012b. Soil Moisture Analyses at ECMWF: Evaluation Using Global Ground-Based In Situ Observations. J. Hydrometeorol. 13, 1442–1460. https://doi.org/10.1175/JHM-D-11-0107.1
- Albrich, K., Rammer, W., Seidl, R., 2020. Climate change causes critical transitions and irreversible alterations of mountain forests. Glob. Change Biol. 26, 4013–4027. https://doi.org/10.1111/gcb.15118
- Attema, E.P.W., Ulaby, F.T., 1978. Vegetation modeled as a water cloud. Radio Sci. 13, 357–364. https://doi.org/10.1029/RS013i002p00357
- Bachmann, M., Schandri, M., Bojarski, A., Buckreuss, S., Zink, M., 2021. Observation Strategies for TanDEM-X and Tandem-L, in: EUSAR 2021; 13th European Conference on Synthetic Aperture Radar. Presented at the EUSAR 2021; 13th European Conference on Synthetic Aperture Radar, pp. 1–6.
- Baghdadi, N., El Hajj, M., Zribi, M., Bousbih, S., 2017. Calibration of the Water Cloud Model at C-Band for Winter Crop Fields and Grasslands. Remote Sens. 9, 969. https://doi.org/10.3390/rs9090969
- Bakian-Dogaheh, K., Chen, R.H., Yi, Y., Kimball, J.S., Moghaddam, M., Tabatabaeenejad, A., 2022. A model to characterize soil moisture and organic matter profiles in the permafrost active layer in support of radar remote sensing in Alaskan Arctic tundra. Environ. Res. Lett. 17, 025011. https://doi.org/10.1088/1748-9326/ac4e37
- Balenzano, A., Mattia, F., Satalino, G., Lovergine, F.P., Palmisano, D., Peng, J., Marzahn, P.,

- Wegmüller, U., Cartus, O., Dąbrowska-Zielińska, K., Musial, J.P., Davidson, M.W.J., Pauwels, V.R.N., Cosh, M.H., McNairn, H., Johnson, J.T., Walker, J.P., Yueh, S.H., Entekhabi, D., Kerr, Y.H., Jackson, T.J., 2021. Sentinel-1 soil moisture at 1 km resolution: a validation study. Remote Sens. Environ. 263, 112554. https://doi.org/10.1016/j.rse.2021.112554
- Barrett, B.W., Dwyer, E., Whelan, P., 2009. Soil Moisture Retrieval from Active Spaceborne Microwave Observations: An Evaluation of Current Techniques. Remote Sens. 1, 210–242. https://doi.org/10.3390/rs1030210
- Barton, E.J., Taylor, C.M., Klein, C., Harris, P.P., Meng, X., 2021. Observed Soil Moisture Impact on Strong Convection over Mountainous Tibetan Plateau. https://doi.org/10.1175/JHM-D-20-0129.1
- Betts, A.K., Ball, J.H., Beljaars, A.C.M., Miller, M.J., Viterbo, P.A., 1996. The land surface-atmosphere interaction: A review based on observational and global modeling perspectives. J. Geophys. Res. Atmospheres 101, 7209–7225. https://doi.org/10.1029/95JD02135
- Bindlish, R., Barros, A.P., 2001. Parameterization of vegetation backscatter in radar-based, soil moisture estimation. Remote Sens. Environ. 76, 130–137. https://doi.org/10.1016/S0034-4257(00)00200-5
- Black, E., Asfaw, D.T., Sananka, A., Aston, S., Boult, V.L., Maidment, R.I., 2023. Application of TAMSAT-ALERT soil moisture forecasts for planting date decision support in Africa. Front. Clim. 4. https://doi.org/10.3389/fclim.2022.993511
- Boas, T., Bogena, H.R., Ryu, D., Vereecken, H., Western, A., Hendricks Franssen, H.-J., 2023. Seasonal soil moisture and crop yield prediction with fifth-generation seasonal forecasting system (SEAS5) long-range meteorological forecasts in a land surface modelling approach. Hydrol. Earth Syst. Sci. 27, 3143–3167. https://doi.org/10.5194/hess-27-3143-2023
- Bosch, D.D., Coffin, A.W., Sheridan, J., Pisani, O., Endale, D.M., Strickland, T.C., 2021. Little River Experimental Watershed, a keystone in understanding of coastal plain watersheds. Hydrol. Process. 35, e14334. https://doi.org/10.1002/hyp.14334
- Boussetta, S., Balsamo, G., Arduini, G., Dutra, E., McNorton, J., Choulga, M., Agustí-Panareda, A., Beljaars, A., Wedi, N., Munoz-Sabater, J., de Rosnay, P., Sandu, I., Hadade, I., Carver, G., Mazzetti, C., Prudhomme, C., Yamazaki, D., Zsoter, E., 2021. ECLand: The ECMWF Land Surface Modelling System. Atmosphere 12, 723. https://doi.org/10.3390/atmos12060723
- Bovolo, F., Bruzzone, L., 2005. A detail-preserving scale-driven approach to change detection in multitemporal SAR images. IEEE Trans. Geosci. Remote Sens. 43, 2963–2972. https://doi.org/10.1109/TGRS.2005.857987

- Brocca, L., Crow, W.T., Ciabatta, L., Massari, C., de Rosnay, P., Enenkel, M., Hahn, S., Amarnath, G., Camici, S., Tarpanelli, A., Wagner, W., 2017. A Review of the Applications of ASCAT Soil Moisture Products. IEEE J. Sel. Top. Appl. Earth Obs. Remote Sens. 10, 2285–2306. https://doi.org/10.1109/JSTARS.2017.2651140
- Brown, M.E., Escobar, V., Moran, S., Entekhabi, D., O'Neill, P.E., Njoku, E.G., Doorn, B., Entin, J.K., 2013. NASA's Soil Moisture Active Passive (SMAP) Mission and Opportunities for Applications Users. Bull. Am. Meteorol. Soc. 94, 1125–1128. https://doi.org/10.1175/BAMS-D-11-00049.1
- Calvet, J.-C., Wigneron, J.-P., Walker, J., Karbou, F., Chanzy, A., Albergel, C., 2011. Sensitivity of Passive Microwave Observations to Soil Moisture and Vegetation Water Content: L-Band to W-Band. IEEE Trans. Geosci. Remote Sens. 49, 1190–1199. https://doi.org/10.1109/TGRS.2010.2050488
- Chan, S.K., Bindlish, R., O'Neill, P., Jackson, T., Njoku, E., Dunbar, S., Chaubell, J., Piepmeier, J., Yueh, S., Entekhabi, D., Colliander, A., Chen, F., Cosh, M.H., Caldwell, T., Walker, J., Berg, A., McNairn, H., Thibeault, M., Martínez-Fernández, J., Uldall, F., Seyfried, M., Bosch, D., Starks, P., Holifield Collins, C., Prueger, J., van der Velde, R., Asanuma, J., Palecki, M., Small, E.E., Zreda, M., Calvet, J., Crow, W.T., Kerr, Y., 2018. Development and assessment of the SMAP enhanced passive soil moisture product. Remote Sens. Environ. 204, 931–941. https://doi.org/10.1016/j.rse.2017.08.025
- Chao, L., Zhang, K., Wang, S., Gu, Z., Xu, J., Bao, H., 2022. Assimilation of surface soil moisture jointly retrieved by multiple microwave satellites into the WRF-Hydro model in ungauged regions: Towards a robust flood simulation and forecasting. Environ. Model. Softw. 154, 105421. https://doi.org/10.1016/j.envsoft.2022.105421
- Chaudhary, S.K., Srivastava, P.K., Gupta, D.K., Kumar, P., Prasad, R., Pandey, D.K., Das, A.K., Gupta, M., 2022. Machine learning algorithms for soil moisture estimation using Sentinel-1: Model development and implementation. Adv. Space Res., Advances in Spaceborne SAR Remote Sensing for Characterization of Natural and Manmade Features Part 1 69, 1799–1812. https://doi.org/10.1016/j.asr.2021.08.022
- Chawla, I., Osuri, K.K., Mujumdar, P.P., Niyogi, D., 2018. Assessment of the Weather Research and Forecasting (WRF) model for simulation of extreme rainfall events in the upper Ganga Basin. Hydrol. Earth Syst. Sci. 22, 1095–1117. https://doi.org/10.5194/hess-22-1095-2018
- Chen, S.-W., Ohki, M., Shimada, M., Sato, M., 2012. Deorientation effect investigation for model-based decomposition over oriented built-up areas. IEEE Geosci. Remote Sens. Lett. 10, 273–277.
- Cho, E., Choi, M., 2014. Regional scale spatio-temporal variability of soil moisture and its relationship with meteorological factors over the Korean peninsula. J. Hydrol. 516, 317–329. https://doi.org/10.1016/j.jhydrol.2013.12.053

- Ciani, D., Santoleri, R., Liberti, G.L., Prigent, C., Donlon, C., Nardelli, B.B., 2019. Copernicus Imaging Microwave Radiometer (CIMR) benefits for the copernicus level 4 Sea-Surface Salinity processing chain. Remote Sens. 11. https://doi.org/10.3390/rs11151818
- Colliander, A., Jackson, T.J., Bindlish, R., Chan, S., Das, N., Kim, S.B., Cosh, M.H., Dunbar, R.S., Dang, L., Pashaian, L., Asanuma, J., Aida, K., Berg, A., Rowlandson, T., Bosch, D., Caldwell, T., Caylor, K., Goodrich, D., al Jassar, H., Lopez-Baeza, E., Martínez-Fernández, J., González-Zamora, A., Livingston, S., McNairn, H., Pacheco, A., Moghaddam, M., Montzka, C., Notarnicola, C., Niedrist, G., Pellarin, T., Prueger, J., Pulliainen, J., Rautiainen, K., Ramos, J., Seyfried, M., Starks, P., Su, Z., Zeng, Y., van der Velde, R., Thibeault, M., Dorigo, W., Vreugdenhil, M., Walker, J.P., Wu, X., Monerris, A., O'Neill, P.E., Entekhabi, D., Njoku, E.G., Yueh, S., 2017. Validation of SMAP surface soil moisture products with core validation sites. Remote Sens. Environ. 191, 215–231. https://doi.org/10.1016/j.rse.2017.01.021
- Colliander, A., Reichle, R.H., Crow, W.T., Cosh, M.H., Chen, F., Chan, S., Das, N.N., Bindlish, R., Chaubell, J., Kim, S., Liu, Q., O'Neill, P.E., Dunbar, R.S., Dang, L.B., Kimball, J.S., Jackson, T.J., Al-Jassar, H.K., Asanuma, J., Bhattacharya, B.K., Berg, A.A., Bosch, D.D., Bourgeau-Chavez, L., Caldwell, T., Calvet, J.-C., Collins, C.H., Jensen, K.H., Livingston, S., Lopez-Baeza, E., Martínez-Fernández, J., McNairn, H., Moghaddam, M., Montzka, C., Notarnicola, C., Pellarin, T., Greimeister-Pfeil, I., Pulliainen, J., Ramos Hernández, J.Gpe., Seyfried, M., Starks, P.J., Su, Z., van der Velde, R., Zeng, Y., Thibeault, M., Vreugdenhil, M., Walker, J.P., Zribi, M., Entekhabi, D., Yueh, S.H., 2022. Validation of Soil Moisture Data Products From the NASA SMAP Mission. IEEE J. Sel. Top. Appl. Earth Obs. Remote Sens. 15, 364–392. https://doi.org/10.1109/JSTARS.2021.3124743
- Correc, Y., Chapuis, E., 1987. Fast computation of Delaunay triangulations. Adv. Eng. Softw. 1978 9, 77–83. https://doi.org/10.1016/0141-1195(87)90028-3
- Crow, W.T., Kim, H., Kumar, S., 2023. Systematic Modeling Errors Undermine the Application of Land Data Assimilation Systems for Hydrological and Weather Forecasting. https://doi.org/10.1175/JHM-D-23-0069.1
- Crow, W.T., Milak, S., Moghaddam, M., Tabatabaeenejad, A., Jaruwatanadilok, S., Yu, X., Shi, Y., Reichle, R.H., Hagimoto, Y., Cuenca, R.H., 2018. Spatial and Temporal Variability of Root-Zone Soil Moisture Acquired from Hydrologic Modeling and AirMOSS P-Band Radar. IEEE J. Sel. Top. Appl. Earth Obs. Remote Sens. 11, 4578–4590. https://doi.org/10.1109/JSTARS.2018.2865251
- Dai, A., 2013. Increasing drought under global warming in observations and models. Nat. Clim. Change 3, 52–58. https://doi.org/10.1038/nclimate1633
- Daly, C., Halbleib, M., Smith, J.I., Gibson, W.P., Doggett, M.K., Taylor, G.H., Curtis, J., Pasteris, P.P., 2008. Physiographically sensitive mapping of climatological temperature and precipitation across the conterminous United States. Int. J. Climatol. 28, 2031–2064. https://doi.org/10.1002/joc.1688

- Daly, C., Neilson, R.P., Phillips, D.L., 1994. A Statistical-Topographic Model for Mapping Climatological Precipitation over Mountainous Terrain.
- Das, K., Paul, P.K., 2015. Soil moisture retrieval model by using RISAT-1, C-band data in tropical dry and sub-humid zone of Bankura district of India. Egypt. J. Remote Sens. Space Sci. 18, 297–310. https://doi.org/10.1016/j.ejrs.2015.09.004
- Das, N.N., Entekhabi, D., Dunbar, R.S., Chaubell, M.J., Colliander, A., Yueh, S., Jagdhuber, T., Chen, F., Crow, W., O'Neill, P.E., Walker, J.P., Berg, A., Bosch, D.D., Caldwell, T., Cosh, M.H., Collins, C.H., Lopez-Baeza, E., Thibeault, M., 2019. The SMAP and Copernicus Sentinel 1A/B microwave active-passive high resolution surface soil moisture product. Remote Sens. Environ. 233, 111380. https://doi.org/10.1016/j.rse.2019.111380
- Das, N.N., Entekhabi, D., Dunbar, R.S., Colliander, A., Chen, F., Crow, W., Jackson, T.J., Berg, A., Bosch, D.D., Caldwell, T., Cosh, M.H., Collins, C.H., Lopez-Baeza, E., Moghaddam, M., Rowlandson, T., Starks, P.J., Thibeault, M., Walker, J.P., Wu, X., O'Neill, P.E., Yueh, S., Njoku, E.G., 2018. The SMAP mission combined active-passive soil moisture product at 9 km and 3 km spatial resolutions. Remote Sens. Environ. 211, 204–217. https://doi.org/10.1016/j.rse.2018.04.011
- Das, N.N., Entekhabi, D., Dunbar, R.S., Njoku, E.G., Yueh, S.H., 2016. Uncertainty Estimates in the SMAP Combined Active—Passive Downscaled Brightness Temperature. IEEE Trans. Geosci. Remote Sens. 54, 640–650. https://doi.org/10.1109/TGRS.2015.2450694
- Das, N.N., Entekhabi, D., Njoku, E.G., 2011. An Algorithm for Merging SMAP Radiometer and Radar Data for High-Resolution Soil-Moisture Retrieval. IEEE Trans. Geosci. Remote Sens. 49, 1504–1512. https://doi.org/10.1109/TGRS.2010.2089526
- Das, N.N., Entekhabi, D., Njoku, E.G., Shi, J.J.C., Johnson, J.T., Colliander, A., 2014. Tests of the SMAP Combined Radar and Radiometer Algorithm Using Airborne Field Campaign Observations and Simulated Data. IEEE Trans. Geosci. Remote Sens. 52, 2018–2028. https://doi.org/10.1109/TGRS.2013.2257605
- Davidson, M., Kubanek, J., Iannini, L., Furnell, R., Di Cosimo, G., Gebert, N., Petrolati, D., Geudtner, D., Osborne, S., 2023. Rose-L The Copernicus L-Band Synthetic Aperture Radar Imaging Mission, in: IGARSS 2023 2023 IEEE International Geoscience and Remote Sensing Symposium. Presented at the IGARSS 2023 2023 IEEE International Geoscience and Remote Sensing Symposium, pp. 4568–4571. https://doi.org/10.1109/IGARSS52108.2023.10281640
- Davidson, M.W.J., Furnell, R., 2021. ROSE-L: Copernicus L-Band Sar Mission, in: 2021 IEEE International Geoscience and Remote Sensing Symposium IGARSS. Presented at the 2021 IEEE International Geoscience and Remote Sensing Symposium IGARSS, pp. 872–873. https://doi.org/10.1109/IGARSS47720.2021.9554018
- De Lannoy, G.J.M., Reichle, R.H., Vrugt, J.A., 2014. Uncertainty quantification of GEOS-5 L-

- band radiative transfer model parameters using Bayesian inference and SMOS observations. REMOTE Sens. Environ. 148, 146–157. https://doi.org/10.1016/j.rse.2014.03.030
- de Lara, A., Longchamps, L., Khosla, R., 2019. Soil Water Content and High-Resolution Imagery for Precision Irrigation: Maize Yield. Agronomy 9, 174. https://doi.org/10.3390/agronomy9040174
- Dee, D.P., Uppala, S.M., Simmons, A.J., Berrisford, P., Poli, P., Kobayashi, S., Andrae, U., Balmaseda, M.A., Balsamo, G., Bauer, P., Bechtold, P., Beljaars, A.C.M., van de Berg, L., Bidlot, J., Bormann, N., Delsol, C., Dragani, R., Fuentes, M., Geer, A.J., Haimberger, L., Healy, S.B., Hersbach, H., Hólm, E.V., Isaksen, L., Kållberg, P., Köhler, M., Matricardi, M., McNally, A.P., Monge-Sanz, B.M., Morcrette, J.-J., Park, B.-K., Peubey, C., de Rosnay, P., Tavolato, C., Thépaut, J.-N., Vitart, F., 2011. The ERA-Interim reanalysis: configuration and performance of the data assimilation system. Q. J. R. Meteorol. Soc. 137, 553–597. https://doi.org/10.1002/qj.828
- Deng, L., Yan, W., Zhang, Y., Shangguan, Z., 2016. Severe depletion of soil moisture following land-use changes for ecological restoration: Evidence from northern China. For. Ecol. Manag. 366, 1–10. https://doi.org/10.1016/j.foreco.2016.01.026
- Deng, Y., Wang, S., Bai, X., Luo, G., Wu, L., Cao, Y., Li, H., Li, C., Yang, Y., Hu, Z., Tian, S., 2020. Variation trend of global soil moisture and its cause analysis. Ecol. Indic. 110, 105939. https://doi.org/10.1016/j.ecolind.2019.105939
- Deng, Y., Wang, S., Bai, X., Tian, Y., Wu, L., Xiao, J., Chen, F., Qian, Q., 2018. Relationship among land surface temperature and LUCC, NDVI in typical karst area. Sci. Rep. 8. https://doi.org/10.1038/s41598-017-19088-x
- Devia, G.K., Ganasri, B.P., Dwarakish, G.S., 2015. A Review on Hydrological Models. Aquat. Procedia, INTERNATIONAL CONFERENCE ON WATER RESOURCES, COASTAL AND OCEAN ENGINEERING (ICWRCOE'15) 4, 1001–1007. https://doi.org/10.1016/j.aqpro.2015.02.126
- Dierking, W., 2021. Synergistic Use of L- and C-Band SAR Satellites for Sea Ice Monitoring, in: 2021 IEEE International Geoscience and Remote Sensing Symposium IGARSS. Presented at the 2021 IEEE International Geoscience and Remote Sensing Symposium IGARSS, pp. 877–880. https://doi.org/10.1109/IGARSS47720.2021.9554359
- Donlon, C., Galeazzi, C., Midthassel, R., Sallusti, M., Triggianese, M., Fiorelli, B., De Paris, G., Kornienko, A., Khlystova, I., 2023. The Copernicus Imaging Microwave Radiometer (CIMR): Mission Overview and Status, in: IGARSS 2023 2023 IEEE International Geoscience and Remote Sensing Symposium. Presented at the IGARSS 2023 2023 IEEE International Geoscience and Remote Sensing Symposium, pp. 989–992. https://doi.org/10.1109/IGARSS52108.2023.10281934

- Dorigo, W., Himmelbauer, I., Aberer, D., Schremmer, L., Petrakovic, I., Zappa, L., Preimesberger, W., Xaver, A., Annor, F., Ardö, J., Baldocchi, D., Bitelli, M., Blöschl, G., Bogena, H., Brocca, L., Calvet, J.-C., Camarero, J.J., Capello, G., Choi, M., Cosh, M.C., van de Giesen, N., Hajdu, I., Ikonen, J., Jensen, K.H., Kanniah, K.D., de Kat, I., Kirchengast, G., Kumar Rai, P., Kyrouac, J., Larson, K., Liu, S., Loew, A., Moghaddam, M., Martínez Fernández, J., Mattar Bader, C., Morbidelli, R., Musial, J.P., Osenga, E., Palecki, M.A., Pellarin, T., Petropoulos, G.P., Pfeil, I., Powers, J., Robock, A., Rüdiger, C., Rummel, U., Strobel, M., Su, Z., Sullivan, R., Tagesson, T., Varlagin, A., Vreugdenhil, M., Walker, J., Wen, J., Wenger, F., Wigneron, J.P., Woods, M., Yang, K., Zeng, Y., Zhang, X., Zreda, M., Dietrich, S., Gruber, A., van Oevelen, P., Wagner, W., Scipal, K., Drusch, M., Sabia, R., 2021. The International Soil Moisture Network: serving Earth system science for over a decade. Hydrol. Earth Syst. Sci. 25, 5749–5804. https://doi.org/10.5194/hess-25-5749-2021
- Dorigo, W., van Oevelen, P., Wagner, W., Drusch, M., Mecklenburg, S., Robock, A., Jackson, T., 2011. A New International Network for in Situ Soil Moisture Data. Eos Trans. Am. Geophys. Union 92, 141–142. https://doi.org/10.1029/2011EO170001
- Dorigo, W., Wagner, W., Albergel, C., Albrecht, F., Balsamo, G., Brocca, L., Chung, D., Ertl, M., Forkel, M., Gruber, A., Haas, E., Hamer, P.D., Hirschi, M., Ikonen, J., de Jeu, R., Kidd, R., Lahoz, W., Liu, Y.Y., Miralles, D., Mistelbauer, T., Nicolai-Shaw, N., Parinussa, R., Pratola, C., Reimer, C., van der Schalie, R., Seneviratne, S.I., Smolander, T., Lecomte, P., 2017. ESA CCI Soil Moisture for improved Earth system understanding: State-of-the art and future directions. Remote Sens. Environ., Earth Observation of Essential Climate Variables 203, 185–215. https://doi.org/10.1016/j.rse.2017.07.001
- Du, Y., Ulaby, F.T., Dobson, M.C., 2000. Sensitivity to soil moisture by active and passive microwave sensors. IEEE Trans. Geosci. Remote Sens. 38, 105–114.
- Dubey, A.K., Lal, P., Kumar, P., Kumar, A., Dvornikov, A.Y., 2021. Present and future projections of heatwave hazard-risk over India: A regional earth system model assessment. Environ. Res. 201, 111573. https://doi.org/10.1016/j.envres.2021.111573
- D'Urso, G., Minacapilli, M., 2006. A semi-empirical approach for surface soil water content estimation from radar data without a-priori information on surface roughness. J. Hydrol. 321, 297–310. https://doi.org/10.1016/j.jhydrol.2005.08.013
- El Hajj, M., Baghdadi, N., Zribi, M., Belaud, G., Cheviron, B., Courault, D., Charron, F., 2016. Soil moisture retrieval over irrigated grassland using X-band SAR data. Remote Sens. Environ. 176, 202–218. https://doi.org/10.1016/j.rse.2016.01.027
- Engman, E.T., Chauhan, N., 1995. Status of microwave soil moisture measurements with remote sensing. Remote Sens. Environ., Remote Sensing of Land Surface for Studies of Global Chage 51, 189–198. https://doi.org/10.1016/0034-4257(94)00074-W
- Entekhabi, D., Njoku, E.G., O'Neill, P.E., Kellogg, K.H., Crow, W.T., Edelstein, W.N., Entin,

- J.K., Goodman, S.D., Jackson, T.J., Johnson, J., Kimball, J., Piepmeier, J.R., Koster, R.D., Martin, N., McDonald, K.C., Moghaddam, M., Moran, S., Reichle, R., Shi, J.C., Spencer, M.W., Thurman, S.W., Tsang, L., Van Zyl, J., 2010. The Soil Moisture Active Passive (SMAP) Mission. Proc. IEEE 98, 704–716. https://doi.org/10.1109/JPROC.2010.2043918
- Escorihuela, M.J., Merlin, O., Stefan, V., Moyano, G., Eweys, O.A., Zribi, M., Kamara, S., Benahi, A.S., Ebbe, M.A.B., Chihrane, J., Ghaout, S., Cissé, S., Diakité, F., Lazar, M., Pellarin, T., Grippa, M., Cressman, K., Piou, C., 2018. SMOS based high resolution soil moisture estimates for desert locust preventive management. Remote Sens. Appl. Soc. Environ. 11, 140–150. https://doi.org/10.1016/j.rsase.2018.06.002
- Ettalbi, M., Baghdadi, N., Garambois, P., Bazzi, H., Ferreira, E., Zribi, M., 2023. Soil Moisture Retrieval in Bare Agricultural Areas Using Sentinel-1 Images. REMOTE Sens. 15. https://doi.org/10.3390/rs15143502
- Fairbairn, D., de Rosnay, P., Weston, P., 2024. Evaluation of an Adaptive Soil Moisture Bias Correction Approach in the ECMWF Land Data Assimilation System. Remote Sens. 16, 493. https://doi.org/10.3390/rs16030493
- Fakharizadehshirazi, E., Sabziparvar, A.A., Sodoudi, S., 2019. Long-term spatiotemporal variations in satellite-based soil moisture and vegetation indices over Iran. Environ. Earth Sci. 78, 342. https://doi.org/10.1007/s12665-019-8347-4
- Fan, L., Al-Yaari, A., Frappart, F., Peng, J., Wen, J., Xiao, Q., Jin, R., Li, X., Liu, X., Wang, M., Chen, X., Zhao, L., Ma, M., Wigneron, J., 2022. Estimating High-Resolution Soil Moisture Over Mountainous Regions Using Remotely-Sensed Multispectral and Topographic Data. IEEE J. Sel. Top. Appl. EARTH Obs. REMOTE Sens. 15, 3637–3649. https://doi.org/10.1109/JSTARS.2022.3166974
- Feng, H., Zhang, M., 2015. Global land moisture trends: drier in dry and wetter in wet over land. Sci. Rep. 5, 18018. https://doi.org/10.1038/srep18018
- Fischer, E.M., Seneviratne, S.I., Vidale, P.L., Lüthi, D., Schär, C., 2007. Soil Moisture–Atmosphere Interactions during the 2003 European Summer Heat Wave. J. Clim. 20, 5081–5099. https://doi.org/10.1175/JCLI4288.1
- Frank, Dorothea, Reichstein, M., Bahn, M., Thonicke, K., Frank, David, Mahecha, M.D., Smith, P., Van Der Velde, M., Vicca, S., Babst, F., Beer, C., Buchmann, N., Canadell, J.G., Ciais, P., Cramer, W., Ibrom, A., Miglietta, F., Poulter, B., Rammig, A., Seneviratne, S.I., Walz, A., Wattenbach, M., Zavala, M.A., Zscheischler, J., 2015. Effects of climate extremes on the terrestrial carbon cycle: concepts, processes and potential future impacts. Glob. Change Biol. 21, 2861–2880. https://doi.org/10.1111/gcb.12916
- Friedl, M.A., McIver, D.K., Hodges, J.C.F., Zhang, X.Y., Muchoney, D., Strahler, A.H., Woodcock, C.E., Gopal, S., Schneider, A., Cooper, A., Baccini, A., Gao, F., Schaaf, C., 2002. Global land cover mapping from MODIS: algorithms and early results. Remote Sens.

- Environ., The Moderate Resolution Imaging Spectroradiometer (MODIS): a new generation of Land Surface Monitoring 83, 287–302. https://doi.org/10.1016/S0034-4257(02)00078-0
- Friedl, M.A., Sulla-Menashe, D., Tan, B., Schneider, A., Ramankutty, N., Sibley, A., Huang, X., 2010. MODIS Collection 5 global land cover: Algorithm refinements and characterization of new datasets. Remote Sens. Environ. 114, 168–182. https://doi.org/10.1016/j.rse.2009.08.016
- Fung, A.K., Li, Z., Chen, K.S., 1992. Backscattering from a randomly rough dielectric surface. IEEE Trans. Geosci. Remote Sens. 30, 356–369. https://doi.org/10.1109/36.134085
- Gao, L., Sadeghi, M., Feldman, A.F., Ebtehaj, A., 2020. A Spatially Constrained Multichannel Algorithm for Inversion of a First-Order Microwave Emission Model at L-Band. IEEE Trans. Geosci. Remote Sens. 58, 8134–8146. https://doi.org/10.1109/TGRS.2020.2987490
- Geudtner, D., Tossaint, M., 2021. Sentinel-1 Next Generation: C-band Data Continuity and Novel Capabilities, in: EUSAR 2021; 13th European Conference on Synthetic Aperture Radar. Presented at the EUSAR 2021; 13th European Conference on Synthetic Aperture Radar, pp. 1–4.
- Geudtner, D., Tossaint, M., Davidson, M., Torres, R., 2021. Copernicus Sentinel-1 Next Generation Mission, in: 2021 IEEE International Geoscience and Remote Sensing Symposium IGARSS. Presented at the 2021 IEEE International Geoscience and Remote Sensing Symposium IGARSS, pp. 874–876. https://doi.org/10.1109/IGARSS47720.2021.9554226
- Gharechelou, S., Tateishi, R., Sri Sumantyo, J.T., Johnson, B.A., 2021. Soil Moisture Retrieval Using Polarimetric SAR Data and Experimental Observations in an Arid Environment. ISPRS Int. J. Geo-Inf. 10, 711. https://doi.org/10.3390/ijgi10100711
- González Perea, R., Camacho Poyato, E., Montesinos, P., Rodríguez Díaz, J.A., 2016. Optimization of Irrigation Scheduling Using Soil Water Balance and Genetic Algorithms. Water Resour. Manag. 30, 2815–2830. https://doi.org/10.1007/s11269-016-1325-7
- Grimm, N.B., Chapin, F.S., Bierwagen, B., Gonzalez, P., Groffman, P.M., Luo, Y., Melton, F., Nadelhoffer, K., Pairis, A., Raymond, P.A., Schimel, J., Williamson, C.E., 2013. The impacts of climate change on ecosystem structure and function. Front. Ecol. Environ. 11, 474–482. https://doi.org/10.1890/120282
- Gruber, A., De Lannoy, G., Crow, W., 2019. A Monte Carlo based adaptive Kalman filtering framework for soil moisture data assimilation. Remote Sens. Environ. 228, 105–114. https://doi.org/10.1016/j.rse.2019.04.003
- Han, Y., Bai, X., Shao, W., Wang, J., 2020. Retrieval of Soil Moisture by Integrating Sentinel-1A and MODIS Data over Agricultural Fields. WATER 12.

- https://doi.org/10.3390/w12061726
- Hassan-Esfahani, L., Torres-Rua, A., Jensen, A., McKee, M., 2015. Assessment of Surface Soil Moisture Using High-Resolution Multi-Spectral Imagery and Artificial Neural Networks. REMOTE Sens. https://doi.org/10.3390/rs70302627
- Hersbach, H., Bell, B., Berrisford, P., Hirahara, S., Horányi, A., Muñoz-Sabater, J., Nicolas, J., Peubey, C., Radu, R., Schepers, D., Simmons, A., Soci, C., Abdalla, S., Abellan, X., Balsamo, G., Bechtold, P., Biavati, G., Bidlot, J., Bonavita, M., De Chiara, G., Dahlgren, P., Dee, D., Diamantakis, M., Dragani, R., Flemming, J., Forbes, R., Fuentes, M., Geer, A., Haimberger, L., Healy, S., Hogan, R.J., Hólm, E., Janisková, M., Keeley, S., Laloyaux, P., Lopez, P., Lupu, C., Radnoti, G., de Rosnay, P., Rozum, I., Vamborg, F., Villaume, S., Thépaut, J.-N., 2020. The ERA5 global reanalysis. Q. J. R. Meteorol. Soc. 146, 1999–2049. https://doi.org/10.1002/qj.3803
- Hijmans, R.J., Van Etten, J., Cheng, J., Mattiuzzi, M., Sumner, M., Greenberg, J.A., Lamigueiro, O.P., Bevan, A., Racine, E.B., Shortridge, A., others, 2015. Package 'raster.' R Package 734, 473.
- Holah, N., Baghdadi, N., Zribi, M., Bruand, A., King, C., 2005. Potential of ASAR/ENVISAT for the characterization of soil surface parameters over bare agricultural fields. Remote Sens. Environ. 96, 78–86. https://doi.org/10.1016/j.rse.2005.01.008
- Holgate, C.M., De Jeu, R.A.M., van Dijk, A.I.J.M., Liu, Y.Y., Renzullo, L.J., Vinodkumar, Dharssi, I., Parinussa, R.M., Van Der Schalie, R., Gevaert, A., Walker, J., McJannet, D., Cleverly, J., Haverd, V., Trudinger, C.M., Briggs, P.R., 2016. Comparison of remotely sensed and modelled soil moisture data sets across Australia. Remote Sens. Environ. 186, 479–500. https://doi.org/10.1016/j.rse.2016.09.015
- Hornacek, M., Wagner, W., Sabel, D., Truong, H.-L., Snoeij, P., Hahmann, T., Diedrich, E., Doubkova, M., 2012. Potential for High Resolution Systematic Global Surface Soil Moisture Retrieval via Change Detection Using Sentinel-1. IEEE J. Sel. Top. Appl. Earth Obs. Remote Sens. 5, 1303–1311. https://doi.org/10.1109/JSTARS.2012.2190136
- Hornbuckle, B.K., England, A.W., 2005. Diurnal variation of vertical temperature gradients within a field of maize: implications for Satellite microwave radiometry. IEEE Geosci. Remote Sens. Lett. 2, 74–77. https://doi.org/10.1109/LGRS.2004.841370
- Hoskera, A.K., Nico, G., Irshad Ahmed, M., Whitbread, A., 2020. Accuracies of Soil Moisture Estimations Using a Semi-Empirical Model over Bare Soil Agricultural Croplands from Sentinel-1 SAR Data. Remote Sens. 12, 1664. https://doi.org/10.3390/rs12101664
- Hu, Y., Dong, Y., Batunacun, 2018. An automatic approach for land-change detection and land updates based on integrated NDVI timing analysis and the CVAPS method with GEE support. ISPRS J. Photogramm. Remote Sens. 146, 347–359. https://doi.org/10.1016/j.isprsjprs.2018.10.008

- Huang, S., Zhang, X., Chen, N., Ma, H., Fu, P., Dong, J., Gu, X., Nam, W.-H., Xu, L., Rab, G., Niyogi, D., 2022. A Novel Fusion Method for Generating Surface Soil Moisture Data With High Accuracy, High Spatial Resolution, and High Spatio-Temporal Continuity. WATER Resour. Res. https://doi.org/10.1029/2021WR030827
- Huffman, G., 2015. GPM IMERG final precipitation L3 1 month 0.1 degree\$\textbackslashtimes\$ 0.1 degree V04, Greenbelt, MD, Goddard Earth Sciences Data and Information Services Center (GES DISC).
- Huffman, G., Bolvin, D., Braithwaite, D., Hsu, K., Joyce, R., Xie, P., 2014. Integrated Multi-satellitE Retrievals for GPM (IMERG), version 4.4. NASA's Precipitation Processing Center.
- Humphrey, V., Berg, A., Ciais, P., Gentine, P., Jung, M., Reichstein, M., Seneviratne, S.I., Frankenberg, C., 2021. Soil moisture—atmosphere feedback dominates land carbon uptake variability. Nature 592, 65–69. https://doi.org/10.1038/s41586-021-03325-5
- Jackson, T.J., Schmugge, T.J., 1991. Vegetation effects on the microwave emission of soils. Remote Sens. Environ. 36, 203–212. https://doi.org/10.1016/0034-4257(91)90057-D
- Jaeger, E.B., Seneviratne, S.I., 2011. Impact of soil moisture—atmosphere coupling on European climate extremes and trends in a regional climate model. Clim. Dyn. 36, 1919–1939. https://doi.org/10.1007/s00382-010-0780-8
- Jalilvand, E., Abolafia-Rosenzweig, R., Tajrishy, M., Kumar, S.V., Mohammadi, M.R., Das, N.N., 2023. Is it Possible to Quantify Irrigation Water-Use by Assimilating a High-Resolution Satellite Soil Moisture Product? Water Resour. Res. e2022WR033342. https://doi.org/10.1029/2022WR033342
- Jin, N., Tao, B., Ren, W., He, L., Zhang, D., Wang, D., Yu, Q., 2022. Assimilating remote sensing data into a crop model improves winter wheat yield estimation based on regional irrigation data. Agric. Water Manag. 266, 107583. https://doi.org/10.1016/j.agwat.2022.107583
- Jones, C.E., P, M., Rao, S., 2021. The NISAR Mission's Capabilities for Natural Hazards Monitoring, in: 2021 IEEE International Geoscience and Remote Sensing Symposium IGARSS. Presented at the 2021 IEEE International Geoscience and Remote Sensing Symposium IGARSS, pp. 1711–1714. https://doi.org/10.1109/IGARSS47720.2021.9553295
- Kannenberg, S.A., Anderegg, W.R.L., Barnes, M.L., Dannenberg, M.P., Knapp, A.K., 2024. Dominant role of soil moisture in mediating carbon and water fluxes in dryland ecosystems. Nat. Geosci. 17, 38–43. https://doi.org/10.1038/s41561-023-01351-8
- Kao, R.H., Gibson, C.M., Gallery, R.E., Meier, C.L., Barnett, D.T., Docherty, K.M., Blevins, K.K., Travers, P.D., Azuaje, E., Springer, Y.P., Thibault, K.M., McKenzie, V.J., Keller, M., Alves, L.F., Hinckley, E.-L.S., Parnell, J., Schimel, D., 2012. NEON terrestrial field

- observations: designing continental-scale, standardized sampling. Ecosphere 3, art115. https://doi.org/10.1890/ES12-00196.1
- Kashyap, B., Kumar, R., 2021. Sensing Methodologies in Agriculture for Soil Moisture and Nutrient Monitoring. IEEE Access 9, 14095–14121. https://doi.org/10.1109/ACCESS.2021.3052478
- Kawanishi, T., Sezai, T., Ito, Y., Imaoka, K., Takeshima, T., Ishido, Y., Shibata, A., Miura, M., Inahata, H., Spencer, R.W., 2003. The Advanced Microwave Scanning Radiometer for the Earth Observing System (AMSR-E), NASDA's contribution to the EOS for global energy and water cycle studies. IEEE Trans. Geosci. Remote Sens. 41, 184–194. https://doi.org/10.1109/TGRS.2002.808331
- Kellogg, K., Hoffman, P., Standley, S., Shaffer, S., Rosen, P., Edelstein, W., Dunn, C., Baker, C., Barela, P., Shen, Y., Guerrero, A.M., Xaypraseuth, P., Sagi, V.R., Sreekantha, C.V., Harinath, N., Kumar, R., Bhan, R., Sarma, C.V.H.S., 2020. NASA-ISRO Synthetic Aperture Radar (NISAR) Mission, in: 2020 IEEE Aerospace Conference. Presented at the 2020 IEEE Aerospace Conference, pp. 1–21. https://doi.org/10.1109/AERO47225.2020.9172638
- Kerr, Y.H., Waldteufel, P., Richaume, P., Wigneron, J.P., Ferrazzoli, P., Mahmoodi, A., Al Bitar, A., Cabot, F., Gruhier, C., Juglea, S.E., Leroux, D., Mialon, A., Delwart, S., 2012. The SMOS Soil Moisture Retrieval Algorithm. IEEE Trans. Geosci. Remote Sens. 50, 1384–1403. https://doi.org/10.1109/TGRS.2012.2184548
- Kerr, Y.H., Waldteufel, P., Wigneron, J.-P., Delwart, S., Cabot, F., Boutin, J., Escorihuela, M.-J., Font, J., Reul, N., Gruhier, C., Juglea, S.E., Drinkwater, M.R., Hahne, A., Martín-Neira, M., Mecklenburg, S., 2010. The SMOS Mission: New Tool for Monitoring Key Elements of the Global Water Cycle. Proc. IEEE 98, 666–687. https://doi.org/10.1109/JPROC.2010.2043032
- Kim, S., Liu, Yi.Y., Johnson, F.M., Parinussa, R.M., Sharma, A., 2015. A global comparison of alternate AMSR2 soil moisture products: Why do they differ? Remote Sens. Environ. 161, 43–62. https://doi.org/10.1016/j.rse.2015.02.002
- Kim, S.-B., Tsang, L., Johnson, J.T., Huang, S., van Zyl, J.J., Njoku, E.G., 2012. Soil Moisture Retrieval Using Time-Series Radar Observations Over Bare Surfaces. IEEE Trans. Geosci. Remote Sens. 50, 1853–1863. https://doi.org/10.1109/TGRS.2011.2169454
- Kim, Y., van Zyl, J.J., 2009. A Time-Series Approach to Estimate Soil Moisture Using Polarimetric Radar Data. IEEE Trans. Geosci. Remote Sens. 47, 2519–2527. https://doi.org/10.1109/TGRS.2009.2014944
- Komma, J., Blöschl, G., Reszler, C., 2008. Soil moisture updating by Ensemble Kalman Filtering in real-time flood forecasting. J. Hydrol. 357, 228–242. https://doi.org/10.1016/j.jhydrol.2008.05.020

- Kornelsen, K.C., Coulibaly, P., 2013. Advances in soil moisture retrieval from synthetic aperture radar and hydrological applications. J. Hydrol. 476, 460–489. https://doi.org/10.1016/j.jhydrol.2012.10.044
- Koster, R.D., Crow, W.T., Reichle, R.H., Mahanama, S.P., 2018. Estimating Basin-Scale Water Budgets With SMAP Soil Moisture Data. Water Resour. Res. 54, 4228–4244. https://doi.org/10.1029/2018WR022669
- Koster, R.D., Dirmeyer, P.A., Guo, Z., Bonan, G., Chan, E., Cox, P., Gordon, C.T., Kanae, S., Kowalczyk, E., Lawrence, D., Liu, P., Lu, C.-H., Malyshev, S., McAvaney, B., Mitchell, K., Mocko, D., Oki, T., Oleson, K., Pitman, A., Sud, Y.C., Taylor, C.M., Verseghy, D., Vasic, R., Xue, Y., Yamada, T., 2004. Regions of Strong Coupling Between Soil Moisture and Precipitation. Science 305, 1138–1140. https://doi.org/10.1126/science.1100217
- Kuang, W., Gao, X., Tenuta, M., Gui, D., Zeng, F., 2019. Relationship between soil profile accumulation and surface emission of N2O: effects of soil moisture and fertilizer nitrogen. Biol. Fertil. Soils 55, 97–107. https://doi.org/10.1007/s00374-018-01337-4
- Kwon, Y., Kumar, S.V., Navari, M., Mocko, D.M., Kemp, E.M., Wegiel, J.W., Geiger, J.V., Bindlish, R., 2022. Irrigation characterization improved by the direct use of SMAP soil moisture anomalies within a data assimilation system. Environ. Res. Lett. 17, 084006. https://doi.org/10.1088/1748-9326/ac7f49
- Lal, P., Dubey, A.K., Kumar, A., Kumar, P., Dwivedi, C.S., 2022a. Measuring the control of landscape modifications on surface temperature in India. Geocarto Int. 1–18. https://doi.org/10.1080/10106049.2022.2102224
- Lal, P., Kumar, A., Saikia, P., Das, A., Patnaik, C., Kumar, G., Pandey, A.C., Srivastava, P., Dwivedi, C.S., Khan, M.L., 2022b. Effect of vegetation structure on above ground biomass in tropical deciduous forests of Central India. Geocarto Int. 37, 6294–6310. https://doi.org/10.1080/10106049.2021.1936213
- Lal, P., Shekhar, A., Gharun, M., Das, N.N., 2023a. Spatiotemporal evolution of global long-term patterns of soil moisture. Sci. Total Environ. 161470. https://doi.org/10.1016/j.scitotenv.2023.161470
- Lal, P., Shekhar, A., Kumar, A., 2021. Quantifying Temperature and Precipitation Change Caused by Land Cover Change: A Case Study of India Using the WRF Model. Front. Environ. Sci. 9, 588. https://doi.org/10.3389/fenvs.2021.766328
- Lal, P., Singh, G., Das, N.N., Colliander, A., Entekhabi, D., 2022c. Assessment of ERA5-Land Volumetric Soil Water Layer Product Using In Situ and SMAP Soil Moisture Observations. IEEE Geosci. Remote Sens. Lett. 19, 1–5. https://doi.org/10.1109/LGRS.2022.3223985
- Lal, P., Singh, G., Das, N.N., Entekhabi, D., Lohman, R., Colliander, A., Pandey, D.K., Setia,

- R.K., 2023b. A multi-scale algorithm for the NISAR mission high-resolution soil moisture product. Remote Sens. Environ. 295, 113667. https://doi.org/10.1016/j.rse.2023.113667
- Le Toan, T., 2014. A P-band SAR for global forest biomass measurement: The BIOMASS mission, in: 2014 XXXIth URSI General Assembly and Scientific Symposium (URSI GASS). Presented at the 2014 XXXIth URSI General Assembly and Scientific Symposium (URSI GASS), pp. 1–2. https://doi.org/10.1109/URSIGASS.2014.6929692
- Leroux, D.J., Das, N.N., Entekhabi, D., Colliander, A., Njoku, E.G., Dunbar, R.S., Yueh, S.H., 2016. Active—Passive Disaggregation of Brightness Temperatures During the SMAPVEX12 Campaign. IEEE Trans. Geosci. Remote Sens. 54, 6859–6867. https://doi.org/10.1109/TGRS.2016.2572107
- Lin, D., Yuan, X., Jia, B., Ji, P., 2023. Assessment of High-Resolution Surface Soil Moisture Products over the Qinghai—Tibet Plateau for 2009–2017. Atmosphere 14. https://doi.org/10.3390/atmos14020302
- Liu, J., Rahmani, F., Lawson, K., Shen, C., 2022. A Multiscale Deep Learning Model for Soil Moisture Integrating Satellite and In Situ Data. Geophys. Res. Lett. 49, e2021GL096847. https://doi.org/10.1029/2021GL096847
- Liu, S., Li, X., Chen, D., Duan, Y., Ji, H., Zhang, L., 2020. Understanding the land use/land cover dynamics and impacts of human activities in the Mekong Delta over the last 40 years. Glob. Ecol. Conserv. e00991. https://doi.org/10.1016/j.gecco.2020.e00991
- Liu, Y., Yang, Y., 2022. Advances in the Quality of Global Soil Moisture Products: A Review. Remote Sens. 14, 3741. https://doi.org/10.3390/rs14153741
- Ma, T., Han, L., Liu, Q., 2021. Retrieving the Soil Moisture in Bare Farmland Areas Using a Modified Dubois Model. Front. Earth Sci. 9. https://doi.org/10.3389/feart.2021.735958
- Mane, S., Das, N., Singh, G., Cosh, M., Dong, Y., 2024. Advancements in dielectric soil moisture sensor Calibration: A comprehensive review of methods and techniques. Comput. Electron. Agric. 218, 108686. https://doi.org/10.1016/j.compag.2024.108686
- Martens, B., Schumacher, D.L., Wouters, H., Muñoz-Sabater, J., Verhoest, N.E.C., Miralles, D.G., 2020. Evaluating the land-surface energy partitioning in ERA5. Geosci. Model Dev. 13, 4159–4181. https://doi.org/10.5194/gmd-13-4159-2020
- Martínez-Fernández, J., Ruiz-Benito, P., Bonet, A., Gómez, C., 2019. Methodological variations in the production of CORINE land cover and consequences for long-term land cover change studies. The case of Spain. Int. J. Remote Sens. 1–19.
- Massari, C., Camici, S., Ciabatta, L., Brocca, L., 2018. Exploiting Satellite-Based Surface Soil Moisture for Flood Forecasting in the Mediterranean Area: State Update Versus Rainfall Correction. Remote Sens. 10, 292. https://doi.org/10.3390/rs10020292

- Mathieu, R., Sbih, M., Viau, A.A., Anctil, F., Parent, L.E., Boisvert, J., 2003. Relationships between Radarsat SAR data and surface moisture content of agricultural organic soils. Int. J. Remote Sens. 24, 5265–5281. https://doi.org/10.1080/0143116031000115247
- Mattar, C., Wigneron, J.-P., Sobrino, J.A., Novello, N., Calvet, J.C., Albergel, C., Richaume, P., Mialon, A., Guyon, D., Carlos Jimenez-Munoz, J., Kerr, Y., 2012. A Combined Optical-Microwave Method to Retrieve Soil Moisture Over Vegetated Areas. IEEE Trans. Geosci. REMOTE Sens. 50, 1404–1413. https://doi.org/10.1109/TGRS.2011.2179051
- Mattia, F., Satalino, G., Dente, L., Pasquariello, G., 2006. Using a priori information to improve soil moisture retrieval from ENVISAT ASAR AP data in semiarid regions. IEEE Trans. Geosci. Remote Sens. 44, 900–912. https://doi.org/10.1109/TGRS.2005.863483
- McNairn, H., Jackson, T.J., Wiseman, G., Bélair, S., Berg, A., Bullock, P., Colliander, A., Cosh, M.H., Kim, S.-B., Magagi, R., Moghaddam, M., Njoku, E.G., Adams, J.R., Homayouni, S., Ojo, E.R., Rowlandson, T.L., Shang, J., Goïta, K., Hosseini, M., 2015. The Soil Moisture Active Passive Validation Experiment 2012 (SMAPVEX12): Prelaunch Calibration and Validation of the SMAP Soil Moisture Algorithms. IEEE Trans. Geosci. Remote Sens. 53, 2784–2801. https://doi.org/10.1109/TGRS.2014.2364913
- Merlin, O., Chehbouni, A., Walker, J.P., Panciera, R., Kerr, Y.H., 2008. A Simple Method to Disaggregate Passive Microwave-Based Soil Moisture. IEEE Trans. Geosci. Remote Sens. 46, 786–796. https://doi.org/10.1109/TGRS.2007.914807
- Metzger, S., Ayres, E., Durden, D., Florian, C., Lee, R., Lunch, C., Luo, H., Pingintha-Durden, N., Roberti, J.A., SanClements, M., Sturtevant, C., Xu, K., Zulueta, R.C., 2019. From NEON Field Sites to Data Portal: A Community Resource for Surface–Atmosphere Research Comes Online. Bull. Am. Meteorol. Soc. 100, 2305–2325. https://doi.org/10.1175/BAMS-D-17-0307.1
- Mishra, A., Alnahit, A., Campbell, B., 2020. Impact of land uses, drought, flood, wildfire, and cascading events on water quality and microbial communities: A review and analysis. J. Hydrol. 125707. https://doi.org/10.1016/j.jhydrol.2020.125707
- Mladenova, I.E., Jackson, T.J., Bindlish, R., Hensley, S., 2013. Incidence Angle Normalization of Radar Backscatter Data. IEEE Trans. Geosci. Remote Sens. 51, 1791–1804. https://doi.org/10.1109/TGRS.2012.2205264
- Moghaddam, M., Entekhabi, D., Goykhman, Y., Li, K., Liu, M., Mahajan, A., Nayyar, A., Shuman, D., Teneketzis, D., 2010. A Wireless Soil Moisture Smart Sensor Web Using Physics-Based Optimal Control: Concept and Initial Demonstrations. IEEE J. Sel. Top. Appl. Earth Obs. Remote Sens. 3, 522–535. https://doi.org/10.1109/JSTARS.2010.2052918
- Moosavi, V., Talebi, A., Mokhtari, M.H., Hadian, M.R., 2016. Estimation of spatially enhanced soil moisture combining remote sensing and artificial intelligence approaches. Int. J.

- Moreira, L., Lübeck, D., Wimmer, C., Castro, F., Góes, J.A., Castro, V., Alcântara, M., Oré, G., Oliveira, L.P., Bins, L., Teruel, B., Gabrielli, L.H., Hernandez-Figueroa, H.E., 2020. Drone-Borne P-band Single-Pass InSAR, in: 2020 IEEE Radar Conference (RadarConf20). Presented at the 2020 IEEE Radar Conference (RadarConf20), pp. 1–6. https://doi.org/10.1109/RadarConf2043947.2020.9266502
- Morrison, K., Wagner, W., 2020. Explaining Anomalies in SAR and Scatterometer Soil Moisture Retrievals from Dry Soils with Subsurface Scattering. IEEE Trans. Geosci. Remote Sens. 58, 2190–2197. https://doi.org/10.1109/TGRS.2019.2954771
- Motohka, T., Kankaku, Y., Miura, S., Suzuki, S., 2021. Overview of ALOS-2 and ALOS-4 L-band SAR, in: 2021 IEEE Radar Conference (RadarConf21). Presented at the 2021 IEEE Radar Conference (RadarConf21), pp. 1–4. https://doi.org/10.1109/RadarConf2147009.2021.9454977
- Muñoz-Sabater, J., Dutra, E., Agustí-Panareda, A., Albergel, C., Arduini, G., Balsamo, G., Boussetta, S., Choulga, M., Harrigan, S., Hersbach, H., Martens, B., Miralles, D.G., Piles, M., Rodríguez-Fernández, N.J., Zsoter, E., Buontempo, C., Thépaut, J.-N., 2021. ERA5-Land: a state-of-the-art global reanalysis dataset for land applications. Earth Syst. Sci. Data 13, 4349–4383. https://doi.org/10.5194/essd-13-4349-2021
- Nanda, A., Das, N., Singh, G., Bindlish, R., Andreadis, K.M., Jayasinghe, S., 2024. Harnessing SMAP satellite soil moisture product to optimize soil properties to improve water resource management for agriculture. Agric. Water Manag. 300, 108918. https://doi.org/10.1016/j.agwat.2024.108918
- Njoku, E.G., Chan, S., 2018. 4.08 Soil Moisture From the Advanced Microwave Scanning Radiometer (AMSR) Instruments, in: Liang, S. (Ed.), Comprehensive Remote Sensing. Elsevier, Oxford, pp. 191–223. https://doi.org/10.1016/B978-0-12-409548-9.10356-2
- Njoku, E.G., Chan, S.K., 2006. Vegetation and surface roughness effects on AMSR-E land observations. Remote Sens. Environ. 100, 190–199. https://doi.org/10.1016/j.rse.2005.10.017
- Njoku, E.G., Entekhabi, D., 1996. Passive microwave remote sensing of soil moisture. J. Hydrol., Soil Moisture Theories and Observations 184, 101–129. https://doi.org/10.1016/0022-1694(95)02970-2
- Notarnicola, C., 2014. A Bayesian Change Detection Approach for Retrieval of Soil Moisture Variations Under Different Roughness Conditions. IEEE Geosci. Remote Sens. Lett. 11, 414–418. https://doi.org/10.1109/LGRS.2013.2264159
- O'Neill, P.E., Chan, S., Njoku, E.G., Jackson, T., Bindlish, R., Chaubell, M.J., Colliander, A.,

- 2021. SMAP Enhanced L3 Radiometer Global and Polar Grid Daily 9 km EASE-Grid Soil Moisture, Version 5. https://doi.org/10.5067/4DQ54OUIJ9DL
- Park, J., Bindlish, R., Bringer, A., Horton, D., Johnson, J.T., 2021. Soil Moisture Retrieval using a Time-Series Ratio Algorithm for the Nisar Mission, in: 2021 IEEE International Geoscience and Remote Sensing Symposium IGARSS. Presented at the 2021 IEEE International Geoscience and Remote Sensing Symposium IGARSS, pp. 5873–5876. https://doi.org/10.1109/IGARSS47720.2021.9554619
- Peel, M.C., Blöschl, G., 2011. Hydrological modelling in a changing world. Prog. Phys. Geogr. Earth Environ. 35, 249–261. https://doi.org/10.1177/0309133311402550
- Peng, J., Albergel, C., Balenzano, A., Brocca, L., Cartus, O., Cosh, M.H., Crow, W.T., Dabrowska-Zielinska, K., Dadson, S., Davidson, M.W.J., de Rosnay, P., Dorigo, W., Gruber, A., Hagemann, S., Hirschi, M., Kerr, Y.H., Lovergine, F., Mahecha, M.D., Marzahn, P., Mattia, F., Musial, J.P., Preuschmann, S., Reichle, R.H., Satalino, G., Silgram, M., van Bodegom, P.M., Verhoest, N.E.C., Wagner, W., Walker, J.P., Wegmüller, U., Loew, A., 2021. A roadmap for high-resolution satellite soil moisture applications confronting product characteristics with user requirements. Remote Sens. Environ. 252, 112162. https://doi.org/10.1016/j.rse.2020.112162
- Peters-Lidard, C.D., Houser, P.R., Tian, Y., Kumar, S.V., Geiger, J., Olden, S., Lighty, L., Doty, B., Dirmeyer, P., Adams, J., Mitchell, K., Wood, E.F., Sheffield, J., 2007. High-performance Earth system modeling with NASA/GSFC's Land Information System. Innov. Syst. Softw. Eng. 3, 157–165. https://doi.org/10.1007/s11334-007-0028-x
- Petrolati, D., Gebert, N., Geudtner, D., Bollian, T., Osborne, S., Cesa, M., Simonini, A., Davidson, M., Iannini, L., Cosimo, G.D., 2023. An Overview of the Copernicus Rose-L SAR Instrument, in: IGARSS 2023 2023 IEEE International Geoscience and Remote Sensing Symposium. Presented at the IGARSS 2023 2023 IEEE International Geoscience and Remote Sensing Symposium, pp. 4310–4313. https://doi.org/10.1109/IGARSS52108.2023.10281670
- Piles, M., Entekhabi, D., Camps, A., 2009. A Change Detection Algorithm for Retrieving High-Resolution Soil Moisture From SMAP Radar and Radiometer Observations. IEEE Trans. Geosci. Remote Sens. 47, 4125–4131. https://doi.org/10.1109/TGRS.2009.2022088
- Raes, D., Sithole, A., Makarau, A., Milford, J., 2004. Evaluation of first planting dates recommended by criteria currently used in Zimbabwe. Agric. For. Meteorol. 125, 177–185. https://doi.org/10.1016/j.agrformet.2004.05.001
- Rahman, M.S., Di, L., Yu, E., Lin, L., Zhang, C., Tang, J., 2019. Rapid Flood Progress Monitoring in Cropland with NASA SMAP. Remote Sens. 11, 191. https://doi.org/10.3390/rs11020191
- Reichle, R.H., Lannoy, G.J.M.D., Liu, Q., Ardizzone, J.V., Colliander, A., Conaty, A., Crow, W.,

- Jackson, T.J., Jones, L.A., Kimball, J.S., Koster, R.D., Mahanama, S.P., Smith, E.B., Berg, A., Bircher, S., Bosch, D., Caldwell, T.G., Cosh, M., González-Zamora, Á., Collins, C.D.H., Jensen, K.H., Livingston, S., Lopez-Baeza, E., Martínez-Fernández, J., McNairn, H., Moghaddam, M., Pacheco, A., Pellarin, T., Prueger, J., Rowlandson, T., Seyfried, M., Starks, P., Su, Z., Thibeault, M., Velde, R. van der, Walker, J., Wu, X., Zeng, Y., 2017. Assessment of the SMAP Level-4 Surface and Root-Zone Soil Moisture Product Using In Situ Measurements. https://doi.org/10.1175/JHM-D-17-0063.1
- Rignot, E.J.M., van Zyl, J.J., 1993. Change detection techniques for ERS-1 SAR data. IEEE Trans. Geosci. Remote Sens. 31, 896–906. https://doi.org/10.1109/36.239913
- Rivera-Marin, D., Dash, J., Ogutu, B., 2022. The use of remote sensing for desertification studies: A review. J. Arid Environ. 206, 104829. https://doi.org/10.1016/j.jaridenv.2022.104829
- Rodell, M., Houser, P., Jambor, U., Gottschalck, J., Mitchell, K., Meng, C.-J., Arsenault, K., Cosgrove, B., Radakovich, J., Bosilovich, M., others, 2004. The global land data assimilation system. Bull. Am. Meteorol. Soc. 85, 381–394.
- Rondinelli, W.J., Hornbuckle, B.K., Patton, J.C., Cosh, M.H., Walker, V.A., Carr, B.D., Logsdon, S.D., 2015. Different Rates of Soil Drying after Rainfall Are Observed by the SMOS Satellite and the South Fork in situ Soil Moisture Network. https://doi.org/10.1175/JHM-D-14-0137.1
- Rosen, P.A., Hensley, S., Shaffer, S., Veilleux, L., Chakraborty, M., Misra, T., Bhan, R., Raju Sagi, V., Satish, R., 2015. The NASA-ISRO SAR mission An international space partnership for science and societal benefit, in: 2015 IEEE Radar Conference (RadarCon). Presented at the 2015 IEEE Radar Conference (RadarCon), pp. 1610–1613. https://doi.org/10.1109/RADAR.2015.7131255
- Rosenqvist, A., Shimada, M., Suzuki, S., Ohgushi, F., Tadono, T., Watanabe, M., Tsuzuku, K., Watanabe, T., Kamijo, S., Aoki, E., 2014. Operational performance of the ALOS global systematic acquisition strategy and observation plans for ALOS-2 PALSAR-2. Remote Sens. Environ. 155, 3–12. https://doi.org/10.1016/j.rse.2014.04.011
- Rucci, A., Ferretti, A., Monti Guarnieri, A., Rocca, F., 2012. Sentinel 1 SAR interferometry applications: The outlook for sub millimeter measurements. Remote Sens. Environ., The Sentinel Missions New Opportunities for Science 120, 156–163. https://doi.org/10.1016/j.rse.2011.09.030
- Schmidt, L., Forkel, M., Zotta, R.-M., Scherrer, S., Dorigo, W.A., Kuhn-Regnier, A., van der Schalie, R., Yebra, M., 2023. Assessing the sensitivity of multi-frequency passive microwave vegetationoptical depth to vegetation properties. BIOGEOSCIENCES 20, 1027–1046. https://doi.org/10.5194/bg-20-1027-2023
- Scipal, K., 2017. The Biomass mission ESA'S P-band polarimetric, interferomtric SAR mission, in: 2017 IEEE International Geoscience and Remote Sensing Symposium

- (IGARSS). Presented at the 2017 IEEE International Geoscience and Remote Sensing Symposium (IGARSS), pp. 3836–3837. https://doi.org/10.1109/IGARSS.2017.8127837
- Seneviratne, S.I., Corti, T., Davin, E.L., Hirschi, M., Jaeger, E.B., Lehner, I., Orlowsky, B., Teuling, A.J., 2010. Investigating soil moisture–climate interactions in a changing climate: A review. Earth-Sci. Rev. 99, 125–161. https://doi.org/10.1016/j.earscirev.2010.02.004
- Sharma, S., Tripathi, S., Sowkhya, B., Arora, P., Tyagi, S., Sanid, C., Agrawal, R., Babu, K.N., Mehra, R., Ramanujam, V.M., Jayasri, P.V., Kesarkar, A.A., Gupta, M., Borsadiya, K.K., Bhandari, V., Agrawal, P.K., Rai, R., Nandy, P.S., Putrevu, D., Ryali, U.S., 2024. Assessment of EOS-04 (RISAT-1A) data calibration. Curr. Sci. 00113891 126, 1033–1040. https://doi.org/10.18520/cs/v126/i9/1033-1040
- Shellito, P.J., Small, E.E., Colliander, A., Bindlish, R., Cosh, M.H., Berg, A.A., Bosch, D.D., Caldwell, T.G., Goodrich, D.C., McNairn, H., Prueger, J.H., Starks, P.J., van der Velde, R., Walker, J.P., 2016. SMAP soil moisture drying more rapid than observed in situ following rainfall events. Geophys. Res. Lett. 43, 8068–8075. https://doi.org/10.1002/2016GL069946
- Shi, H., Zhao, L., Yang, J., Lopez-Sanchez, J.M., Zhao, J., Sun, W., Shi, L., Li, P., 2021. Soil moisture retrieval over agricultural fields from L-band multi-incidence and multitemporal PolSAR observations using polarimetric decomposition techniques. Remote Sens. Environ. 261, 112485. https://doi.org/10.1016/j.rse.2021.112485
- Shimada, M., Isoguchi, O., Tadono, T., Isono, K., 2009. PALSAR Radiometric and Geometric Calibration. IEEE Trans. Geosci. Remote Sens. 47, 3915–3932. https://doi.org/10.1109/TGRS.2009.2023909
- Sikdar, M., Cumming, I., 2004. A modified empirical model for soil moisture estimation in vegetated areas using SAR data, in: IGARSS 2004. 2004 IEEE International Geoscience and Remote Sensing Symposium. Presented at the IGARSS 2004. 2004 IEEE International Geoscience and Remote Sensing Symposium, pp. 803–806. https://doi.org/10.1109/IGARSS.2004.1368526
- Singh, G., Das, N., Colliander, A., Entekhabi, D., Yueh, S., 2023. Impact of SAR-based vegetation attributes on the SMAP high-resolution soil moisture product. REMOTE Sens. Environ. 298. https://doi.org/10.1016/j.rse.2023.113826
- Singh, G., Das, N.N., 2022. A data-driven approach using the remotely sensed soil moisture product to identify water-demand in agricultural regions. Sci. Total Environ. 837, 155893. https://doi.org/10.1016/j.scitotenv.2022.155893
- Singh, G., Das, N.N., Panda, R.K., Colliander, A., Jackson, T.J., Mohanty, B.P., Entekhabi, D., Yueh, S.H., 2019a. Validation of SMAP Soil Moisture Products Using Ground-Based Observations for the Paddy Dominated Tropical Region of India. IEEE Trans. Geosci. Remote Sens. 57, 8479–8491. https://doi.org/10.1109/TGRS.2019.2921333

- Singh, G., Das, N.N., Panda, R.K., Mohanty, B.P., Entekhabi, D., Bhattacharya, B.K., 2021. Soil Moisture Retrieval Using SMAP L-Band Radiometer and RISAT-1 C-Band SAR Data in the Paddy Dominated Tropical Region of India. IEEE J. Sel. Top. Appl. Earth Obs. Remote Sens. 14, 10644–10664. https://doi.org/10.1109/JSTARS.2021.3117273
- Singh, G., Panda, R.K., Mohanty, B.P., 2019b. Spatiotemporal Analysis of Soil Moisture and Optimal Sampling Design for Regional-Scale Soil Moisture Estimation in a Tropical Watershed of India. Water Resour. Res. 55, 2057–2078. https://doi.org/10.1029/2018WR024044
- Sishodia, R.P., Ray, R.L., Singh, S.K., 2020. Applications of Remote Sensing in Precision Agriculture: A Review. Remote Sens. 12, 3136. https://doi.org/10.3390/rs12193136
- Skulovich, O., Gentine, P., 2023. A Long-term Consistent Artificial Intelligence and Remote Sensing-based Soil Moisture Dataset. Sci. Data 10, 154. https://doi.org/10.1038/s41597-023-02053-x
- Srivastava, H.S., Sivasankar, T., Gavali, M.D., Patel, P., 2024. Soil moisture estimation underneath crop cover using high incidence angle C-band Sentinel-1 SAR data. Kuwait J. Sci. 51, 100101. https://doi.org/10.1016/j.kjs.2023.07.007
- Su, C.-H., Ryu, D., Crow, W.T., Western, A.W., 2014. Beyond triple collocation: Applications to soil moisture monitoring. J. Geophys. Res. Atmospheres 119, 6419–6439. https://doi.org/10.1002/2013JD021043
- Tabassum, A., Hong, S.-H., Park, K., Baik, J.-J., 2024. Impacts of Changes in Soil Moisture on Urban Heat Islands and Urban Breeze Circulations: Idealized Ensemble Simulations. Asia-Pac. J. Atmospheric Sci. https://doi.org/10.1007/s13143-024-00369-1
- Taylor, C.M., de Jeu, R.A.M., Guichard, F., Harris, P.P., Dorigo, W.A., 2012. Afternoon rain more likely over drier soils. Nature 489, 423–426. https://doi.org/10.1038/nature11377
- Thoma, D.P., Moran, M.S., Bryant, R., Rahman, M.M., Collins, C.D.H., Keefer, T.O., Noriega, R., Osman, I., Skrivin, S.M., Tischler, M.A., Bosch, D.D., Starks, P.J., Peters-Lidard, C.D., 2008. Appropriate scale of soil moisture retrieval from high resolution radar imagery for bare and minimally vegetated soils. Remote Sens. Environ. 112, 403–414. https://doi.org/10.1016/j.rse.2007.06.021
- Thompson, A.A., 2015. Overview of the RADARSAT Constellation Mission. Can. J. Remote Sens. 41, 401–407. https://doi.org/10.1080/07038992.2015.1104633
- Toan, T.L., Chave, J., Dall, J., Papathanassiou, K., Paillou, P., Rechstein, M., Quegan, S., Saatchi,
  S., Seipel, K., Shugart, H., Tebaldini, S., Ulander, L., Williams, M., 2018. The Biomass Mission: Objectives and Requirements, in: IGARSS 2018 2018 IEEE International Geoscience and Remote Sensing Symposium. Presented at the IGARSS 2018 2018 IEEE International Geoscience and Remote Sensing Symposium, pp. 8563–8566.

- https://doi.org/10.1109/IGARSS.2018.8518491
- Tong, C., Wang, H., Magagi, R., Goïta, K., Zhu, L., Yang, M., Deng, J., 2020. Soil Moisture Retrievals by Combining Passive Microwave and Optical Data. Remote Sens. 12, 3173. https://doi.org/10.3390/rs12193173
- Torbert, H.A., Potter, K.N., Hoffman, D.W., Gerik, T.J., Richardson, C.W., 1999. Surface Residue and Soil Moisture Affect Fertilizer Loss in Simulated Runoff on a Heavy Clay Soil. Agron. J. 91, 606–612. https://doi.org/10.2134/agronj1999.914606x
- Torres, R., Lokas, S., Di Cosimo, G., Geudtner, D., Bibby, D., 2017. Sentinel 1 evolution: Sentinel-1C and -1D models, in: 2017 IEEE International Geoscience and Remote Sensing Symposium (IGARSS). Presented at the 2017 IEEE International Geoscience and Remote Sensing Symposium (IGARSS), pp. 5549–5550. https://doi.org/10.1109/IGARSS.2017.8128261
- Torres, R., Snoeij, P., Geudtner, D., Bibby, D., Davidson, M., Attema, E., Potin, P., Rommen, B., Floury, N., Brown, M., Traver, I.N., Deghaye, P., Duesmann, B., Rosich, B., Miranda, N., Bruno, C., L'Abbate, M., Croci, R., Pietropaolo, A., Huchler, M., Rostan, F., 2012. GMES Sentinel-1 mission. Remote Sens. Environ., The Sentinel Missions New Opportunities for Science 120, 9–24. https://doi.org/10.1016/j.rse.2011.05.028
- Tridon, D.B., Sica, F., De Zan, F., Bachmann, M., Krieger, G., 2018. Observation Strategy and Flight Configuration for Monitoring Earth Dynamics with the Tandem-L Mission, in: IGARSS 2018 2018 IEEE International Geoscience and Remote Sensing Symposium. Presented at the IGARSS 2018 2018 IEEE International Geoscience and Remote Sensing Symposium, pp. 5651–5654. https://doi.org/10.1109/IGARSS.2018.8517757
- Ulaby, F., 1974. Radar measurement of soil moisture content. IEEE Trans. Antennas Propag. 22, 257–265. https://doi.org/10.1109/TAP.1974.1140761
- Ulaby, F., Moore, R., Fung, A., 1986. Microwave remote sensing: Active and passive, vol. iii, volume scattering and emission theory, advanced systems and applications. Inc Dedham Mass. 1797–1848.
- Ulaby, F.T., Dubois, P.C., van Zyl, J., 1996. Radar mapping of surface soil moisture. J. Hydrol., Soil Moisture Theories and Observations 184, 57–84. https://doi.org/10.1016/0022-1694(95)02968-0
- Ulaby, F.T., Moore, R.K., Fung, A.K., 1981. Microwave remote sensing. 1: Microwave remote sensing, fundamentals and radiometry. Artech House, Norwood, Mass.
- Ulaby, F.T., Sarabandi, K., Mcdonald, K., Whitt, M., Dobson, M.C., 1990. Michigan microwave canopy scattering model. Int. J. Remote Sens. 11, 1223–1253.
- Vanin, F., Laberinti, P., Donlon, C., Fiorelli, B., Barat, I., Sole, M.P., Palladino, M., Eggers, P.,

- Rudolph, T., Galeazzi, C., 2020. Copernicus Imaging Microwave Radiometer (CIMR): System Aspects and Technological Challenges, in: IGARSS 2020 2020 IEEE International Geoscience and Remote Sensing Symposium. Presented at the IGARSS 2020 2020 IEEE International Geoscience and Remote Sensing Symposium, pp. 6535–6538. https://doi.org/10.1109/IGARSS39084.2020.9324259
- Vergopolan, N., Chaney, N.W., Beck, H.E., Pan, M., Sheffield, J., Chan, S., Wood, E.F., 2020. Combining hyper-resolution land surface modeling with SMAP brightness temperatures to obtain 30-m soil moisture estimates. Remote Sens. Environ. 242, 111740. https://doi.org/10.1016/j.rse.2020.111740
- Vergopolan, N., Sheffield, J., Chaney, N.W., Pan, M., Beck, H.E., Ferguson, C.R., Torres-Rojas, L., Eigenbrod, F., Crow, W., Wood, E.F., 2022. High-Resolution Soil Moisture Data Reveal Complex Multi-Scale Spatial Variability Across the United States. Geophys. Res. Lett. 49, e2022GL098586. https://doi.org/10.1029/2022GL098586
- Verhoest, N.E.C., Lievens, H., Wagner, W., Álvarez-Mozos, J., Moran, M.S., Mattia, F., 2008. On the Soil Roughness Parameterization Problem in Soil Moisture Retrieval of Bare Surfaces from Synthetic Aperture Radar. Sensors 8, 4213–4248. https://doi.org/10.3390/s8074213
- Vermote, E., Ellicott, E., Dubovik, O., Lapyonok, T., Chin, M., Giglio, L., Roberts, G.J., 2009. An approach to estimate global biomass burning emissions of organic and black carbon from MODIS fire radiative power. J. Geophys. Res. Atmospheres 114. https://doi.org/10.1029/2008JD011188
- Vittucci, C., Guerriero, L., Ferrazzoli, P., 2023. Influence of Vegetation Height, Plant Area Index, and Forest Intactness on SMOS L-VOD, for Different Seasons and Latitude Ranges. IEEE Trans. Geosci. REMOTE Sens. 61. https://doi.org/10.1109/TGRS.2023.3299529
- Wagner, W., Hahn, S., Kidd, R., Melzer, T., Bartalis, Z., Hasenauer, S., Figa-Saldana, J., de Rosnay, P., Jann, A., Schneider, S., Komma, J., Kubu, G., Brugger, K., Aubrecht, C., Züger, J., Gangkofner, U., Kienberger, S., Brocca, L., Wang, Y., Blöschl, G., Eitzinger, J., Steinnocher, K., Zeil, P., Rubel, F., 2013. The ASCAT soil moisture product: a review of its specifications, validation results, and emerging applications. Meteorol. Z. https://doi.org/10.1127/0941-2948/2013/0399
- Wagner, W., Lindorfer, R., Melzer, T., Hahn, S., Bauer-Marschallinger, B., Morrison, K., Calvet, J.-C., Hobbs, S., Quast, R., Greimeister-Pfeil, I., Vreugdenhil, M., 2022. Widespread occurrence of anomalous C-band backscatter signals in arid environments caused by subsurface scattering. Remote Sens. Environ. 276, 113025. https://doi.org/10.1016/j.rse.2022.113025
- Walker, J.P., Houser, P.R., 2001. A methodology for initializing soil moisture in a global climate model: Assimilation of near-surface soil moisture observations. J. Geophys. Res. Atmospheres 106, 11761–11774. https://doi.org/10.1029/2001JD900149

- Walker, J.P., Willgoose, G.R., Kalma, J.D., 2004. In situ measurement of soil moisture: a comparison of techniques. J. Hydrol. 293, 85–99. https://doi.org/10.1016/j.jhydrol.2004.01.008
- Wanders, N., Karssenberg, D., de Roo, A., de Jong, S.M., Bierkens, M.F.P., 2014. The suitability of remotely sensed soil moisture for improving operational flood forecasting. Hydrol. Earth Syst. Sci. 18, 2343–2357. https://doi.org/10.5194/hess-18-2343-2014
- Wang, H., Magagi, R., Goïta, K., 2018. Potential of a two-component polarimetric decomposition at C-band for soil moisture retrieval over agricultural fields. Remote Sens. Environ. 217, 38–51. https://doi.org/10.1016/j.rse.2018.08.003
- Wang, H., Xiao, W., Zhao, Y., Wang, Y., Hou, B., Zhou, Y., Yang, H., Zhang, X., Cui, H., 2019. The Spatiotemporal Variability of Evapotranspiration and Its Response to Climate Change and Land Use/Land Cover Change in the Three Gorges Reservoir. Water 11, 1739. https://doi.org/10.3390/w11091739
- White, J., Berg, A.A., Champagne, C., Zhang, Y., Chipanshi, A., Daneshfar, B., 2020. Improving crop yield forecasts with satellite-based soil moisture estimates: An example for township level canola yield forecasts over the Canadian Prairies. Int. J. Appl. Earth Obs. Geoinformation 89, 102092. https://doi.org/10.1016/j.jag.2020.102092
- Wickel, A.J., Jackson, T.J., Wood, E.F., 2001. Multitemporal monitoring of soil moisture with RADARSAT SAR during the 1997 Southern Great Plains hydrology experiment. Int. J. Remote Sens. 22, 1571–1583. https://doi.org/10.1080/01431160120291
- Wickham, H., 2011. ggplot2. WIREs Comput. Stat. 3, 180–185. https://doi.org/10.1002/wics.147
- Wickham, H., François, R., Henry, L., Müller, K., Vaughan, D., others, 2020. dplyr: A grammar of data manipulation.
- Winkler, A.J., Myneni, R.B., Alexandrov, G.A., Brovkin, V., 2019. Earth system models underestimate carbon fixation by plants in the high latitudes. Nat. Commun. 10. https://doi.org/10.1038/s41467-019-08633-z
- Wongchuig, S., Paiva, R., Siqueira, V., Papa, F., Fleischmann, A., Biancamaria, S., Paris, A., Parrens, M., Al Bitar, A., 2024. Multi-Satellite Data Assimilation for Large-Scale Hydrological-Hydrodynamic Prediction: Proof of Concept in the Amazon Basin. Water Resour. Res. 60, e2024WR037155. https://doi.org/10.1029/2024WR037155
- Xu, L., Chen, N., Zhang, X., Moradkhani, H., Zhang, C., Hu, C., 2021. In-situ and triple-collocation based evaluations of eight global root zone soil moisture products. Remote Sens. Environ. 254, 112248. https://doi.org/10.1016/j.rse.2020.112248
- Yadav, V.P., Prasad, R., Bala, R., Vishwakarma, A. kumar, 2019. Estimation of soil moisture through water cloud model using sentinel -1A SAR data, in: IGARSS 2019 2019 IEEE

- International Geoscience and Remote Sensing Symposium. Presented at the IGARSS 2019 2019 IEEE International Geoscience and Remote Sensing Symposium, pp. 6961–6964. https://doi.org/10.1109/IGARSS.2019.8900203
- Yang, Z.-L., Niu, G.-Y., Mitchell, K.E., Chen, F., Ek, M.B., Barlage, M., Longuevergne, L., Manning, K., Niyogi, D., Tewari, M., Xia, Y., 2011. The community Noah land surface model with multiparameterization options (Noah-MP): 2. Evaluation over global river basins. J. Geophys. Res. 116, D12110. https://doi.org/10.1029/2010JD015140
- Zakharov, I., Kapfer, M., Hornung, J., Kohismith, S., Puestow, T., Howell, M., Henschel, M., 2020. Retrieval of Surface Soil Moisture From Sentinel-1 Time Series for Reclamation of Wetland Sites. IEEE J. Sel. Top. Appl. EARTH Obs. REMOTE Sens. 13, 3569–3578. https://doi.org/10.1109/JSTARS.2020.3004062
- Zappa, L., Forkel, M., Xaver, A., Dorigo, W., 2019. Deriving Field Scale Soil Moisture from Satellite Observations and Ground Measurements in a Hilly Agricultural Region. Remote Sens. 11, 2596. https://doi.org/10.3390/rs11222596
- Zeng, J., Li, Z., Chen, Q., Bi, H., 2015. Method for Soil Moisture and Surface Temperature Estimation in the Tibetan Plateau Using Spaceborne Radiometer Observations. IEEE Geosci. Remote Sens. Lett. 12, 97–101. https://doi.org/10.1109/LGRS.2014.2326890
- Zeng, J., Shi, P., Chen, K.-S., Ma, H., Bi, H., Cui, C., 2022. On the Relationship Between Radar Backscatter and Radiometer Brightness Temperature From SMAP. IEEE Trans. Geosci. Remote Sens. 60, 1–16. https://doi.org/10.1109/TGRS.2021.3115140
- Zhao, W., Wen, F., Wang, Q., Sanchez, N., Piles, M., 2021. Seamless downscaling of the ESA CCI soil moisture data at the daily scale with MODIS land products. J. Hydrol. 603. https://doi.org/10.1016/j.jhydrol.2021.126930
- Zhong, L., Hawkins, T., Biging, G., Gong, P., 2011. A phenology-based approach to map crop types in the San Joaquin Valley, California. Int. J. Remote Sens. 32, 7777–7804. https://doi.org/10.1080/01431161.2010.527397
- Zhu, L., Si, R., Shen, X., Walker, J.P., 2022. An advanced change detection method for time-series soil moisture retrieval from Sentinel-1. Remote Sens. Environ. 279, 113137. https://doi.org/10.1016/j.rse.2022.113137
- Zribi, M., Dechambre, M., 2003. A new empirical model to retrieve soil moisture and roughness from C-band radar data. Remote Sens. Environ. 84, 42–52. https://doi.org/10.1016/S0034-4257(02)00069-X
- Zribi, M., Le Morvan, A., Baghdadi, N., 2008. Dielectric Constant Modelling with Soil–Air Composition and Its Effect on Sar Radar Signal Backscattered over Soil Surface. Sensors 8, 6810–6824. https://doi.org/10.3390/s8116810

Zwieback, S., Hensley, S., Hajnsek, I., 2015. Assessment of soil moisture effects on L-band radar interferometry. Remote Sens. Environ. 164, 77–89. https://doi.org/10.1016/j.rse.2015.04.012

## **APPENDIX**

To avoid unreliable data, SMAP radiometer passive enhanced soil moisture products were checked through a quality control procedure using certain data flags and surface flags provided within the product to identify and discard missing data, values outside the acceptable range, and open water body, precipitation, unreliable soil moisture retrievals. Some of the surface flags were ignored such as grid cell in northern latitude and dense forest for pixel-to-pixel comparison.

The *in-situ* measurements are quality controlled by SMAP mission which has been for validating the product from SMAP project. The procedure for CVS *in-situ* quality control includes checks for missing data, out of range values, spikes, sudden drops and physical temperature limits. Additionally, the physical temperature is checked to be above 4 °C because some sensors begin to exhibit unpredictable behavior below this threshold. Finally, stations deemed not to represent the surrounding environment are excluded.

RMSE represents the root mean square error/difference between estimated soil moisture and observations. It measures the absolute difference between *in-situ*/SMAP and ERA5-Land. A small RMSE value (toward 0) indicates a small error in ERA5-Land soil moisture observations.

RMSE = RMSD

$$RMSE = \sqrt{\frac{1}{M} \sum_{k=1}^{M} (\theta_{retrieved}(k) - \theta_{in-situ}(k))^2}$$
(A1)

Mean Difference (MD) shows the difference between estimated soil moisture and observed soil moisture. The value toward  $\pm$  zero shows small bias and vice-versa.

$$Mean \ Difference(MD) = \frac{1}{M} \sum_{k=1}^{M} \theta_{retrieved}(k) - \frac{1}{M} \sum_{k=1}^{M} \theta_{in-situ}(k)$$
 (A2)

The ubRMSE is similar to RMSE, but it excludes the mean signal and measures the absolute difference between two-time series.

$$ubRMSE = \sqrt{\frac{\frac{1}{M}\sum_{k=1}^{M} \left( \left(\theta_{retrieved}(k) - \frac{1}{M}\sum_{k=1}^{M} \theta_{retrieved}(k)\right) - \right)^{2}}{\left(\theta_{in-situ}(k) - \frac{1}{M}\sum_{k=1}^{M} \theta_{in-situ}(k)\right)}}$$
(A3)

The correlation coefficient (R) represents the linear correlation between SMAP and ERA5-Land soil moisture. The R-value of  $\pm$  1 depicts a high correlation, and a value nearby zero represents no correlation.

$$Correlation(R) =$$

$$\left(\frac{\frac{1}{M}\sum_{k=1}^{M}\left(\left(\theta_{retrieved}(k)-\frac{1}{M}\sum_{k=1}^{M}\theta_{retrieved}(k)\right)\times\left(\theta_{in-situ}(k)-\frac{1}{M}\sum_{k=1}^{M}\theta_{in-situ}(k)\right)\right)}{\sigma_{retrieved}\times\sigma_{in-situ}}\right)$$
(A4)

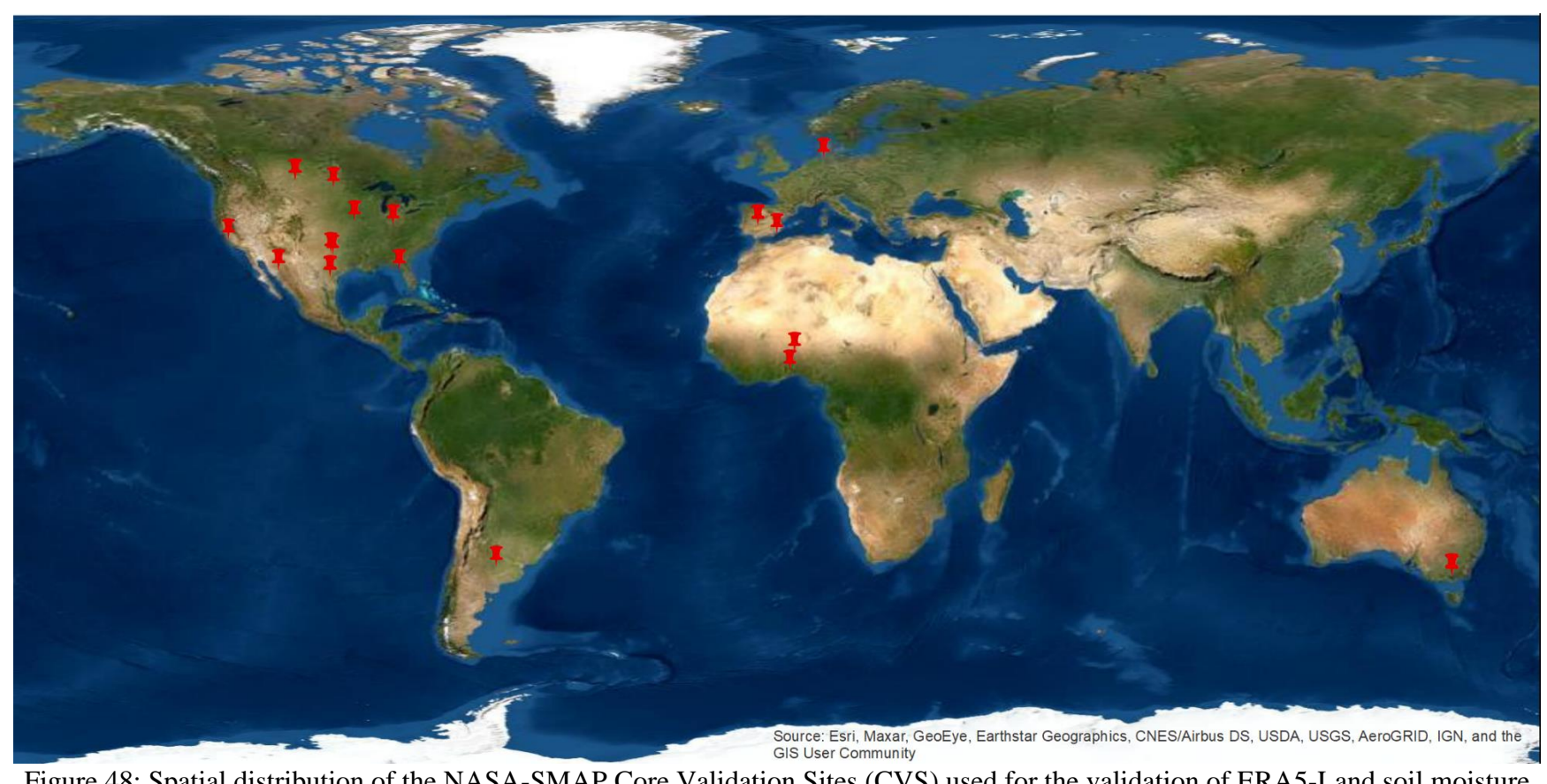


Figure 48: Spatial distribution of the NASA-SMAP Core Validation Sites (CVS) used for the validation of ERA5-Land soil moisture products.

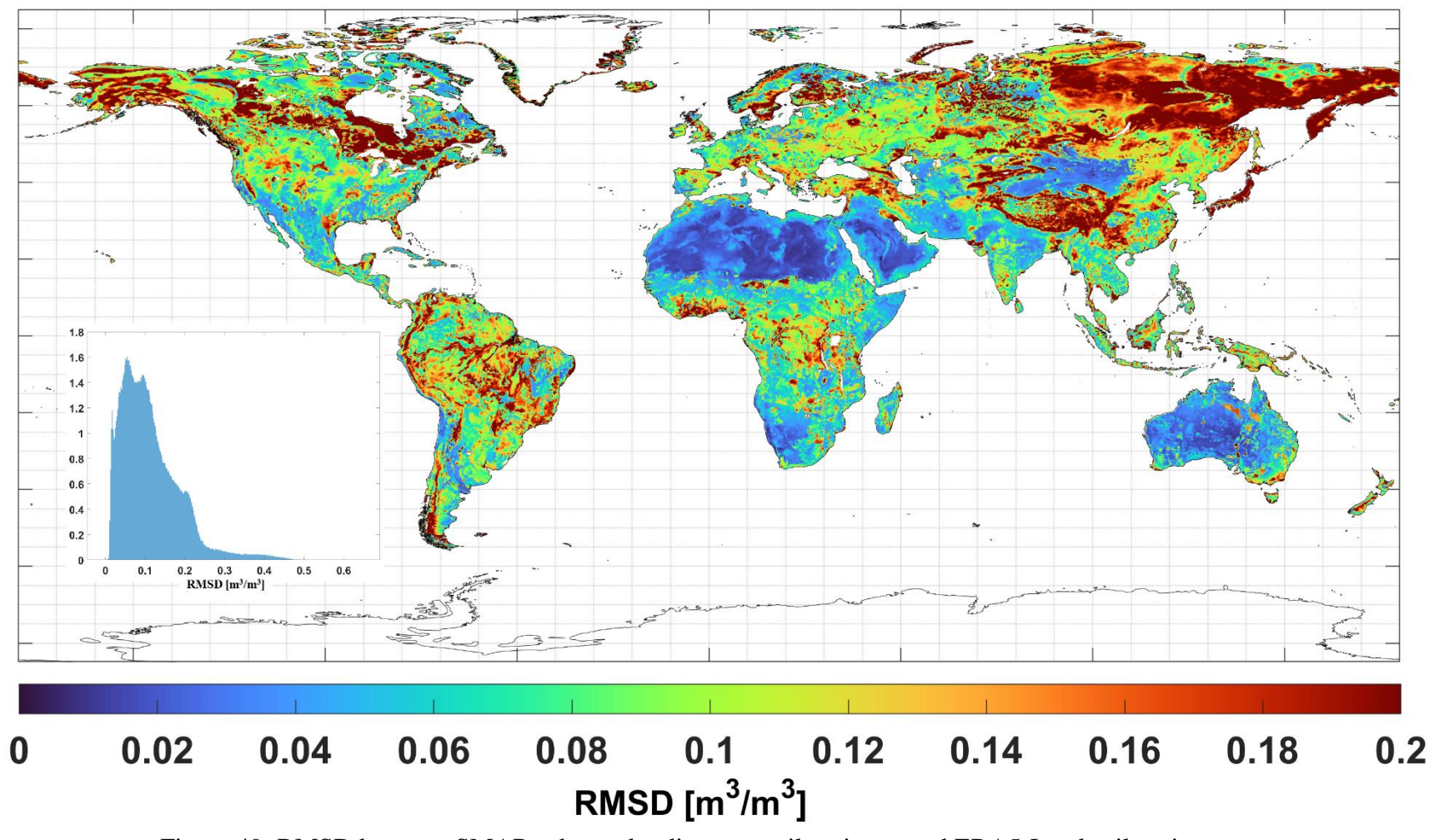


Figure 49: RMSD between SMAP enhanced radiometer soil moisture and ERA5-Land soil moisture.

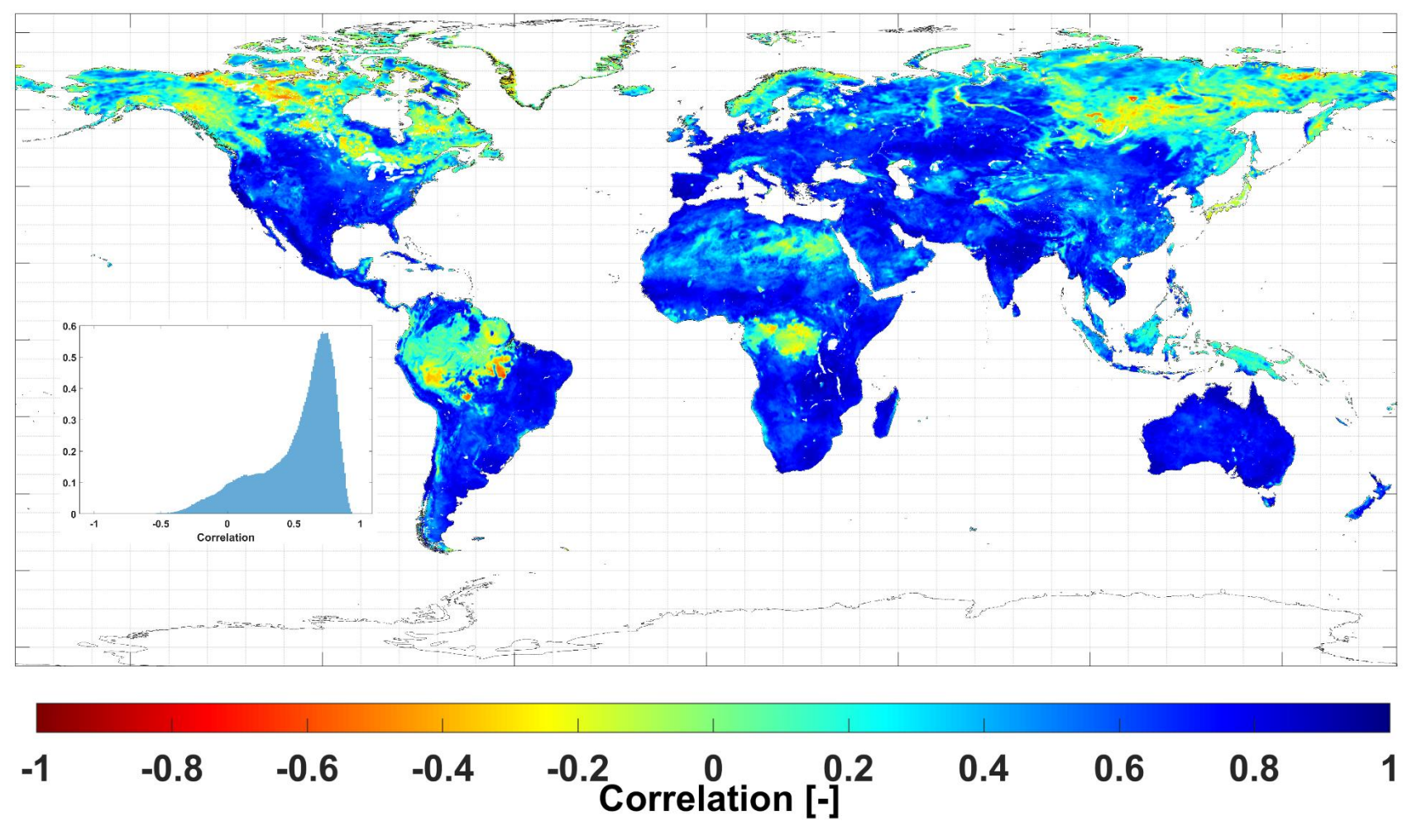


Figure 50: (a) Anomaly correlation between SMAP enhanced radiometer soil moisture (L3\_SM\_P\_E) and ERA5-Land soil moisture.

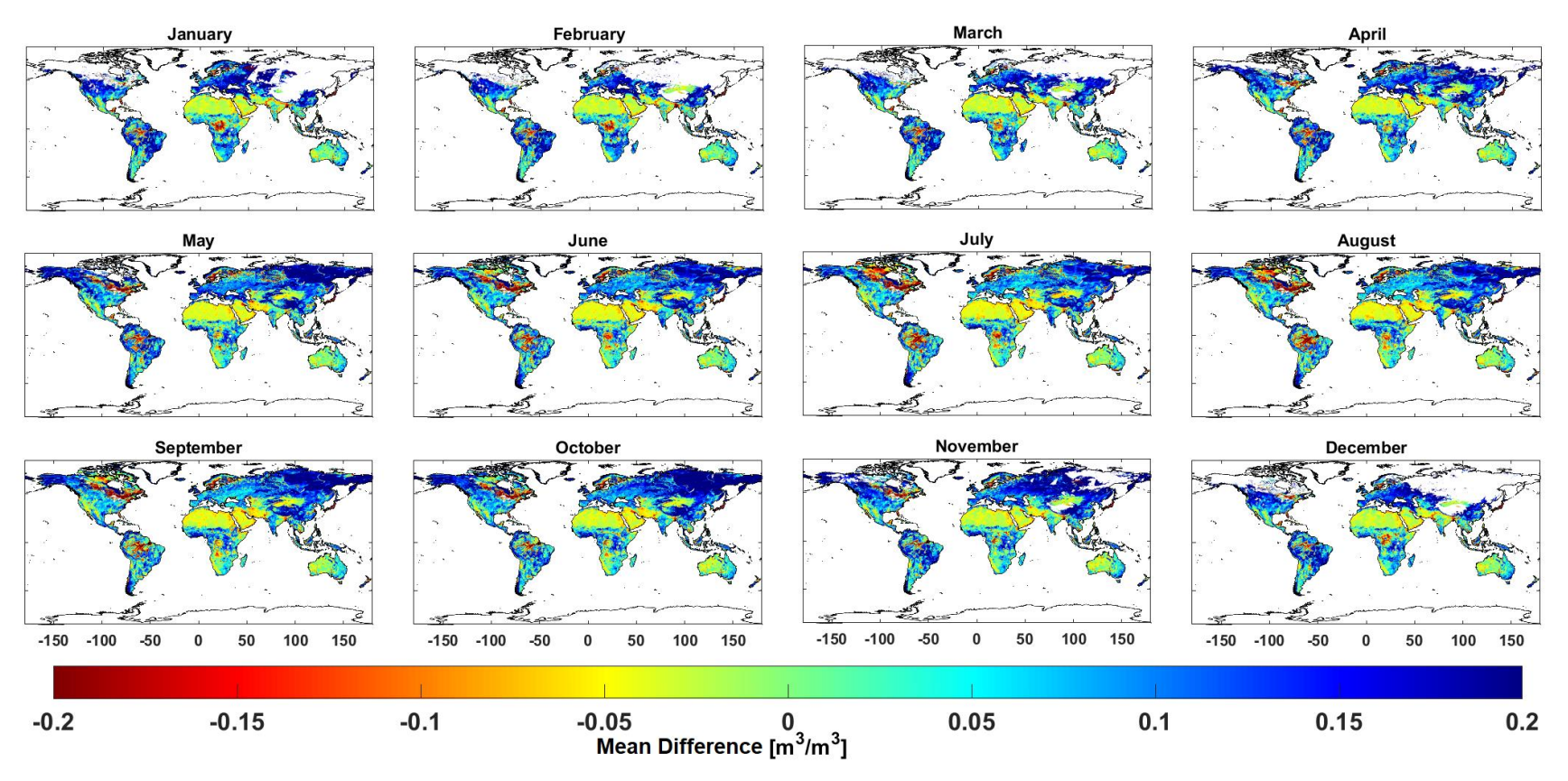


Figure 51: Global monthly mean difference between SMAP enhanced radiometer soil moisture (L3\_SM\_P\_E) and ERA5-Land soil moisture.

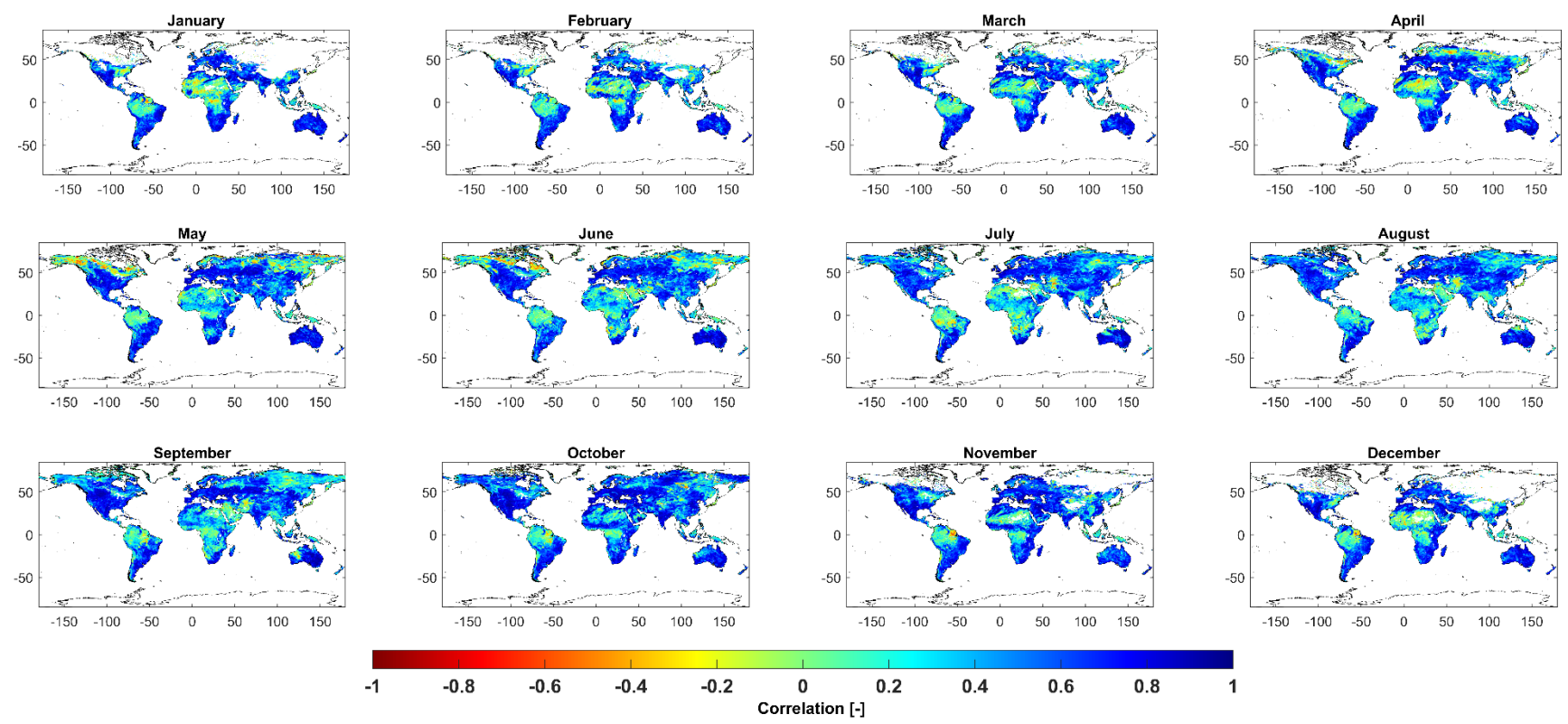
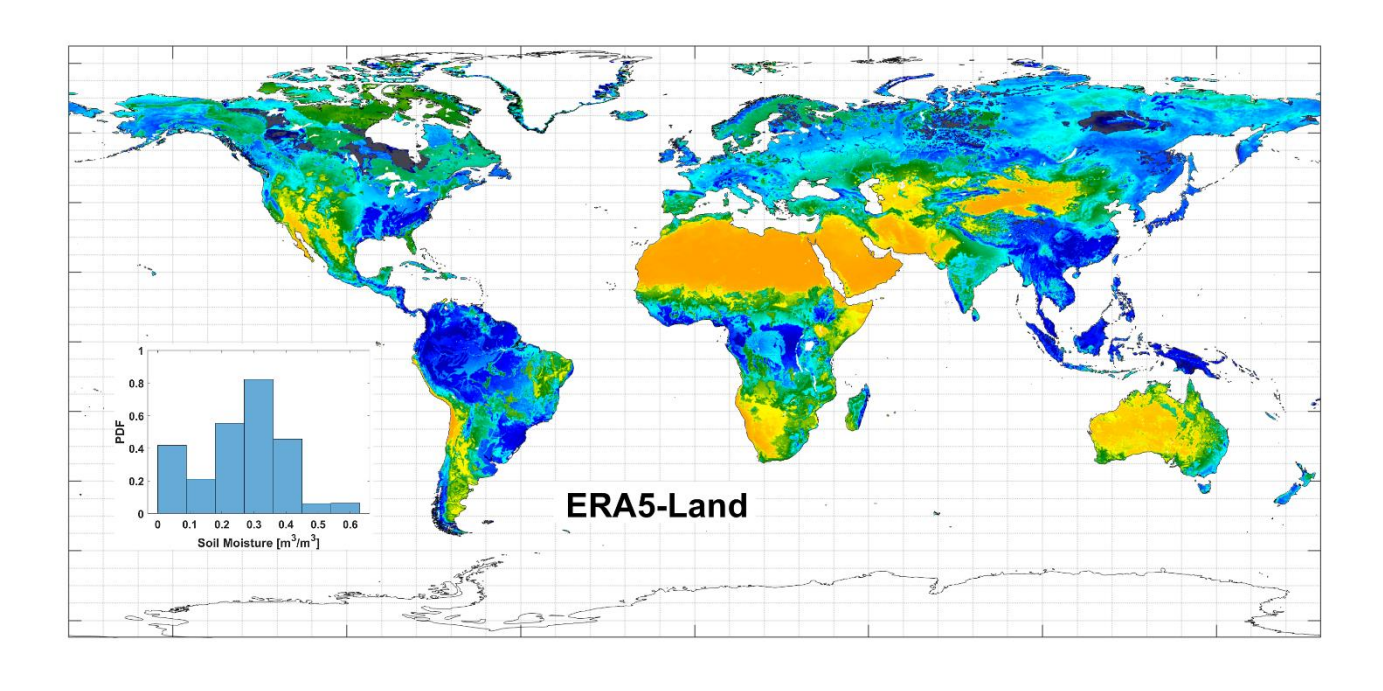


Figure 52: Global monthly correlation between SMAP enhanced radiometer soil moisture (L3\_SM\_P\_E) and ERA5-Land soil moisture.



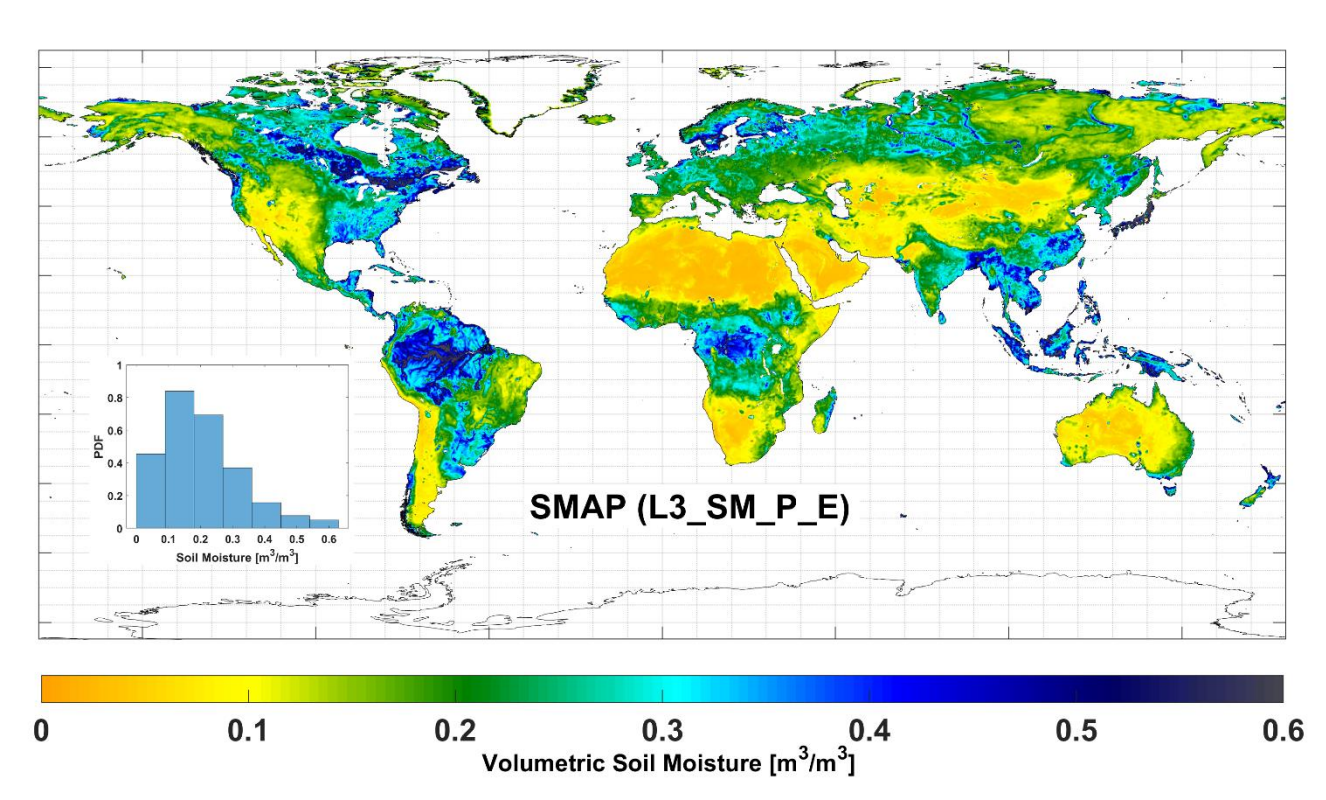


Figure 53: Global mean soil moisture pattern between March 31, 2015, to October 26, 2021 (a) ERA5-Land and (b) SMAP enhanced radiometer soil moisture (L3\_SM\_P\_E).

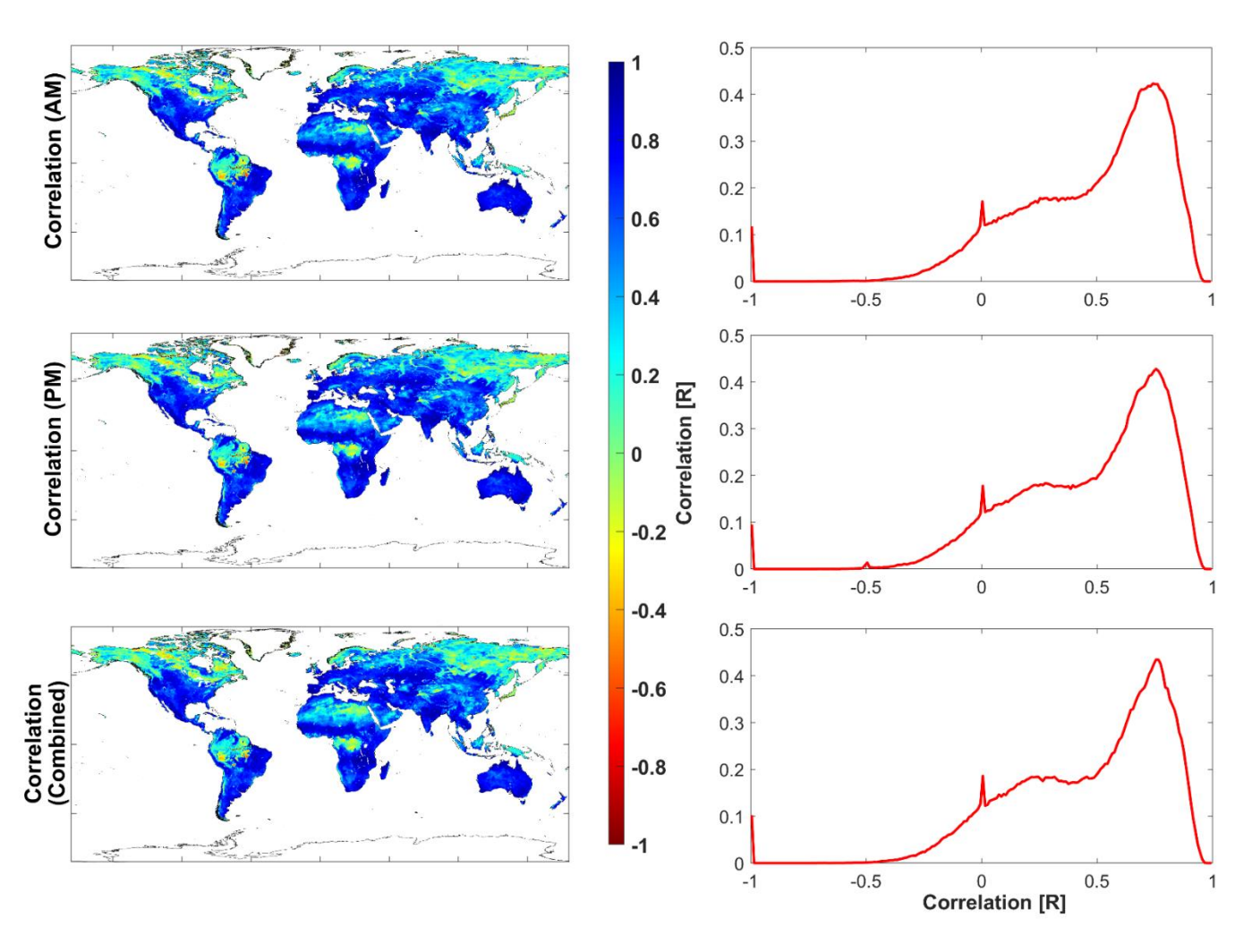


Figure 54: First column shows the spatial representation of correlation between ERA5-Land and SMAP L3\_SM\_P\_E soil moisture for AM (top panel), PM (middle panel), and combined of AM and PM (bottom panel). A probability density function (PDF) plot of spatial correlation is shown in the second column.

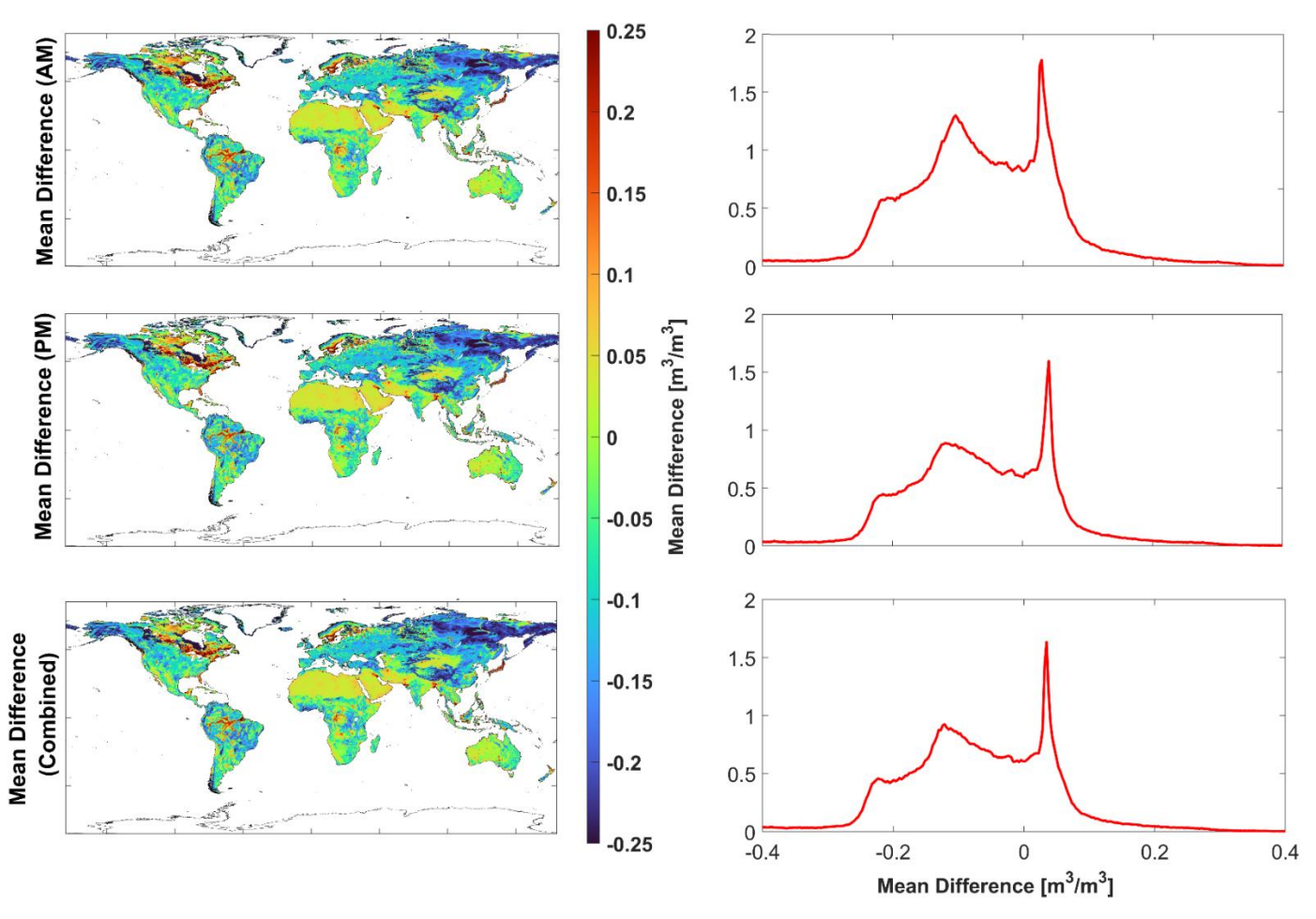


Figure 55: First column shows the spatial representation of the Mean Difference (MD) between ERA5-Land and SMAP L3\_SM\_P\_E for AM (top panel), PM (middle panel) and combined AM and PM (bottom panel). A probability density function (PDF) plot of MD is shown in the second column.

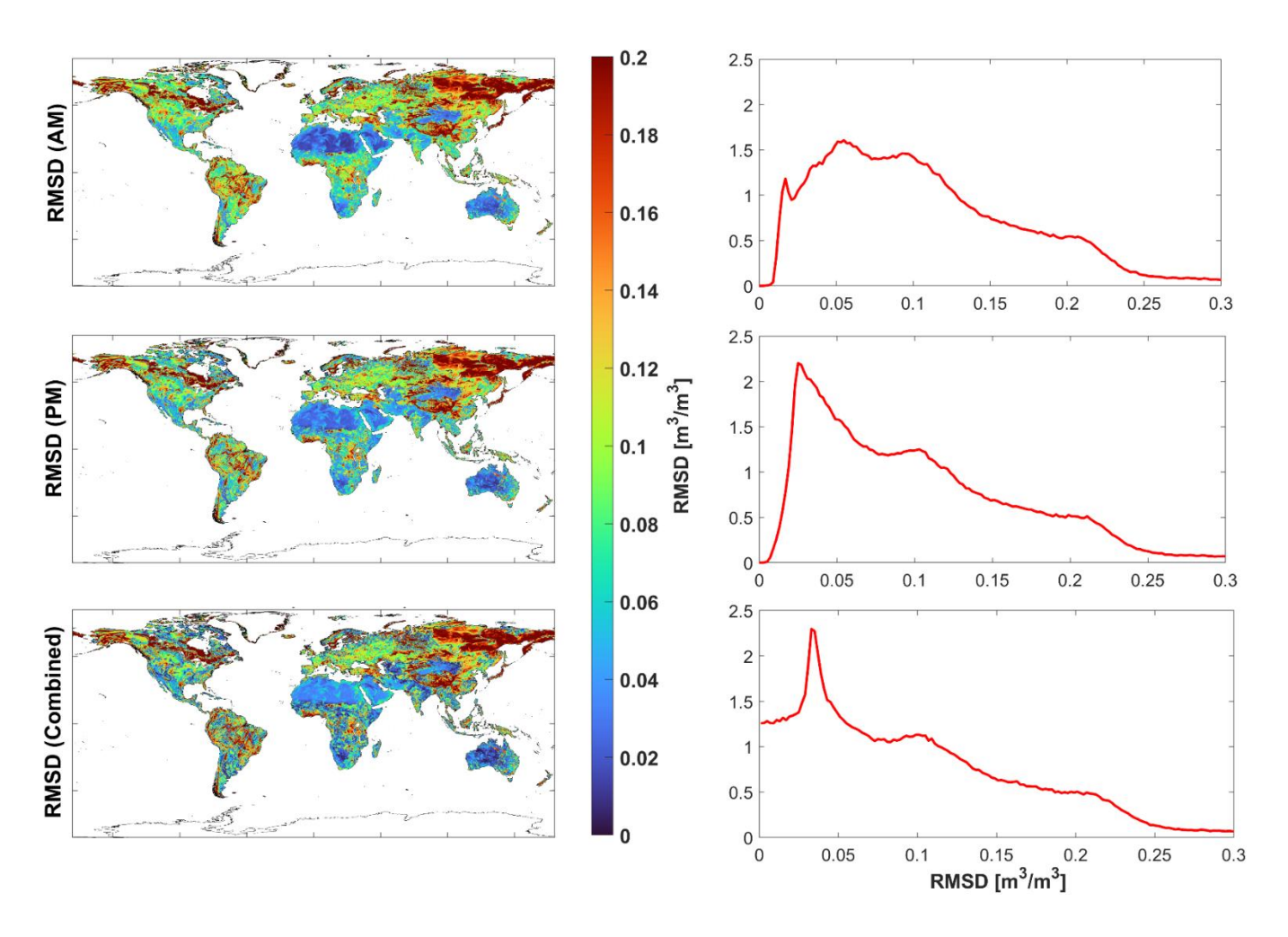


Figure 56: First column shows the spatial representation of root mean square difference (RMSD) between ERA5-Land and SMAP L3\_SM\_P\_E for AM (top panel), PM (middle panel) and combined AM and PM (bottom panel). A probability density function (PDF) plot of RMSD is shown in the second column.

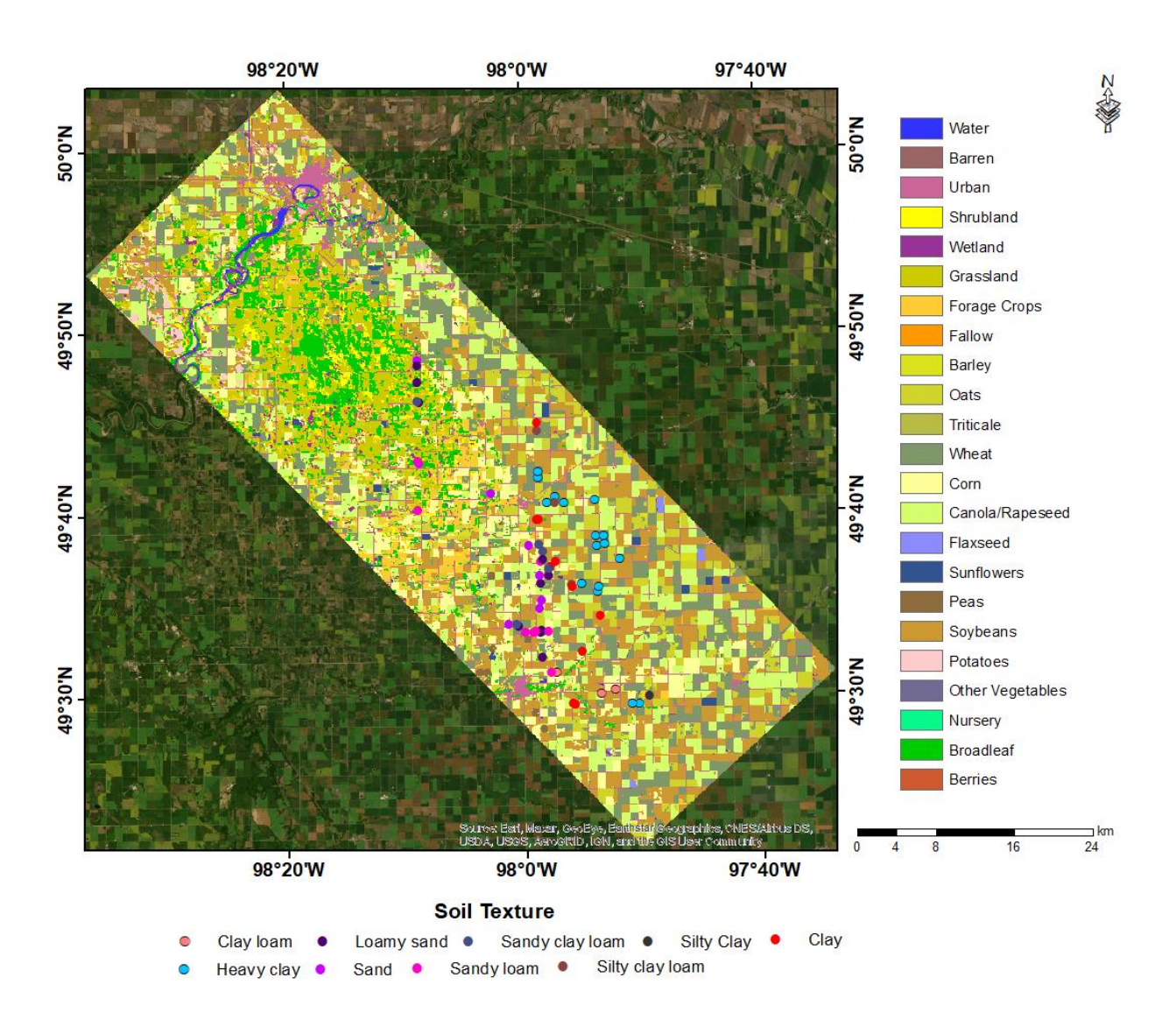


Figure 57: Land cover and crop type map of SMAPVEX12 campaign. Base map service Layer Credits: Source: Esri, Maxar, GeoEye, Earthstar Geographics, CNES/Airbus DS, USDA, USGS, AeroGRID, IGN, and the GIS User Community.

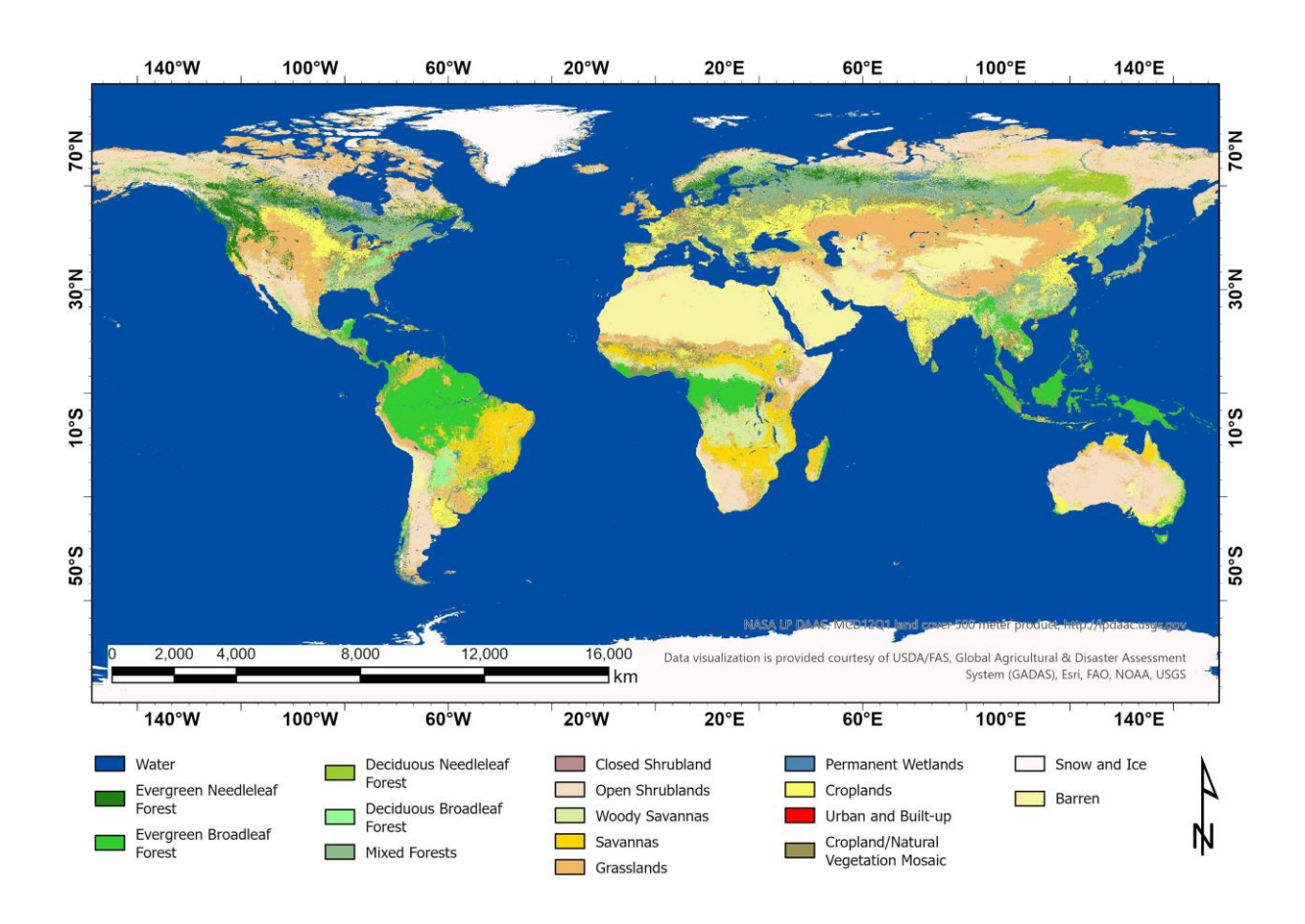


Figure 58: International Geosphere–Biosphere Programme (IGBP) Land Use and Land cover map of year 2020. This LULC has been used for extraction of β value.

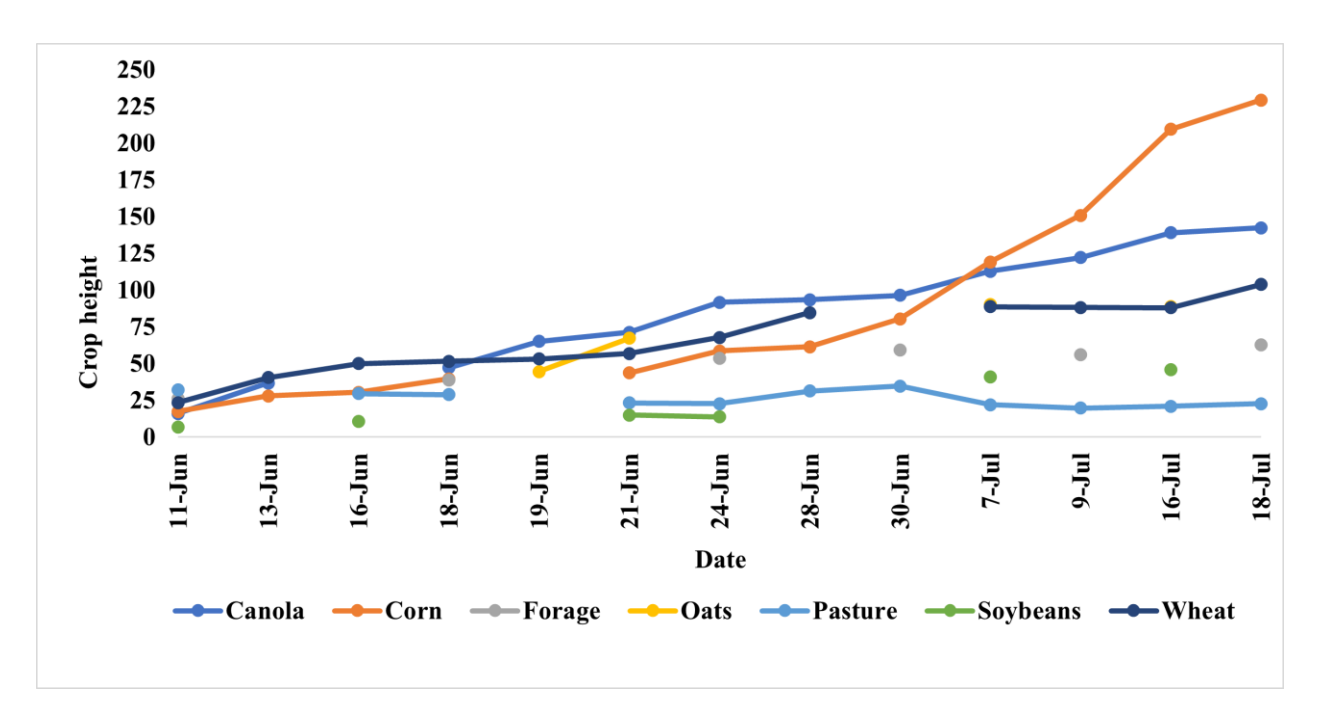


Figure 59: Crop height represents different vegetation growth phases in the SMAPVEX12 campaign.

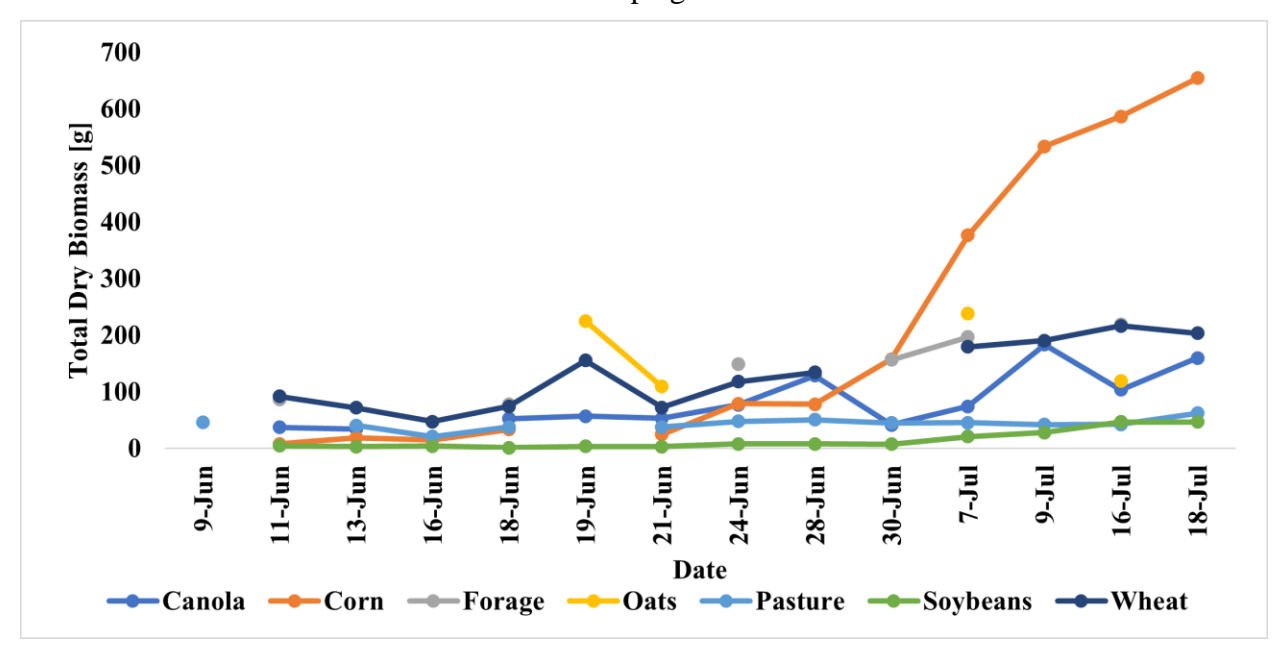


Figure 60: Total dry biomass in different phases of vegetation growth in the SMAPVEX12 campaign.

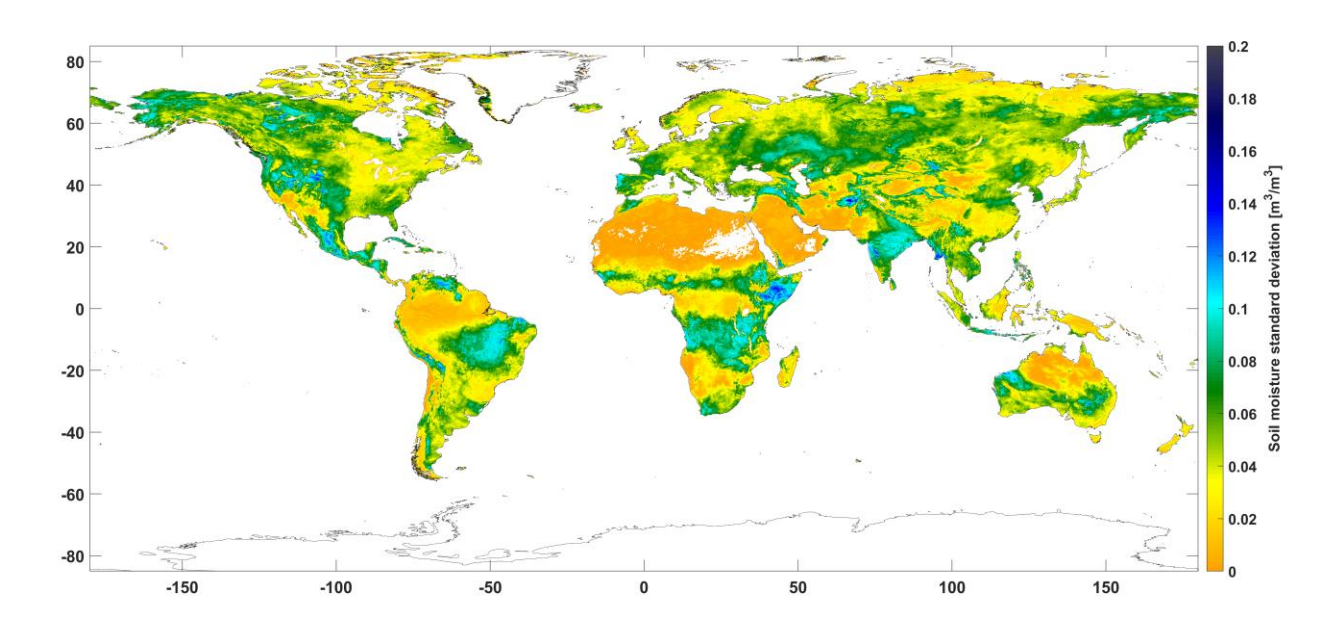


Figure 61: Standard deviation of ERA5-Land soil moisture for selected 84 days period.

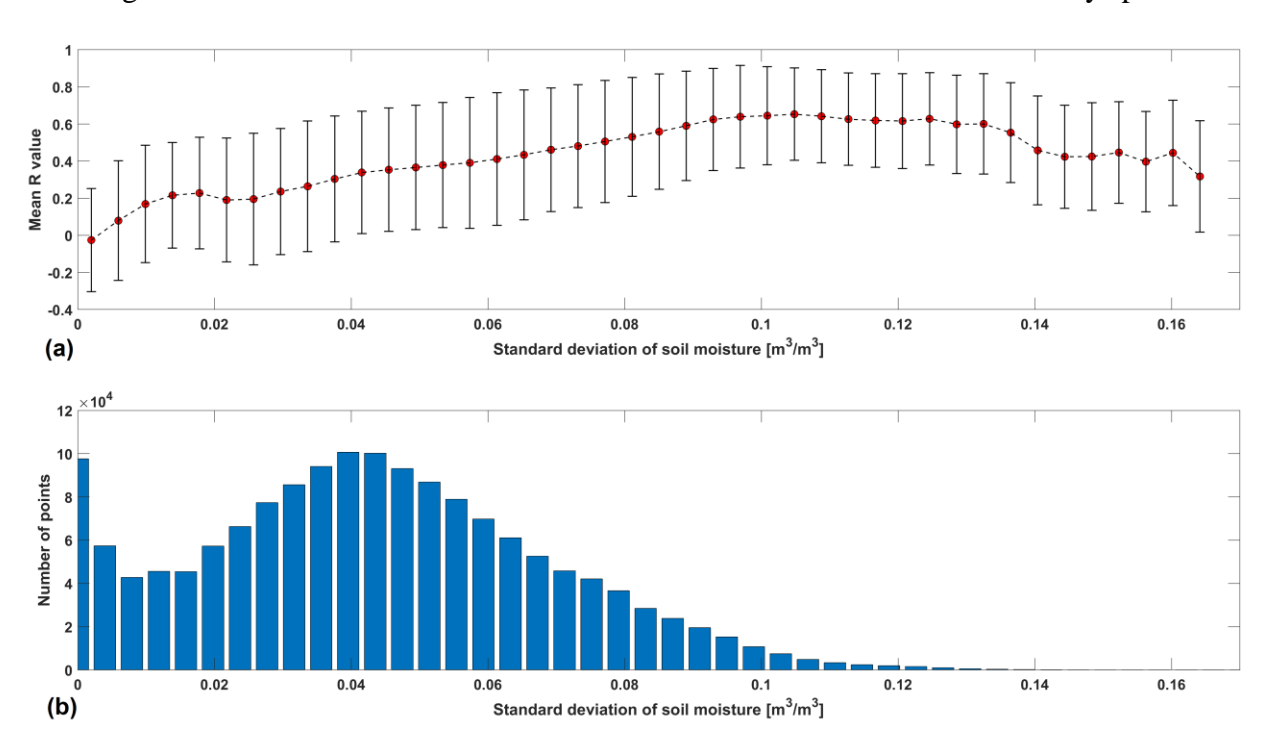


Figure 62: (a) Scatter plot between standard deviation in ERA5-Land soil moisture (see Fig.A5) divided in different bins and the corresponding grid-based R-value between ERA5-Land soil moisture and SMAP HH-pol backscatter. The mean R-value of all the grid-cells corresponding to the standard deviation grid-cells in each bin is represented with circle and error bar represents the ±1 standard deviation of R-values. and (b) the number of points/grids within each bin of standard deviation in ERA5-Land soil moisture.

In Figure 62, it is explained how the standard deviation of ERA5-Land soil moisture impact

the relationship (R-value) between ERA5-Land soil moisture and SMAP HH-pol backscatter. The standard deviation of ERA5-Land soil moisture was distributed in 43 bins and a mean R-value of all the grid-cells corresponding to the standard deviation grid-cells in each bin was estimated. The scatter plot shows that the R-value increases as the standard deviation in soil moisture increases. The increase in R-values suggests that the estimation of the  $\beta$  parameter is more robust if high temporal variability is observed in soil moisture. However, the scatter plot also shows that R-value starts decreasing when the standard deviation is greater than  $\sim 0.1 \text{ m}^3/\text{m}^3$ , but this is not a reliable statistic due to the very lower number of grid cells used for estimating the R-Value (See Fig. A6b). In the future, after the launch of NISAR and once sufficient L-band data is archived, a detailed study will be conducted to analyze the linearity in co-pol SAR observation from L-band and soil moisture, and for a robust estimation of the  $\beta$  parameter.

Relationship of 
$$var[10log10(\sigma_{HH}*(1+\omega KpC_{HH}))] = ((10/ln10)^2 KpC_{HH}^2):$$

$$var[10.log_{10}(\sigma_{HH}.(1+\omega*KpC_{HH}))]$$

$$= 10^2 var[log_{10}(\sigma_{HH})] + var[log_{10}(1+\omega*KpC_{HH})]$$

$$= 10^2 var[log_{10}(1+\omega*KpC_{HH})]$$
(A5)

Since  $var[log_{10}(\sigma_{HH})]=0$ , it's because the  $\sigma_{HH}$  represents the fine-scale measurement of a single grid, and variance cannot be calculated for a single value.

In addition

$$10^{2} var \left[ \frac{1}{log_{e}10} * log_{e} (1 + \omega * KpC_{HH}) \right] = \frac{10^{2}}{log_{e}10^{2}} * var [log_{e} (1 + \omega * KpC_{HH})]$$
 (A6)

$$log_e(1-p) \approx -p - \frac{p^2}{2} \approx -p \tag{A7}$$

$$log_{e}(1 + \omega * KpC_{HH}) = -\omega KpC_{HH} \frac{10^{2}}{log_{e}10^{2}} * var[log_{e}(1 + \omega * KpC_{HH})]$$

$$= \frac{10^{2}}{log_{e}10^{2}} * var[-\omega KpC_{HH}]$$

$$= \frac{10^{2}}{log_{e}10^{2}} * KpC_{HH}^{2} * var[\omega]$$
(A8)

with  $var[\omega] = 1$ 

$$var[10log_{10}(\sigma_{HH} * ((1 + \omega KpC_{HH}))] = \frac{10^2}{log_e 10^2} * KpC_{HH}^2$$
(A9)

The linear regression coefficient model for  $var[\beta']$  and  $var[\Gamma']$  to estimate uncertainty in the algorithm parameters and  $\beta$  and  $\Gamma$ :

$$\hat{y} = \alpha + \beta * \hat{x} + \varepsilon \tag{A10}$$

where for the  $\beta$  calculations, y = SM(C) and  $x = \sigma_{HH}(F_n)$  for a time-series of n - length. If  $\hat{y}$  and  $\hat{x}$  include independent model/instrument noise then,

$$\hat{y} = y + \omega_{y} \tag{A11}$$

$$\hat{\chi} = \chi + \omega_{\chi} \tag{A12}$$

Combining Eq. A10, A11 and A12,

$$y + \omega_{v} = \alpha + \beta * x + \beta \omega_{x} + \varepsilon \tag{A13}$$

Taking average over time series of n - length

$$\bar{y} = \alpha + \beta * \bar{x} \tag{A14}$$

Subtracting above

$$y - \bar{y} + \omega_v = \beta(x - \bar{x}) + \beta * \omega_x + \varepsilon \tag{A15}$$

Now solving for  $\varepsilon$  results in:

$$\varepsilon = (y - \bar{y}) - \beta(x - \bar{x}) + \beta * \omega_x + \omega_y \tag{A16}$$

Squaring above and taking expectations

$$\varepsilon = (y - y) - \beta(x - \bar{x}) - \beta * \omega_x + \omega_y \tag{A17}$$

$$E[\varepsilon^{2}] = E[(y - \bar{y})^{2}] + \beta^{2} * E[(x - \bar{x})^{2}] - \beta^{2} * E[(y - \bar{y})(x - \bar{x})] + \beta^{2} * E[\omega_{x}^{2}] + E[\omega_{y}^{2}]$$
(A18)

 $E[(y-\bar{y})^2] = S_y^2$  is the true physical variability of SM(C) over window n of estimation.  $E[(x-\bar{x})^2] = S_x^2$  is the true physical variability of  $\sigma_{HH}(C)$  over window n of estimation. The term  $E[(y-\bar{y})(x-\bar{x})]$  is the covariance between y and x.

Therefore,

$$E[(y - \vec{y}) * (x - \bar{x})] = \text{cov}[x, y] = r(x, y) * [s_y * s_x]$$
(A19)

Substituting above Eq. A18 in Eq. A19:

$$E[\varepsilon^2] = v\omega[\varepsilon] = S_v^2 + \beta^2 * S_x^2 - \beta^2 * r(x, y) \cdot [Sy \cdot S_x] + \beta^2 * var[\omega_x] + var[\omega_y]$$
 (A20)

Where  $var[\beta] = var[\varepsilon]/(S_x^2 * (n-1))$ 

$$var[\beta'] = \frac{1}{S_x^2*(n-1)} \left\{ S_y^2 + \beta^2 * S_x^2 - \beta * r(x,y) \left[ S_y * S_x \right] + \beta^2 * var[\omega_x] + var[\omega_y] \right\}$$
 (A21)

 $S_y^2 = variance \ of \ SM(C) \ in \ a \ C \ resolution \ grid - cell.$ 

 $S_x^2 = variance \ of \ \sigma_{HH}(C) \ in \ a \ C \ resolution \ grid - cell.$ 

 $\beta$  = nominal slope obtained through linear regression.

 $r(x,y) = correlation \ between \ \sigma_{HH}(C) \ and \ SM(C) \ in \ a \ C \ resolution \ grid - cell.$ 

 $var[\omega_x] = is$  the variance in C resolution soil moisture product.

 $var[\omega_y] = variance \ of \ SAR \ co-pol \ measurement \ noise.$ 

$$var[\Gamma'] = \frac{1}{D_z^2 * (nz - 1)} \left\{ D_x^2 + \Gamma^2 * D_z^2 - \Gamma * k(z, x) [D_z * D_x] + \Gamma^2 * var[\omega_z] + var[\omega_y] \right\}$$
(A17)

 $D_x^2$  = spatial variance of  $\sigma_{HH}(F_n)$  within C resolution grid – cell.

 $D_z^2 = spatial \ variance \ of \ \sigma_{HV}(F_n) \ within \ C \ resolution \ grid - cell.$ 

 $nz = number\ of\ F\ resolution\ grid cells\ within\ C\ resolution\ grid - cell.$ 

 $k(z,x) = correlation \ between \ \sigma_{HH}(F_n) \ and \ \sigma_{HV}(F_n) \ at \ C \ resolution \ grid - cell.$ 

 $\Gamma = nominal slope obtained through linear regression.$ 

 $var[\omega_z] = variance \ of \ SAR \ cross - pol \ measurement \ noise$